



Etudes et évaluation de processus océaniques par des hiérarchies de modèles

Achim Wirth

► To cite this version:

Achim Wirth. Etudes et évaluation de processus océaniques par des hiérarchies de modèles. Planète et Univers [physics]. Université Joseph-Fourier - Grenoble I, 2010. tel-00545911

HAL Id: tel-00545911

<https://theses.hal.science/tel-00545911>

Submitted on 13 Dec 2010

HAL is a multi-disciplinary open access archive for the deposit and dissemination of scientific research documents, whether they are published or not. The documents may come from teaching and research institutions in France or abroad, or from public or private research centers.

L'archive ouverte pluridisciplinaire **HAL**, est destinée au dépôt et à la diffusion de documents scientifiques de niveau recherche, publiés ou non, émanant des établissements d'enseignement et de recherche français ou étrangers, des laboratoires publics ou privés.

Mémoire de Recherche
présenté par

Achim Wirth

pour l'obtention du diplôme
d'Habilitation à Diriger des Recherches
spécialité sciences de la planète
de l'Université de Grenoble

Études et Évaluation de Processus Océaniques par des Hiérarchies de Modèles

date de soutenance
14 / 09 / 2010

composition du jury :

Michael Ghil (ENS / UCLA)	Président
Eric Blayo (Université de Grenoble)	Rapporteur
Yves Morel (SHOM / LEGOS)	Rapporteur
Jürgen Willebrand (IfM Geomar)	Rapporteur
Bernard Barnier (LEGI Grenoble)	Examineur
Uriel Frisch (Observatoire de la Côte d'Azur)	Examineur

Mémoire préparé au Laboratoire des Ecoulements Géophysiques et Industriels
LEGI - 5519 (CNRS / Université de Grenoble)

Vor dem Gesetz (Franz Kafka)

Vor dem Gesetz steht ein Türhüter. Zu diesem Türhüter kommt ein Mann vom Lande und bittet um Eintritt in das Gesetz. Aber der Türhüter sagt, daß er ihm jetzt den Eintritt nicht gewähren könne. Der Mann überlegt und fragt dann, ob er also später werde eintreten dürfen. "Es ist möglich", sagt der Türhüter, "jetzt aber nicht." Da das Tor zum Gesetz offensteht wie immer und der Türhüter beiseite tritt, bückt sich der Mann, um durch das Tor in das Innere zu sehn. Als der Türhüter das merkt, lacht er und sagt : "Wenn es dich so lockt, versuche es doch, trotz meines Verbotes hineinzugehn. Merke aber : Ich bin mächtig. Und ich bin nur der unterste Türhüter. Von Saal zu Saal stehn aber Türhüter, einer mächtiger als der andere. Schon den Anblick des dritten kann nicht einmal ich mehr ertragen." Solche Schwierigkeiten hat der Mann vom Lande nicht erwartet ; das Gesetz soll doch jedem und immer zugänglich sein, denkt er, aber als er jetzt den Türhüter in seinem Pelzmantel genauer ansieht, seine große Spitznase, den langen, dünnen, schwarzen tatarischen Bart, entschließt er sich, doch lieber zu warten, bis er die Erlaubnis zum Eintritt bekommt. Der Türhüter gibt ihm einen Schemel und läßt ihn seitwärts von der Tür sich niedersetzen. Dort sitzt er Tage und Jahre. Er macht viele Versuche, eingelassen zu werden, und ermüdet den Türhüter durch seine Bitten. Der Türhüter stellt öfters kleine Verhöre mit ihm an, fragt ihn über seine Heimat aus und nach vielem andern, es sind aber teilnahmslose Fragen, wie sie große Herren stellen, und zum Schlusse sagt er ihm immer wieder, daß er ihn noch nicht einlassen könne. Der Mann, der sich für seine Reise mit vielem ausgerüstet hat, verwendet alles, und sei es noch so wertvoll, um den Türhüter zu bestechen. Dieser nimmt zwar alles an, aber sagt dabei : "Ich nehme es nur an, damit du nicht glaubst, etwas versäumt zu haben." Während der vielen Jahre beobachtet der Mann den Türhüter fast ununterbrochen. Er vergißt die andern Türhüter, und dieser erste scheint ihm das einzige Hindernis für den Eintritt in das Gesetz. Er verflucht den unglücklichen Zufall, in den ersten Jahren rücksichtslos und laut, später, als er alt wird, brummt er nur noch vor sich hin. Er wird kindisch, und, da er in dem jahrelangen Studium des Türhüters auch die Flöhe in seinem Pelzkragen erkannt hat, bittet er auch die Flöhe, ihm zu helfen und den Türhüter umzustimmen. Schließlich wird sein Augenlicht schwach, und er weiß nicht, ob es um ihn wirklich dunkler wird, oder ob ihn nur seine Augen täuschen. Wohl aber erkennt er jetzt im Dunkel einen Glanz, der unverlöschlich aus der Türe des Gesetzes bricht. Nun lebt er nicht mehr lange. Vor seinem Tode sammeln sich in seinem Kopfe alle Erfahrungen der ganzen Zeit zu einer Frage, die er bisher an den Türhüter noch nicht gestellt hat. Er winkt ihm zu, da er seinen erstarrten Körper nicht mehr aufrichten kann. Der Türhüter muß sich tief zu ihm hinunterneigen, denn der Größenunterschied hat sich sehr zuungunsten des Mannes verändert. "Was willst du denn jetzt noch wissen?" fragt der Türhüter, "du bist unersättlich." "Alle streben doch nach dem Gesetz", sagt der Mann, "wieso kommt es, daß in den vielen Jahren niemand außer mir Einlaß verlangt hat?" Der Türhüter erkennt, daß der Mann schon an seinem Ende ist, und, um sein vergehendes Gehör noch zu erreichen, brüllt er ihn an : "Hier konnte niemand sonst Einlaß erhalten, denn dieser Eingang war nur für dich bestimmt. Ich gehe jetzt und schließe ihn."

Devant la Loi (Franz Kafka)

Devant la loi se dresse le gardien de la porte. Un homme de la campagne se présente et demande à entrer dans la loi. Mais le gardien dit que pour l'instant il ne peut pas lui accorder l'entrée. L'homme réfléchit, puis demande s'il lui sera permis d'entrer plus tard. "C'est possible", dit le gardien, "mais pas maintenant". Le gardien s'efface devant la porte, ouverte comme toujours, et l'homme se baisse pour regarder à l'intérieur. Le gardien s'en aperçoit, et rit. "Si cela t'attire tellement", dit-il, "essaie donc d'entrer malgré ma défense. Mais retiens ceci : je suis puissant. Et je ne suis que le dernier des gardiens. Devant chaque salle il y a des gardiens de plus en plus puissants, je ne puis même pas supporter l'aspect du troisième après moi." L'homme de la campagne ne s'attendait pas à de telles difficultés ; la loi ne doit-elle pas être accessible à tous et toujours, mais comme il regarde maintenant de plus près le gardien dans son manteau de fourrure, avec son nez pointu, sa barbe de Tartare longue et maigre et noire, il en arrive à préférer d'attendre, jusqu'à ce qu'on lui accorde la permission d'entrer. Le gardien lui donne un tabouret et le fait asseoir auprès de la porte, un peu à l'écart. Là, il reste assis des jours, des années. Il fait de nombreuses tentatives pour être admis à l'intérieur, et fatigue le gardien de ses prières. Parfois, le gardien fait subir à l'homme de petits interrogatoires, il le questionne sur sa patrie et sur beaucoup d'autres choses, mais ce sont là questions posées avec indifférence à la manière des grands seigneurs. Et il finit par lui répéter qu'il ne peut pas encore le faire entrer. L'homme, qui s'était bien équipé pour le voyage, emploie tous les moyens, si coûteux soient-ils, afin de corrompre le gardien. Celui-ci accepte tout, c'est vrai, mais il ajoute : "J'accepte seulement afin que tu sois bien persuadé que tu n'as rien omis". Des années et des années durant, l'homme observe le gardien presque sans interruption. Il oublie les autres gardiens. Le premier lui semble être le seul obstacle. Les premières années, il maudit sa malchance sans égard et à haute voix. Plus tard, se faisant vieux, il se borne à grommeler entre les dents. Il tombe en enfance et comme, à force d'examiner le gardien pendant des années, il a fini par connaître jusqu'aux puces de sa fourrure, il prie les puces de lui venir en aide et de changer l'humeur du gardien ; enfin sa vue faiblit et il ne sait vraiment pas s'il fait plus sombre autour de lui ou si ses yeux le trompent. Mais il reconnaît bien maintenant dans l'obscurité une glorieuse lueur qui jaillit éternellement de la porte de la loi. A présent, il n'a plus longtemps à vivre. Avant sa mort toutes les expériences de tant d'années, accumulées dans sa tête, vont aboutir à une question que jusqu'alors il n'a pas encore posée au gardien. Il lui fait signe, parce qu'il ne peut plus redresser son corps roidi. Le gardien de la porte doit se pencher bien bas, car la différence de taille s'est modifiée à l'entier désavantage de l'homme de la campagne. "Que veux-tu donc savoir encore ?" demande le gardien. "Tu es insatiable." "Si chacun aspire à la loi", dit l'homme, "comment se fait-il que durant toutes ces années personne autre que moi n'ait demandé à entrer ?" Le gardien de la porte, sentant venir la fin de l'homme, lui rugit à l'oreille pour mieux atteindre son tympan presque inerte : "Ici nul autre que toi ne pouvait pénétrer, car cette entrée n'était faite que pour toi. Maintenant, je m'en vais et je ferme la porte."

Remerciements

Je tiens à remercier en premier lieu tous les membres du jury. Merci à Eric Blayo, Yves Morel et Jürgen Willebrand d'avoir accepté d'être rapporteur et à Bernard Barnier, Michael Ghil et Uriel Frisch d'avoir examiné mon travail.

Ce mémoire est aussi une occasion de remercier tout ceux qui m'ont guidé et accompagné dans ma recherche. C'est Uriel Frisch qui m'a appris la démarche scientifique et qui m'a permis de conserver nos relations scientifiques et personnelles. Michael Ghil et Jürgen Willebrand m'ont guidé vers l'océanographie et l'assimilation de données avec beaucoup de confiance. Bernard Barnier et Jacques Verron ont accompagné ma recherche dans ces dernières années avec de bons conseils.

Je remercie aussi Jean-Michel Brankart, Pierre Brasseur, Emmanuel Cosme, Maeva Doron et Jacques Verron pour leur lecture critique d'une première version du manuscrit et les autres membres de l'équipe MEOM et du LEGI pour leurs conseils, leur aide et leur soutien.

Un grand merci à tous ceux qui ont travaillé, discuté avec moi et m'ont aidé durant ces dernières années.

Table des matières

I	Etudes de processus océaniques à petites échelles et leurs paramétrisations	1
1	Avant-propos	3
2	Comprendre la dynamique océanique	5
2.1	Simuler n'est pas expliquer	5
2.2	Études et réseau de processus	6
2.3	Hierarchie de Types de Modèles	7
2.4	Rôle de l'assimilation de données	10
2.5	Ma recherche dans le contexte conceptuel	11
3	Dynamique océanique et notion d'échelle	15
3.1	La circulation océanique à grande echelle soumise à l'influence de la submésoscale	15
3.2	Processus submésoscales et leurs actions	21
3.3	Modèles mathématiques et numériques adaptées aux études de la dynamique submésoscale	22
3.4	Retour à la grande echelle par l'assimilation de données	23
3.5	Ma Recherche dans le Contexte Dynamique	24
II	Curriculum Vitae	31
III	Publicaions récentes	39
4	Etudes de Processus Océanographiques	41
4.1	Variability of the Great Whirl from observations and models	41
4.2	The parametrization of baroclinic instability in a simple model	59
4.3	A non-hydrostatic flat-bottom ocean model entirely base on Fourier expansion	73
4.4	Tilted convective plumes in numerical experiments	91
4.5	Mean Circulation and Structures of Tilted Ocean Deep Convection	103
4.6	Estimation of friction parameters and laws in 1.5D shallow-water gravity currents on the f-plane by data assimilation	118

4.7	On the basic structure of oceanic gravity currents	130
4.8	Estimation of friction laws and parameters in gravity currents by data assimilation in a model hierarchy	144
4.9	On the numerical resolution of the bottom layer in simulations of oceanic gravity currents	161
IV	Cours d'Océanographie Physique	173
A	Attestation de réussite au diplôme	243
B	Rapports du jury et des rapporteurs	245

Première partie

Etudes de processus océaniques à petites échelles et leurs paramétrisations

Chapitre 1

Avant-propos

Ce mémoire, préparé en vue d’une habilitation à diriger des recherches, contient mes travaux scientifiques principaux effectués depuis ma thèse.

Cette monographie est composée de trois parties. Dans la première j’expose d’abord quelques réflexions personnelles sur des questions conceptuelles de la recherche en océanographie physique d’aujourd’hui. Cette discussion considère la relation entre observations, expériences de laboratoire, modèles physiques, mathématiques, numériques et assimilation de données. Je me place dans le contexte de l’océanographie physique mais les idées sont applicables à tous les domaines des sciences de la terre bénéficiant d’une description mathématique. Je trouve que de telles réflexions, même si elles ne sont pas au goût de tout le monde, sont essentielles pour considérer notre démarche avec un certain recul par rapport à notre travail de recherche de tous les jours, et qu’une thèse d’habilitation à diriger des recherches est une bonne occasion d’en parler. En effet, cette thèse d’habilitation n’est pas seulement un résumé des travaux effectués, mais plus encore ; son utilité principale est qu’elle présente une base pour mes futurs orientations et directions de recherche. Dans ce contexte les questions conceptuelles sont au moins aussi importantes que les considérations scientifiques.

Je discute ensuite quelques aspects de la dynamique des processus à petite échelle, c.a.d. des processus qui ne sont aujourd’hui pas explicitement résolus par les modèles océaniques de la circulation globale (OGCM) et qui doivent être paramétrés dans de tels modèles. Ces processus sont le sujet principal scientifique de cette habilitation à diriger des recherches. Ces échelles, trop petites pour l’océanographie “classique” et trop grandes pour la dynamique des fluides “classique”, s’étalent sur environ quatre ordres de magnitude. Les études de leur dynamique montrent qu’elles ne jouent pas un rôle passif, animées par les échelles supérieures, mais au contraire, elles sont un participant actif, agissant sur la dynamique à grande échelle. En même temps il me semble peu probable qu’une “théorie universelle” de la dynamique océanique à ces échelles puisse exister, mais au contraire, que nous nous dirigeons vers une “zoologie” des différents processus dont chacun demande et mérite d’être étudié séparément avant de regarder leurs interactions et actions sur la dynamique à des échelles supérieures ainsi que leur importance dans des processus de la dynamique globale, comme le transfert d’énergie des grandes vers les

petites échelles. La recherche de tels processus, leurs études et leurs paramétrisation a été le sujet principal de mes recherches des six dernières années. C'est cette direction de recherche que je continuerai.

Dans la deuxième partie se trouve mon *Curriculum Vitae* avec la liste de mes principales publications scientifiques.

La troisième partie expose mes travaux scientifiques principaux effectués après ma thèse, au sujet des processus océaniques à petite échelle.

La quatrième partie représente mon cours d'océanographie physique que j'ai enseigné à plusieurs reprises dans le master M2R "Océan, Atmosphère, Hydrologie, Génie hydraulique et Environnement" de l' "Observatoire des sciences de l'Université de Grenoble" (OSUG) et au master M1 "Sciences de la Terre" à l'Ecole Normale Supérieure de Lyon dans le département "Sciences de la Terre". Ce cours donne une vue personnelle de l'océanographie et essaye de montrer qu'on peut enseigner l'océanographie de façon rigoureuse et systématique à des étudiants non spécialistes ayant des notions sur les équations aux dérivées partielles. Ce cours est basé sur la discussion des résultats de modèles mathématiques, dérivés de façon systématique des équations de Navier-Stokes, et sa démarche s'accorde parfaitement avec les idées soulevées dans le chapitre suivant cet avant-propos.

Le rapport du jury et des rapporteurs se trouvent en annexe.

Chapitre 2

Comprendre la dynamique océanique

“Je ne sais si je dois vous entretenir des premières méditations que j’y ai faites ; car elles sont si métaphysiques et si peu communes, qu’elles ne seront peut-être pas au goût de tout le monde : et toutefois, afin qu’on puisse juger si les fondements que j’ai pris sont assez fermes, je me trouve en quelque façon contraint d’en parler.” (Descartes, Discours sur la méthode, Quatrième Partie)

2.1 Simuler n’est pas expliquer

Le titre de cette section nous propulse dans la difficulté de la compréhension du système terrestre, dont l’océan n’est qu’une partie, ainsi qu’un exemple. Les modèles numériques et les ordinateurs sur lesquels on les intègre, ont atteint aujourd’hui un niveau tel que leurs résultats nous montrent des images qui sont qualitativement et quantitativement comparables à nos impressions et mesures du monde réel. Nous possédons alors des outils qui font la connexion directe entre les mesures de la dynamique des océans et les lois fondamentales de la physique, à la base de ces modèles. Comme les modèles numériques sont de purs produits de la création humaine, il semble évident de conclure que notre compréhension de la nature est quasi parfaite car nous pouvons calculer ou imiter cette même nature quasi parfaitement. L’expression : *“je comprends ce que j’ai créé”* ne représente, toutefois, pas la réalité. Même si la création est faite à partir d’éléments compris. Les modèles numériques sont, en effet, construits à partir des équations exprimant des lois fondamentales de la physique que nous comprenons. Le saut entre ces lois physiques et les résultats des intégrations d’un modèle océanique réaliste global est souvent trop grand pour permettre une vraie compréhension humaine. La définition de la “compréhension humaine” pour un scientifique que j’adopte est la suivante : *nous avons compris un processus si nous pouvons expliquer avec des mots, son fonctionnement ainsi que sa réaction à des variations des conditions initiales ou des paramètres extérieurs.* Cette explication inclut nécessairement une capacité de prédiction déterministe ou statistique.

Nous avons aujourd’hui en océanographie à notre disposition des modèles de plus en plus complets, donnant des prévisions de plus en plus précises de la circulation océanique, que nous comprenons de moins en moins, car actuellement la complexité des modèles

croît plus vite que la compréhension humaine. Comme la croissance de la complexité des modèles est liée à l'explosion de la puissance de calcul des ordinateurs, le fossé entre la compréhension et les résultats des simulations s'élargira dans le futur, et il est le devoir des chercheurs de veiller à ce que le fossé ne devienne pas trop large. Eviter une séparation entre modèles numériques et compréhension est, aujourd'hui, un défi dans plusieurs domaines de recherche.

Mais qu'est-ce que veut dire comprendre un système naturel, comme la dynamique océanique ? D'abord restreignons nous à comprendre certains processus importants de la dynamique naturelle. Si nous avons identifié et compris les processus importants ainsi que leurs interactions, nous avons élargi notre compréhension de la dynamique d'un système naturel.

2.2 Études et réseau de processus

La seule façon d'assurer notre compréhension de la dynamique océanique est de la décomposer en processus. La première étape est alors d'identifier les processus importants pour la dynamique étudiée. La deuxième étape est le choix d'un ou plusieurs modèles physiques dans lesquels le processus en question est (quasi) isolé. Un modèle physique représente une expérience de laboratoire ou une situation physique, réelle ou hypothétique. Ce modèle doit être assez complet et réaliste pour inclure les principaux aspects du processus mais assez simple pour permettre une compréhension à l'échelle humaine. Le choix du modèle physique est une étape décisive en recherche, demandant de l'intuition et de l'expérience scientifique. Le travail sur le modèle, ensuite, est souvent systématique.

Si tout processus important peut être compris (pas nécessairement par une seule personne) et sa dynamique expliquée à l'aide des résultats d'un ou plusieurs modèles, et si nous pouvons construire un réseau de processus compris, connectant un modèle océanique réaliste global aux équations de Navier-Stokes et les conditions aux limites, nous avons certainement augmenté notre compréhension de la dynamique des océans.

Le point de départ est un petit nombre de lois fondamentales de la physique comme la conservation de la masse et de l'inertie pour l'écoulement d'un fluide. La plupart des modèles sont directement dérivés de ces lois, mais beaucoup de résultats provenant de tels modèles ne peuvent pas être compris à partir des seules lois fondamentales de la physique. Il faut construire un réseau de modèles ou expériences physiques intermédiaires divisant le grand saut en petits pas, chacun compréhensible à l'échelle humaine, à l'aide des résultats provenant d'autres modèles. Ces modèles physiques forment un réseau complexe qui ne possède pas nécessairement une structure hiérarchique. Prenons l'exemple des modèles pour étudier la convection profonde océanique, quelques-uns des modèles physiques utilisés sont : un bassin avec une géométrie donnée, avec ou sans rotation, avec un forçage convectif homogène ou localisé, avec un ou plusieurs traceurs actifs, avec ou sans stratification, avec ou sans écoulement à grande échelle. Cette liste peut être étendue, mais il est clair qu'il n'y a pas un ordre hiérarchique entre ces modèles. Plus encore, ces modèles et leurs résultats ne peuvent souvent pas être comparés ou mis en relation directe, car ils considèrent des

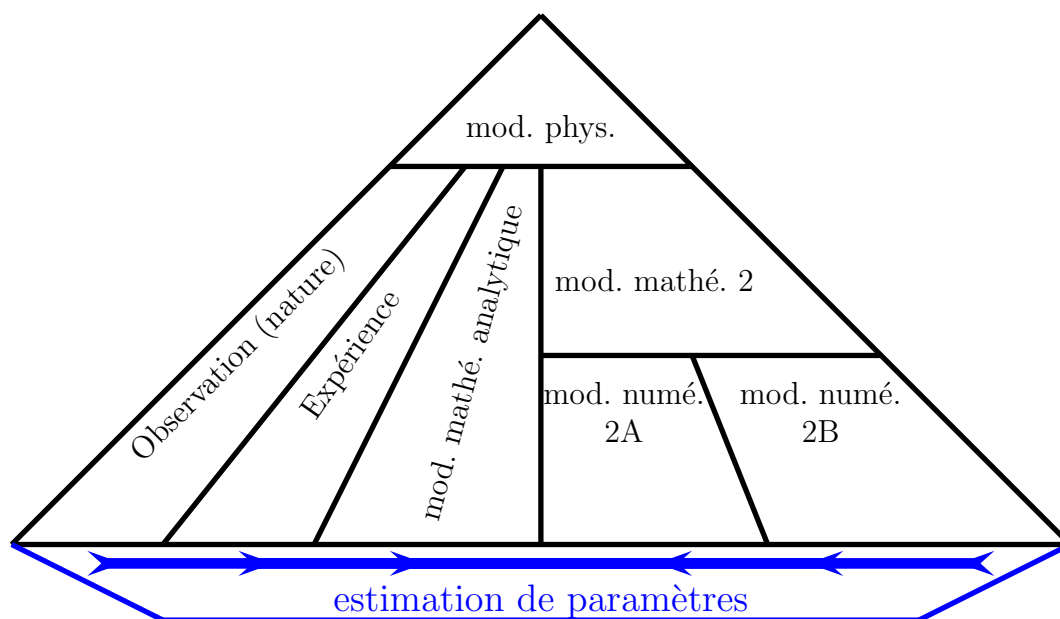


FIG. 2.1 – Pyramides (diamant) de la hiérarchie de modèles physiques, mathématiques et numériques ainsi que l'effet connectant, solidifiant, de l'estimation de paramètres

aspects différents d'un même processus. Chaque modèle physique considère un aspect différent du même processus, la convection. Mais à chaque modèle ou situation physique, on peut associer une *hiérarchie de types de modèles* comme on le démontrera dans la section suivante.

2.3 Hiérarchie de Types de Modèles

Avant de poursuivre, il est essentiel de bien cerner ce que nous appelons un "modèle" et, surtout, de distinguer entre des différents types de modèle, au nombre de trois :

(i) **Modèle physique** : présente une expérience ou situation physique (réelle, idéalisée, virtuelle). Ce modèle peut être une partie d'un système naturel, une expérience de laboratoire ou un gedankenexperiment (expérience virtuelle) pouvant être décrit par des mots sans faire référence au langage mathématique. Des exemples sont un canal rectangulaire, de taille donnée, avec un gradient de densité donné ou un bassin rectangulaire avec un forçage de traînée à la surface donné. En effet le modèle physique peut correspondre à une situation virtuelle comme la dynamique océanique sur une planète sans continent ni structure topographique (water planet), ou la circulation dans un plan β équatorial, pour ne mentionner que deux modèles physiques souvent considérés et ne possédant pas de réalisation réelle. Souvent il peut être formulé comme un modèle mathématique, mais il existe indépendamment d'une telle formulation.

(ii) **Modèle mathématique** : est l'écriture d'un modèle physique en langage mathématique (équations) comme, par exemple, les équations quasi-géostrophiques bicouches avec un

gradient vertical de vitesse, pour étudier l'instabilité barocline (modèle de Phillips) ou les équations primitives dans un bassin réaliste soumise à des flux de surface avec une fonction d'état plus ou moins réaliste ; le modèle de Lorenz pour étudier des aspects chaotiques de la dynamique convective. Le modèle mathématique bien posé ne possède aucune ambiguïté. Un même modèle physique, comme par exemple un tourbillon océanique, peut être modélisé par différents modèles mathématiques, basés sur différents types d'équations, comme : les équations de Navier-Stokes, les équations primitives, les équations quasi-géostrophiques, les équations de Saint-Venant, mono- ou multi-couches. Ce modèle mathématique peut être étudié avec des méthodes analytiques, semi-analytiques ou numériques. Tout modèle mathématique sensé fait nécessairement référence à un modèle physique, mais existe indépendamment de son éventuelle formulation comme modèle numérique. Nous disons qu'un modèle mathématique est analytique si on obtient des solutions sans passer par un modèle numérique.

(iii) **Modèle numérique** : est la mise en œuvre d'un modèle mathématique qui peut être intégré par un ordinateur. Les modèles numériques sont des outils. Dans sa réalisation des choix numériques, modèle aux différences finies, éléments finis ou spectraux, schéma d'advection, de discrétisation temporelle, sont importants. Des exemples sont des codes océaniques comme NEMO, ROMS, HAROMOD, ...

Il y a clairement une *hiérarchie* parmi ces trois types de modèles, car il n'y a pas de sens de construire un modèle numérique sans qu'il soit dérivé d'un modèle mathématique. Un modèle mathématique qui ne fait pas référence à un modèle physique, une situation physique réelle ou hypothétique, est un objet purement mathématique sans utilité réelle. Le modèle physique représente ou est le seul lien avec le monde réel, sensé et que donc, s'il n'est pas clairement identifié aucune comparaison à des données d'observations n'est (même potentiellement) possible. La structure hiérarchique se voit aussi dans le fait, déjà mentionné, qu'un modèle physique peut être décrit par plusieurs modèles mathématiques, qui à leur tour peuvent être approchés par des modèles numériques différents. Par contre, pour un modèle numérique il y a un et un seul modèle mathématique, et à un modèle mathématique correspond une seule dynamique de système naturel. Cette situation engendre naturellement une structure hiérarchique schématisée en fig. 2.1. En recherche, cette hiérarchie entre les trois types de modèles n'est souvent pas respectée, par ignorance ou par abus de langage, et amène à des confusions. Un exemple : on dit : "un modèle de la circulation océanique globale (OGCM) à deux degrés de résolution". Mais les équations qu'on résout, le modèle mathématique, ne font pas référence à la résolution. La résolution du modèle numérique choisi est une fonction des coefficients de friction et d'autres paramètres du modèle mathématique, ainsi que du modèle numérique comme le schéma d'advection, le type du schéma temporel et la longueur du pas de temps. L'ambiguïté apparaît clairement si on parle d' "un modèle à deux degrés de résolution" tout court, car d'une simulation à l'autre le choix du coefficient de friction (turbulente) peut varier et il n'est pas clair ce que "un modèle à deux degrés de résolution" veut dire. Aucune ambiguïté n'existe si on définit clairement le modèle mathématique d'abord, fixant entre autres les paramètres de friction, et ensuite on l'intègre avec un ou plusieurs modèles numériques. Le modèle mathématique bien posé possède une seule solution que l'on peut approcher

par des calculs numériques. Cette approche fonctionne de mieux en mieux en augmentant par exemple la résolution ou en diminuant le pas de temps. Des chercheurs peuvent être en désaccord sur la résolution à utiliser ; c'est un choix important, mais secondaire si le modèle mathématique est bien posé. Un "modèle à deux degrés de résolution" n'a pas de solution unique. En effet, il n'a pas de solution du tout si on choisit par exemple les valeurs de friction trop petite : il "explose".

En reprenant des arguments de la section précédente nous pouvons argumenter qu'un ensemble de modèles physiques forme un réseau auquel on ne peut pas toujours associer une structure hiérarchique. La même chose est vraie pour des modèles mathématiques ou numériques. Mais à chaque modèle physique on peut associer une *hiérarchie de types de modèles* comme démontré ici et chaque modèle, de tout type, doit être membre d'une telle hiérarchie.

Comparer ou mettre en relation des modèles de types différents revient à comparer des carottes et des navets ; c'est un contresens scientifique. Mais attention deux modèles physiques (ou mathématiques) peuvent être comparés sur la base des résultats de leurs modèles numériques.

Le développement de l'océanographie de nos jours peut être vu comme un développement de telles structures hiérarchiques. Si le réseau qu'elles forment est assez dense, et si chaque structure est assez solide, la compréhension d'un processus est assurée. Chaque structure hiérarchique doit ressembler à un diamant, solide, clair, complètement transparent et sans défaut majeur (voir Fig. 2.1). Le but principal de notre recherche doit toujours être l'étude des modèles physiques et nous ne devons jamais perdre le contact avec de tels modèles. Ce n'est pas toujours facile, car nous passons presque tout notre temps à travailler avec des modèles mathématiques et numériques.

A côté des trois types de modèles cités il y a des expériences de laboratoire et les observations du système naturel pour compléter l'étude d'un processus, comme nous l'enseigne la fig. 2.1.

L'expérience physique permet de confronter les théories scientifiques à la réalité, créant une connexion entre le monde des pensées et le monde matériel. Le progrès galopant des ordinateurs a permis, à partir de la deuxième moitié du XX^{ème} siècle, d'ajouter aux expériences physiques des expériences numériques. L'expérience numérique de Fermi-Pasta-Ulam en 1953 sur l'équipartition d'énergie d'un système non-linéaire est souvent citée comme point de départ de cette nouvelle science, l'expérience numérique, qui domine aujourd'hui tant de domaines scientifiques. En science de la terre, les expériences numériques sont souvent la seule source de données en l'absence de données d'expériences physiques. Aujourd'hui il n'existe pas d'expérience physique de l'écoulement d'un fluide sur une surface sphérique avec une surface libre, pour ne nommer qu'un seul exemple. Dans le cas où des expériences physiques sont possibles, elles sont souvent beaucoup plus coûteuses que l'expérience numérique correspondante. Toutefois, il ne faut jamais oublier que les expériences numériques sont des solutions approchées d'un modèle mathématique et ne remplace en aucun cas les observations ou des expériences physiques représentant le monde réel.

La relation entre le modèle physique, un modèle mathématique et un modèle numérique

au sein d'une hiérarchie, c'est-à-dire les relations dans la direction verticale dans la fig. 2.1, sont souvent systématiques. Trouver un modèle mathématique pour un modèle physique consiste dans la plupart des cas en un choix raisonné parmi certains candidats, comme modèles de Boussinesq, quasi-géostrophique ou de Saint Venant pour un problème de dynamique de fluide géophysique. Les cas pour lesquels l'émergence du modèle mathématique est le pas innovateur, comme le modèle de Lorenz pour l'étude de la dynamique chaotique de la convection, sont des exceptions remarquables.

La relation entre une expérience de laboratoire, une expérience numérique et un modèle analytique dans une même hiérarchie, correspondant à un même modèle physique, c'est-à-dire les relations dans la direction horizontale dans la fig. 2.1, ne bénéficient aujourd'hui pas encore d'un tel cadre systématique. Ces relations verticales et horizontales sont d'une nature différente. Les premières sont déductives, et les secondes sont de nature essentiellement statistiques. Une comparaison entre observations et/ou expériences et/ou modèle analytique et/ou modèle numérique est inductive par nature et repose nécessairement sur une connaissance statistique des incertitudes des éléments à comparer (voir Poincaré 1899) Nous essayons de rendre ces relations horizontales systématiques en utilisant l'assimilation de données comme décrite dans la section suivante. L'assimilation de données peut rendre ces relations horizontales plus systématiques, solidifier la pyramide de types de modèles et la rendre plus solide, comme on le démontre dans la section suivante.

2.4 Rôle de l'assimilation de données

Dans les sciences de la terre l'assimilation de données est, de nos jours, principalement utilisée pour assimiler ou intégrer des observations dans un modèle numérique et mieux estimer l'état du système. L'exemple type est la prévision météorologique dans laquelle l'assimilation des données d'observations sert à estimer au mieux l'état actuel de l'atmosphère pour une meilleure prévision de son évolution future. Dans ce cas l'assimilation de données peut être vue comme un outil technique.

Pour évaluer une théorie analytique à l'aide des résultats d'expériences, physiques ou numériques, il suffit souvent de mesurer une ou plusieurs variables clés. La même chose est vraie si on demande d'ajuster une ou quelques variables dans un modèle analytique linéaire. De cette façon, on arrive à connecter le modèle analytique aux résultats des expériences physiques ou numériques. Pour connecter un modèle mathématique, avec une grande nombre de degrés de libertés et/ou une dynamique chaotique, directement, sans passer par un modèle analytique, à une expérience physique ou à un autre modèle mathématique, un formalisme systématique est nécessaire. L'assimilation de données fournit un tel formalisme.

Dans nos applications, nous utilisons l'assimilation pour cerner la physique en estimant quelques paramètres clés dans un modèle mathématique, qui ne permet pas de solution analytique, mais nécessite une intégration numérique. Plus précisément l'exemple considéré dans ma recherche (voir 4.6 & 4.8) sont les lois et paramètres de friction d'un courant gravitaire que nous estimons en comparant, à l'aide de l'assimilation de données,

des modèles mathématiques de complexités différentes. Le premier est un modèle basé sur les équations de Navier-Stokes avec une condition aux limites d'adhérence au fond, la friction est alors engendrée implicitement par la dynamique interne du modèle. Le deuxième est un modèle de Saint-Venant dans lequel les lois de friction sont paramétrées par des termes de friction. En ajoutant un schéma d'assimilation de données au modèle de Saint Venant et en assimilant les données du modèle de Navier-Stokes, nous avons pu déterminer les coefficients et lois de friction (voir 4.6 & 4.8). L'assimilation nous a permis de connecter deux modèles mathématiques de complexité différent de façon systématique et d'augmenter notre compréhension du processus étudié.

En systématisant la connexion horizontale de la fig. 2.1 à l'aide de l'assimilation de données, notre structure hiérarchique devient plus claire, plus solide, plus transparente, comme un diamant.

2.5 Ma recherche dans le contexte conceptuel

Dans ce contexte des différents modèles et types de modèles, réseaux et hiérarchies, les directions et démarches de recherche sont nombreuses afin d'augmenter la compréhension de la dynamique océanique. Dans ma recherche je me suis toujours fixé le but d'étudier un certain nombre de processus non-linéaires de la dynamique océanique comme : le Great Whirl (voir section 4.1), l'instabilité barocline (voir section 4.2), la convection (voir section 4.5) et la dynamique d'un courant gravitaire (voir section 4.6 4.7 4.8 & 4.9). Je travaille alors toujours sur un modèle physique en construisant moi-même toute la structure hiérarchique associée. Le premier pas, le choix du bon modèle physique est souvent le plus difficile demandant une bonne intuition et expertise scientifique. Ensuite, vient le choix du ou des bons modèles mathématiques, souvent il est astucieux d'en avoir plusieurs de complexités différentes, pour permettre une meilleure compréhension de la dynamique étudiée.

Prenons l'exemple de mes travaux sur le Great Whirl. Ce tourbillon de 300km de diamètre apparaît tous les ans au large de la côte Somalienne. J'ai étudié sa dynamique dans des observations in situ, de données satellitaires, à l'aide d'un modèle de la dynamique de l'Océan Indien basé sur les équations primitives et un modèle shallow water avec une haute résolution spatiale dans les directions horizontales. En construisant un modèle shallow water et en validant son comportement j'ai pu différencier entre la variabilité inter-annuelle externe de la dynamique du Great Whirl, c.a.d. les différences de son comportement causées par la variabilité inter-annuelle du forçage du vent, et la variabilité interne due à la dynamique chaotique du système. Une telle différenciation est clef pour évaluer la capacité de prévision des courants, qui dans cette région gouvernent la production biologique. Cette différenciation est aussi essentielle pour clarifier les relations horizontales dans une structure hiérarchique (transformer la pyramide en diamant dans fig 2.1), pour comparer les observations d'un système chaotique aux résultats des simulations d'une dynamique chaotique. En effet, on ne peut pas espérer que la différence entre les observations et les résultats de simulations numériques sont inférieurs à la variabilité

interne, chaotique, du système, même si on dispose d'un modèle parfait. Ce travail peut être vu d'une part comme une étude de la dynamique du Great Whirl avec plusieurs modèles et d'autre part comme une étude conceptuelle de comparaison de données de deux modèles chaotiques.

La convection océanique est un processus clef de la circulation thermohaline. Dans ma recherche sur la convection, certains aspects des résultats des simulations des équations de Boussinesq tri-dimensionnelles sur l'alignement des panaches convectifs dans la direction du vecteur de rotation sont interprétés par un modèle analytique linéaire, dérivé directement du théorème de Taylor-Proudman-Poincaré. J'ai démontré ceci dans le cas d'une seule panache convectif ainsi que pour le cas d'un refroidissement homogène amenant à un ensemble des plumes interagissant de façon chaotique. La stratification de température dans la zone convective est interprétée par un modèle semi analytique d'équation KPP. La paramétrisation KPP est largement utilisée en océanographie numérique pour représenter les processus d'échange des traceurs et de l'inertie dans la direction verticale. Dans ce cas j'ai pu déterminer les valeurs des paramètres libres du modèle KPP à l'aide des résultats de mes simulations des équations de Boussinesq, faites avec mon propre code HAROMOD (voir 4.3).

Au cours de mes travaux sur la dynamique des courants gravitaires, j'ai construit une chaîne de trois modèles mathématiques de complexité décroissante, tous dérivés du même modèle physique idéalisé : un courant gravitaire homogène dans la direction transverse à la pente. Les modèles mathématiques sont : un modèle de Boussinesq de 2.5 dimensions, un modèle de Saint Venant de 1.5 dimensions et un modèle basé sur l'équation de la chaleur uni-dimensionnelle. J'ai construit et programmé ces trois modèles moi même. La comparaison entre les résultats des simulations numériques de ces trois modèles permet une très bonne compréhension de la dynamique du modèle physique, à partir duquel les trois modèles mathématiques sont dérivés. L'ajustement des paramètres dans le modèle de Saint Venant a été fait de façon systématique à l'aide de l'assimilation de données provenant du modèle de Boussinesq. L'assimilation de données a permis une liaison systématique de ces deux modèles mathématiques en liant leurs modèles numériques. De telle façon nous avons démontré que la friction de fond, linéaire et quadratique, gouverne la dynamique d'un tel courant gravitaire. Le modèle de Saint Venant à son tour nous renseigne sur le comportement du modèle de Boussinesq. La dynamique de la veine, la partie épaisse, du courant gravitaire est bien décrit par un modèle basé sur l'équation de la chaleur où le coefficient de diffusion est calculé analytiquement dans le cas d'une friction linéaire. Ceci démontre que la dynamique de la veine est bien gouvernée par le pompage d'Ekman au fond. Nous arrivons, alors, à une meilleure compréhension de la dynamique du modèle physique : un courant gravitaire sur un plan incliné en rotation, en combinant et comparant de façon systématique des modèles mathématiques de complexité différente, ainsi que leurs représentants numériques. Cette structure hiérarchique est liée par une comparaison où ceci est possible. Dans le cas contraire la liaison est faite de façon systématique avec l'assimilation de données.

Toute ma recherche peut être interprétée par la pyramide (diamant) représentée en fig. 2.1. C'est dans ce cadre conceptuel que j'envisage de poursuivre ma recherche choi-

sisant des processus de la dynamique océanique qui sont à la fois importants et dont la complexité permet une compréhension des propriétés non triviales. Pour un tel processus je construirai la pyramide ou le diamant composés d'un ou plusieurs modèles mathématiques et numériques que je comparerai et lierai par l'assimilation de données.

Chapitre 3

Dynamique océanique et notion d'échelle

Après un premier chapitre où j'ai dessiné le cadre conceptuel de la recherche en science de la terre en général et de ma recherche en particulier, je place ici mes études sur les processus océaniques à petite échelle, dans le contexte de la recherche sur la dynamique des océans à grande échelle et du climat. L'écriture de ce chapitre est partiellement inspiré par Müller *et al.* (2002, 2005), Wunsch & Ferrari (2004) et Vallis (2006).

3.1 La circulation océanique à grande échelle soumise à l'influence de la submésoscale

Si on considère la circulation globale des océans, à l'échelle des bassins océaniques en espace et de plusieurs années en temps, nous distinguons aujourd'hui principalement deux types de circulation. La première, et la plus facilement observée, est la *circulation de gyre*. Elle consiste dans la circulation horizontale des masses d'eau avec une forte intensification des courants sur les bords ouest, due à la variation latitudinale du paramètre de Coriolis, conduisant à des vitesses maximales dépassant 1 m/s, ainsi qu'une plus faible recirculation à l'intérieur des océans. Cette circulation de gyre peut être représentée par une fonction de courant dans le plan horizontal. La fonction de courant d'une telle circulation, le gyre de l'Atlantique du Nord, est visible dans la fig. 3.1. La circulation gyre joue un rôle important dans le transport de chaleur des faibles vers les hautes latitudes et gouverne une partie du climat à l'échelle régionale et globale.

Superposée à cette circulation est la *circulation d'overtopping méridionale*, aussi appelée *circulation thermohaline*, une circulation qui consiste dans la plongée des masses d'eaux denses, car salées et froides, en haute latitude ainsi qu'une remontée de ces masses d'eau à des latitudes plus faibles. Cette circulation peut être représentée par une fonction de courant dans le plan formé par la direction latitudinale et verticale. Une telle fonction de courant est représentée dans la fig. 3.2. Le transport en masse d'eau associé à la circulation thermohaline est plus petit que celui de la circulation de gyre. L'intérêt de

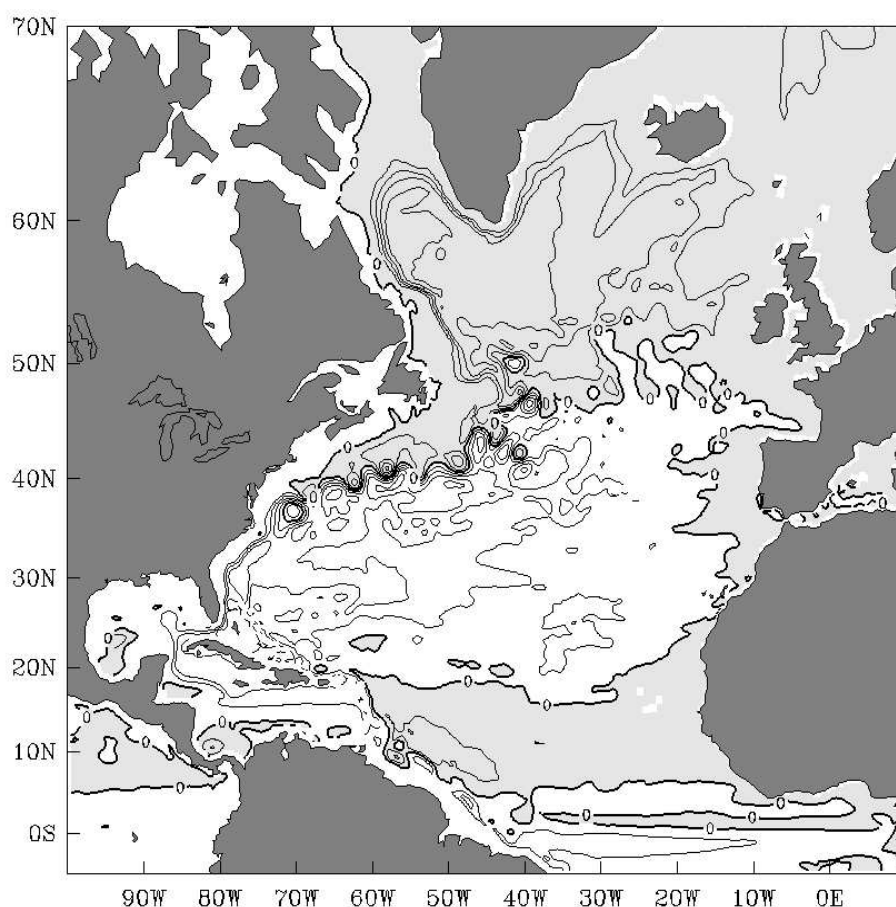


FIG. 3.1 – Moyenne annuelle de la fonction de courant de transport de la circulation gyre de l'Atlantique du Nord est pour l'année 1988. Les lignes de contour sont espacées de 10 Sv ($1\text{Sv} = 10^6\text{m}^3\text{s}^{-1}$). Les résultats proviennent d'une intégration numérique à une résolution d'un $1/4^\circ$ réalisée dans le cadre du projet DRAKKAR. On voit clairement le Gulf Stream sur le bord ouest et une recirculation plus faible à l'intérieur de l'océan.

l'étude de la circulation thermohaline réside dans son importance pour la dynamique du climat. Elle transporte de fortes quantités de chaleur des faibles aux hautes latitudes, et évacue le CO_2 présent dans les couches de surface vers les profondeurs des océans où il est coupé du contact avec l'atmosphère pendant plusieurs centaines d'années. La circulation thermohaline montre une variabilité sur des échelles de temps climatiques. Cette circulation est aussi très sensible au changement de densité de l'eau de surface en haute latitude. En effet, des changements d'apport d'eau douce par la fonte de glaciers en Amérique du Nord et du Groenland sont responsables de réponses catastrophiques de la circulation thermohaline. Un exemple est donné par les événements de Heinrich, espacés de quelques milliers d'années : la libération d'une grande quantité d'eau douce et d'icebergs dans l'Atlantique Nord, due à l'effondrement de la calotte glaciaire sur l'Amérique du Nord est à la source du changement de la circulation thermohaline. On peut aussi citer

3.1. LA CIRCULATION OCÉANIQUE À GRANDE ECHELLE SOUMISE À L'INFLUENCE DE LA S

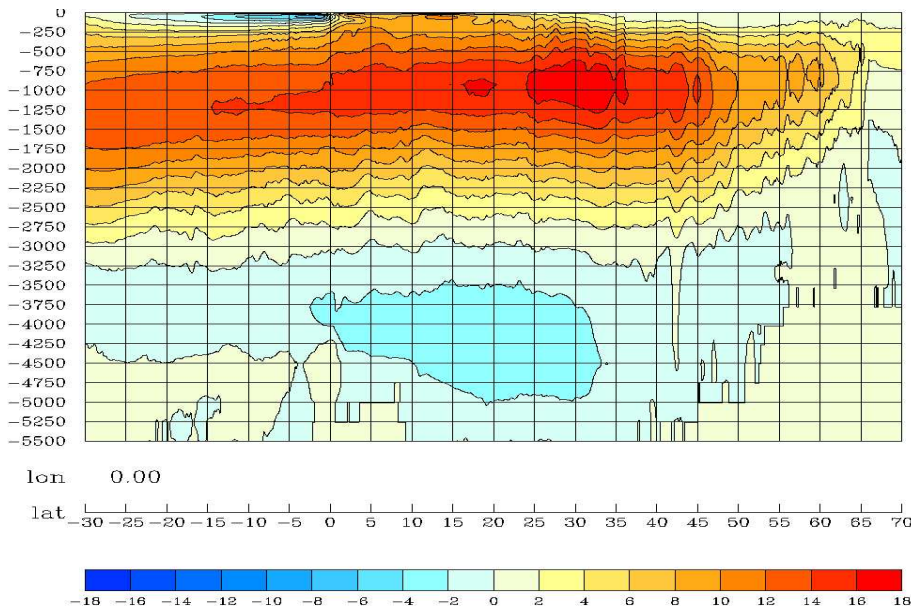


FIG. 3.2 – Moyenne annuelle de la fonction de courant de la circulation de overturning de l'Atlantique du Nord pour l'année 1988. Les lignes de contour sont espacées de 2 Sv ($1\text{Sv} = 10^6\text{m}^3\text{s}^{-1}$). Les résultats proviennent d'une intégration numérique à une résolution d'un $1/4^\circ$ réalisé dans le cadre du projet DRAKKAR. On voit clairement la descente des eaux en haute latitude, une progression vers le sud en profondeur et une légère remontée à l'intérieur, et une recirculation à la surface.

les événements de Dansgaard-Oeschger : une variation de la température glaciaires avec une période de environ 1500 ans, retrouvé dans des analyses des calottes glaciaires. Ces deux types d'événements climatiques majeurs sont aujourd'hui liés à des variations de la circulation thermohaline.

La projection de la circulation océanique dans le plan horizontal d'une part et dans le plan longitudinal-vertical d'autre part, a permis de mettre en évidence la circulation de gyre et la circulation d'overturning ce qui a amené de cerner le problème de la circulation à grande échelle et de poser des questions fondamentales sur la circulation des océans. Les premiers modèles, pour la circulation thermohaline comme celui proposé par Stommel, sont des modèles en boîtes, qui ont permis d'étudier la nature non-linéaire et bi-stable, décrite par un comportement d'hystérésis de cette circulation en fonction des forçages en température et flux de salinité. Des modèles simples de ce type ont facilité la compréhension du changement rapide du climat lié à la variabilité de la circulation thermohaline.

Les derniers décennies en recherche océanique ont clairement démontré qu'une meilleure compréhension et qu'une simulation plus réaliste de ses deux types de circulation, ainsi que leurs interactions, n'est pas possible sans l'inclusion de la dynamique à des échelles plus petites en espace et courtes en temps. En langage du mécanicien de fluides : la description de ces circulations présente un *problème de fermeture*. Cette inclusion de la

dynamique à des échelles plus petites peut se faire par une résolution explicite ou une paramétrisation de ses effets sur la dynamique à grande échelle, si elle est efficace.

Pour la circulation de gyre il est reconnu que la dynamique dites de méso-échelle, l'échelle du premier rayon de Rossby barocline (environ 50km dans la région du Gulf Stream), est essentielle pour la compréhension de la circulation gyre. En effet, on estime que l'énergie cinétique dans les structures de méso-échelle est supérieure à l'énergie cinétique de la circulation gyre, dont, toutefois, la plus grande partie de l'énergie totale est stockée sous forme d'énergie potentielle disponible. La dynamique méso-échelle est supposée chaotique (voir section 4.2). Une très grande partie des efforts de recherche des dernières années en océanographie ont pour but de trouver des fermetures efficaces modélisant les effets de la dynamique méso-échelle sur la circulation de gyre. Une supposée séparation d'échelles entre la circulation de gyre ($\approx 1000\text{km}$) et les structures méso-échelles a laissé espérer de trouver une telle fermeture. En révisant certaines hypothèses sur lesquelles une majeure partie de ces paramétrisations sont basées, et à l'aide des résultats de simulations numériques, j'ai montré leurs faiblesses (voir section 4.2). Toutefois, l'état de l'art de la simulation numérique de la dynamique des océans ainsi que les moyens de calcul ont aujourd'hui atteint un niveau où la dynamique méso-échelle commence à être explicitement résolue. Dans un futur proche, les simulations de la circulation globale seront réalisées à une résolution inférieure à environ 5km. La majeure partie de la dynamique méso échelle sera explicitement résolue, et ne nécessitera plus de paramétrisation.

La dynamique des océans ne s'arrête toutefois pas à la méso-échelle. En effet, il y a sept ordres de grandeur entre la méso-échelle et la très petite échelle à laquelle l'énergie est dissipée. Les images satellitaires récentes de la couleur de l'eau de surface montrent en effet clairement des structures filamentaires subméso-échelle d'une extension horizontale de seulement quelques kilomètres (voir fig. 3.3). La dynamique à ces échelles est influencée ou dominée par la rotation, la stratification et la topographie dont l'importance relative varie avec l'espace, le temps et l'échelle considérée. Toute échelle inférieur à la méso-échelle, j'appelle la subméso-échelle. Des processus de subméso-échelles, le sujet principal de ma recherche récente, ne jouent pas un rôle passif, ne sont pas gouvernés par la dynamique méso échelle (voir Müller *et al.* 2005). Au contraire, les processus de subméso-échelles agissent sur la dynamique à des échelles de taille supérieure, la méso-échelle et influencent de façon indirecte la dynamique de gyre. On peut supposer qu'une compréhension fine de la dynamique océanique à la méso-échelle, et de la circulation globale des océans, n'est pas possible sans tenir compte de l'influence de la sub-méso-échelle.

L'énergie cinétique est injectée dans l'océan à des grandes échelles spatiales, principalement par la tension du vent à sa surface (voir fig. 3.4). L'instabilité barocline et l'instabilité barotrope transfèrent une partie de cette énergie à la méso-échelle. La dynamique des échelles supérieures à la méso-échelle est bien représentée par la dynamique des "balanced equations" et possède une cascade d'énergie inverse vers les grandes échelles. L'énergie peut toutefois seulement être dissipée, transformée en énergie interne, aux très petites échelles, de l'ordre du centimètre, où les termes de dissipation et de viscosité moléculaire dominant. Les mécanismes du transport d'énergie de la grande ou la méso-



FIG. 3.3 – Dynamique méso et subméso-échelle dans le Golf de Gascogne (06/05/2005) composition en fausse couleur (rgb) à partir des données du capteur MERIS (ENVISAT, ESA), la domaine montrée mesure environ 400km de côté.

échelle vers la très petite échelle restent une énigme à ce jour. Les couches limites aux frontières verticales jouent un rôle important dans l'extraction de l'énergie cinétique, et l'importance de la dynamique intérieur, où la majeure partie de l'énergie se trouve, n'est pas comprise aujourd'hui. Certains processus de subméso-échelle jouent forcément un rôle prééminent dans le transport de l'énergie de la grande échelle où elle est injectée vers les très petites échelles où elle est dissipée. Ils sont susceptibles de drainer de l'énergie des échelles supérieures à la méso-échelle vers les subméso échelles, à partir desquelles la turbulence tri-dimensionnelle permet une cascade d'énergie vers les échelles où des effets visqueux dominent. La subméso-échelle est alors susceptible de contenir une gamme d'échelles où une transition d'une dynamique gouvernée par les "balanced equations" avec une cascade d'énergie inverse, vers une dynamique d'une cascade directe a lieu. Cette transition est clé pour la compréhension de la dynamique océanique. La gamme d'échelle de la méso à l'échelle dissipative comporte sept ordres de grandeurs. Les observations et simulations montrent que la dynamique à ces échelles est composée de plus que des structures fines et passives de la dynamique quasi géostrophique à la méso-échelle, mais la dynamique subméso-échelle est un acteur qui influence la dynamique de l'océan global. La

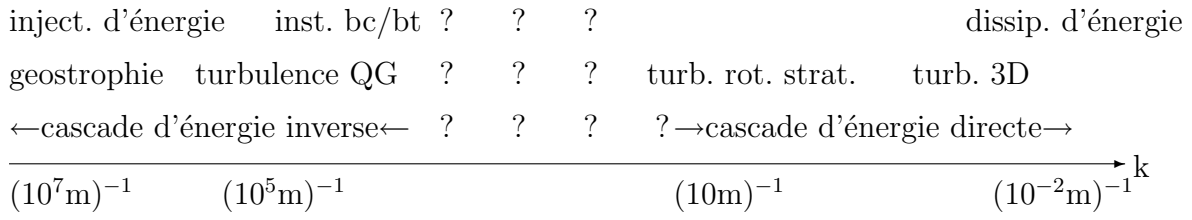


FIG. 3.4 – Processus physiques principaux (première ligne); modèles mathématiques adaptés (deuxième ligne); transport d'énergie (troisième ligne). Les points d'interrogations montrent la submésoscale échelle inexplorée.

dynamique à ces échelles est aujourd'hui en grande partie inexplorée, son étude présente un défi formidable en recherche de l'océanographie physique pour les décennies à venir.

Pour la circulation d'overtuning le rôle de la submésoscale est encore amplifié car la dynamique submésoscale a un effet direct sur sa dynamique à l'échelle globale. Récemment des simulations numériques ont révélé que certains aspects à long terme et à grande échelle sont dominés par des processus non-hydrostatiques fortement localisés en temps et en espace. L'exemple est la circulation d'overtuning de l'Atlantique du Nord dominée par la convection en mer de Labrador et de Norvège ainsi que par le courant gravitaire passant par le Détroit du Danemark (Willebrand *et al.* 2000). La localisation est telle qu'une représentation explicite de tels phénomènes dans des modèles numériques de la circulation globale semble impossible même dans un futur lointain. La plongée des eaux denses, car froides et riches en sel, dans les hautes latitudes se fait dans un processus convectif sur des régions de plusieurs dizaines de kilomètres de diamètre, appelés cheminées, qui sont composées de panaches convectifs mesurant quelques centaines de mètres en diamètres seulement (voir section 4.4 et 4.5). La simulation réaliste des panaches convectifs nécessite donc des résolutions bien inférieures à 100m dans les directions horizontales et verticale. Quand ces masses d'eau denses rencontrent la topographie, des courants gravitaires sont créés, dont la dynamique est gouvernée par des processus turbulents à petites échelles, de l'ordre d'un mètre (voir section 4.7). L'épaisseur de la veine d'eau dense dans des courants gravitaires est autour de 100m incluant une couche d'Ekman de l'ordre de 10m et les structures dominantes de l'entraînement par instabilité de Kelvin-Helmholtz ont une épaisseur autour de dix mètres et une extension horizontale inférieure à 100m . Jusqu'ici on a considéré que la descente des masses d'eau denses vers les profondeurs de l'océan, ce qui ne représente qu'une partie de la circulation thermohaline. La suite du parcours des masses d'eau est moins étudiée à ce jour et plus incertaine. Ces eaux poursuivent leurs parcours dans la forme d'un courant de bord ouest profond (DWBC) dont la dynamique est encore peu étudiée. La remontée de ses masses d'eau est à ces jours encore mal comprise. Plusieurs processus submésoscale sont supposés de jouer un rôle important, comme la dynamique côtière, l'instabilité symétrique, la dynamique de la couche de mélange et le déferlement des ondes internes, pour citer que quelques-uns.

3.2 Processus submésos échelles et leurs actions

La représentation précise des champs de température et de salinité dans l’océan et de leurs évolutions au cours du temps est cruciale pour la détermination de la dynamique des océans sur toutes les échelles spatiales et temporelles ainsi que la dynamique du climat. Comme une grande partie de l’océan est fortement stratifié les processus avec une forte advection ou un mélange dans la direction verticale sont essentiels pour l’évolution du champ thermohalin. La dynamique à grande échelle montre des vitesses horizontales plusieurs ordres de magnitude supérieur aux vitesses verticales. Cette anisotropie résulte principalement de trois propriétés de la circulation océanique : la première est géométrique, la faible profondeur des océans comparée à leurs extension horizontale amenant à des structures plates. La deuxième est la forte stratification dans la direction verticale, sur une majeure partie des océans, inhibant les échanges dans cette direction. La troisième, la rotation terrestre, agit comme expliqué par le théorème de Taylor-Proudman-Poincaré (Colin de Verdière 2002) et inhibe les vitesses verticales, même dans le cas où l’approximation traditionnelle, qui néglige la composante horizontale du vecteur de rotation terrestre et rend le vecteur de rotation parallèle à la verticale, n’est pas appliquée (Wirth & Barnier 2008).

Pour la dynamique à petite échelle, ces contraintes concernant les vitesses verticales sont moindres. La contrainte géométrique disparaît à des échelles horizontales comparables à la profondeur. Dans un écoulement turbulent l’importance de la stratification est moindre pour une dynamique en dessous de l’échelle d’Ozmidov, à laquelle l’accélération par la flottaison est égale à l’accélération inertielle. L’échelle de temps caractéristique associé aux petites échelles est souvent inférieure à l’inverse du paramètre de Coriolis, les contraintes liées à la rotation terrestre sont alors moindres et les vitesses verticales se développent plus librement. C’est ainsi que les vitesses verticales sont plus prononcées aux petites échelles.

Une variété de processus à petite échelle pouvant amener à un transport vertical considérable ont déjà été identifiés :

- la convection
- les courants gravitaires
- l’instabilité symétrique
- le déferlement des ondes internes
- la dynamique de la couche de mélange
- la dynamique côtières et effet de la topographie
- la dynamique et l’instabilité des fronts
- la turbulence tri-dimensionnelle à petite échelle.

La liste n’est pas exhaustive, la recherche pour des nouveaux processus amenant à des vitesses verticales considérables doit être faite par l’analyse et la comparaison des données d’observations, de laboratoires, des modèles numériques et des approches analytiques.

Les phénomènes non-hydrostatiques sont aussi déterminants pour la bio-géochimie, notamment pour le cycle et le stockage du carbone. Les processus dans la couche de mélange sont déterminants pour la dissolution du carbone. La convection profonde et

les courants gravitaires sont responsables du transport du carbone dissout vers l'océan profond où il est privé de contact avec l'atmosphère pour plusieurs centaines d'années.

3.3 Modèles mathématiques et numériques adaptées aux études de la dynamique submésos-échelle

Les quatre dernières décennies en recherche océanique sont marquées par le grand succès des modèles numériques de la dynamique des océans. Depuis une trentaine d'années de tels modèles sont employés pour étudier la circulation globale (DRAKKAR, MERCATOR).

Les processus dynamiques océaniques à grande échelle, à l'exception des zones équatoriales, sont pour leur majeure partie près d'un équilibre géostrophique. Nous distinguons ici "la dynamique à grande échelle" des "processus dynamiques à grande échelle", ces derniers excluant l'influence des processus à plus petite échelle sur cette dynamique. L'équation géostrophique forcée amène à la relation de Sverdrup qui a permis au milieu du XX^{ème} siècle d'expliquer les propriétés principales de la circulation à l'échelle du bassin. La linéarité de ce modèle a permis un traitement analytique ou semi analytique des équations de Sverdrup.

La variabilité des processus dynamiques, depuis la grande échelle jusqu'à la méso-échelle, à l'exception des régions équatoriales, est bien décrite par les équations quasi-géostrophiques. C'est à l'aide de ces équations et leurs intégrations numériques, obtenues au cours des trente dernières années du XX^{ème} siècle, que nous devons une majeure partie de notre connaissance de la circulation océanique de l'échelle globale jusqu'à la méso-échelle (de l'ordre de 100km). Ces équations sont basées sur la quasi bi-dimensionalité de la dynamique à ces échelles.

Pendant les dernières décennies le modèle de base pour l'étude de la dynamique des océans est devenu celui des équations primitives, basées sur l'approximation hydrostatique de la dynamique des océans. Cette approximation suppose une forte dominance de l'accélération horizontale sur l'accélération verticale, cette dernière est donc négligée. Les raisons dynamiques pour cette anisotropie sont détaillées dans la section précédente. Ces arguments, ainsi que les expériences numériques, montrent que pour des phénomènes à des échelles horizontales grandes par rapport à l'extension verticale, l'approximation hydrostatique est une approximation bien justifiée et qu'elle continuera d'être à la base de la modélisation de la circulation dans les bassins océaniques. La reconnaissance de l'importance des tourbillons méso-échelles et l'absence de paramétrisations efficaces (voir section 4.2) pour représenter leurs effets sur la dynamique à grande échelle, a amené à des discrétisations spatiales de plus en plus fines dans des modèles numériques, pour inclure explicitement cette dynamique méso-échelle. Les résolutions fines actuellement utilisées dans des simulations pluriannuelle de la circulation générale des océans permettent une bonne représentation des tourbillons méso-échelles. Ces modèles sont basés sur les équations hydrostatiques de la dynamique de l'océan. Aujourd'hui existent plusieurs modèles numériques, d'accès public, et ils sont utilisés pour l'étude, la réanalyse et

la prédiction de la circulation océanique sur une grande variété d'échelles temporelles et spatiales.

Pour les phénomènes de submésos-échelle cités dans le chapitre précédent, et qui sont le sujet de ma recherche, nous ne pouvons plus appliquer l'approximation hydrostatique, car les accélérations verticales sont du même ordre, voir supérieures, aux accélérations horizontales. Le modèle mathématique adapté sont alors les équations de Navier-Stokes dans un repère en rotation avec l'approximation de Boussinesq. En même temps l'approximation traditionnelle, dans laquelle on néglige la composante horizontale du vecteur de rotation, n'est plus valable. Nous avons en effet démontré que cette composante horizontale est importante pour le processus de la convection océanique (voir section 4.4 et 4.5). Le modèle mathématique à la base de mes recherches sur la dynamique de submésos-échelle de l'océan sont les équations de Navier-Stokes incompressible avec l'approximation de Boussinesq dans un repère en rotation, sans la restriction de l'approximation traditionnelle.

Pour la mise en œuvre numérique du modèle mathématique, les équations de Navier-Stokes, j'ai choisi de construire mon propre modèle pseudo spectral basé sur la série de Fourier dans les trois directions spatiales. J'ai développé une nouvelle méthode pour imposer des conditions aux limites de type d'adhérence et de glissement libre, basées sur les conditions aux limites virtuelles, dans un tel modèle numérique spectral (voir section 4.3). Ma méthode permet d'enlever les vitesses résiduelles sur le bord, présentes dans des méthodes classiques des conditions aux limites virtuelles. Le modèle numérique s'appelle HARmonic Ocean MODEL (HAROMOD). Récemment j'ai réécrit ce modèle en incluant une parallélisation MPI et OpenMP, ce qui permet de facilement adapter le code à l'architecture d'un ordinateur parallèle. Ce modèle est l'outil principal de ma recherche sur les processus océaniques à petite échelle. Des modèles de la circulation océanique générale (OGCM) ont atteint une telle complexité que leur écriture, compréhension et évaluation demande la collaboration d'une grande nombre de personnes, chacune spécialisée sur une partie du code. La situation est différente pour des modèles spécialisés et optimisés pour étudier un certain processus. Construire son propre modèle aujourd'hui, alors que d'autres modèles peuvent être obtenus avec un simple clic sur l'internet, peut sembler archaïque. Mais pour bien utiliser un modèle on doit le connaître, afin d'être en mesure de le modifier et l'adapter à son besoin. Dans les cas des modèles numériques il est souvent plus facile de coder soi-même que de comprendre le modèle écrit par quelqu'un d'autre. Ecrire son propre modèle demande un investissement initial considérable mais ce temps est récupéré au moment où on doit le modifier.

3.4 Retour à la grande échelle par l'assimilation de données

La recherche sur la dynamique océanique globale, et la modélisation de la dynamique océanique globale des quarante dernières années peuvent être vues comme un voyage vers des échelles de plus en plus petites. Une fois les processus à petites échelles bien compris,

mais surtout pas avant, le voyage dans la direction opposée évalue leurs influences sur la dynamique à grande échelle.

Une amélioration des modèles hydrostatiques de la circulation globale des océans utilisés pour l'étude de la dynamique du climat passe par une meilleure compréhension et paramétrisation de la dynamique de la submésos-échelle comme la dynamique convective, des courants gravitaires, des ondes internes générées par les marées et de couche de mélange à la surface. Ce qui impose de chercher des meilleures paramétrisations et valeurs de paramètres pour ces processus à petite échelle. Une méthode systématique pour ce retour aux grandes échelles est l'utilisation de l'assimilation de données pour estimer les paramètres et évaluer les paramétrisations.

L'assimilation de données en océanographie a des applications multiples. L'une est la prévision des circulation océaniques à court et moyen terme (MERCATOR <http://www.mercator-ocean.fr/>). On essaye d'extrapoler dans le temps l'état de l'océan en combinant observations et intégrations du modèle numérique. Une autre application sont les réanalyses dans lesquelles on interpole les données dans le temps pour obtenir une vue plus complète de l'océan. Dans les deux cas l'assimilation inclut l'estimation des valeurs des variables non directement observées et une inter- et extra-polation dans l'espace, comme l'extrapolation ou la propagation de l'information, des observations satellitaires de surface vers les profondeurs de l'océan.

Une application, assez différente dans ses objectifs des deux premières, est l'estimation de paramètres. Dans ce contexte, l'assimilation de données n'est plus seulement un outil permettant l'estimation optimale de l'état de l'océan, mais un outil scientifique pour étudier, par exemple, des processus océaniques submésos-échelle, leurs influences sur la dynamique à grande échelle, et pour améliorer leurs paramétrisation dans les modèles numériques. Dans un grand nombre de cas, une forme analytique d'une telle paramétrisation peut être obtenue en utilisant quelques simplifications de la dynamique. Ces formes analytiques contiennent toutefois des champs de paramètres qui ne peuvent être déterminés analytiquement que dans les cas les plus idéalisés. En utilisant l'assimilation de données on peut déterminer les paramètres et évaluer les paramétrisations proposées. Un exemple type choisi dans ma recherche est la dynamique des courants gravitaires. Des paramétrisations pour des flux turbulents d'inertie et de masse existe, leurs pertinence reste à être évaluer et les valeurs de paramètres à déterminer (voir sections 4.6, 4.7, 4.8 & 4.9).

3.5 Ma Recherche dans le Contexte Dynamique

La dynamique du Great Whirl, dont nous avons brièvement parlé en section 2.5, montre une forte variabilité intra- et inter-annuelle. Le long de la côte Somalienne, le courant tourne vers le large et une forte remontée des masses d'eau est observée. Les courants dans ces régions atteignent des valeurs supérieurs à 1m/s. Ces masses d'eau froides et riches en nutriment sont essentielles pour la circulation d'overturing de l'Océan Indien et la production biologique dans cette région où les populations vivent principalement de

la pêche et du piratage. La variabilité de la position du Great Whirl se décompose en une variabilité interannuelle externe, par le forçage du vent, et interne, par la chaotité du système. Nous avons montré que la deuxième est importante dans des simulation à plus grand nombre de Reynolds, permettant une dynamique méso échelle. Ceci montre que les données de simulations d'une dynamique chaotique, mais également des observations, doivent être interprétées comme des membres d'un ensemble de réalisations possibles. Une prédiction déterministe doit alors faire place à une interprétation statistique des données, d'observation et numériques, même dans le cas où on considère des phénomènes et variables à grande échelle. Ceci montre qu'une comparaison entre modèles et observations nécessite toujours une évaluation de la variabilité interne du phénomène. Ce concept est bien appliqué dans la prédiction météorologique où on est passé à des simulations d'ensembles, mais il est encore souvent ignoré en océanographie.

Les observations ainsi que les simulations numériques montrent que la plupart des courants océaniques forts sont instables et donnent naissance à une forte dynamique tourbillonnaire. Dans les premières simulations numériques globales de la dynamiques des océans, la résolution n'était pas suffisante pour permettre une représentation explicite de ces tourbillons. Les tourbillons ont, toutefois, un effet important sur la dynamique à des échelles supérieures : ils transfèrent une partie de l'énergie potentielle disponible, à grande échelle, en énergie cinétique, à la méso-échelle. Ce processus est clef pour la dynamique à grande échelle et si la génération des tourbillons n'a pas explicitement lieu dans un modèle de la dynamique de l'océan, son effet sur la grande échelle par extraction de l'énergie potentielle disponible, doit être paramétré. Une variété de paramétrisations existent, la plus utilisée étant celle proposée par Gent & McWilliams 1990. A l'aide de simulations numériques idéalisées, j'ai pu démontrer que certaines hypothèses sur lesquelles une majorité de ces paramétrisations est basée sont fausses. En effet, ces paramétrisations sont basées sur l'idée que la conversion d'énergie potentielle est une fonction linéaire du courant moyen à grande échelle. Je démontre, au contraire, que cette conversion suit un comportement de seuil. Si le forçage est tel que le courant à grande échelle a atteint son seuil une injection d'énergie supplémentaire ne change pas l'état moyen. Ceci montre que la conversion d'énergie par les tourbillons, qui est égale à l'injection d'énergie dans un état statistiquement stationnaire, n'augmente plus la magnitude du courant à grande échelle s'il a atteint son seuil. Il n'y a alors pas de relation univoque entre l'état moyen et le flux tourbillonnaire. J'ai également montré que le drainage d'énergie potentielle par les flux turbulents n'est pas de type diffusif mais au contraire les tourbillons enlèvent cette énergie dans un processus advectif. Ceci n'est pas étonnant car les tourbillons se déplacent de façon linéaire plutôt que d'avoir fait un marche aléatoire. Cet aspect est approfondi dans le chapitre 4.2.

Dans mes travaux sur les panaches convectifs (voir section 4.4) et la convection homogène (voir section 4.5) nous avons montré que la composante horizontale du vecteur de rotation, qui est négligée dans l'approximation traditionnelle, est essentielle pour la dynamique convective. Les panaches convectifs commencent leur descente dans la direction verticale mais après seulement un tiers de la période de rotation ils sont déviés par la rotation et poursuivent leur descente dans la direction de l'axe de rotation plutôt que celle

de la gravité. La composante horizontale du vecteur de rotation brise l'isotropie dans les directions horizontales. En effet une particule qui monte est déviée vers l'est sous l'action de la composante horizontale du vecteur de rotation et une particule qui descend est déviée vers l'ouest. Dans le cas de la convection homogène ceci amène à un cisaillement vertical de la vitesse horizontale qui s'étend sur toute la zone convective. La caractéristique principale d'une zone de convection est sa stratification en température et/ou densité. A l'aide de mes simulations, j'ai clairement montré que ce n'est pas la première dérivée verticale de la température qui est constante, comme souvent supposé, mais la deuxième. Cette propriété nous permet de déterminer explicitement les paramètres du transport diffusif et non-local de la paramétrisation KPP. Ces résultats sont décrits dans les publications reproduites en section 4.4 et 4.5.

Si l'eau plongeant grâce à un processus convectif rencontre le fond de l'océan ou si l'eau dense passe un détroit, un courant gravitaire est créé. Les courants gravitaires sont omniprésents dans l'océan. J'ai étudié la dynamique d'un courant gravitaire et déterminé ses caractéristiques principales. J'ai démontré que un courant gravitaire dans un repère en rotation est composé de deux parties, une veine, la partie épaisse, et une couche fine en aval de la veine, le couche de friction (voir section 4.7). Des masses d'eau denses sont éjectées de la veine vers le couche de friction. Pour des courants gravitaires idéalisés j'ai démontré que la dynamique de l'épaisseur de la veine est décrite par l'équation de la chaleur. Ce processus est gouverné par la friction de fond. J'ai également eu la possibilité de faire des expériences de laboratoire sur la plaque tournante Coriolis à Grenoble. Je me suis intéressé à l'évolution de l'épaisseur du courant gravitaire et son évolution temporelle et spatiale. Les résultats de ses expériences de laboratoire m'ont permis de valider résultats numériques et analytiques. Les résultats sur la dynamique d'un courant gravitaire idéalisé se trouve dans la section 4.7

Après avoir constaté que la friction de fond est un processus important, la détermination des lois et paramètres de friction est essentielle. J'utilise alors l'assimilation de données pour estimer les paramètres de friction. Plusieurs types de données peuvent être assimilées pour permettre une estimation de ces paramètres, toutefois, la variable la plus facilement observable dans un courant gravitaire est son épaisseur. La vitesse montre en effet une trop grande variabilité en espace et en temps pour permettre une détermination suffisante même des valeurs moyennes. La question qui se pose est alors : Est-ce que les lois et paramètres de friction peuvent être estimées à partir des observations de l'épaisseur d'un courant gravitaire ? J'ai exploré cette question d'abord à l'aide d' "expériences jumelles." La réponse est positive mais mes résultats montrent aussi que la détermination de la friction totale, linéaire plus non-linéaire, se fait facilement ; la répartition de la friction totale entre les deux lois est plus difficile. Les détails de cette étude se trouvent en section 4.6. Après avoir déterminé que l'observation de l'évolution temporelle de l'épaisseur d'un courant gravitaire permet d'estimer les paramètres de friction entre le courant et le fond dans des "expériences jumelles," j'ai étudié la détermination des paramètres de friction dans des données provenant d'une série de simulations non-hydrostatiques d'un courant gravitaire. Là encore j'ai pu déterminer les paramètres et les lois de friction. Les résultats montrent une loi linéaire pour des faibles nombre de Reynolds, suivie de l'augmentation

du comportement non-linéaire pour des nombres de Reynolds plus élevés. Les valeurs des paramètres de friction ainsi que le nombre de Reynolds critique du passage linéaire - non linéaire se comparent bien aux résultats des expériences de laboratoires pour des lois de friction. Plus de détails se trouvent en section 4.8

En même temps nous considérons la dynamique d'un courant gravitaire dans un modèle océanique, NEMO / OPA, avec deux système de coordonnées, "z" et " σ ". Dans ce travail nous cherchons la grille de calcul qui donne le meilleur compromis entre une bonne représentation de la dynamique d'un courant gravitaire et le coût numérique. Nous avons en effet montré que quelques couches "sigma" fines au fond de l'océan sont nécessaires pour permettre une représentation réaliste de la dynamique du courant gravitaire même en ce qui concerne sa partie épaisse, la veine. En effet, nos simulations montrent que la descente du courant gravitaire augmente de presque un ordre de grandeur simplement en augmentant la discrétisation verticale. Les océanographes numériques ont bien l'habitude de raffiner leurs maillage à la surface. Nos résultats montrent qu'un raffinement près du fond est également important, pour une meilleur représentation des effets de friction de fond sur les courants gravitaire ainsi que sur la circulation océanique toute entière. Les résultats concernant l'effet de discrétisation sur la dynamique d'un courant gravitaire idéalisé se trouvent dans la section 4.7.

Comme j'ai montré dans ce chapitre, le sujet de ma recherche sont les processus sub-méso échelle, c.a.d. les échelles à la fois trop petites pour l'océanographie "classique", étudiant la dynamique quasi géostrophique, et trop grande pour le dynamicien de fluide "classique", étudiant la turbulence stratifié en rotation. Une gamme d'échelle qui s'étend sur environ 4 ordres de grandeur. Je suis convaincu que la dynamique à ces échelles ne possède pas une théorie universelle mais est au contraire composé de différents processus importants. L'identification et l'étude de ces processus, de leurs interactions et de leurs influences sur la dynamique à des grandes et petites échelles sont essentielles pour notre compréhension de la dynamique océanique dans le futur.

Ma formation de dynamicien de fluide "classique" pendant ma thèse ainsi que ma formation d'océanographe "classique" après, m'aide à attaquer l'étude de la dynamique à ces échelles intermédiaires. C'est ce travail que j'envisage de poursuivre.

"De quoi je fais ici une déclaration que je sais bien ne pouvoir servir à me rendre considérable dans le monde ; mais aussi n'ai aucunement envie de l'être ; et je me tiendrai toujours plus obligé à ceux par la faveur desquels je jouirai sans empêchement de mon loisir, que je ne ferais à ceux qui m'offriraient les plus honorables emplois de la terre". (Descartes, Discours de la méthode, Sixième Partie)

Bibliographie

- [1] DRAKKAR (2003), The ocean circulation in the North Atlantic and the Nordic seas : Variability, processes and interactions with the global ocean. Drakkar Research Proposal, Laboratoire des Ecoulements Gophysiques et Industriels, Grenoble, July 2003, 34 pp. (<http://www.ifremer.fr/lpo/drakkar>)
- [2] E. Fermi, J. Pasta & S. Ulam, Los Alamos Scientific Laboratory report LA-1940 (1955). Published later in E. Segré, ed., Collected Papers of Enrico Fermi, Vol. 2, U. Chicago Press, Chicago (1965).
- [3] A. Colin de Verdière (2002), Un fluid lent entre deux sphères en rotation rapide : les théories de la circulation océanique, *Annales Mathématiques Blaise Pascals*, **9**, 245–268.
- [4] P.R. Gent & J.C. McWilliams (1990), Isopycnal mixing in ocean circulation models. *J. Phys. Oceanogr.*, **20**, 150-155.
- [5] P. Müller & C. Garrett (2002), From stirring to mixing in a stratified ocean, *Oceanography*, **15**, 12–19.
- [6] Müller, P., J. McWilliams and J. Molemaker (2005) Routes to dissipation. The 2D/3D turbulence conundrum. In : Marine Turbulence. Cambridge University Press. 397-405.
- [7] H. Poincaré, *La Science et l'Hypothèse* 1899. Flammarion , Paris, ISBN : 2-08-081056-1 (1968).
- [8] G. Vallis 2006, *Atmospheric and Oceanic Fluid Dynamics*, Cambridge University Press.
- [9] J. Willebrand, B. Barnier, C. Bönnig, C. Dietrich, P.D. Killworth, C. LeProvost, Y. Yia, J.-M. Molines, A.L. New (2000), Circulation characteristics in three eddy-permitting models of the North Atlantic. *Progr. in Oceanogr.* **48**, 123–161.
- [10] C. Wunsch & R. Ferrari Vertical mixing, energy, and the general circulation of the oceans (2004), *Annu. Rev. Fluid Mech.* **36** 281–314.

Deuxième partie

Curriculum Vitae

Curriculum Vitae du Dr. Achim WIRTH

Janvier 2010

Informations personnelles

Né à Munich (Allemagne), Décembre 23, 1968, nationalité allemande.

Langues : Allemand, Français, Anglais et un peu d'Italien.

Adresse professionnelle :

LEGI, BP 53, 38041 Grenoble Cedex 9

courriel : achim.wirth@hmg.inpg.fr

Education :

2005 – : Chercheur CR1 CNRS/Section 19, au LEGI équipe MEOM.

2003 – 2005 : Collabotateur expert contractuel (contrat EPSHOM), LEGI Université de Grenoble.

2001 – 2003 : Instructor au Dep. de Physique à l'University of Georgia, Athens, USA. Consultant scientifique de l' Institut für Meereskunde Kiel (Allemagne). Visiting Scientist au Dep. of Marine Sciences UGA.

1999 – 2001 : Collaborateur scientifique (Wissenschaftlicher Angestellter) à l'Institut für Meereskunde Kiel (Allemagne), avec J. Willebrand.

1997 – 1999 : Chercheur post-doctoral à l'Institute of Geophysics and Planetary Physics, UCLA (USA), avec M. Ghil .

1993 – 1996 : Thèse de doctorat préparée sous la direction de U. Frisch à l'Observatoire de la Côte d'Azur, au laboratoire G.D. Cassini (rémunéré comme boursier MESR puis DRET). Soutenance : 13/12/96, mention Très Honorable avec Félicitations. titre : Méthodes perturbatives, numériques et probabilistes en turbulence. Jury : C. Bardos (président), R. Benzi et A. Pumir (rapporteurs), U. Frisch (directeur), T. Dombre, D. Lohse, Z. She

1992 – 1993 : DEA de Turbulence et Systèmes Dynamiques à l'Université de Nice Sophia Antipolis, mention TB.

1991 – 1992 : Maîtrise de mathématiques pures à l'Université de Nice Sophia Antipolis, avec stage de recherche de 2 mois (directeur : F. Pham).

1988 – 1991 : Etudes de mathématique et physique à la Technische Universität München.

Activités scientifiques (mots-clés :) :

Océanographie, assimilation de données, écoulements gravitaires, convection, turbulence et paramétrisation, modélisation numérique, méthodes numériques spectrales, équations différentielle (partielle) stochastique.

LISTE DES PUBLICATIONS (rang A)

- Wirth, A., “Complex eddy-viscosity : a three-dimensional effect”, *Physica D*, **76**, 312–317, 1994.
- Wirth, A., Gama, S. & Frisch, U., “Eddy viscosity of three-dimensional flow”, *J. Fluid Mech.*, **288**, 249–264, 1995.
- Wirth, A. & Biferale, L., “Anomalous scaling in random shell models for passive scalars”, *Phys. Rev. E*, **54**, 4982–4991, 1996.
- Vergassola, M. & Wirth, A., “Large-scale dynamics in Burgers equation”, *J. de Physique*, **6**, 1841–1849, 1996.
- Frisch, U. & Wirth, A., “Inertial-diffusive range for a passive scalar advected by a white-in-time velocity field”, *Europhys. Lett.*, **35**, 683–687, 1996.
- Wirth, A., “An extension of spectral methods to quasi-periodic and multiscale problems”, *J. Comp. Phys.*, **132**, 285–290, 1997.
- Benzi, R., Biferale, L. & Wirth, A., “Analytic calculations of anomalous scaling in random shell models for passive scalar”, *Phys. Rev. Lett.*, **78**, 4926–4929, 1997.
- A. Lanotte, A. Noullez, M. Vergassola & A. Wirth, “Large-scale dynamo produced by negative magnetic eddy diffusivities,” *Geophys. Astrophys. Fluid Dynamics*, **91**, 131–146, 1999.
- Karaca, M., A. Wirth & M. Ghil, “A box model for the paleoceanography of the black sea”, *Geophys. Resea. Lett.*, **26**, 497–500, 1999.
- Wirth, A. & M. Ghil, “Error evolution in the Dynamics of an ocean general circulation model”, *Dynam. Atmos. Oceans*, **32**, 419–431, 2000.
- Wirth, A., “The parameterization of baroclinic instability in a simple model”, *J. of Mar. Resea.*, **58**, 571–583, 2000.
- Wirth, A., J. Willebrand & F. Schott, “Variability of the Great-Whirl from Observations and Models” *Deep Sea Resea. II*, **49**, 1279–1295, 2002.
- Wirth, A. “A non-hydrostatic flat-bottom ocean model entirely based on Fourier Expansion”, *Ocean Mod.*, **9**, 71 – 87, 2004.
- Wirth, A & B. Barnier, “Tilted plumes in numerical convection experiments”, *Ocean Mod.*, **12**, 101 – 111, 2006.
- Wirth, A & B. Barnier, “Mean circulation and structures of tilted ocean deep convection”, *J. Phys. Oceanogr.*, **38**, 803 – 816, 2008.
- Wirth, A & J. Verron, “Estimation of Friction Parameters and Laws in 1.5D Shallow-Water Gravity Currents on the f-Plane, by Data Assimilation” *Ocean Dynamics* **58**, 247–257, 2008. DOI 10.1007/s10236-008-0151-8
- Frisch U., S. Kurien, R. Pandit, W. Pauls, S. Sankar Ray, A. Wirth, and J.-Z. Zhu, “Hyperviscosity, Galerkin Truncation, and Bottlenecks in Turbulence” *Phys. Rev. Lett.*, **101**, 144501, 2008.
- Wirth, A “On the basic structure of oceanic gravity currents” *Ocean Dynamics* **59**, 551–563, 2009. DOI 10.1007/s10236-009-0202-9
- Wirth, A “Estimation of Friction Parameters in Gravity Currents by Data Assimilation in a Model Hierarchy” sousmis *Ocean Dynamics*.
- Laanaia, N., A. Wirth, J.M. Molines, B. Barnier & J. Verron “On the resolution of

the bottom Ekman layer in numerical models of gravity currents” soumis *Ocean Sciences*

Autres Publications

- Wirth, A., “Dynamique à grande échelle de perturbations d’écoulements tri-dimensionnels périodiques”, (“Diplome d’Etudes Approfondies”). Juin 1993.
- Wirth, A., “Méthodes perturbatives, numériques et probabilistes en turbulence” Thèse de doctorat préparée sous la direction de U. Frisch à l’Observatoire de la Côte d’Azur, au laboratoire G.D. Cassini (rémunéré comme boursier MESR puis DRET). Soutenance : 13/12/96, mention Très Honorable avec Félicitations. Jury : C. Bardos (président), R. Benzi et A. Pumir (rapporteurs), U. Frisch (directeur), T. Dombre, D. Lohse, Z. She
- Wirth, A., Gama, S. & Frisch, U., “Eddy viscosity of three-dimensional flow”, in *Advances Turbulence V, Proceedings Fifth European Turbulence Conference*, ed. R. Benzi, pp. 565-568, Kluwer 1995.
- Wirth, A., Gama, S. & Frisch, U., “Analytical and numerical multiscale calculations for eddy viscosity”, *Proceedings IUTAM Symposium on Asymptotic Methods for Turbulent Shear Flows at High Reynolds Numbers, Fluid Mechanics and its Applications 37*, ed. K. Gersten, pp. 257-266, Kluwer 1996.
- Frisch, U. & Wirth, A., “Intermittency of passive scalars in delta-correlated flow : introduction to recent work”, *Proceedings of Workshop on Turbulent modeling and Vortex Dynamics, Istanbul, Springer Lecture Notes in Physics*, pp. 53–64, 1997.
- Biferale, L. & Wirth, A., “A minimal model for intermittency of passive scalars”, *Proceedings of Workshop on Turbulent modeling and Vortex Dynamics, Istanbul, Springer Lecture Notes in Physics*, pp. 65–73, 1997.
- Wirth, A. & M. Ghil, “The diagnostic layer data assimilation scheme for primitive-equation models”, (rapport 2000).
- Wirth, A., “Anisotropic and anomalous mixing in the Iceland Basin from RAFOS floats”, (rapport 2001).
- Wirth, A. & J. Verron “Vertical Transport and Mixing Induced by Eddy Instability in the Ocean”, *Proceedings, 19^{ème} Congrès Français de Mécanique, Grenoble, 2007*.
- Wirth, A. “Non-traditional Ocean Deep Convection” *Proceedings, 20^{ème} Congrès Français de Mécanique, Marseille, 2009*.
- Wirth, A. “Ocean deep convection”, *Proceedings ICCM3E, Sousse, Tunisi, 2009*.

Enseignement

- depuis 2007 : Cours “Océanographie” M1, ENS-Lyon (15 heures/an)
- depuis 2006 : Cours “Océanographie” M2R, OSUG (15 heures/an)
- 2001 – 2003 : Cours de “mécanique et thermodynamique” (2×3 h par semaine devant 80 étudiants) et TP physique (5×2 h par semaine devant 32 étudiants) au Dep. de Physique à l’University of Georgia, Athens, USA.
- 2000 : TD “Océanographie théorique” L3, Université de Kiel (Allemagne).
- 1996 : TP “analyse de données” en license MASS à l’Université de Nice (4 heures par semaine pendant un semestre).

Contras

- EPSHOM 2006 – 2008 : Coordinateur de la partie numérique.
- LEFE 2006 – 2008 : Responsable du Projet COUGAR ; 12 kEuros.
- ANR jeune chercheur 2006 – 2009 : Responsable du Projet COUGAR (Etudes et Paramétrisation des Flux Turbulents pour les **C**ourants **G**ravitaires par **A**ssimilation de Données) ; 95 kEuros
- LEFE 2009 – 2011 : Responsable du Projet COUGAR ; 7 kEuros.

Fonctions Administratives

- Organisateur du séminaire du laboratoire LEGI depuis 2007.
- Coordinateur thématique (turbulence et mélange) du laboratoire LEGI.
- Membre de la commission prospectives du LEGI depuis 2008.
- Membre nommé de la commission des spécialités section 37, de l’Université de Bretagne Occidentale, collège B, 2008.
- Membre nommé de la commission des spécialités CSE-Mixte MCF LGGE à l’OSUG, 2008.
- Convenir à la “European Geophysical Union” de la session “Small-scale processes and their parametrization” depuis 2009.
- HYMEX : co-leader of subtask TTM3-e (ocean mixing and convection parameterization)
- Rapporteur de stages L3 et M2R.
- Rapporteur de thèse de Manuel Baptista (2007), Universidade do Porto (Portugal).
- Examineur de thèse de Stéphanie Leroux (2009), Université Joseph Fourier Grenoble I.

Encadrement

- Stage L3 : “Modélisation numérique de la dynamique des fluides géophysiques à l’aide des équations de Saint Venant” T. Grangeon (2007).
- Stage L3 : “Modélisation numérique du Courant Circumpolaire Antarctique (ACC) à l’aide des équations de Saint Venant” Charlotte Deligny (2008).
- Stage L3 : “Stochastic resonance in a simple model of the thermohaline circulation” Lucie Bazin (2009)
- Stage M1 : “Etude de la variabilité de la circulation méridienne de retournement et des vitesses verticales dans l’océan Indien nord simulés par un modèle de circulation générale océanique” T. Grangeon (2008)
- Stage de fin d’études de l’Ecole Nationale d’Ingénieur de Monastir : “Dynamique Shallow Water du Courant Antarctique Circumpolaire” Hamdi Missaoui (2009).
- Septembre 2006 – Décembre 2007, Post-Doc : Denis Zyryanov, projet COUGAR, financement EPSHOM.
- Septembre 2008 – Décembre 2009, Post-Doc : Nabil Laanaia, projet COUGAR, financement ANR.

Ecoles, conférences et séminaires

Conférences

Plus de 40 présentations données à des conférences et colloques internationaux.

Conférences invitées récentes

- A. Wirth, “Estimation de paramètres dans un modèle par assimilation de données”,

Colloque bilan LEFE, Plouzané, Mai 2009.

- A. Wirth, “Non-traditional Ocean Deep Convection”, 20^{eme} Congrès Français de Mécanique, Marseille, Août 2009.
- A. Wirth, “Small scale processe in the ocean”, ICCM3E, Sousse, Tunisi, Novembre 2009.

Visites

- Visite au ‘Center of Fluid Dynamics Research’, Princeton, Avril 8–May 8, 1994.
- Visite au ‘Mittag-Leffler Institut’ Stockholm, Septembre 5–Octobre 1, 1994.
- Visite au ‘Center of Fluid Dynamics Research’, Princeton, Septembre 3–Octobre 3, 1995.

Troisième partie

Publications récentes

Chapitre 4

Etudes de Processus Océanographiques

4.1 Variability of the Great Whirl from observations and models



PERGAMON

Deep-Sea Research II 49 (2002) 1279–1295

DEEP-SEA RESEARCH
PART II

www.elsevier.com/locate/dsr2

Variability of the Great Whirl from observations and models

A. Wirth*, J. Willebrand, F. Schott

Institut für Meereskunde, Universität Kiel, Duesternbrooker Weg 20, 24105 Kiel, Germany

Accepted 20 September 2001

Abstract

Observations from cruises in the Arabian Sea and data from satellites are interpreted using different realizations of a multi-level primitive equation model and an eddy-permitting reduced-gravity shallow water model of the Indian Ocean. The focus is on the interannual circulation variability of the Arabian Sea, and especially of the meridional location of the Great Whirl (GW). The results suggest that the variability in the western Arabian Sea is not only due to the interannual variability in the wind field, but that a substantial part is caused by the chaotic nature of the ocean dynamics. Decreasing the friction coefficient from 1000 to 500 $\text{m}^2 \text{s}^{-1}$ in a $\frac{1}{9}^\circ$ numerical reduced-gravity model, the variance of the GW location increases dramatically, and the mean position moves southward by one degree. In the eddy-permitting experiments analyzed, both mechanisms appear to determine the GW location at the onset of the GW dynamics in late summer. © 2002 Published by Elsevier Science Ltd.

1. Introduction

During the German Meteor and Sonne cruises in 1993, 1995 and 1996 and related moored observations in the western Arabian Sea, considerable year-to-year differences in the ocean circulation were found (e.g., Schott and McCreary, 2001). The cruises, which took place in late summer, investigated the dynamics in the western Arabian Sea. In that time of year, strong south westerly Monsoon winds lead to a strong Somali current flowing northward along the coast of Africa. The most conspicuous phenomenon in this area is the Great Whirl (GW), a large anti-cyclonic eddy that develops every year after the onset of the summer monsoon (Schott and Quadfasel, 1982).

The GW not only causes substantial upwelling along the coast of Africa but also transports and mixes the cold upwelled water eastward into the interior Arabian Sea (Schott, 1983). The dynamics of the GW is thus important for the region's sea-surface temperature and for the meridional heat transport. The signature of the GW is also clearly visible when considering biological production in the Arabian Sea (McCreary et al., 1996). It is thus of great importance to consider variability, especially the interannual variability of the GW system.

The interannual variability of the ocean circulation in principle can have two sources, an external and an internal one. Year-to-year changes in atmospheric forcing, which in the Arabian Sea mainly result from variability of the wind field, obviously lead to externally-forced variability in ocean dynamics. Internal oceanic variability can

*Corresponding author. Fax: +49-0431-597-3882.
E-mail address: awirth@ifm.uni-kiel.de (A. Wirth).

result from the instability of ocean currents due to the nonlinearity of the equations governing the dynamics of the ocean.

The distinction between internal and external variability is important for the interpretation of the observed data, and for any comparison of model results with observations. If the internal variability is negligible, a one-to-one comparison between model results of the Indian Ocean circulation and observations should be feasible, provided that the ocean model and wind forcing are sufficiently accurate. On the other hand, if the internal variability is not negligible, a direct model-data comparison even with a perfect model is meaningless except in the context of data assimilation, and one can only compare statistical parameters such as mean values, variances or correlations of quantities important to the ocean circulation.

When interannual variability in the Indian Ocean has been considered in previous modeling studies, the emphasis has been focused almost entirely on external variability. Internal variability has been argued to play no substantial role since the early work by Luther and O'Brien (1989) and usually is neglected altogether (e.g., Anderson and Carrington, 1993; Luther, 1999). Obviously, this neglect is meaningful only when using models with relatively coarse resolution and/or rather high values of the friction parameters where the internal variability is small or nonexistent. When models of higher resolution and smaller friction values are employed, the chaotic nature of the underlying ocean dynamics is revealed, showing up not only at small scales but potentially also at large scales.

Based on the results of eddy-permitting and eddy-resolving models, we argue here that in the western Arabian Sea the internal variability is indeed substantial. Specifically, our purpose is to quantify and compare external and internal variability in the western Arabian Sea.

2. Observations

The observations used are from recent WOCE measurements and from TOPEX/Poseidon satellite altimetry. The in situ observations consist of

shipboard hydrography and acoustic doppler current profiling (ADCP) sections across the Northern Somali Current and Great Whirl during the summer monsoons of 1993 (Fischer et al., 1996) and 1995 (Schott et al., 1997), and also of moored current measurements. The mooring records cover a period of 18 months in 1995–96, including both summer monsoons, with stations deployed along a near-meridional line running southward from the island of Socotra at approximately 54°E.

As described above, the “Great Whirl” develops with the monsoon onset in June in the 4–10°N latitude range, with a cold wedge at 10–12°N, the latitude where it turns offshore (Fig. 1). The cross-equatorial flow continues during this time, carrying a transport of about 20 Sv in the upper 500 m. It leaves the coast south of 4°N, where it partially turns eastward, also with an upwelling wedge at its northern shoulder, and partially flows back across the equator to form the “Southern Gyre” (Fig. 1). Water-mass signatures of both gyres indicate little exchange between the Great Whirl and the Southern Gyre at this time, at least in the upper layers. Thus, water that crosses the equator does not continue to flow up the Somali coast, but rather bends eastward at low latitudes to flow into the interior of the Arabian Sea.

In the late phase of the summer monsoon, the Great Whirl has become an almost-closed circulation cell (Fig. 1) with very little exchange between its offshore recirculation branch and the interior Arabian Sea, as is apparent from the differences in surface salinities between the GW and the region to the east of it (Fig. 1). To the north, another anticyclonic feature, the Socotra Gyre (Fig. 1), develops in some seasons. GW transports in this late summer monsoon phase can exceed 70 Sv (Fischer et al., 1996; Schott et al., 1997), and strong upwelling exists where the flow turns offshore. During particularly strong upwelling episodes, upwelled waters can be colder than 17°C (Swallow and Bruce, 1966), but typical upwelling temperatures are in the 19–23°C range.

When the Southwest Monsoon dies down, the cross-equatorial Somali Current turns offshore again at 3°N, while the Great Whirl continues to spin in its original position. The Great Whirl is

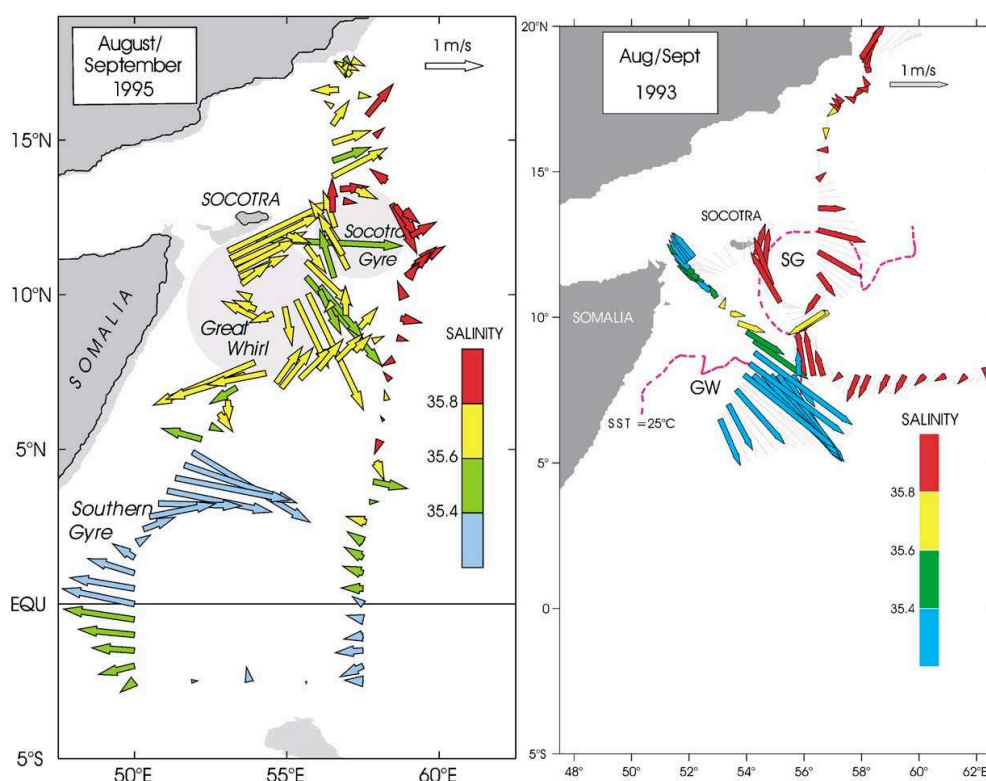


Fig. 1. Somali Current flow patterns during the late summer monsoon phases of (a) 1993 and (b) 1995. Marked are the Southern Gyre, Great Whirl and Socotra Gyre. Near-surface salinities (color-coded on the current vectors) indicate that lower-salinity waters originating from the southwestern and upwelling regions recirculate in the Great Whirl. Note that the GW in 1995 was located much more northerly, against the banks of southern Socotra, than in 1993 (after Fischer et al., 1996 and Schott et al., 1997).

even discernible underneath the developing North-east Monsoon circulation well toward the end of the year (Bruce et al., 1981).

Significant interannual differences in the system of cold upwelling wedges off Somalia and their movements during the course of the Southwest Monsoon have already been reported (Evans and Brown, 1981; Schott, 1983). Recently, based on the WOCE moored and shipboard observations during 1993–96, new analyses as to the location and intensity of the Great Whirl have been made (Fig. 2). In 1993, the northern boundary of the Great Whirl was located about 200 km south of

the banks of Socotra (Fischer et al., 1996). In 1995, it was banked right against the slope south of Socotra (Schott et al., 1997), and it was well developed as one large organized circulation cell until mid-October. In 1996, it was again located much more to the south, similar to the 1993 situation, the gyre transports were weaker than in 1995, and the Great Whirl was already becoming disorganized in August (Fig. 2).

For an analysis of the changes in the GW position, we have used altimetry data from the CLS Space Oceanography Division giving the sea-surface anomaly every 10 days. These data can be

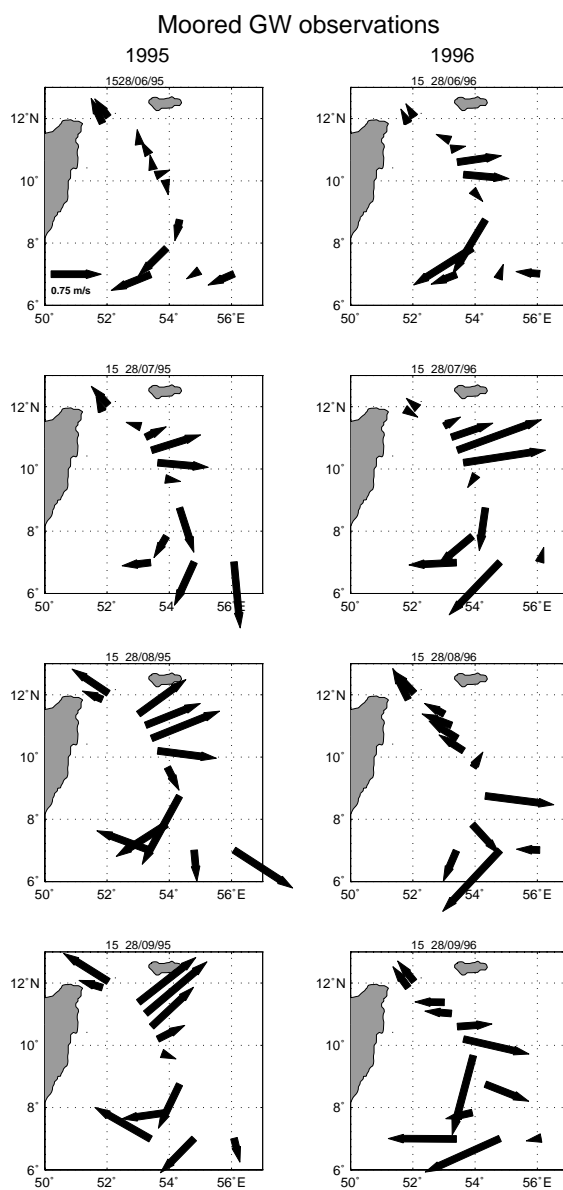


Fig. 2. Time series of near-surface current vector plots from the Great Whirl and Socotra Passage region (15 day means) for June–September (a) 1995, (b) 1996. Note the differences in GW intensities of both years and that the 1996 GW collapsed much earlier (from Schott and McCreary, 2001).

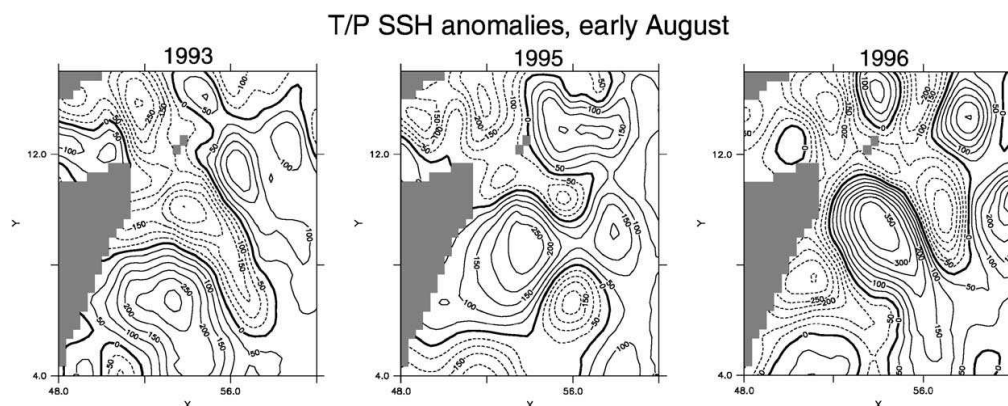


Fig. 3. Altimetric sea-surface height anomalies (in mm) in early August for the years 1993, 1995, and 1996.

downloaded from: <ftp.cls.fr/pub/oceano/AVISO/MSLA>; details can be found in Le Traon et al. (1998) and Le Traon and Ogor (1998). During the months of July and August, the GW could be detected by a sea-surface height anomaly (SSHA) which is maximum in the regions between 6°N and 12°N and between 50°E and 56°E. As seen from Fig. 3, the location of the GW maximum is usually located within this area. Each SSHA map was also inspected visually. At later times of the GW evolution, that is, in September and October, the identification of the GW was ambiguous as it sometimes splits up, was dominated by a stronger Socotra gyre (see Fig. 1), or had left the region described above. We therefore have restricted our analysis of the GW position to the months of July and August.

3. The models

When analyzing ocean dynamics with the use of complex numerical models, a balance between realism, comprehension and feasibility has to be found. To this end, it is often useful to employ a hierarchy of models of different complexities, to untangle the ocean dynamics. We therefore have employed two different classes of models, namely a fully thermodynamic multi-level primitive

equation (PE) model and a reduced-gravity (RG) model.

The rationale for this choice is as follows. The PE model permits a fairly realistic simulation of the circulation, however, at a high computational expense so that only very few integrations were possible. The RG model is much simpler and lags many important processes that are represented in the PE model such as, for example, baroclinic instability, the influence of salinity and realistic topography. This has important effects on the solution, as mentioned in Section 5. However, a large number of experiments with a higher horizontal resolution are possible with the RG model that can help to evaluate the chaotic nature of the ocean circulation.

Each model has been used in two configurations, with high and low friction, in order to estimate the sensitivity of the solution to the dissipation parametrization.

3.1. Primitive equation model

The PE model was constructed on the basis of the MOM2.1 code with a $1/3^\circ \times 1/3^\circ$ resolution and 35 vertical levels, 10 of which are in the upper 110 m. The model extends from 30°S to 26°N and from 30°E to 110°E, with open boundaries at 30°S and at 115°E (Indonesian Throughflow) that are

treated following Stevens (1990). Values for the transport streamfunction and the tracers at inflow points were taken from the model of Semtner and Chervin (1992). The vertical mixing of tracers and momentum depends on the Richardson number, following Pacanowski and Philander (1981). Surface salinity is relaxed to the monthly mean values given by Levitus and Boyer (1994). A description of the model is given by Rix (1998), who also discusses some general aspects of the model's circulation.

In its standard version, the model has biharmonic horizontal diffusion and friction, with a coefficient of $3 \times 10^{11} \text{ m}^4 \text{ s}^{-1}$, which is chosen as small as possible to be compatible with numerical requirements. Alternatively, a version with horizontal Laplacian diffusion was employed with a coefficient of $1 \times 10^3 \text{ m}^2 \text{ s}^{-1}$. While biharmonic mixing is physically somewhat less justified than Fickian diffusion, it has the advantage that it acts only at the smallest resolved scales, and at the mesoscale is, therefore, less dissipative than Laplacian diffusion. For example, for a length scale of 100 km, the diffusive time scale in the Laplacian version is 100 days, compared to 3000 days in the biharmonic version.

3.2. Reduced gravity model

In the construction of the RG model, we closely followed the model proposed by McCreary and Kundu (1989). The model domain extends from 10°S to 20°N and from 38°E to 98°E with closed

boundaries in the south and east (no Indonesian Throughflow), and has a horizontal resolution of $\frac{1}{9}^\circ \times \frac{1}{9}^\circ$. The model consists of a dynamic layer of average thickness 200 m, including a 50 m thick mixed layer. The dynamic layer and the mixed layer that both have a horizontally varying temperature lie above a deep inert layer with a temperature of 16°C . The effects of salinity are neglected. When the dynamic layer becomes shallower than the mixed layer, deep water is entrained into the mixed layer and the thickness of the dynamic layer is set to the mixed-layer depth. This process parameterizes the upwelling that usually occurs at one or two coastal wedges along the coast of Somalia (see Schott, 1983).

In the RG model, the lateral viscosity coefficient equals the diffusivity coefficient and will henceforth be referred to as the “friction” coefficient. It has a standard value of $5 \times 10^2 \text{ m}^2 \text{ s}^{-1}$, which is again chosen as small as possible to keep the numerical noise at an insignificant level. For comparison, a high-friction version with twice that value is also used.

4. The experiments

4.1. Primitive equation solutions

Two experiments with the PE model spanning the period from 1970 to 1996 were performed (Table 1). Experiment PE-hi used Laplacian friction, while experiment PE-lo used the

Table 1
Overview of the numerical experiments performed

Exp.	Forcing	Friction ($10^3 \text{ m}^2/\text{s}$)	Horiz. res. (deg)	Ensemble size
PE-hi	FSU70-96	1	1/3	1
PE-lo	FSU70-96	(biharm. ^a) $3 \times 10^{11} \text{ m}^4 \text{ s}^{-1}$	1/3	1
RG-hi93	FSU93	1	1/9	10
RG-lo93	FSU93	0.5	1/9	10
RG-hi95	FSU95	1	1/9	10
RG-lo95	FSU95	0.5	1/9	10
RG-hi96	FSU96	1	1/9	10
RG-lo96	FSU96	0.5	1/9	10
RG-200	Climatology	0.7	1/9	200

^aViscosity = 3 and diffusivity = $5 \times 10^{11} \text{ m}^4 \text{ s}^{-1}$.

biharmonic formulation. Both the experiments started from the same 30-year-long spin-up using climatological forcing (no interannual variability). The wind forcing has been derived from the observed monthly mean pseudostress data of Florida State University (FSU) for the years 1970–1996. For the surface heat flux, we have used the formulation by Barnier et al. (1995), which can be interpreted as a relaxation of the model surface temperature towards an equivalent surface temperature determined from a climatology based on the data from ECMWF.

A snapshot (August 1) of the depth-integrated transport in both model versions in the western Arabian Sea is shown in Fig. 4 (left panel). Both models display a GW structure in this variable with roughly the same overall magnitude. As expected, the biharmonic version (Exp. PE-low) shows a narrower boundary current and more intense flow around the GW, and is accompanied by a cyclonic eddy that is barely seen in Exp. PE-hi.

4.2. Reduced-gravity solutions

In the experiments with the RG model, it has been attempted to distinguish between the external variability forced by the wind and the internal variability generated by ocean processes. For this reason, integrations with the RG model using FSU wind forcing of each of the perpetual years 1993, 1995 and 1996 have been performed, both for high and low values of the friction coefficient (Table 1). Each integration consisted of a 5-year spin-up followed by 10 years, which were used for the analysis. By considering large-scale quantities like the meridional heat transport and the GW location, it was checked that the model reached a statistically stationary state after only about three years.

By forcing the model repeatedly with a perpetually repeated annual-cycle wind pattern, we implicitly assume that the model dynamics has an effective memory time of less than 1 year. This has been checked by performing one integration over 200 years (Exp. RG-200) with perpetual winds. In this experiment, the spectrum of annual averaged variables such as the meridional heat

transport was indistinguishable from a white spectrum, suggesting that the memory of the model is indeed smaller than 1 year. This rather short time scale is in agreement with the equatorial and low latitude dynamics of the RG model. Equatorial waves in the Indian Ocean and planetary waves in the Arabian Sea take considerably less than 1 year to cross the corresponding basin (e.g., Philander, 1990). It is therefore, justified to consider the result from two consecutive years in the RG model as approximately statistically independent, so that each integration effectively yields an ensemble of 10 independent realizations.

Fig. 4 (right panel) shows the mean layer thickness in Exps. RG-lo95 and RG-hi95. In order to suppress the internal variability, an average of 10 subsequent realizations was taken. Note that in the low-friction experiments, the average GW intensity is higher and the meridional location of the GW position is more southward by about 1° for all wind forcings considered compared to the high-friction cases. This is most probably caused by the earlier occurrence of instability in the low-friction case.

In the RG model, the center of the GW was defined as the point with the maximum thickness of the dynamic layer in the Arabian sea. Likewise, in the PE model, the center of the GW is defined as the location where the 20°C thermocline is the deepest. The meridional location of the GW center obtained in this way from July 1 to September 1 in the different experiments is given in Table 2. As discussed above, at later times during the year the GW location is no longer meaningful due to turbulent eddies.

5. Wind-induced (external) variability

In order to investigate the extent to which the observed variability in the GW region can be attributed to the wind, we first consider the wind stress curl for August 1 of the years 1993, 1995 and 1996. The flat-bottom Sverdrup transport stream function has a maximum in the GW area for the years 1993 and 1996, while the maximum is more southward in 1995. As seen from Table 2, in both the altimeter observations and the numerical

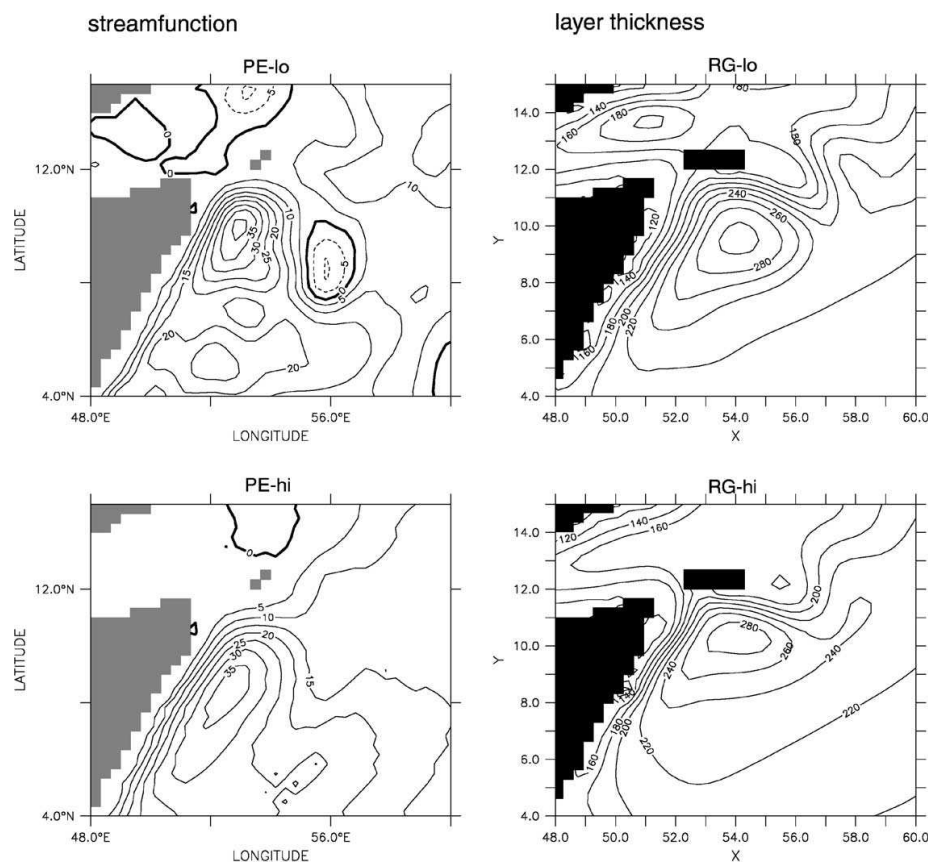


Fig. 4. Circulation patterns in 4 different experiments. Left panels: Snapshots of the depth integrated transport stream function from experiments PE-lo (top) and PE-hi (bottom), taken on August 1, 1995. Contour interval 5 Sv. Right panels: Mean layer thickness of the reduced-gravity model (averaged over 10 subsequent August 1) for experiments RG-lo95 (top) and RG-hi95 (bottom). Contour interval 20 m.

simulations, the center of the GW is more northward in the year 1995 compared to 1993, in contrast to the results obtained from the flat-bottom Sverdrup balance (see also Table 2). Hence, the linear flat-bottom Sverdrup balance is obviously not the key to determine the position of the GW, as was already discussed by Cox (1979).

For Exp. PE-lo, which can be considered to be more realistic than PE-hi, the near-surface temperature and velocity for the summers 1993 and

1995 (Fig. 5) can be compared directly with the observations in Fig. 1. As in the observations, the GW center in 1993 is 200 km more southward than in 1995 (cf., Table 2). Fig. 6 shows the difference between the years 1995 and 1993 for the altimetric observations and the two PE models. Despite the different nature of the variables (SSH for the observations, barotropic transport stream function for the models) the change from 1993 to 1995 is at least qualitatively reproduced in PE-lo,

Table 2
Meridional GW location on August 1 of the years 1993, 1995, and 1996 in observations and models^a

Obs./model	GW Pos 93	GW Pos 95	GW Pos 96
Altimetry	6.6	8.4	9.2
Sverdrup trans.	10.0	8.7	9.0
RG—high	9.8	10.1	9.8
RG—low	8.7±0.5	9.5±0.3	9.0±0.3
PE—high	8.0	9.0	8.1
PE—low	7.1	9.1	7.1

^aNote that for the altimetry, the location of the *anomaly* maximum is given so that only the year-to-year differences can be compared.

and to a lesser extent also in PE-hi where that difference is considerably smaller.

As also seen from Fig. 6, however, the changes from 1993 to 1996 are not well reproduced in either of the PE models. In both experiments, the GW in 1996 has only about half the transport compared to 1993 and 1995 (not shown). The observed sea-surface height anomalies on August 1 of 1996 however, are, comparable in magnitude to the years 1993 and 1995 (cf. Fig. 3). A closer analysis for the year 1996 reveals that observations and numerical simulations still agree to some extent in July, but the GW starts to disappear early in 1996. On August 1, the GW disappearance in the two PE experiments has already proceeded, while in the observations it happens only about 10 days later.

On average, the RG models agree with the observations in giving a more southward position of the GW in 1993 compared to 1995. This is true for both high- and low-friction experiments. In the low-friction runs, individual realizations of Exps. RG-lo93 and RG-lo95 can, however, be found where this is not the case. Furthermore, in all realizations of Exps. RG-hi96 and RG-lo96, the RG model fails to reproduce the early break down of the GW that occurred in 1996. This is in contrast to the PE model, which shows this breakdown in both experiments, although not always at the same time as in the observations. A likely explanation could be that the dynamics of the single-layer RG model does not allow for baroclinic instability which plays an important role in

the breakup of the GW according to Jensen (1993). Another possible reason might be the influence of the southern Indian Ocean, which is only partly (down to 10°S) included in the RG model.

6. Internal variability

The experiments with the RG model were conducted to determine the internally generated contribution to the interannual variability of the circulation in the Arabian Sea. Fig. 7 shows the layer thickness anomaly (relative to ensemble mean) in early August for three consecutive years of Exp. RG-lo95. Although there is no interannual variability in the forcing fields, substantial changes in the strength, shape and location of the circulation anomalies occur in the western Arabian Sea. This year-to-year variability is to be expected because, due to the chaotic dynamics of the model, every year the integration starts with different initial conditions which amplify in areas where the nonlinearity in the governing equations plays a substantial role. In the western-half of the Arabian Sea, the internal variability is elevated during the entire year. In the eastern part, the dynamics in the RG model is, however, more linear and the internal variability plays no substantial role.

Fig. 8 gives a comparison between externally and internally forced variability for the thickness anomaly. The upper figure shows the rms difference between the three mean values of the ensembles RG-lo93, RG-lo95 and RG-lo96 which result from the different wind forcing in the 3 years, and thus is a measure for the external variability. Maximum rms values reach more than 30 m in the western Arabian Sea. The lower part of Fig. 8 is the average rms within the three ensembles, and hence is a measure for the internal variability. It follows from Fig. 8 that the overall magnitude of the external and the internal variability is very similar in the GW region.

It is remarkable that increasing the friction coefficient by a factor of 2 is sufficient to virtually eliminate the internal variability. As seen in Fig. 9, the internally caused layer thickness variability is less than 5 m except in a small part of the area around the southern gyre and the GW, whereas

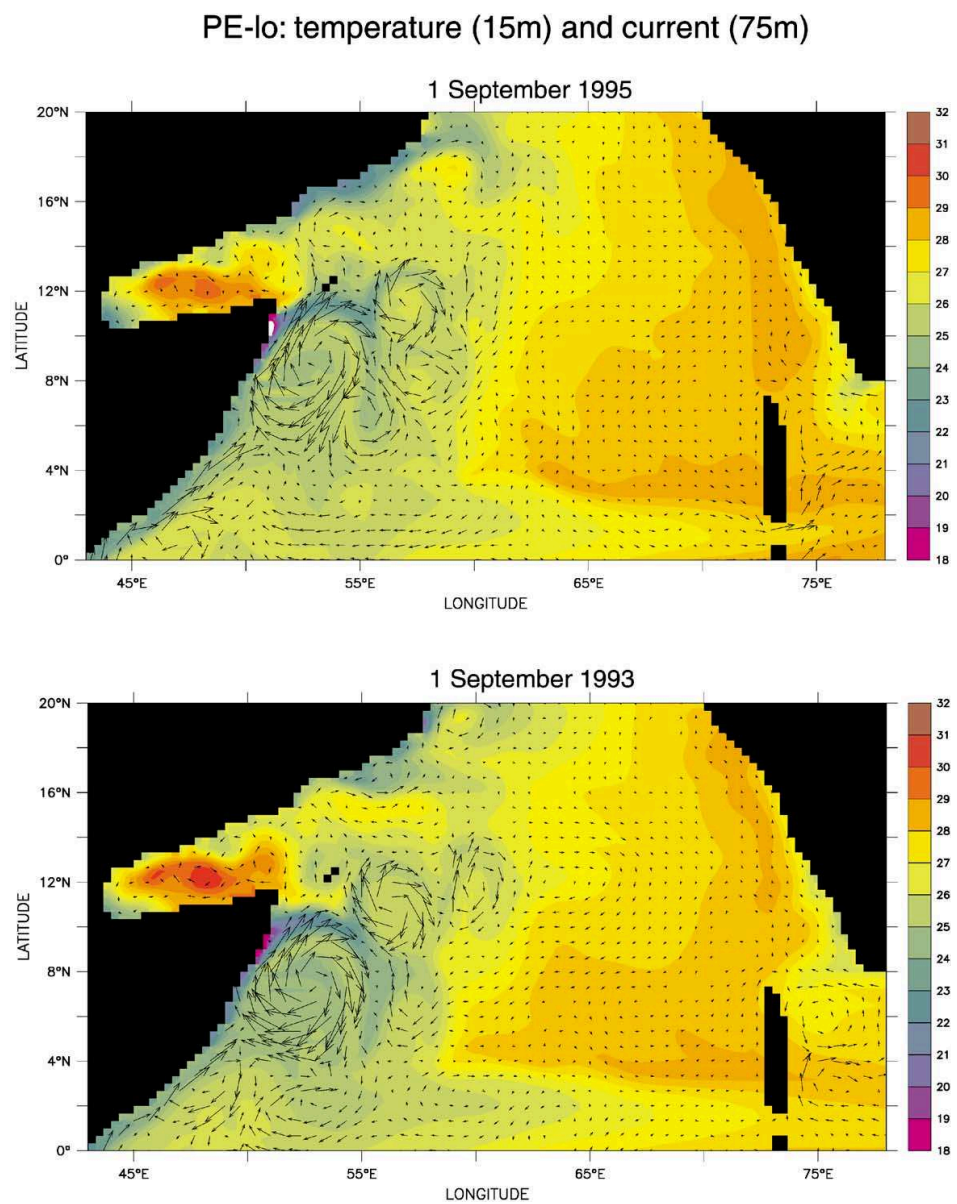


Fig. 5. Temperature at 15 m depth and velocity at 75 m depth on September 1 of 1995 (upper) and 1993 (lower) in the PE model (exp. PE-lo).

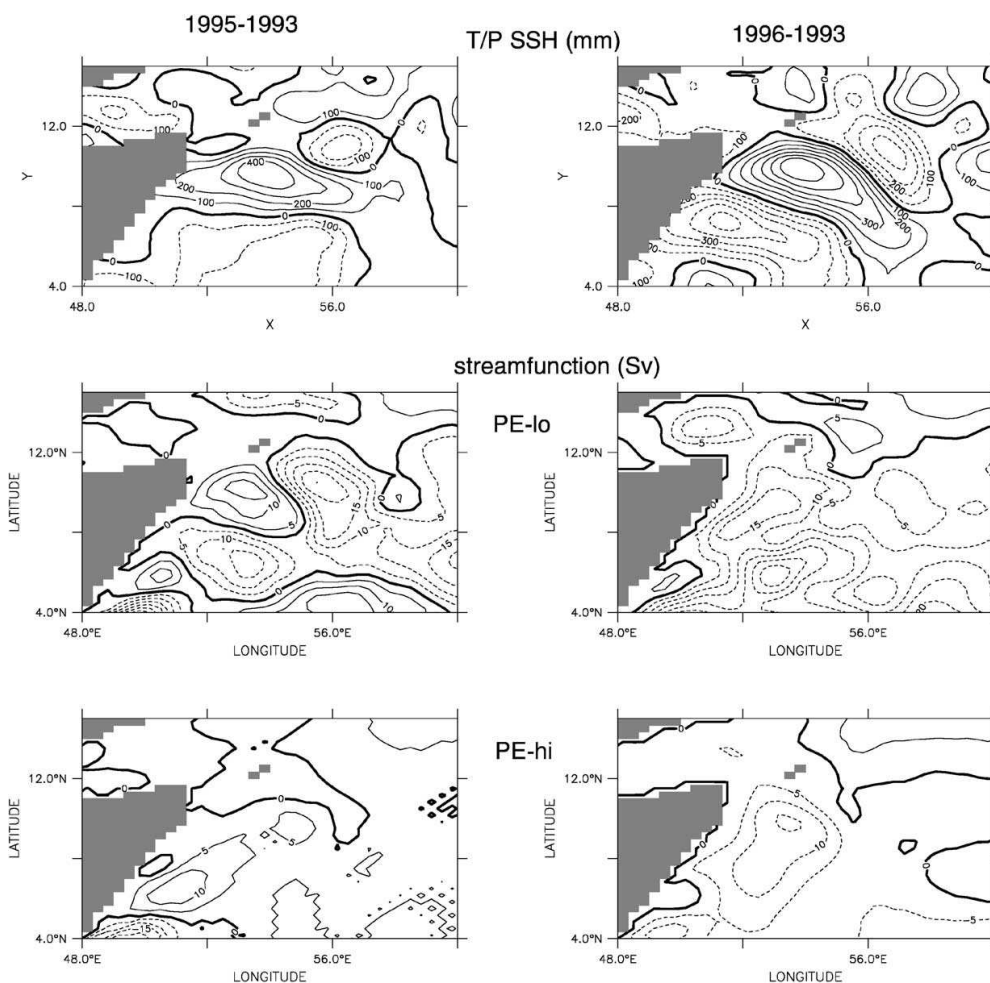


Fig. 6. Interannual variability of the GW on August 1. Left panels show values for 1995 minus 1993, right panels 1996 minus 1993. Top panels give SSH from Topex/Poseidon (in mm), middle and bottom panels show depth integrated transport stream function from exp. PE-lo (middle) and PE-hi (bottom), both in Sv.

the externally forced interannual variability is only moderately reduced (maximum near 20 m layer thickness). In the RG-hi models, the GW therefore shows no substantial internal variability, a result that is consistent with Luther and O'Brien (1989).

Fig. 10 shows the GW meridional location vs. intensity as measured by the mean maximum layer thickness for the integrations with the RG model. In the high viscosity experiments, the wind forcing leaves a clear imprint in the GW intensity and to a lesser extent also in the GW location, with 1993

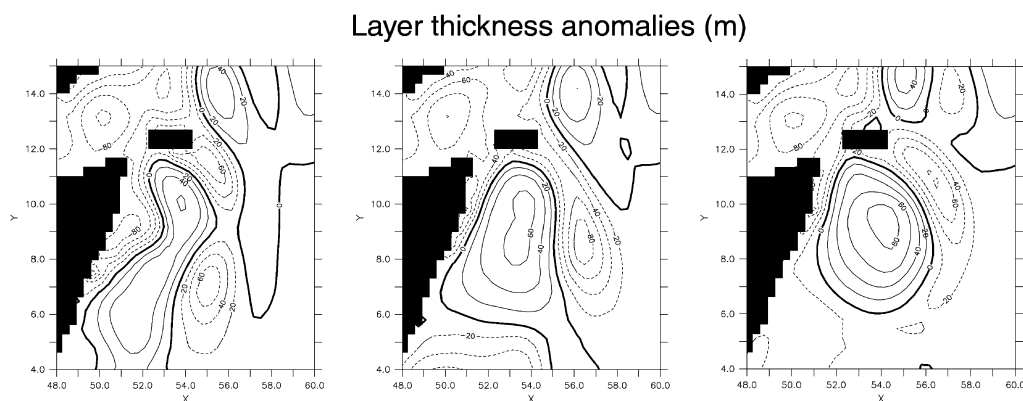


Fig. 7. Layer thickness anomalies (in m) relative to 10-year mean of all months at 3 consecutive August 1 in the low-friction experiment RG-lo95.

being the strongest and 1996 the weakest, and very little internal variations among the different ensemble members. In the low-friction experiments, the wind influence remains clearly visible but is superposed by a considerable scatter among the different ensemble members, with on average stronger GW realizations located more southward. Since the different members of each ensemble are subject to identical forcing, this scatter, which amounts to differences in meridional location by more than 100 km and in maximum layer thickness by more than 30 m, can only have internal causes.

The differences in GW location between the three ensembles also follow from Table 2 where the meridional GW positions for the 3 years, and the respective standard deviations are given. Furthermore, from the observed SSH anomalies it follows that the differences in location of the altimetric anomalies are larger than the differences in GW location between any of the models, suggesting that in the ocean the large-scale variability is even higher than in the models considered here. Indeed, experiments with the RG model with even lower friction values (not shown) indicate that the variability of large-scale features increases even further.

Within each of the three sets of Exps. RG-lo93, RG-lo95 and RG-lo96, we also have calculated the

correlation of GW location and strength between July 1 and August 1 and between July 1 and September 1. The results are similar for the GW location and GW strength, showing significant correlations between July 1 and August 1 ranging from 0.45 to 0.72. The correlations between July 1 and September 1 are however insignificant. This suggests that the knowledge of the GW position and strength on July 1 does not improve a prediction of the same variables on September 1. This alludes to a correlation time for the GW location of roughly one month.

7. Discussion

The western Arabian Sea, like the western parts of all the ocean basins, is dominated by strong boundary currents that lead to instabilities, especially in low latitudes. In these areas, non-linearity is higher than in the interior and eastern parts of the basins, leading to a higher ratio of internal vs. external variability. At the beginning of this work, it was intended to describe and classify the behavior of the GW during its life cycle in comparison with observations. We found, however, that this was not possible in eddy-permitting models. After a more or less annually recurrent birth period of the GW in July and

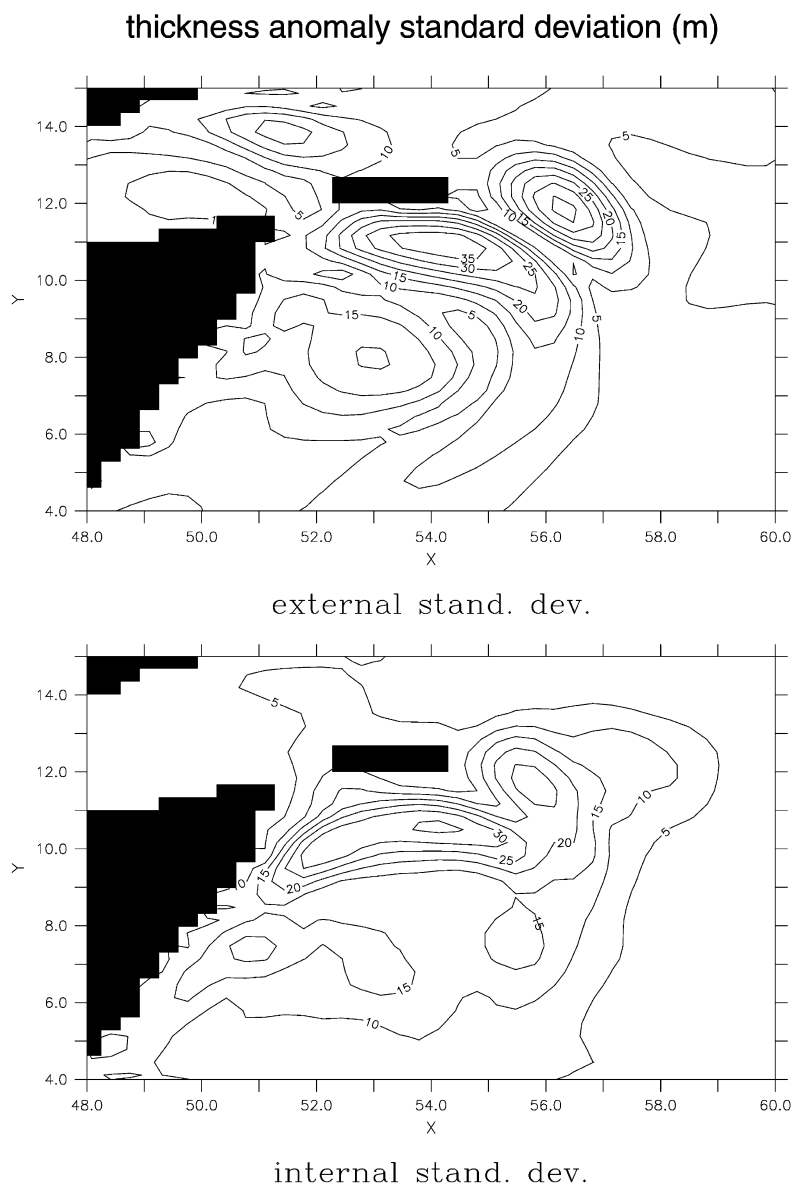


Fig. 8. Standard deviation due to external (upper) and internal (lower) variability for the low-viscosity exps. RG-lo (contour interval is 5 m). The standard deviation due to the external part is calculated using the variance of the means over 10 realizations for each of the years 1993, 1995 and 1996. The standard deviation of the internal part is calculated using the average variance for the years 1993, 1995 and 1996.

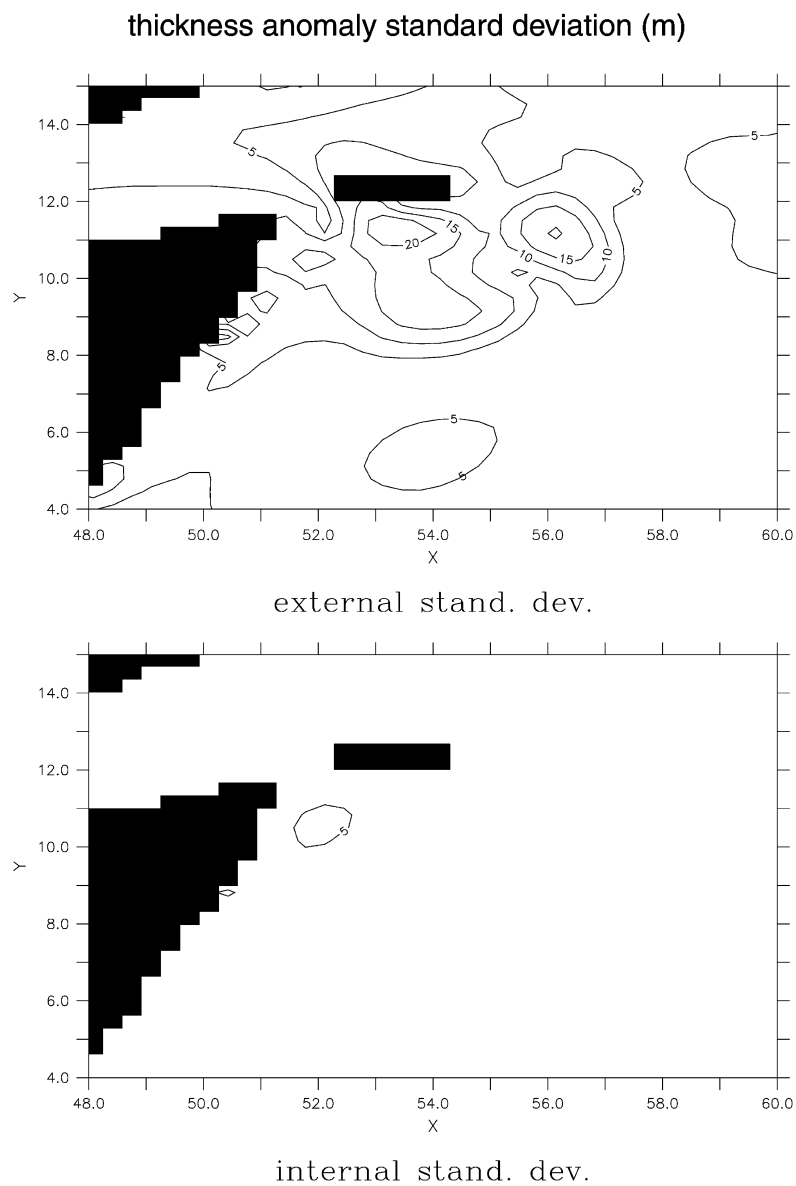


Fig. 9. As Fig. 8, but for the high-viscosity experiments RG-hi.

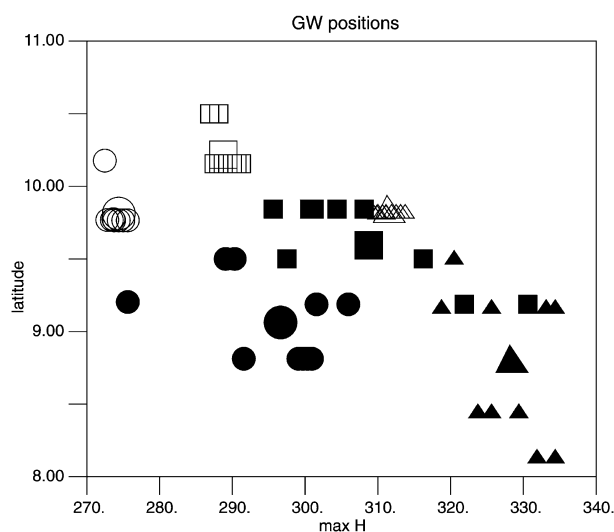


Fig. 10. Mean layer thickness vs. meridional position of the GW in the different experiments with the RG model. Triangles, squares and circles correspond to expts. with forcings of the years 1993, 1995 and 1996, respectively; solid and open symbols are for low and high-friction experiments, respectively; large symbols represent the mean values.

August, the circulation in the western Arabian Sea is strongly influenced by turbulent (mostly anti-cyclonic) eddies. Consequently, from September on the GW is characterized by chaotic dynamics rather than a regular life cycle.

We have demonstrated that the year-to-year variability of ocean currents in the western Arabian Sea is not only influenced by variability in the wind forcing but is substantially influenced by internally generated variability. This latter variability has a white spectrum on interannual time scales, and a prediction of the internally caused variability seems impossible on time scales longer than a month.

A critical parameter in the RG model is dissipation values that have been chosen here for reasons of numerical stability and smoothness. This choice, while common, is not based on physical considerations, and an uncomfortable conclusion is that the model results depend on the value of that parameter. Preliminary experiments with a friction coefficient of $0.3 \times 10^3 \text{ m}^2 \text{ s}^{-1}$ suggest that the variability of large-

scale quantities still increases with decreasing friction.

As remarked above, Exp. PE-lo can be considered as the most realistic of all runs and can best be compared with observations. For the interpretation of such a comparison, it would be necessary to assess the internal variability in that model. If the differences in GW position as shown in Table 2 were indicative of the overall dissipation, it would follow that the internal variability in PE-lo were higher than in any of the RG models. From our experiments we have, however, no direct estimate of the internal part of the variability in either of the PE models, due to the prohibitive computational expenses.

In summary, our findings suggest that internal variability is so high that a direct comparison between observations and eddy-resolving models of large-scale quantities like the GW is only meaningful if an ensemble of model experiments is considered. A comparison of actual model realizations to observations would be meaningful only in the context of data assimilation where the

model can be forced to simulate the actual realization of the ocean dynamics.

Friction employed for numerical stability alters the behavior of large-scale quantities, which makes the comparison between data and noneddy-resolving experiments problematic. The meridional location of the GW in the high-friction experiments is significantly different from the low-friction experiments in all the years considered, although the variability in the low-friction experiments is rather high. Observations and experiments with even lower values of friction (not discussed here) indicate that values of about 1° variation for the external and internal variability are at best a lower bound of their real world values. It follows that numerical experiments with higher resolution and/or lower friction values are necessary to model the observed ocean variability of large-scale quantities even at low latitudes as considered here.

Acknowledgements

We thank C. Eden for many helpful remarks and M. Kawamiya for extensive discussions. We are grateful to J.P. McCreary and an anonymous referee for many comments which helped to improve the paper considerably. The altimeter products were produced by the CLS Space Oceanography Division as part of the Environment and Climate EU AGORA (ENV4-CT9560113) and DUACS (ENV44-T96-0357). Support from the German CLIVAR-Ocean project BMBF 03F0246A is gratefully acknowledged. A first version of the PE model used here was set up by N. Rix. We thank the Geophysical Fluid Dynamics Laboratory/NOAA for the prototype code for the OGCM used in the present study, and A. Semtner and R. Chervin for sharing their model data used here at the open boundaries. Figures are prepared using FERRET software.

References

- Anderson, D.L.T., Carrington, D.J., 1993. Modeling interannual variability in the Indian Ocean using momentum fluxes from the operational weather analyses of the United Kingdom Meteorological Office and European Centre for Medium Range Weather Forecasts. *Journal of Geophysical Research* 98, 12 483–12 499.
- Barnier, B., Siefridt, L., Marchesiello, P., 1995. Thermal forcing for a global ocean circulation model using a three year climatology of ECMWF analysis. *Journal of Marine Systems* 6, 363–380.
- Bruce, J.G., Fieux, M., Gonella, J., 1981. A note on the continuance of the Somali eddy after the cessation of the Southwest Monsoon. *Oceanology Acta* 4, 7–9.
- Cox, M.D., 1979. A numerical study of Somali current eddies. *Journal of Physical Oceanography* 9, 311–326.
- Evans, R.H., Brown, O.B., 1981. Propagation of thermal fronts in the Somali Current system. *Deep-Sea Research* 1 28A, 521–527.
- Fischer, J., Schott, F., Stramma, L., 1996. Currents and transports of the Great Whirl–Socotra Gyre System during the summer monsoon august 1993. *Journal of Geophysical Research* 101, 3573–3587.
- Jensen, T.G., 1993. Equatorial variability and resonance in a wind-driven Indian Ocean Model. *Journal of Geophysical Research* 98, 22 533–22 552.
- Le Traon, P.-Y., Ogor, F., 1998. ERS-1/2 orbit error improvement using Topex/Poseidon: the 2 cm challenge. *Journal of Geophysical Research* 103, 8045–8057.
- Le Traon, P.-Y., Nadal, F., Ducet, N., 1998. An improved mapping method of multi-satellite altimeter data. *Journal of Atmospheric and Oceanic Technology* 15, 522–534.
- Levitus, S., Boyer, T.P., 1994. NOAA Atlas NESDIS 3: World Ocean Atlas 1994, Vol. 3. Technical report, NODC.
- Luther, M.E., 1999. Interannual variability in the Somali Current 1954–1976. *Non-linear Analyses* 35, 59–83.
- Luther, M.E., O'Brien, J.J., 1989. Modeling the variability in the Somali Current. In: Nihoul, J.C.J., Jamart, B.M. (Eds.), *Mesoscale/Synoptic Coherent Structures in Geophysical Turbulence*. Elsevier, Amsterdam, pp. 373–386.
- McCreary, J.P., Kundu, P.K., 1989. A numerical investigation of Sea surface temperature variability in the Arabian Sea. *Journal of Geophysical Research* 94, 16 097–16 114.
- McCreary, J.P., Kohler, K.E., Hood, R.R., Olson, D.B., 1996. A four-component ecosystem model of biological activity in the Arabian Sea. *Progress in Oceanography* 37, 117–165.
- Pacanowski, R.C., Philander, S.G.H., 1981. Parameterization of vertical mixing in numerical models of tropical oceans. *Journal of Physical Oceanography* 11, 1443–1451.
- Philander, S.G., 1990. *El Niño, La Niña, and the Southern Oscillation*. Academic Press, New York, p. 293.
- Rix, N., 1998. Variabilität und Wärmetransport in einem numerischen Modell des Indischen Ozeans. Ph.D. Thesis, Institut für Meereskunde Kiel, Germany.
- Schott, F., 1983. Monsoon response of the Somali Current and associated upwelling. *Progress in Oceanography* 12, 357–381.
- Schott, F., McCreary Jr., J.P., 2001. The monsoon circulation of the Indian Ocean. *Progress in Oceanography* 51, 1–123.

- Schott, F., Quadfasel, D., 1982. Variability of the Somali Current and associated upwelling. *Progress in Oceanography* 12, 357–381.
- Schott, F., Fischer, J., Garternicht, U., Quadfasel, D., 1997. Winter monsoon circulation of the northern Arabian Sea and Somali Current, 1995. *Geophysical Research Letters* 24, 2565–2568.
- Semtner, A.J., Chervin, R.M., 1992. Ocean general circulation from a global eddy-resolving model. *Journal of Geophysical Research* 97, 5493–5550.
- Stevens, D.P., 1990. On open boundary conditions for three dimensional primitive equation ocean circulation models. *Geophysical and Astrophysical Fluid Dynamics* 51, 103–133.
- Swallow, J.C., Bruce, J.G., 1966. Current measurements off the Somali coast during the southwest monsoon of 1964. *Deep-sea Research* 13, 861–888.

4.2 The parametrization of baroclinic instability in a simple model

Journal of Marine Research, 58, 571–583, 2000

The parameterization of baroclinic instability in a simple model

by A. Wirth¹

ABSTRACT

Baroclinic instability of zonally forced flow in a two mode quasi-geostrophic numerical model with periodic boundary conditions is considered. Only the largest scale of the baroclinic mode is forced and the scale dependence of a diffusive parameterization of baroclinic layer thickness is determined. It is shown that the effect of baroclinic instability is a decreasing function of scale with an exponent of about half of that corresponding to the commonly used Laplace operator. We furthermore show that there is no linear relation between the time averaged amplitude of the large scale streamfunction (or quasi-geostrophic potential vorticity) and the bolus velocity.

1. Introduction

One of the major challenges in ocean modeling is the parameterization of small-scale processes not explicitly resolved in the models themselves. Many attempts have been made in this direction. The difficulty arises from the nonlinear interaction of processes on a wide range of length and time scales.

Recently, interest has focused on the parameterization of a specific process, that is baroclinic instability. This process, of paramount importance in atmosphere and ocean dynamics, dominantly occurs at a small range of length and time scales. The typical length scale for the ocean is of a few times the baroclinic Rossby radius of deformation (≈ 50 km), while the typical time scale is of the order of tenth of days. This rather strong localization of baroclinic instability in wavenumber and frequency space might permit a successful parameterization.

More precisely, when using Global Circulation Models to determine the climate variability over several hundreds of years the grid resolution of the ocean models currently used is a few hundreds to several hundreds of kilometers. Such resolution is by far too poor to explicitly represent the effects of baroclinic instability on the large-scale motion and they have thus to be parameterized.

It is too ambitious to ask for a parameterization that exactly mimics the effects of the small scales on the larger ones. Two necessary conditions of such a parameterization would be: (i) that the dynamics of the small scales are completely slaved to the large scales, and

1. Institut für Meereskunde, Universität Kiel, Dusternbrooker Weg 20, D4105 Kiel, Germany. *email:* awirth@ifm.uni-kiel.de

(ii) that the dimension of the chaotic attractor of the full problem is smaller than the number of degrees of freedom of our numerical model. Both conditions are unlikely to be satisfied. The parameterization should, however, approach the effects of the parameterized scales in a statistical sense.

A new way of parameterizing baroclinic instability was proposed by Gent and McWilliams (1990), based on diffusion of isopycnal thickness. Another, but not new, feature of the same parameterization is the down-gradient diffusion along isopycnals (see e.g. Redi, 1982). An interesting feature of this parameterization is that it can be interpreted as a quasi-adiabatic advection as explained in Gent *et al.* (1995). We like to refer the reader to this paper for a detailed discussion on the parameterization proposed by Gent and McWilliams.

There are different ways of analyzing such parameterization. A pragmatic approach is to implement such parameterization in a large-scale ocean model (Danabasoglu and McWilliams, 1995) and evaluate its performance. Another way is to verify the foundations of the theory in numerical experiments (Treguier, 1999).

The approach adapted here as in a variety of other experiments (see e.g. Killworth, 2000 and references therein) is to estimate the influence of the small scales on the larger ones in a fine resolution model, that is, a model resolving the Rossby radius of deformation. We like to emphasize here that for resolving a length scale l_0 it is not enough to have the grid-size d_0 of the order or slightly smaller than l_0 . It is rather necessary that the length scale l_0 is in the inertial range of the nonlinear dynamics (see e.g. Frisch, 1996). This usually means that the grid size d_0 has to be chosen at least an order of magnitude smaller than the length scale l_0 . It is indeed true that the dynamics on scales only a few times greater than the grid scale is dominated by linear dissipation being very different to the dynamics in the inertial range, which is dominated by nonlinear advection. The recent awareness of this problem in the ocean modeling community is apparent by the fact that models previously referred to as “eddy resolving” are now referred to as “eddy permitting.”

The second point we like to dwell on is statistical significance. Our numerical results (see Section 4) show that even for the estimation of mean values and variances, that is the lowest order moments, averaging times of about a hundred years are necessary. When such long times are necessary for a parameterized quantity to relax to their mean value the results using such parameterization have to be handled with care. An immediate consequence is that parameterized models can only be interpreted in an ensemble sense.

The points mentioned in the previous two paragraphs put severe constraints on the feasibility of analyzing such parameterization. The experiment has thus to be set up very carefully, containing only the absolutely necessary ingredients. We thus consider the problem of “parameterizing baroclinic instability” in its numerically most feasible way. That is, we used a quasi-geostrophic two-mode model, which is periodic, both in the latitudinal and longitudinal direction. This is a simple model to test a parameterization of baroclinic instability.

Another important choice is the implementation of periodic boundary conditions. In

2000]

Wirth: Parameterization of baroclinic instability

573

previously published idealized experiments the dynamics far from the boundary appear to be completely slaved to the boundary conditions. Important quantities vary almost linearly between their extremal values at or near the boundary. Using periodic boundary conditions eliminates this problem completely.

A novelty of the present work is that a variety of experiments are performed with varying box-size, strength of forcing and viscous dissipation (model parameters) to estimate their (non-) influence on large-scale quantities like the diagnosed parameters for large-scale parameterization. It is indeed a crucial point of a large-scale parameterization that it should not, or only very weakly, depend on the above mentioned model parameters and this should be checked whenever a parameterization is proposed.

An advantage of testing parameterizations of baroclinic instability in a quasi-geostrophic experiment is that in this simplified frame work the parameterization of layer thickness as proposed by Gent and McWilliams (1990) is identical to the parameterization of vertical mixing, as favored by Greatbatch and Lamb (1990). This means that the results presented here apply to the same extent to a whole class of parameterizations but also means that the results presented here can give us no hint to which parameterization in this class is better.

A disadvantage of the simplicity is that some of the important questions related to the parameterization of baroclinic instability cannot be addressed in this simplified frame work. One is the important effect on the long-term tracer dynamics (see e.g. Lee *et al.*, 1997). The determination of the vertical dependence of a parameterization would require more baroclinic modes. We also neglect in our discussion the important point of the effect of baroclinic instability on the barotropic mode and the related question of how to implement vertical boundary conditions. For more details on this important point we refer the reader to Killworth (2000) and Treguier *et al.* (1997). The latter paper also contains a detailed discussion on eddy parameterization in quasi-geostrophic models. All the experiments presented here are restricted to the special case of purely zonal forcing. Thus, we could not consider the question of anisotropy of the diagnosed large-scale parameters as found by Rix and Willebrand (1996).

The next short section is devoted to the question of the compatibility between the β -plane approximation and periodic boundary conditions in both horizontal directions. In Section 3 we present the theoretical description of our numerical experiment which is introduced in Section 4. The results are then discussed in Section 5.

2. The periodic β -plane

This section may be skipped by people familiar with simulations on the doubly-periodic β -plane. We use spatially periodic boundary conditions in both horizontal directions. This is mathematically consistent with the β -plane approximation, for all evolution and diagnostic equations (see e.g. Hua *et al.*, 1998, for a detailed discussion of this point).

A more subtle point, however, is the validity of the β -plane approximation in a domain having infinite extension in the meridional direction. The quasi-geostrophic potential

vorticity is conserved along stream-lines of the quasi-geostrophically evolving geostrophic velocity field. When meridional boundaries are present at distance L_y , it is clear that the β -plane approximation is valid if $L_y\beta \ll f_0$. When no such boundaries are present, the condition for the β -plane approximation to be valid is that the distance a fluid parcel transported in the meridional direction, L_y , during a time-interval, T_0 , by the geostrophic velocity field is small, $L_y\beta \ll f_0$. Where T_0 is the time length of the specific process under consideration, that is baroclinic instability in our case. This condition is usually verified as the β -term inhibits meridional-transport over large distances.

We are aware of the fact that the doubly periodic β -plane imposes some constraints on the dynamics. These constraints are somewhat of a different nature than those imposed by lateral walls, used in all other tests of baroclinic instability. Repeating the presented experiments in a channel geometry and comparing both would be very fruitful.

3. The governing equations

The equations governing the dynamics of this two-mode quasi-geostrophic model are,

$$\begin{aligned} \partial_t q_1 + J(\psi_1, q_1) + J(\psi_2, q_2) + \beta \partial_x \psi_1 \\ + b_1 b_1 \nabla^2 \psi_1 + b_1 b_2 \nabla^2 \psi_2 = -v \nabla^6 \psi_1 + w_1 \end{aligned} \quad (1)$$

$$\begin{aligned} \partial_t q_2 + J(\psi_1, q_2) + J(\psi_2, q_1) + \xi J(\psi_2, q_2) + \beta \partial_x \psi_2 \\ + b_2 b_1 \nabla^2 \psi_1 + b_2 b_2 \nabla^2 \psi_2 = -v \nabla^6 \psi_2 + w_2, \end{aligned} \quad (2)$$

where q_i represents the quasi-geostrophic potential vorticity of the i -th mode,

$$q_i = (\nabla^2 - \lambda_i^2) \psi_i. \quad (3)$$

ψ_i is the corresponding streamfunction and λ_i the inverse Rossby radius of deformation. The first mode, $i = 1$, representing the depth-averaged velocity will be called barotropic and the second, $i = 2$, baroclinic. The forcing is represented by the variables w_i , the bottom friction by b_i and $\xi = 1/H \int_{-H}^0 F_2(z)^3 dz$ is the triple auto-interaction coefficient for the baroclinic mode, where $F_2(z)$ gives the vertical structure of the baroclinic mode. For further details the reader is referred to Flierl (1978) and Hua and Haidvogel (1986).

The (unphysical) parameter v represents the dissipation at the smallest scales; its value is connected to the resolution of the numerical model and large-scale quantities such as the diagnosed parameters should be independent of v when chosen in a sensible range.

We are now interested in the dynamics of the largest scale, L , of the model which is forced by $w_2 = \overline{w}_2 \sin(k_0 y)$, where $k_0 = 2\pi/L$. For that purpose we define the projection on this horizontal sine mode,

$$\overline{A} = 2 \int_D A \sin(k_0 y) dx dy. \quad (4)$$

It immediately follows from (3) that $\overline{\psi}_i = -\overline{q}_i / (k_0^2 + \lambda_i^2)$. We choose $w_1 = 0$, as in most of the previously performed numerical experiments (Killworth 2000; Lee *et al.*, 1997;

2000]

Wirth: Parameterization of baroclinic instability

575

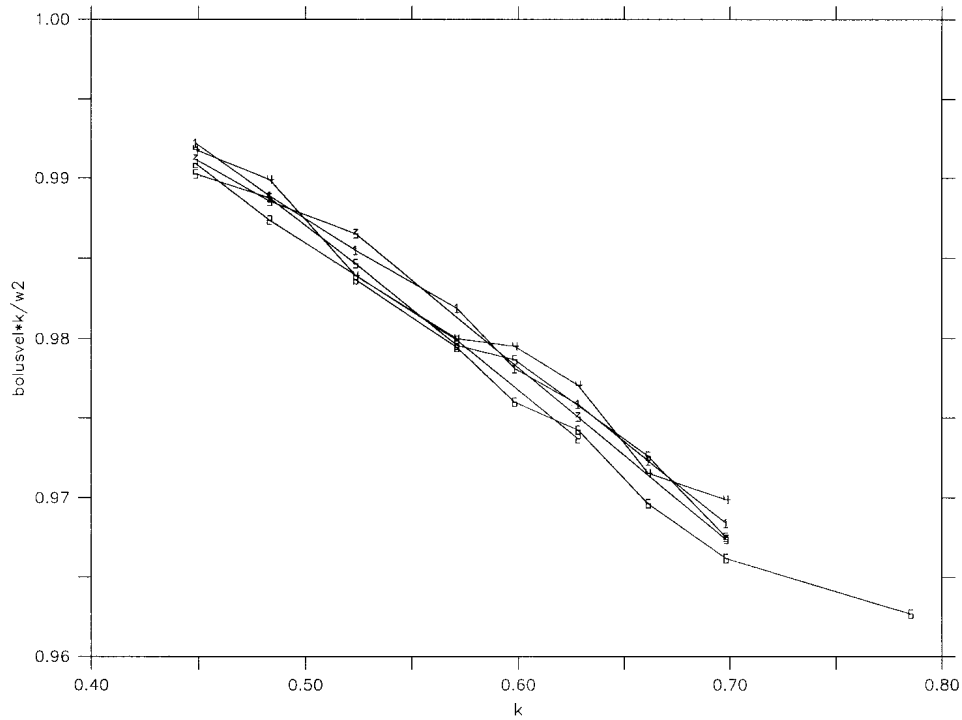


Figure 1. The quantity $\overline{\partial_y \langle (\partial_x \psi_1) \psi_2 \rangle} / \lambda_2^{-2} \overline{w_2}$ is plotted as a function of wavenumber for the six sets of experiments; experiments 1, 2, 3, 4, 5, 6 (see Table 1) as labeled, differences between the graphs are within statistical errors.

Treguier, 1999). This corresponds to thermal forcing as commonly used in atmospheric dynamics. Furthermore, we focus our attention on Eq. (2) as the perturbation of layer thickness is proportional to perturbations of ψ_2 when assuming a rigid lid at the surface. Applying (4) onto (2) we obtain,

$$-(k_0^2 + \lambda_2^2) \partial_t \overline{\psi_2} - b_2 b_1 k_0^2 \overline{\psi_1} - b_2 b_2 k_0^2 \overline{\psi_2} + \overline{J(\psi_1, q_2)} + \overline{J(\psi_2, q_1)} + \xi \overline{J(\psi_2, q_2)} = \nu k_0^6 \overline{\psi_2} + \overline{w_2}. \quad (5)$$

We suppose that the system is in a statistically stationary state, and that in the nonlinear terms the relative vorticity can be neglected which is a good approximation for scales larger than the baroclinic radius of deformation λ_2^{-1} . Averaging over time and keeping only the dominant terms we obtain:

$$\overline{J(\psi_1, q_2)} \approx -\lambda_2^2 \overline{J(\psi_1, \psi_2)} \approx \overline{w_2}. \quad (6)$$

The subdominance of the two last nonlinear terms on the left-hand side of Eq. (5) and the above relation follows from simple scaling arguments when $k_0 \rightarrow 0$, and is also verified numerically (see Section 4 and Fig. 1). The behavior of the baroclinic streamfunction at

scales larger than the first baroclinic radius of deformation is to leading order identical to the behavior of a passive scalar advected by the barotropic velocity field and subject to a source w_2 . This was already mentioned by Salmon (1980).

Using the mathematical identity,

$$\langle \overline{J(\Psi_1, \Psi_2)} \rangle = \overline{\partial_y \langle (\partial_x \Psi_1) \Psi_2 \rangle}, \quad (7)$$

we then suppose that the following parameterization holds:

$$-\lambda_2^{-2} \overline{w_2} \approx \overline{\partial_y \langle (\partial_x \Psi_1) \Psi_2 \rangle} = \kappa^{(\omega)} (-k_0^2)^{\alpha+1} \langle \overline{\Psi_2} \rangle. \quad (8)$$

When $\alpha = 0$ the last equality represents the classical Gent-McWilliams parameterization as the perturbation of layer thickness is linearly related to the amplitude of the baroclinic mode in quasi-geostrophic theory.

In the above averaged equations the β -term has completely disappeared as the forcing and the averaged large-scale flow is zonal. The whole dynamics, however, depend on the β -term and so do the parameter values. An extreme example of this is to consider the case with $\beta = 0$, where the dynamics are dominated by stable eddies that survive for very long times. This leads to a strongly intermittent behavior and no parameterization is reasonable in this case as time-averaged quantities relax too slowly to their mean value.

It is now easy to numerically measure the parameter α by determining the scale dependence of

$$\kappa^{(\alpha)} k_0^{2\alpha} = \frac{\overline{w_2}}{\lambda_2^2 k_0^2 \langle \overline{\Psi_2} \rangle}. \quad (9)$$

The problem is thus reduced to determining the scaling law of the streamfunction average in the forced mode, $\sin(k_0 y)$, as a function of the meridional wave number k_0 ,

$$\langle \overline{\Psi_2} \rangle \sim k_0^{-\gamma} \quad (10)$$

where $\alpha = -1 + \gamma/2$.

4. The numerical experiment

When setting up the numerical experiment different constraints have to be considered:

- (i) the results should be statistically significant,
- (ii) the baroclinically most unstable modes should be in the inertial range,
- (iii) the results should be compared for a variety of parameters.

The first constraint asks for long integration times, while the second requires high horizontal resolution. To satisfy all three points the experiment has to be carefully chosen. The results presented here are obtained by using Fourier series in the longitudinal and meridional direction. The nonlinear terms were treated using a pseudo spectral method (see

2000]

Wirth: Parameterization of baroclinic instability

577

Table 1. Overview of the parameters varied in the experiments performed.

Exp.	Physical parameters		Numerical parameters	
	\overline{w}_2	λ_2/k_0	ν	Horizontal resolution
1	$3.6e-3$	9, 9.5, 10, 10.5, 11, 12, 13, 14	$1.e-4$	128^2
2	$3.8e-3$	10, 11, 13, 14	$1.e-4$	128^2
3	$3.8e-3$	9, 9.5, 10.5, 11, 12, 13, 14	$1.2e-4$	128^2
4	$4.0e-3$	9, 9.5, 10, 10.5, 11, 12, 13, 14	$1.e-4$	128^2
5	$4.0e-3$	9, 9.5, 10.5, 11, 12, 13, 14	$1.2e-4$	128^2
6	$4.4e-3$	8, 9, 9.5, 10, 10.5, 11, 12	$1.e-4$	128^2

e.g. Gottlieb and Orszag, 1977) and the resolution was 128 points in each horizontal direction.

In the vertical two modes, a barotropic and a first baroclinic, were used. The corresponding parameters for the nondimensionalized equations (1) and (2) are: $\lambda_1 = 2\pi/\sqrt{1000}$, $\lambda_2 = 2\pi$, $\xi = 15/4$, $b_1 = 4 \cdot 10^{-2}$, $b_2 = -1 \cdot 10^{-2}$ and $\beta = 4.5 \cdot 10^{-2}$.

In dimensional parameters the baroclinic Rossby radius of deformation is 50 km while the average velocity in the forced large-scale baroclinic mode is about 6 cm/s. Velocities in eddies near the surface reach up to 100 cm/s. The value of β corresponds to a latitude of about 39° . Each run covers at least 50,000 days of integration to insure statistical significance.

The largest scale L which is also the forcing scale is chosen to be between 8 and 14 times the baroclinic Rossby radius of deformation. The “thermal” forcing is varied from $\overline{w}_2 = 3.6 \cdot 10^{-3}$ to $4.4 \cdot 10^{-3}$. The hyper-viscosity parameter $\nu = 1 \cdot 10^{-4}$ and $1.2 \cdot 10^{-4}$ was varied to check that the results are independent from this unphysical parameter (being a function of the numerical resolution). An overview of the model parameters varied in the numerical experiments can be found in Table 1.

In Figure 1 it can be clearly seen that the approximation in the left part of Eq. (7) is very well verified for the scales chosen here, and that it deteriorates with decreasing scale separation, when the forcing scale becomes comparable to the Rossby radius of deformation. In Figure 2 the scaling behavior of $\langle \overline{\Psi}_2 \rangle$ versus the forcing scale can be seen showing that for scales of about 10-times the baroclinic Rossby radius of deformation the scaling is close to k^{-1} and clearly not equal to k^{-2} . This can be seen more clearly in Figure 3 where the parameter $\kappa^{(0)}$ is plotted versus wavenumber suggesting that $\gamma \approx 13/12$. This leads to a value of $\alpha \approx -11/24$. This value is only a good fit to the numerical data but it shows that we clearly do not have normal diffusion ($\gamma = 2$) and also that the transport is close to, but different from, ballistic transport ($\gamma = 1$).

In the different sets of numerical experiments we also varied the forcing by $\pm 10\%$ and found about the same variation in κ (see Fig. 1), while $\langle \overline{\Psi}_2 \rangle$ showed no variation (see Fig. 2). The reason is that for increased forcing (see Fig. 1) baroclinic instability occurs more often (Fig. 4), leading to a linear increase in the bolus velocity while the average streamfunction amplitude of the forced mode $\langle \overline{\Psi}_2 \rangle$ stays almost constant. This behavior can be verified in

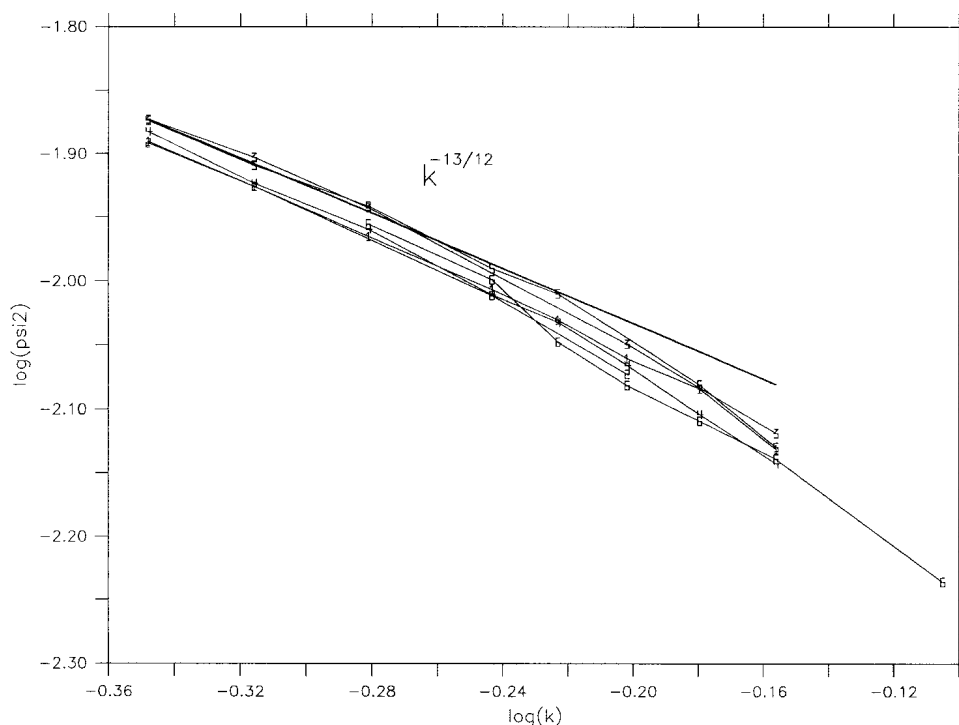


Figure 2. Scale dependence of $\overline{\psi^2}$ for the six sets of experiments as labeled, differences between the graphs are within statistical errors.

Figure 4 where the strongly smoothed temporal energy spectrum of $\overline{\psi^2(t)}$ is plotted for three experiments having the largest scale that is 11-times the baroclinic Rossby radius of deformation and differing only in the forcing amplitude $\overline{w_2}$. It can be clearly seen that although the mean value $\overline{\psi^2}$ is unchanged by the forcing (Fig. 2), the temporal energy spectrum is larger and peaked at higher frequencies when forcing increases. These findings are not astonishing and explained by the fact that baroclinic instability occurs at a critical shear. When applying a stronger forcing this critical shear is reached in a shorter time. Similar conclusions are obtained in other publications on slightly different subjects (see e.g. Straub, 1993).

We also increased the (nonphysical) lateral friction coefficient ν by 20% and found a decrease of κ^0 by about 3% (see Fig. 3). This slight dependence should disappear when using even higher spatial resolutions and lower lateral friction coefficients ν .

5. Discussion

The above results force us to rethink some concepts of parameterizing baroclinic instability, as they demonstrate that: (i) the effect of baroclinic instability on larger and larger scales decreases slower than predicted by a Laplace operator and furthermore, (ii)

2000]

Wirth: Parameterization of baroclinic instability

579

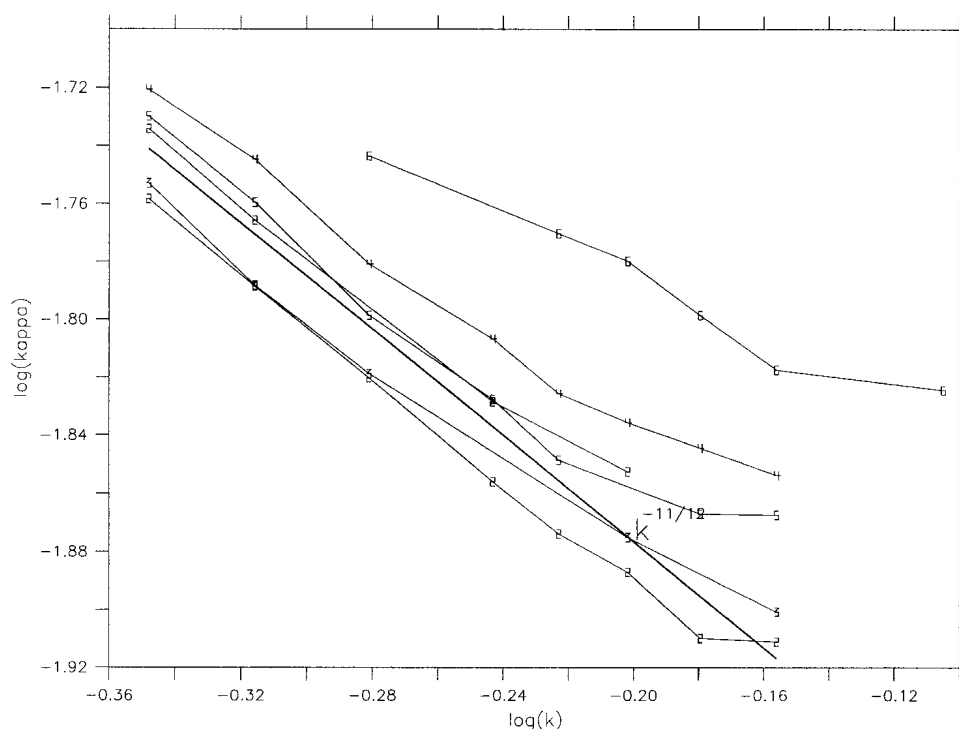


Figure 3. Scale dependence of $\kappa^{(0)}$ (obtained using Eq. (9)) for the experiments 6, 4, 5, 2, 3, 1 from top to bottom.

the bolus velocity grows linearly with the amplitude of the forcing, while the amplitude of the baroclinic streamfunction does not vary.

The latter findings seem to contradict the results of Rix and Willebrand (1996) who found a reasonable fit for linear relation of “layer-thickness” versus bolus velocity in a primitive equation North Atlantic model, when averaging results over $4^\circ \times 4^\circ$ boxes. However this is entirely due to the fact that we show results as a function of the ratio scale/(baroclinic Rossby radius of deformation). In the calculations by Rix and Willebrand (1996) a primitive equation model is used having many levels and a variety of baroclinic Rossby radii, unlike our simple model possessing only one. They also performed averages over different areas and seasons having different baroclinic Rossby radii of deformation. We produced a similar plot with our data. In Figure 5 we show the bolus velocity plotted against the amplitude of the forced mode weighted by the appropriate power of the streamfunction, that is: $(\sqrt{\Psi_2})k^{1/12}$. To summarize this point we can say that although there is no linear relation between the bolus velocity and the baroclinic large-scale streamfunction when all other model parameters are kept constant, this relation can be found in a statistical sense when averaging over data from regions with different and a variety of baroclinic Rossby radii of deformation.

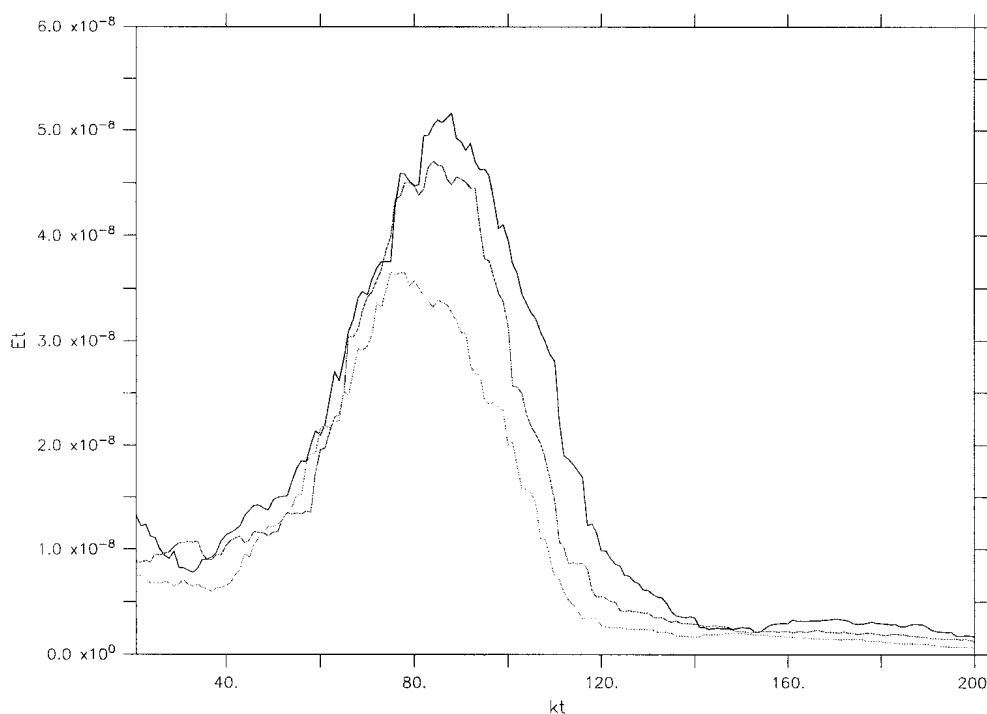


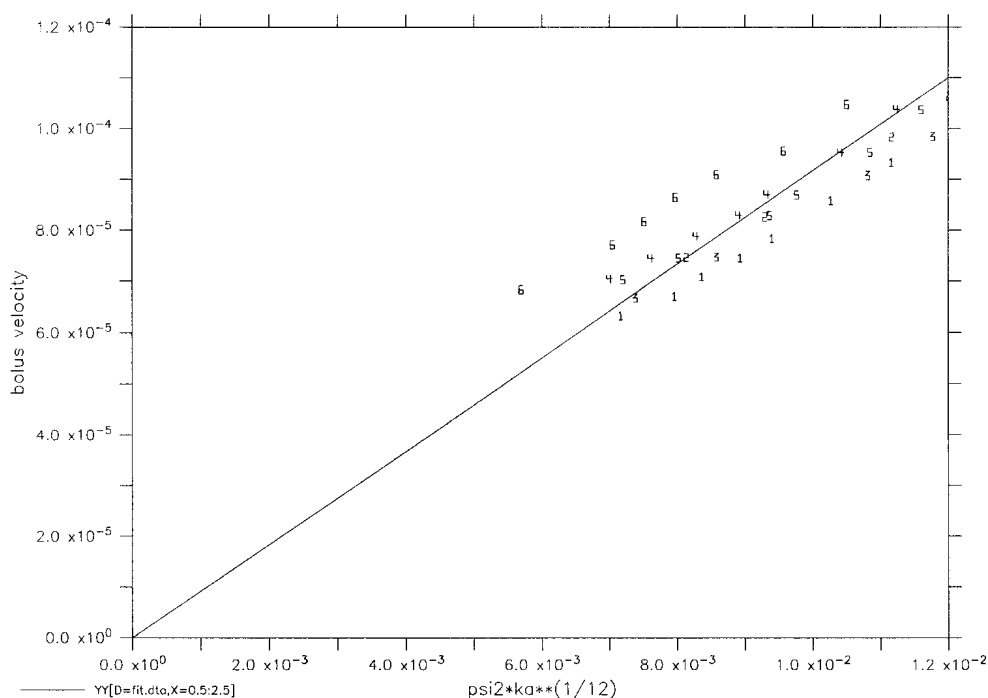
Figure 4. Temporal energy spectrum of $\overline{\Psi_2}$ for $k = 2\pi \cdot 11$ in three experiments 1, 2 and 4 (from top to bottom) after a 35-point-wide boxcar smoother was applied. The peaks correspond to the time scale of about 200 days.

The first point, (i), saying that the effect of baroclinic instability on the baroclinic large-scale gradient is super diffusive seems to contradict intuition. The intuitive picture is indeed that the dynamics at the (small) scale of the baroclinically most unstable mode has a diffusive effect on the large-scale gradient. The point, however, is that energy injected in the barotropic mode does not stay at such small scales but cascades to the large scales, as explained by the two-dimensional inverse energy cascade (Kraichnan, 1967). The effect of this barotropic large-scale dynamics, caused by baroclinic instability, on the baroclinic large-scale gradient has to be parameterized as a super diffusive behavior. It is indeed well known that a lack of scale separation between the “large” scale and the parameterized scales lead to super diffusive behavior (Avellaneda and Majda, 1992). The inverse cascade is, however, halted by the β -effect at the Rhines scale; that is, the scale at which the meridional change of the Coriolis parameter balances nonlinearity (see e.g., Rhines, 1975, and Held and Larichev, 1996). This indicates that a normal diffusive parameterization might be adapted for scales much larger than the Rhines scale, that is for scales on the order of thousands of kilometers. Calculations of much higher resolution would be needed to determine such behavior. This also shows that for the practical use of parameterizing baroclinic instability in non-eddy-permitting ocean models and climate models, a super

2000]

Wirth: Parameterization of baroclinic instability

581

Figure 5. Bolus velocity versus $(\Psi_2)k^{1/12}$.

diffusive parameterization should be more adaptable as their small scales range from roughly 100 km to 1000 km. These are the scales where parameterization acts strongest and these are the scales considered in this paper.

The lack of scale separation is only one possible source for super diffusive behavior; spatio-temporal correlations between the barotropic and baroclinic dynamics might be another one.

For the case of the f -plane it was recently shown by Gryanik *et al.* (2000), that vortex-dominated transport is indeed ballistic. The situation on the β -plane considered here is somehow different as no such coherent structures exist.

To conclude we have to address the question of how good do the previously used parameterizations do and what is a better parameterization in view of the above presented results? In non-eddy-resolving ocean models one should include some kind of sink for layer thickness or baroclinic potential vorticity and most parameterizations can be seen as a first-order approach. Using a linear relation between the large-scale layer thickness and the bolus velocity is a simple and reasonable approach at least in a statistical sense. A more serious point is the commonly used diffusive law for layer thickness or potential vorticity which is here shown to be wrong. Implementing a dissipation scheme that represents a fractional power of the Laplacian is, however, cumbersome in the framework of finite differences. Please note that this is different from using a coefficient that depends on the

local deformation rate as introduced into ocean modeling by Smagorinsky (1963). The former represents a linear operation, while the latter is not.

We emphasize once more that the experiments presented here are done with a simple model and generalizations to ocean general circulation models should be taken with care. In this sense this paper does not propose a new parameterization based on the above findings nor does it indicate which previously introduced parameterization does best. Rather, the purpose of this paper is to point out major difficulties in the parameterization of baroclinic instability that were not mentioned in previous discussions.

Acknowledgments. I am grateful to J. C. McWilliams and J. Willebrand for extensive discussions and to an anonymous referee for remarks that helped to improve the paper.

REFERENCES

- Avelaneda, M. and A. J. Majda. 1992. Super diffusion in nearly stratified flows. *J. Stat. Phys.*, *69*, 689–729.
- Danabasoglu, G. and J. C. McWilliams. 1995. Sensitivity of the global ocean circulation to parameterizations of mesoscale transports. *J. Climate*, *8*, 2967–2987.
- Flierl, G. R. 1978. Models of vertical structure and the calibration of two-layer models. *Dyn. Atmos. Oceans*, *2*, 341–381.
- Frisch, U. 1996. *Turbulence: The Legacy of A. N. Kolmogorov*, Cambridge University Press, 296 pp.
- Gent, P. R. and J. C. McWilliams. 1990. Isopycnal mixing in ocean circulation models. *J. Phys. Oceanogr.*, *20*, 150–155.
- Gent, P. R., J. Willebrand, T. J. McDougall and J. C. McWilliams. 1995. Parameterizing eddy-induced transports in ocean circulation models. *J. Phys. Oceanogr.*, *25*, 463–474.
- Gottlieb, D. and S. Orszag. 1977. *Numerical analysis of spectral methods: theory and applications*, SIAM, Philadelphia, PA.
- Greatbatch, R. J. and K. G. Lamb. 1990. On parameterizing vertical mixing of momentum in non-eddy-resolving ocean models. *J. Phys. Oceanogr.*, *20*, 1634–1637.
- Gryanik, V., T. Doronina, D. Olbers and T. Warnecke. 2000. The theory of 3D hetons and vortex dominated spreading in localized convection in a rotating stratified fluid. *J. Fluid Mech.*, (in press).
- Held, I. M. and V. D. Larichev. 1996. A scaling theory for horizontally homogeneous, baroclinically unstable flow on a beta plane. *J. Atmos. Sci.*, *53*, 946–952.
- Hua, B. L. and D. B. Haidvogel. 1986. Numerical simulation of the vertical structure of quasi-geostrophic turbulence. *J. Atmos. Sci.*, *43*, 2923–2936.
- Hua, B. L., J. C. McWilliams and P. Klein. 1998. Lagrangian accelerations in geostrophic turbulence. *J. Fluid Mech.*, *366*, 87–108.
- Killworth, P. D. 2000. Boundary conditions on TRM velocities in parameterisations. *J. Phys. Oceanogr.* (in press).
- Kraichnan, R. H. 1967. Inertial ranges in two dimensional turbulence. *Phys. Fluids*, *10*, 1417–1423.
- Lee, M., D. P. Marshall and R. G. Williams. 1997. On the eddy transfer of tracers: advective or diffusive? *J. Mar. Res.*, *55*, 483–505.
- Redi, M. H. 1982. Oceanic isopycnal mixing by coordinate rotation. *J. Phys. Oceanogr.*, *12*, 1154–1158.
- Rhines, P. 1975. Waves and turbulence on a beta-plane. *J. Fluid Mech.*, *69*, 417–433.
- Rix, N. H. and J. Willebrand. 1996. Parameterization of mesoscale eddies as inferred from a high-resolution circulation model. *J. Phys. Oceanogr.*, *26*, 2281–2285.

2000] *Wirth: Parameterization of baroclinic instability* 583

- Roberts, M. and D. Marshall. 1998. Do we require adiabatic dissipation schemes in eddy-resolving ocean models? *J. Phys. Oceanogr.*, 28, 2050–2063.
- Salmon, R. 1980. Baroclinic instability and geostrophic turbulence. *Geophys. Astrophys. Fluid Dyn.*, 15, 11–37.
- Smagorinsky, J. 1963. General circulation experiments with the primitive equations: I. The basic experiment. *Mon. Wea. Rev.*, 91, 99–164.
- Straub, D. N. 1993. On the transport and angular momentum balance of channel models of the Antarctic Circumpolar Current. *J. Phys. Oceanogr.*, 23, 776–782.
- Treguier, A. M. 1999. Evaluating eddy mixing coefficients from eddy-resolving ocean models: A case study. *J. Mar. Res.*, 57, 89–108.
- Treguier, A. M., I. M. Held and V. D. Larichev. 1997. Parameterization of quasi-geostrophic eddies in primitive equation ocean models. *J. Phys. Oceanogr.*, 27, 567–580.
- Welander, P. 1973. Lateral friction in the ocean as an effect of potential vorticity mixing. *Geophys. Fluid Dyn.*, 5, 173–189.

Received: 3 January, 2000; revised: 8 May, 2000.

4.3 A non-hydrostatic flat-bottom ocean model entirely base on Fourier expansion

Available online at www.sciencedirect.com

SCIENCE @ DIRECT®

Ocean Modelling 9 (2005) 71–87

**Ocean
Modelling**www.elsevier.com/locate/ocemod

A non-hydrostatic flat-bottom ocean model entirely based on Fourier expansion

A. Wirth

LEGI, BP 53, 38041 Grenoble Cedex 9, France

Received 15 December 2003; received in revised form 22 March 2004; accepted 15 April 2004
Available online 8 May 2004

Abstract

We show how to implement free-slip and no-slip boundary conditions in a three dimensional Boussinesq flat-bottom ocean model based on Fourier expansion. Our method is inspired by the immersed or virtual boundary technique in which the effect of boundaries on the flow field is modeled by a virtual force field. Our method, however, explicitly depletes the velocity on the boundary induced by the pressure, while at the same time respecting the incompressibility of the flow field. Spurious spatial oscillations remain at a negligible level in the simulated flow field when using our technique and no filtering of the flow field is necessary. We furthermore show that by using the method presented here the residual velocities at the boundaries are easily reduced to a negligible value. This stands in contradistinction to previous calculations using the immersed or virtual boundary technique.

The efficiency is demonstrated by simulating a Rayleigh impulsive flow, for which the time evolution of the simulated flow is compared to an analytic solution, and a three dimensional Boussinesq simulation of ocean convection. The second instance is taken from a well studied oceanographic context: A free slip boundary condition is applied on the upper surface, the modeled sea surface, and a no-slip boundary condition to the lower boundary, the modeled ocean floor. Convergence properties of the method are investigated by solving a two dimensional stationary problem at different spatial resolutions.

The work presented here is restricted to a flat ocean floor. Extensions of our method to ocean models with a realistic topography are discussed.

© 2004 Elsevier Ltd. All rights reserved.

PACS: 65N35; 76M22; 76R05; 86A05

Keywords: Computational fluid dynamics; Boundary value problems; Pseudo-spectral methods; Convection

E-mail address: achim.wirth@hmg.inpg.fr (A. Wirth).

1463-5003/\$ - see front matter © 2004 Elsevier Ltd. All rights reserved.
doi:10.1016/j.ocemod.2004.04.003

1. Introduction

Most of the world ocean is known to be in hydrostatic balance at large scales. However, ocean dynamics at scales smaller than about 10 km, convection, circulation in coastal areas, surface mixed layer dynamics, and the dynamics of overflows in straits are instances of ocean dynamics where non-hydrostatic effects are essential. These instances of non-hydrostatic ocean dynamics are important dynamical problems in their own right and also influence the large scale dynamics of the world ocean and the climate system of our planet.

To study the aforementioned instances of non-hydrostatic ocean dynamics numerical models based on the hydrostatic primitive equations are not adapted, and the full three dimensional Navier–Stokes equations have to be implemented instead. The pioneering work by Marshall et al. (1997) is not only an example of this endeavor, but also discusses non-hydrostatic instances in ocean dynamics in detail. The here presented numerical model for the study of non-hydrostatic processes in the ocean is based on Fourier expansions. The virtual boundary technique is used and refined to implement the ocean surface as well as a flat (no-slip) ocean floor. A great variety of non-hydrostatic processes in the ocean do *not* depend on the topography of the ocean floor and an ocean model specialized to these cases represents a powerful tool in understanding such processes.

Spectral methods based on Fourier expansions are widely used in the simulation of turbulent flow when subject to periodic boundary conditions. For such cases this method is unbeaten in accuracy and speed. This success is based on the pseudo-spectral method Gottlieb and Orszag (1977), where derivatives are performed in Fourier and non-linear operations in physical space, and the fast Fourier transform is used to pass from one space to the other. The efficiency of the pseudo-spectral method resides in the locality of the operations performed in the corresponding spaces and, overall the efficiency of the fast Fourier transform, the sole non-local operation, which only requires $O(n \log n)$ operations.

Spectral methods based on Fourier expansions in one, two or three directions are widely spread in ocean modeling when specific processes are studied and periodic boundary conditions are present in these directions (Julien et al., 1996; Wirth, 2000). Methods based on Fourier expansions have, so far, not seen the same success when it comes to flows involving boundaries. In such cases Chebyshev polynomials are usually employed in the directions subject to non-periodic boundary conditions (Davies and Lawrence, 1994; Julien et al., 1996). The difficulty lies in the fact that two very different kinds of conditions have to be imposed: First, the condition of zero divergence which is easily imposed in Fourier space, second, the boundary conditions which are imposed in physical space. As both conditions “reside” in different spaces, the challenge lies in imposing them simultaneously. New momentum in surmounting the apparent incompatibility of imposing simultaneously a zero divergence condition and boundary conditions in models based on Fourier expansion came with the introduction of the immersed or virtual boundary method Peskin (1977) (see also Iaccarino and Verzicco (2003) for a recent review). The term *immersed* is usually used for boundaries that vary in time while virtual boundaries are stationary. As we are here only considering stationary boundaries we will be using the term virtual boundaries.

In their pioneering work on the implementation of virtual boundaries in a model based on Fourier expansion, Goldstein et al. (1993) used a feedback forcing that reduced the velocities at boundary points. The forcing depended on two parameters and introduced considerable stiffness resulting in a very short time step. Their flow showed global spatial oscillations although they

used a smoothed force field. Such smearing of the force field and thus of the boundary reduces the accuracy of the solution especially near the boundary. Furthermore, a spectral smoothing technique had to be employed to obtain a smooth flow field even for temporally steady flow. An important point of their paper is the finding, that the spurious oscillations can be reduced by adjusting a fictitious flow field inside the solid body.

This technique is explored further in the present paper. We indeed demonstrate a way of applying a force at the boundary and inside the solid body *only*, resulting in a flow field with no spurious oscillations. Contrary to Goldstein et al. (1993) we do not use a feedback forcing in which the velocity at boundary points is damped towards the required value, but we use the direct forcing method, see Mohd-Yosuf (1997), in which a force field on the boundary insures the boundary conditions. For a detailed discussion of feedback and direct forcing we refer the reader to the review by Iaccarino and Verzicco (2003) and to references therein. By using the direct forcing method rather than a feedback forcing we do not have any time step limitations due to the virtual boundaries and there are no additional parameters to adjust.

In our method the direct forcing is split in two parts, the first correcting the spurious velocity at the boundary due to the advective, buoyancy and diffusive terms and the second accounting for the spurious contributions due to the pressure term. It is the second part that is usually not explicitly accounted for when virtual boundary conditions are used.

In previous calculations using virtual boundaries a residual velocity of 10^{-3} – 10^{-4} times the maximal velocity was observed at the boundary Iaccarino and Verzicco (2003). For oceanic applications these levels of residual velocity through the boundary are not acceptable. With our method the reduction of the residual error is only subject to limitations due to the machine precision.

In the next section we explain our method. Section 3 discusses the extension of the introduced method to more complex boundaries. The two test cases are exposed and numerical details are explained in Section 4. Concluding remarks appear in Section 5. The important but technical question of convergence properties of the method presented here are discussed in Appendix A.

2. The method

The present numerical method deals with simulating the motion of an incompressible Boussinesq fluid in two and three dimensions. The governing equations are

$$\partial_t \mathbf{u} + \mathbf{u} \cdot \nabla \mathbf{u} + \nabla P = \alpha T \mathbf{e}_\perp + \nu \nabla^2 \mathbf{u} + \mathbf{F}, \quad (1)$$

$$\nabla \cdot \mathbf{u} = 0, \quad (2)$$

$$\partial_t T + \mathbf{u} \cdot \nabla T = \kappa \nabla^2 T + S, \quad (3)$$

where \mathbf{u} is the velocity field, T the temperature field, P the pressure field and α the thermal expansion coefficient of the fluid. The upward pointing unit vector is denoted by \mathbf{e}_\perp . The viscosity and diffusivity are given by ν and κ , respectively. The force \mathbf{F} enforces the boundary condition for the velocity and the source term S insures the prescribed heat fluxes through the boundaries. It is clear that the force and the source term have to vanish within the fluid, but not so on the boundary and beyond.

We restrict ourselves to the case of horizontal upper and lower boundaries. On the upper boundary we apply a free-slip boundary condition, that is a vanishing vertical (normal) velocity component ($\mathbf{u} \cdot \mathbf{e}_\perp = 0$) while there is no direct influence of the boundary on the horizontal velocity component. The lower boundary is subject to a no-slip boundary condition, which means that all components of the velocity vector vanish at the lower boundary ($\mathbf{u} = 0$). We thus model the dynamics in a part of an ocean of constant depth, with a rigid lid, and subject to periodic boundary conditions in the horizontal direction(s).

In the following we will proceed by guiding the reader through one time step of integration with our method. To integrate the Navier–Stokes equations we use the splitting technique (Chorin, 1968; Temam, 1969; Lamb, 1994), where the momentum equation is first solved without considering the pressure term and the thus obtained velocity field is then, in the second part, projected into the space of vector fields with zero divergence.

We start the integration from a velocity field that not only satisfies the boundary conditions, but its components are also symmetric or skew symmetric across the boundary with respect to the vertical direction (normal to the boundary). To this end it is necessary to have a buffer zone above the top and below the bottom boundary as indicated in Fig. 1. More precisely, components that vanish at the boundary as for example, all velocity components at a no slip boundary or the normal velocity at a free slip boundary are continued skew symmetrically beyond the boundary in the buffer zone. For quantities of which the first derivative vanishes, as for example the tangent velocity at a free slip boundary or a scalar like temperature, the boundary value has to be extrapolated from the interior of the flow and the fictitious values inside the solid body (= buffer zone) are continued using even symmetry. The thickness of the buffer zone plays an important role in the implementation due to the non-local nature of spectral representations, and thus the avoidance of spurious oscillations.

We then integrate the momentum equation ignoring contributions from the pressure term

$$\frac{\tilde{\mathbf{u}} - \mathbf{u}}{\Delta t} = -\mathbf{u} \nabla \mathbf{u} + \alpha T \mathbf{e}_\perp + \nu \nabla^2 \mathbf{u} + \mathbf{F}_1. \quad (4)$$

It is easily verified that the even and skew symmetry with respect to the boundary are conserved by the advective and the diffusive term. As a consequence, the resulting velocity field $\tilde{\mathbf{u}}$ verifies the

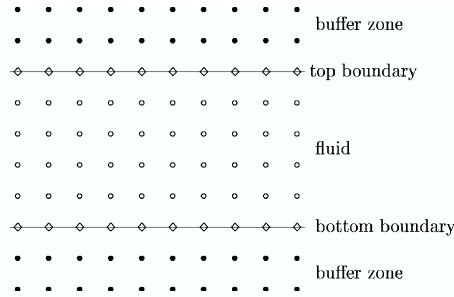


Fig. 1. Decomposition of domain; grid points are marked as open circles for fluid, diamonds for boundary and full circles for buffer points.

boundary condition except for the discretization error and the error due to the finite thickness of the buffer zone, provided that the buoyancy force αT is zero on the boundary. This means that the force \mathbf{F}_1 , which insures the boundary conditions, is small at the boundary (and zero elsewhere) and will not give rise to spurious oscillations in the fluid flow.

In the next step we orthogonally and linearly project the velocity field $\tilde{\mathbf{u}}$ in the space of divergence free vector fields,

$$\tilde{\tilde{\mathbf{u}}} = \Pi(\tilde{\mathbf{u}}), \quad (5)$$

using the projector $\Pi(\mathbf{u}) = \nabla^{-2} \nabla(\nabla \cdot \mathbf{u})$, where ∇^{-2} is the inverse Laplace operator, a well defined operator when applied to functions of vanishing mean (see Peyret, 2002).

Thus the resulting velocity field, $\tilde{\tilde{\mathbf{u}}}$, is of zero divergence, but does *not* satisfy the boundary conditions. The crucial idea in our method is now to change the velocity field at the boundary (by applying the force \mathbf{F}_2 that changes $\tilde{\tilde{\mathbf{u}}}$ to $\tilde{\tilde{\mathbf{u}}} + \mathbf{u}_\pi$) so that after a second projection we obtain

$$\mathbf{u} = \Pi(\tilde{\tilde{\mathbf{u}}} + \mathbf{u}_\pi), \quad (6)$$

where the final velocity field \mathbf{u} is divergence free *and* satisfies the boundary conditions. Although the force \mathbf{F}_2 , acting at the boundary only, is the only force having a substantial amplitude, it does not create spurious oscillations within the fluid, as the projection itself is a linear operation which is local in Fourier space. The actual calculation of the force \mathbf{F}_2 is the essence of our method and will be given in just a moment.

Let us first put all the parts of our calculation together and we find that our scheme can be written as

$$\frac{\mathbf{u}^{n+1} - \mathbf{u}^n}{\Delta t} = \Pi(-\mathbf{u}^n \nabla \mathbf{u}^n - \alpha T^n + \nu \nabla^2 \mathbf{u}^n + \mathbf{F}_1^n + \mathbf{F}_2^n). \quad (7)$$

In this condensation we used the linearity and idempotents of the projector Π .

We emphasize once more, that the two forces act only on the boundary or inside the solid body and vanish within the fluid. The crucial question is now of course how to obtain the two forces: The first is actually never calculated but the components of the velocity field are either set to zero at the boundary and continued inside the solid body so that it is skew symmetric along the vertical direction with respect to the boundary, or the boundary value is extrapolated from inside the flow and continued inside the solid body so that it is even symmetric along the normal direction with respect to the boundary, depending on whether the component is to vanish on the boundary or not. Instead of calculating the force \mathbf{F}_2 we use the equivalent procedure of adding a velocity field \mathbf{u}_π at the boundary which after the projection exactly cancels the residual velocity at the boundary ($\tilde{\tilde{\mathbf{u}}}(\partial B)$). That is

$$\tilde{\tilde{\mathbf{u}}} + \Pi(\mathbf{u}_\pi) = 0 \quad \text{on } \partial B. \quad (8)$$

It is important to notice that although \mathbf{u}_π vanishes in the fluid interior the same thing does not apply for $\Pi(\mathbf{u}_\pi)$. This is an immediate consequence of the projection $\Pi(\cdot)$, being local in Fourier space and therefore non-local in physical space.

To obtain \mathbf{u}_π we first decompose the residual velocity at the boundary in its normal and tangential components, and denote by \mathbf{e}_\perp , the unit vector in the direction normal to the boundary.

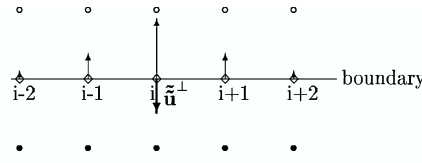


Fig. 2. The thick vector represents the spurious velocity at the boundary $\tilde{\mathbf{u}}(i)$ the thin vectors give the velocity field $\mathbf{u}_{\pi,i}^\perp$, where $\Pi(\mathbf{u}_{\pi,i}^\perp) = -\tilde{\mathbf{u}}(i)$.

We will start by explaining our method as applied to the normal velocity component in a two dimensional model.

More precisely, if the normal velocity component along the boundary $(\tilde{\mathbf{u}}(\partial B) \cdot \mathbf{e}_\perp)$ vanishes except at the boundary grid-point i (thick vector in Fig. 2), the velocity field $\mathbf{u}_{\pi,i}^\perp$ will be non-local along the boundary (thin vectors in Fig. 2). The indices refer to grid points along the boundary, the reference to other directions is omitted for clarity.

As the projection is a linear operation, the vector field $\mathbf{u}_{\pi,i}^\perp(j)$ can be calculated in advance with $\Pi(\mathbf{u}_{\pi,i}^\perp(j)) = -\mathbf{e}_\perp \delta_i(j)$, where the discrete delta function is one at the boundary point i and zero elsewhere.

We then multiply every vector of the vector field by the magnitude of the spurious velocity component at the boundary point i and then sum over all the boundary points. We thus obtain the desired velocity field

$$\mathbf{u}_\pi^\perp(j) = \sum_i (\tilde{\mathbf{u}}(i) \cdot \mathbf{e}_\perp) \mathbf{u}_{\pi,i}^\perp(j). \quad (9)$$

In the case of flat boundaries the problem is homogeneous in the horizontal direction and the vector at a location j of the unit vector field $\mathbf{u}_{\pi,i}^\perp(j)$ is a function of the distance along the boundary $(i - j)$, only. This means only one unit vector field at the boundary (e.g., $\mathbf{u}_{\pi,1}^\perp$) has to be precalculated. This calculation is performed, before the actual integration of the model in a negligible amount of computation time, the result is stored in a scalar field having the size of the horizontal extension of the model.

The procedure is then repeated for the tangential component(s) of the residual velocities at no-slip boundaries. One additional difficulty however arises in the context of depleting the tangential velocity component(s) with our method. The tangent vector field that vanishes everywhere on the boundary except at one grid point can not be divergence free, and can thus not be the result of the projection operator. This is because at the highest wavenumber resolved in the model (the Nyquist wavenumber) only the cosine and not the sine wave is represented. The problem is however easily resolved by allowing the vector field to possess a divergence at the Nyquist wavenumber for wave-vectors aligned with the boundary. This is not a problem as the velocity field is put to zero on the boundary and is thus trivially divergence free with respect to horizontal wave-vectors. The correction is thus composed of vector-fields having a non-vanishing divergence, but the divergence cancels when these vector-fields are added together. No artificial divergence at the smallest scale is introduced in the model.

An additional problem arises due to the existence of two distinct boundaries. When the velocity correction at the boundary is added and the projection performed, the non-locality of the projection operation results in a (small) violation of the velocity boundary condition at the opposite

boundary. This problem is solved by calculating the correction velocity field $\mathbf{u}_{\pi,i}$ not only for the boundary where the correction is being performed, but also at the opposite boundary $\mathbf{u}_{\pi,i}^{\text{op}}$. The velocity field $\mathbf{u}_{\pi,i}^{\text{op}}$ does indeed insure, that the velocity at one boundary is not affected by changes performed on the opposite boundary.

In a last step of the integration the fictitious velocity field in the solid body is again constructed by using even symmetry or skew symmetry across the vertical boundary. The integration then proceeds with the next time step.

3. Non-horizontal boundary

In the case of an arbitrary boundary with no symmetries all the vector fields on the boundary $\mathbf{u}_{\pi,i}$ (i ranging over all the boundary points) have to be precalculated and stored for the actual integration. In a two dimensional model having $n_1 \times n_2$ grid points this would require the storage of $2 \times n_1^2$ scalars for one arbitrary free-slip boundary. In a three dimensional model having $n_1 \times n_2 \times n_3$ grid points this the storage requirement increases to $2 \times (n \times n_2)^2$ scalars. For larger models this is clearly unfeasible.

If, however, the boundary has some additional symmetry, the storage might be highly reduced. Considering the case of a riblet surface: Such surface is homogeneous in one direction and periodic in the other, with a periodic structure repeating itself every m grid points. For such case the storage is reduced to $2 \times m \times n_1 \times n_2$ scalars for one boundary. With typical values of $m \approx 10$, this represents a negligible amount of storage in the overall numerical integration.

The same idea can be applied to any symmetry present in boundaries as for example a cylinder or a sphere submerged in the fluid. In both cases the implementation of our method is almost analogous to the case of a horizontal boundary.

Extensions of the method presented here to a lower boundary (ocean floor) of arbitrary shape are currently under way and will be published elsewhere.

4. Validation

To test our method we used several test cases of varying complexity two of which are presented here: The first is the Rayleigh impulsive flow for which the time evolution of the simulated flow can be compared to an analytic solution. The second is a convection experiment from an oceanographic context in two and three dimensions. We will here present the results from our three dimensional calculations. Convection experiments present a very good test case for methods of imposing boundary conditions as the largest velocities reside near those boundaries. We choose a standard numerical convection experiment (see, e.g., Jones and Marshall (1993), Padilla-Barbosa and Métais (2000), and Maxworthy and Narimousa (1994) for laboratory experiments) to facilitate comparison to published results.

The calculations are performed using a pseudo-spectral method based on Fourier expansion. The time stepping is done using a third-order low-storage Runge–Kutta scheme, and the size of the time step is subject to the CFL condition, only.

All calculations presented here were performed on a Pentium 4 lap-top computer.

4.1. The Rayleigh impulsive flow

The fluid domain is a rectangular box measuring $1 \text{ m} \times 1 \text{ m} \times (66/64) \text{ m}$ length. We suppose that our fluid is initially motionless. At a time $t = 0$ a flat horizontal plate in the middle of the fluid impulsively starts to move with a speed of 1 m/s in the horizontal direction \mathbf{e}_1 . Viscous effects ($\nu = 1 \text{ m}^2/\text{s}^2$) will spread motion over the entire fluid. The equations are non-dimensionalized by dividing length by 1 m , time by 1 s , velocity by 1 m/s and viscosity by $1 \text{ m}^2/\text{s}^2$. As the spreading of motion is governed by a heat equation, an analytic solution of the velocity field can be obtained for every time $t \geq 0$ even when subject to boundary conditions (see, e.g., John (1991)).

The calculations are done with a resolution of 16×16 points in the horizontal directions. The vertical resolution is 44, grid points within the fluid. The extension of the buffer zones above the upper surface and below the lower surface are 10 grid points.

The comparison of the model calculation to the analytic solution at different times can be seen in Fig. 3, which shows a generally very good agreement. Deviations are only visible for the first panel ($t = 0.01$). The small deviations in the first panel can be explained by two things: (i) the slightly different initial condition (at $t = 0$) for the model calculation and the analytic solution. The horizontal velocity in the analytic solution starts with a flow being non-vanishing only at one horizontal level of vanishing thickness, whereas the model starts from the discretized equivalent; (ii) the extrapolation method to obtain the boundary value at a free-slip boundary is of only second order (could easily be extended to higher order).

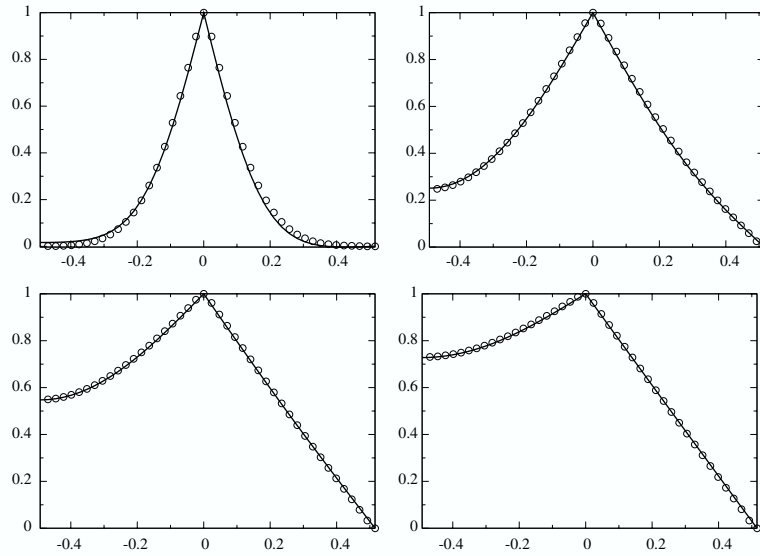


Fig. 3. Comparison of the horizontal velocity at the 44 vertical grid points (circles) to the analytical solution (line) at times 0.01 (upper left), 0.05 (upper right), 0.1 (lower left), 0.15 (lower right). Horizontal axis in the plot corresponds to vertical extension in the model, vertical axis in the plot gives the non-dimensional velocity.

In this test case the pressure vanishes everywhere and the velocity is always parallel to the boundaries. We have thus not tested the pressure correction, the key part of our method. The pressure correction will however be the key in the next test case.

4.2. Convection

In this test case we simulate the sinking of water cooled at the surface in a homogeneous ocean. The simulation is based on the non-hydrostatic Boussinesq equations in a rotating frame and has a free-slip boundary at the top and a no-slip boundary at the bottom. The simulated domain extends 32 km in both horizontal directions and 2 km in the vertical. A cooling of $Q_0 = 800 \text{ W/m}^2$ is applied at a perfectly mixed surface layer from zero to 211 m depth, in a circular horizontal area of radius $R = 8 \text{ km}$, outside this disk the heating is rapidly reduced to zero (heating outside the disk $r \geq R : Q(r) = Q_0 \exp(1 - r^4/R^4)$). The cooling lasts for 48 h. The specific heat capacity of water is $C_w = 3900 \text{ J/(kg K)}$, the constant thermal expansion coefficient is $\epsilon = 2 \times 10^{-4} \text{ K}^{-1}$ and the density is $\rho = 1000 \text{ kg/m}^3$. The Coriolis parameter is given by $f = 1.0 \times 10^{-4} \text{ s}^{-1}$. These values give the buoyancy flux

$$B_0 = \frac{\epsilon Q_0 g}{C_w \rho} = 4.025 \times 10^{-7} \text{ m}^2/\text{s}^3. \quad (10)$$

Following the scaling arguments of Maxworthy and Narimousa (1994) we get $u_{\text{rot}} = (B_0/f)^{1/2} = 0.063 \text{ m/s}$.

The physical model is inspired by observations Schott et al. (1977) and Schott and Leaman (1991), the experimental set up of Maxworthy and Narimousa (1994), and almost identical to the reference experiment of Jones and Marshall (1993) and experiment H4 in Padilla-Barbosa and Métais (2000) to facilitate comparison. One difference of our model to the two models cited above is, that we used a no-slip boundary at the bottom while they used free-slip. We refer the reader to the above mentioned references for a thorough discussion of the physical processes involved.

We add a small amount ($\sigma = 55 \text{ W/m}^2$) of white-in-space noise to the surface cooling. The horizontal resolution is 128×128 grid points and there are 44 grid points within the fluid in the vertical direction. Ten grid points above and below the fluid form the buffer zones. The time step, subject to the CFL condition, is 150 s.

The maximal error allowed for the residual normal velocity at the boundaries is smaller than 10^{-10} times the maximal velocity in the fluid. At the no-slip boundary the residual tangential velocity is smaller than 10^{-3} times the maximal velocity in the fluid. The reduction of the tangential velocity at the lower boundary, using our method, creates a small normal velocity at the upper boundary, and vice versa. Instead of correcting for this contributions explicitly, as it is done for the normal velocities at the lower and upper boundary (see end of Section 2), we choose to iterate the projection and thus reduce such error. The number of iterations needed per step is 3, for the aforementioned error limits.

By performing several experiments we found the onset of convection being very sensitive not only to the amount and nature of noise added, but also to how the heating at the rim of the disk is reduced to zero. It is also worth mentioning that large eddy simulations were performed in Padilla-Barbosa and Métais (2000) which results in much larger Reynolds and Peclet numbers especially at the onset of the experiment. We thus choose to validate our numerical method to

compare to the aforementioned published results at the end of the heating period, that is at $t = 48$ h.

At $t = 48$ h and $z = 1$ km the vertical velocity ranges from $w_{\min} = -0.14$ to $w_{\max} = 0.11$ m/s (see Fig. 4), this values are close to the results from Jones and Marshall (1993) ($w_{\min} = -0.18$ to $w_{\max} = 0.09$ m/s, see their Fig. 7d) and to the results from Padilla-Barbosa and Métais (2000), see their Fig. 3. The horizontal scale and structure of the plumes also compare very well in both figures. The temperature isosurface for $T = 6.0 \times 10^{-3}$ K at $t = 48$ h in Fig. 5 are in qualitative and quantitative agreement with those of Padilla-Barbosa and Métais (2000), see their Fig. 2c and f and those of Jones and Marshall (1993), see their Fig. 5.

In Fig. 6 the three velocity components in the middle of the convective disk at all vertical levels are given. All velocity components are comparable to u_{rot} . The horizontal r.m.s. velocity (averaged over the convective disk) compares perfectly to the results by Jones and Marshall (1993) (see their Fig. 6a and b) for the upper half of the domain. Deviations in the lower half are due to the different boundary condition in our model at the lower boundary. A detailed study of the horizontal r.m.s. velocity (averaged over the convective disk) shows spurious oscillations of small amplitude originating from the lower boundary (no-slip). Please note that the Ekman layer ($\Delta_{\text{Ekman}} = 32$ m) is not resolved in our model ($\Delta z = 45$ m). Such problem can be avoided when the vertical resolution is increased or a large eddy simulation scheme is used which increases the friction within boundary layers. These spurious oscillations are hidden by the natural variability when the horizontal velocity components are considered (see Fig. 6). They however appear when the natural variability is averaged out. The vertical velocity component is free of such spurious oscillations. This problem is avoided in Jones and Marshall (1993), and Padilla-Barbosa and Métais (2000) by using a free-slip boundary at the bottom.

In all comparisons performed, not all of which are mentioned here, a good overall agreement with the results of Jones and Marshall (1993), and Padilla-Barbosa and Métais (2000) was found.

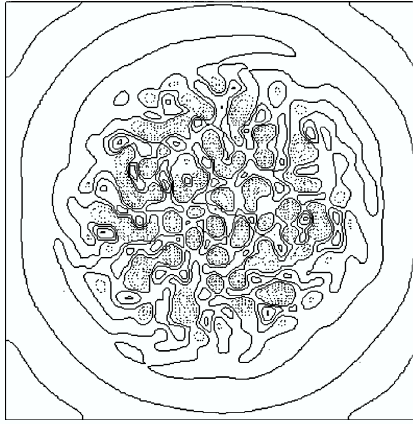


Fig. 4. Vertical velocity at $t = 48$ h and depth of 1 km. Contours are drawn every 0.02 m/s ($w_{\min} = -0.14$ m/s maximum value is $w_{\max} = 0.10$ m/s). Dashed lines correspond to negative values (downward velocity).

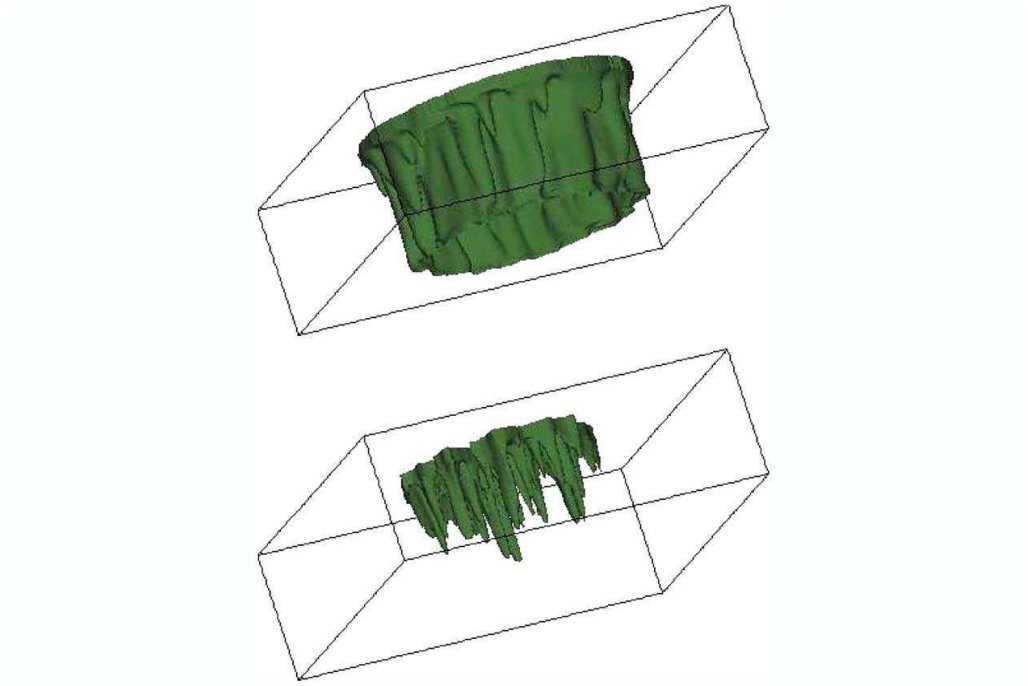


Fig. 5. Temperature isosurface at $t = 48$ h for $\Delta T = 0.006$ K (top) and $\Delta T = 0.03$ K (bottom).

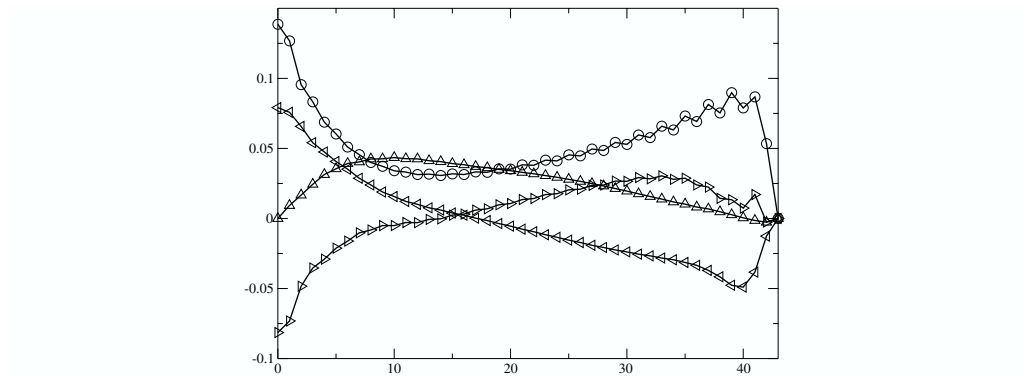


Fig. 6. Horizontal r.m.s. velocity (averaged over the convective disk) at the 44 depth levels (circles). Vertical velocity (triangles up), horizontal velocity u_1 (triangles left), horizontal velocity u_2 (triangles right), in the center of the convective disk at the 44 depth levels. All data at $t = 48$ h. Horizontal axis in the plot corresponds to vertical extension in the model (measured in grip points), vertical axis in the plot gives the velocity in m/s.

When the results from both publications differed, our results were closer to those from Jones and Marshall (1993). A finding comes at no surprise as we used their values for the friction and dissipation parameters and we did not use the more sophisticated large eddy simulation scheme of Padilla-Barbosa and Métais (2000) to parameterize the small scales.

5. Conclusions

We have introduced a new method of implementing a free-slip rigid-lid and a flat-bottom no-slip boundary conditions in ocean models based on Fourier expansion (in all spatial directions). The method is inspired by the immersed or virtual boundary technique. Our method, however, explicitly depletes the velocity on the boundary induced by the pressure while at the same time respecting the incompressibility of the flow field. Using our method the reduction of spurious velocities at the boundaries is only constrained by the computer precision. No constraints, other than CFL, on the time step due to imposing boundary conditions appear. No filtering of the velocity field is necessary and spurious oscillations remain at a negligible level.

The method was tested in various flow configurations involving horizontal boundaries, three of which were shown here. The method is not restricted to horizontal boundaries. Extensions of our method to ocean models with a realistic topography are discussed and further research on this matter is currently under way.

We conclude by reminding the reader that the power of pseudo-spectral method based on Fourier expansion lies not only in their convergence properties but even more in the fact, that the number of operations needed for one time-step is $O(n \log(n))$, where n is the number of degrees of freedom in the problem. An increase of computer power over time, thus, continually increases the advantage of models based on Fourier expansion.

Acknowledgements

I am grateful to A. Lanotte, B. Barnier, Y. Morel, K. Schneider and the participants of the “St. Pierre de Chartreuse” workshop for discussion. Help from P. Begou with using the visualisation software is highly appreciated. The work was funded by EPSHOM-UJF No. 00.87.070.00.470.29.25.

Appendix A. Convergence properties

In this appendix, we explore the convergence properties of the spatial discretization by numerical experiment. To this end errors due to the temporal discretization, being third order in time, have to be reduced. We thus consider a spin-up integration towards a stationary state. The same problem has then to be integrated for different spatial resolutions using the same time-step. To insure the feasibility of such endeavour a simple but challenging test problem has to be chosen. The problem chosen is two dimensional, that is a vertical slice through the ocean that spans 1000 m in the horizontal and the vertical direction. The sea surface is modeled by a free-slip and the

ocean floor by a no-slip boundary condition. The boundary condition in the horizontal direction is periodic. In the middle of the domain a vertical (downward) force, with a circular Gaussian profile, is added ($G(x_1, x_2) = \exp(-32 \times 10^{-6} \text{ m}^{-2} (x_1^2 + x_2^2))$). Such flow leads to a well studied instance of a non-linear boundary layer at the lower boundary, the so called Hiemenz flow (see e.g. Schlichting, 1968, pp. 96–99). Seven experiments are performed with varying spatial resolution. The number of grid points in the domain (including boundary points) are 8×8 , 16×16 , 32×32 , 64×64 , 128×128 , 256×256 , 512×512 . The buffer zone above and below the fluid area is 250 m, each. The friction parameters are $\nu = \kappa = 1.0 \text{ m}^2/\text{s}$ and the time-step is $\Delta t = 60 \text{ s}$ in all calculations.

The integration started from a vanishing velocity field and was performed for $t_{\max} = 2.16 \times 10^5 \text{ s}$. For the 256×256 resolution run the integration was continued until $t_{\text{long}} = 3.00 \times 10^5 \text{ s}$. Almost no differences are visible between the velocity fields at t_{\max} and t_{long} (see Figs. 8–10).

A contour plot of the horizontal velocity component for the lowest and the highest resolution run is given in Fig. 7.

At the lower boundary a Hiemenz flow is generated, and the boundary-layer thickness is about 200 m. We like to mention that in order to capture the non-linear dynamics in the (non-linear) boundary layer about 10 grid points have to be within the boundary layer.

The horizontal velocity along $x = 250 \text{ m}$ and the vertical velocity along $x = 500 \text{ m}$, as a function of depth are shown in Fig. 8.

The horizontal velocity component clearly exhibits Gibbs oscillations at the lower (no-slip) boundary, the amplitude of the oscillation however decreases linearly with resolution. These oscillations are exposed in Fig. 9.

A linear decrease of the amplitude in the Gibbs oscillations reveals a discontinuity in the first derivative at the boundary. This comes at no surprise as the horizontal velocity component is extended skew symmetrically across the lower boundary. This forces the second derivative to vanish at the boundary which is inconsistent to the real dynamics (see Schlichting, 1968, pp. 96–99). No such oscillation occur in the vertical velocity component at the lower boundary (Fig. 10), as a vanishing second derivative is consistent with the real dynamics (see Schlichting, 1968, pp. 96–99). Gibbs oscillations are absent for both velocity components at the upper (free-slip) boundary (Fig. 8).

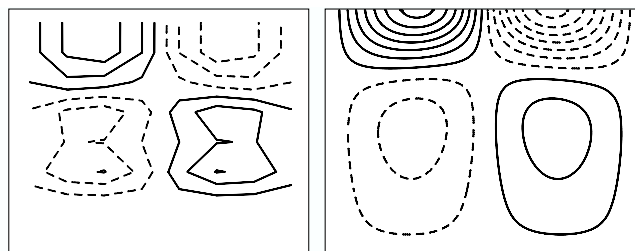


Fig. 7. Contour plot of the horizontal velocity, in the lowest resolution run (8×8) (left) and the highest resolution run (512×512) (right). Contour intervals are drawn every 0.005 m/s, starting from -0.0375 m/s , dashed lines show negative values.

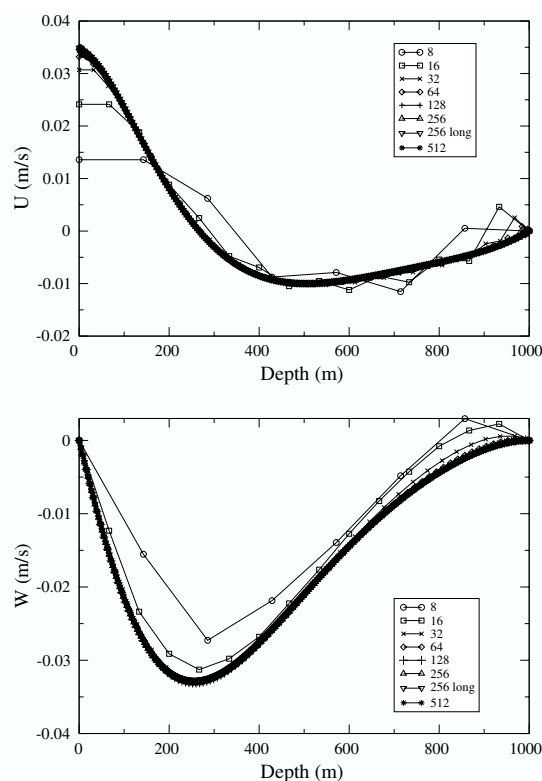


Fig. 8. Horizontal velocity along $x = 250$ m (top) and the vertical velocity along $x = 500$ m (bottom), as a function of depth. Symbols correspond to the different spatial resolution (as given in the figures).

In Fig. 11 we plot the absolute value of the difference between the highest resolution run and every other run for different variables as a function of the resolution. This difference will be called the “error”, we thus chose the highest resolution run as the reference case.

The log–log plot reveals the linear decrease of the amplitude of the Gibbs oscillation of the horizontal velocity component at the lower boundary, already mentioned above. At a fixed distance from the boundary the error however decreases quadratically with the resolution, a behavior typical for Gibbs oscillations. The error in the other quantities measured also points towards the same quadratic decrease of the error with resolution. This decrease is however masked by inaccuracies stemming from the time stepping scheme. For the highest resolution the vertical velocity reaches the CFL-limit (the time step is the same for all the integrations performed), and the error increases for the minimum value of the vertical velocity along $x = 500$ m for the high resolution runs.

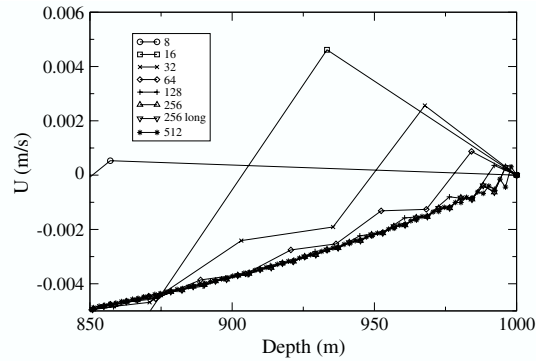


Fig. 9. Horizontal velocity along $x = 250$ m near the lower boundary. Symbols correspond to the different spatial resolution (as given in the figure).

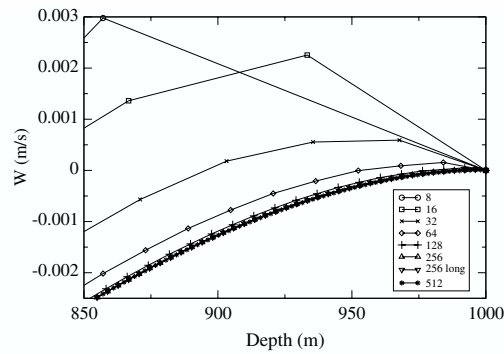


Fig. 10. Vertical velocity along $x = 500$ m near the lower boundary. Symbols correspond to the different spatial resolution (as given in the figure).

No spectral convergence is observed in this test-case. This comes at no surprise as the dynamics even in the interior of the domain is completely slaved to the dynamics at the boundaries and thus shows the corresponding convergence properties. It is indeed clearly visible from Fig. 7 that no structures smaller than the basin scale appear in the problem. A problem involving scales smaller than those imposed by the boundaries would cease to be stationary and the here presented analysis could not be performed.

With the insight obtained from boundary-layer theory, the velocity components in the buffer zone can be adjusted so that the real dynamics at the boundary is modeled to higher order. The convergence properties of the dynamics in the interior fluid would then follow. This is the subject of future research.

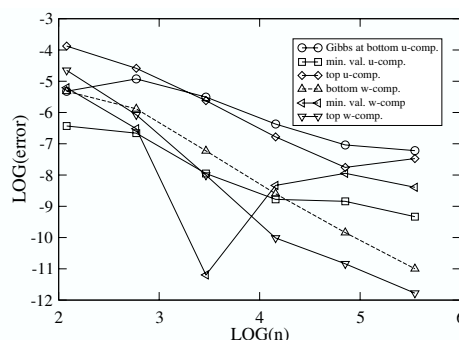


Fig. 11. Log–log plot of the error for different variables: amplitude of the Gibbs oscillation in the horizontal velocity component along $x = 250$ m at the lower boundary (circles), minimum value of the horizontal velocity component along $x = 250$ m (squares), horizontal velocity component at $x = 250$ m, $y = 125$ m (diamonds), vertical velocity component at $x = 500$ m, $y = 875$ m (upward triangles), minimum value of the vertical velocity component along $x = 250$ m (leftward triangles) vertical velocity component at $x = 500$ m, $y = 175$ m (downward triangles).

References

- Chorin, J.A., 1968. Numerical solution of the Navier–Stokes equations. *Math. Comput.* 22, 745–762.
- Davies, A.M., Lawrence, J., 1994. Examining the influence of wind and wind wave turbulence on tidal currents, using a three-dimensional hydrodynamic model including wave current interaction. *J. Phys. Oceanogr.* 24, 2441–2460.
- Goldstein, D., Handler, R., Sirovich, L., 1993. Modeling a no-slip flow boundary with an external force field. *J. Comp. Phys.* 105, 354–366.
- Gottlieb, D., Orszag, S., 1977. *Numerical Analysis of Spectral Methods: Theory and Applications*. SIAM, Philadelphia.
- Iaccarino, G., Verzicco, R., 2003. Immersed boundary technique for LES/RANS simulations. *Applied Mech. Rev.*, ASME, in press.
- John, F., 1991. *Partial Differential Equations*, fourth ed. Springer-Verlag, New York.
- Jones, H., Marshall, J., 1993. Convection with rotation in a neutral ocean: a study of open-ocean deep convection. *J. Phys. Oceanogr.* 23, 1009–1039.
- Julien, K., Legg, S., McWilliams, J., Werne, J., 1996. Rapidly rotating Rayleigh–Bénard convection. *J. Fluid Mech.* 322, 243–273.
- Lamb, K.G., 1994. Numerical experiments of internal wave generation by strong tidal flow across a finite amplitude bank edge. *J. Geophys. Res.* 99, 843–864.
- Marshall, J., Hill, C., Perelman, L., Adcroft, A., 1997. Hydrostatic, quasi-hydrostatic, and nonhydrostatic ocean modeling. *J. Phys. Oceanogr.* 27, 5733–5752.
- Maxworthy, T., Narimousa, S., 1994. Unsteady, turbulent convection into a homogeneous, rotating fluid, with oceanographic applications. *J. Phys. Oceanogr.* 24, 865–887.
- Mohd-Yosuf, J., 1997. Combined immersed boundary/B-spline methods for simulation in complex geometries. *Annual Research Briefs, Center for Turbulence Research*, pp. 317–328.
- Padilla-Barbosa, J., Métais, O., 2000. Large-eddy simulations of deep-ocean convection: analysis of the vorticity dynamics. *J. Turbul.*, 1009.
- Peskin, C.S., 1977. Flow patterns around heart valves: a numerical method. *J. Comp. Phys.* 25, 220–252.
- Peyret, R., 2002. *Spectral Methods with Application to Incompressible Viscous Flow*. Springer-Verlag, New York. 432 pp.
- Schlichting, H., 1968. *Boundary-Layer Theory*. McGraw-Hill, New York. 817 pp.

- Schott, F., Leaman, K.D., 1991. Observation with moored acoustic Doppler current profiles in the convection regime in the Gulf de Lion. *J. Phys. Oceanogr.* 21, 558–574.
- Schott, F., Visbeck, M., Fischer, J., 1977. Observations of vertical currents and convection in the Central Greenland Sea during the winter of 1988–1989. *J. Geophys. Res.* 98, 14401–14421.
- Temam, R., 1969. Sur l'approximation de la solution des équations de Navier–Stokes par la méthode des pas fractionnaires II. *Archiv. Rat. Mech. Anal.* 32, 377–385.
- Wirth, A., 2000. The parameterization of baroclinic instability in a simple model. *J. Mar. Res.* 58, 571–583.

4.4 Tilted convective plumes in numerical experiments

Available online at www.sciencedirect.com

SCIENCE @ DIRECT®

Ocean Modelling 12 (2006) 101–111

**Ocean
Modelling**www.elsevier.com/locate/ocemod

Tilted convective plumes in numerical experiments

A. Wirth *, B. Barnier

LEGI BP 53, 38041 Grenoble Cedex 9, France

Received 25 October 2004; received in revised form 8 March 2005; accepted 21 April 2005

Available online 20 June 2005

Abstract

The dynamics of a single convective plume in an isothermal ocean is investigated by numerically integrating the three dimensional Boussinesq equations. Our study emphasizes on the important consequences of a non-vanishing angle between the axis of rotation and the buoyancy force (gravity). Experiments are performed for four different values of the angle corresponding to open-ocean convection at latitude: 90° N, 60° N, 45° N and 0° N.

We show that the horizontal component of the rotation vector leads to qualitative and quantitative changes in the convective dynamics of a single plume. Plume structures are aligned along the axis of rotation rather than the direction of gravity (tilted convection), the vertical velocity of the plume is reduced, and the mixing is enhanced by the horizontal component of the rotation vector. These results suggest that in future parametrisations of ocean convection the effect of the horizontal component of the rotation vector should be included.

© 2005 Elsevier Ltd. All rights reserved.

PACS: 65N35; 76M22; 76R05; 86A05

Keywords: Geophysical fluid dynamics; Ocean convection; Traditional approximation

* Corresponding author. Tel.: +33 0 6 32 97.

E-mail address: achim.wirth@hmg.inpg.fr (A. Wirth).

1. Introduction

The important role of deep convection on the overturning circulation at global scale is now well established and its impact on the climate dynamics recognized (Willebrand et al., 2000). Deep convection is also a principal component of the carbon cycle and has a strong influence on the biological dynamics in parts of the world's ocean (Wood et al., 1999).

Convection in the world ocean is a highly intermittent process in space and time. Convective regions, also called convective chimneys, typically span a few hundreds of kilometers in the horizontal directions. The actual convection process, that is, the vertical exchange and mixing of water masses only takes a few days. During this time the convective chimney is composed of a large number of convective plumes measuring up to 1 km in the horizontal directions (Schott and Leaman, 1991). The downward transport of the heavy water within the plumes is almost perfectly compensated by an upward transport in between the plumes (Send and Marshall, 1995). The plumes are the coherent structures governing the convective dynamics. A detailed understanding of the convection process is thus not conceivable without a detailed understanding of the plume dynamics. For a review on open-ocean convection we refer the reader to Killworth (1983) and Marshall and Schott (1999). The plumes can indeed be seen as the “atoms of convection” which, however cannot be explicitly resolved in the numerical models of the ocean circulation at basin scale. Their impact on the resolved dynamics has to be parametrised in such models. Efficient parameterizations are and will be key to the model development. Indeed, the rapid advancement of numerical ocean models and their improvement asks for an increasing accuracy in the representation of several phenomena. Current parameterisations of convection used in state of the art numerical models are inspired by the physics of the convection process and respond to the necessity of removing unstable stratifications in a numerical ocean. Improving parameterisation of the convection process does require a detailed understanding of the dynamics and the important processes and parameters involved. In this paper we demonstrate that the “traditional approximation”, that is, neglecting the horizontal component of the rotation vector, is not appropriate when considering the deep convection processes, even at higher latitudes.

Convective plumes in an isothermal ocean are investigated by numerically integrating the three dimensional Boussinesq equations. The effects of rotation on the plume dynamics are considered. We not only vary the magnitude of the rotation vector but also its direction. More precisely, in the majority of numerical calculations considering ocean dynamics, the traditional approximation is employed which completely neglects the horizontal component of the rotation vector. Rotation is thus supposed to be colinear with gravity (see e.g. Marshall et al., 1997; for a discussion on the traditional approximation in an oceanic context). The traditional approximation may be justified in instances where vertical velocities are small compared to their horizontal counterparts, that is, when non-hydrostatic terms can be neglected. When, however, the non-hydrostatic terms are essential for the dynamics, as in the case of convection, the traditional approximation has to be relaxed, especially in regions of the world ocean of not too high latitudes. For the here presented numerical investigation we choose an inclination of the rotation vector corresponding to open-ocean convection at latitudes: 90° N, 60° N, 45° N and 0° N a case of no rotation is added for the completeness of the dynamical picture. The angles of 45° N and 60° N correspond to the Gulf of Lions and the Labrador Sea, respectively, two major convection sites of the world oceans (Killworth, 1983; Marshall and Schott, 1999). The angle of 90° N, the North Pole where gravity

and rotation are aligned, presents the “traditional” convection case. Most Ocean General Circulation Models (OGCMS) use the traditional approximation.

While preparing this manuscript the work by Sheremet (2004) was brought to our attention which clearly demonstrates the influence of a finite angle between the buoyancy and the axis of rotation in laboratory experiments. These pioneering laboratory experiments by Sheremet determine not only the influence of the axis of rotation on the direction of convection but also present a theoretical discussion of the phenomena. Our here presented work can indeed be seen as the numerical supplement to the laboratory experiments of Sheremet (2004), which present a fortuitous possibility to validate our calculations. To determine the influence of a finite angle between the axis of rotation and the direction of gravity we, however, performed calculations for four different angles. Following the work by Sheremet (2004) we also use the term “tilted” to describe the convection in instances where the axis and rotation and the buoyancy force are not colinear.

2. Model description

The mathematical model of the here presented ocean convection experiment are the Boussinesq equations (Eq. (1)) of an incompressible flow (Eq. (2)) in a rotating frame, supplemented by boundary conditions. The flow field is given by \mathbf{u} and the scalar (temperature) field by T . The buoyant scalar is transported by the flow (3). The source term S insures the prescribed heat fluxes through the upper boundary and the equation of state is linear with the expansion coefficient α . The ocean surface is modeled by a free-slip rigid-lid boundary condition, while the ocean floor is modeled by a no-slip boundary condition. In the horizontal directions periodic boundary conditions are employed.

$$\partial_t \mathbf{u} + \mathbf{u} \cdot \nabla \mathbf{u} + 2\Omega \times \mathbf{u} + \nabla P = \alpha g T \mathbf{e}_\perp + \nu \nabla^2 \mathbf{u} \quad (1)$$

$$\nabla \cdot \mathbf{u} = 0 \quad (2)$$

$$\partial_t T + \mathbf{u} \cdot \nabla T = \kappa \nabla^2 T + S \quad (3)$$

The mathematical model is solved numerically using a pseudo-spectral scheme entirely based on Fourier expansion. The boundary conditions are implemented using a technique inspired by the immersed boundary condition (see Peskin, 1977; Goldstein et al., 1993). For a detailed discussion on the model and the new boundary technique we refer the reader to Wirth (2004). Our model will forth–worth be called HARmonic Ocean MODEL (HAROMOD).

The coherent structures dominating the convective dynamics are known to have comparable horizontal and vertical scales. A fact that has to be reflected in the aspect ratio of the numerical grid, which is unity in all the calculations presented here. We also choose the friction coefficients equal in the horizontal and vertical direction and the Prandtl number is unity ($\kappa = \nu$) in all calculations.

The area of integration spans $2 \text{ km} \times 2 \text{ km}$ in the horizontal directions and 3 km in the vertical. The friction coefficients are, $\nu = \kappa = 0.1 \text{ m}^2/\text{s}$ the expansion coefficient $\alpha = 2.0 \times 10^{-4} \text{ K}^{-1}$, gravity is $g = 9.81 \text{ m/s}^2$, density $\rho = 1000 \text{ kg/m}^3$ and the specific heat capacity $c = 3900 \text{ J/(kg K)}$. The temperature in the upper 40 m is perfectly mixed, that is, the temperature is homogenized in this

layer at every time-step. The ocean is cooled in a circular region attached to the surface, using a Gaussian profile given by

$$H = 1.28 \frac{W}{m^3} \exp \left(-\frac{x^2 + y^2}{(200m)^2} - \frac{z^2}{(70m)^2} \right) \quad (4)$$

leading to a surface heat flux of

$$H_s = 80 \frac{W}{m^2} \exp \left(-\frac{x^2 + y^2}{(200m)^2} \right) \quad (5)$$

The total heating is thus $P = \int_{R^3} H dV = 1.0 \times 10^7$ W and the buoyancy flux is $F_0 = (P\alpha g)/(c\rho) = 5.03 \times 10^{-3} \text{ m}^4/\text{s}^3$. The source term in Eq. (3) is given by

$$S = H/(c\rho)$$

The numerical resolution in the horizontal is 128×128 grid points, there are 192 grid points in the vertical direction and the time-step is $\Delta t = 60$ s.

3. Tilted plumes

The surface heat flux of 80 W/m^2 is smaller than the maximum values of heat exchange during specific convection events in the Labrador Sea, Greenland Sea and the Mediterranean (Marshall and Schott, 1999). We express the non-alignment of rotation and gravity by giving the latitude θ of the corresponding situation, that is: $\theta = 90^\circ$ N for an alignment of rotation and gravity on the North Pole (NP), $\theta = 60^\circ$ N for the situation in the Labrador Sea (LS), $\theta = 45^\circ$ N for the situation in the Gulf of Lions (GL) and $\theta = 0^\circ$ for the situation at the equator (EQ) (rotation being perpendicular to gravity). We are aware of the fact that there is no deep convection at the equator but included the case for completeness of the dynamical picture. We also performed calculations for the case with vanishing rotation (NR) in this case the horizontal expansion of the plume is not arrested, as it is in the rotating case. One-and-a-half days after the onset of cooling the NR-plume's horizontal extension is such that the plume dynamics is strongly influenced by the finite (periodic) domain size (Fig. 1(a)). In the cases with rotation, the horizontal expansion of the plume is arrested and it only spans a fraction of the horizontal domain size.

The most conspicuous feature in tilted convection is that the plumes extend in the direction of the axis of rotation rather than gravity (see Fig. 1). This finding, which has been explored by Sheremet (2004) in laboratory experiments for the oceanic context, is well known to researchers considering convection in rotating spheres (see e.g. Busse et al., 1998). The elongation of dynamical structures along the axis of rotation is attributed to the Taylor–Proudman theorem, which states that, in flows dominated by rotation the velocity vector is constant along the axis of rotation.

For the first 5–8 h of the convection experiment the influence of rotation is not visible and all experiments look identical during this time the plume has dropped by about 500 m, being in perfect agreement with the scaling in time $t_1 = 2.4/\Omega$ and distance $h_{c1} = 3.3(F_0/\Omega^3)^{1/4}$ proposed by Fernando et al. (1998) (based on laboratory experiments). After that period the plume starts

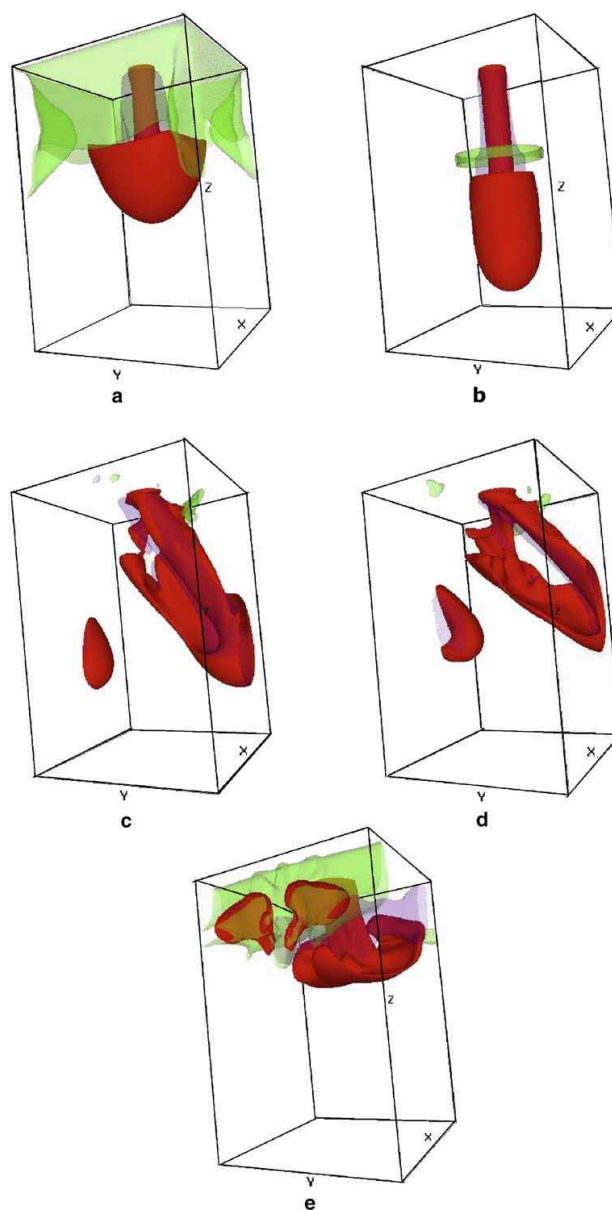


Fig. 1. Temperature isosurface $\Delta T = 5.0 \times 10^{-4}$ K (red) and vertical velocity isosurfaces $w = -0.01$ m/s (violet) and $w = 0.01$ m/s (green) at $t = 1.5$ days after the onset of cooling, for different latitudes on earth (a) NR (no rotation), (b) NP (90° N), (c) LS (60° N), (d) GL (45° N) and (e) EQ (0° N).

to deviate and follow the axis of rotation. By that time, the rotation inhibits changes of velocity along the axis of rotation (Taylor–Proudman theorem) in the entire domain and the cooled surface water now deviates immediately without an initial vertical sinking. This can be seen in Figs. 1(c) and (d), 2 and 3, where two venes of cold water are visible, a lower one formed by the initially vertically converting and the deviated water, and an upper one formed by the immediately deviating water cooled at later times.

A closer analysis in Figs. 2 and 3, showing a north–south cross-section of the plumes suggests indeed that the plume dynamics is composed of a sinking in the direction of buoyancy force combined with a stretching along the axis of rotation forming “Taylor ink walls” or “Taylor curtains”. These figures compare well to photos of laboratory experiments by Sheremet (2004) and the description in his article. Films composed of snapshots from the numerical data reveal that the heavier fluid actually spirals along the axis of rotation. The motion does indeed resemble a charged particle in a magnetic field, an analogy that is often advanced. The spiraling motion explains also the eastward drift and the downward drift with respect to the axis of rotation. Indeed, when a buoyant parcel spirals its gravitational acceleration depends on the steepness of the slope, the parcel has thus a faster velocity on the steeper and the following eastward leg, and is slower on the shallower and the following westward leg. This leads to a downward and eastward drift of the plume with respect to the axis of rotation (Figs. 2(b) and 3(b)), a fact also observed by Sheremet (2004).

After having determined the direction of convection we proceed by looking at the vertical plume speed. After 1 h into the experiment and for the following next 7 h a constant acceleration

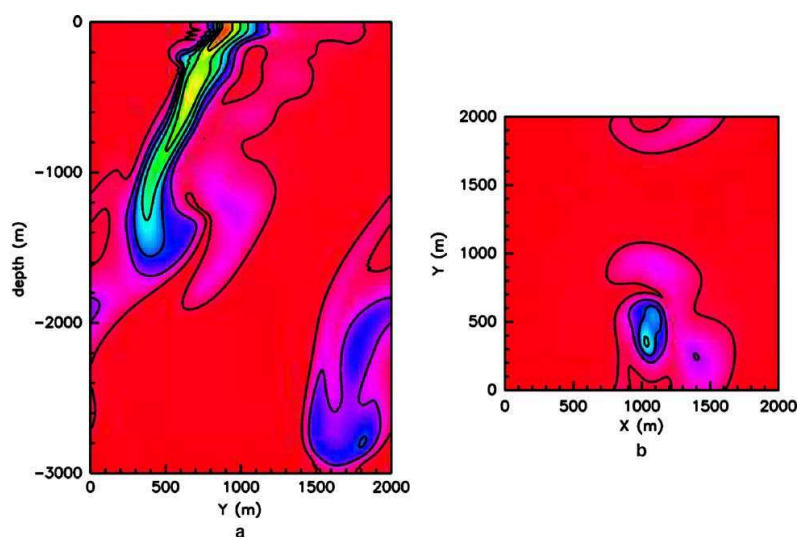


Fig. 2. LS case ($\theta = 60^\circ$ N): (a) south–north cut through the center of the domain and (b) horizontal cut at 1500 m depth, temperature contour lines every $\Delta T = 5.0 \times 10^{-4}$ K starting from $\Delta T = 3.1 \times 10^{-3}$ K at $t = 2$ days after the onset of cooling.

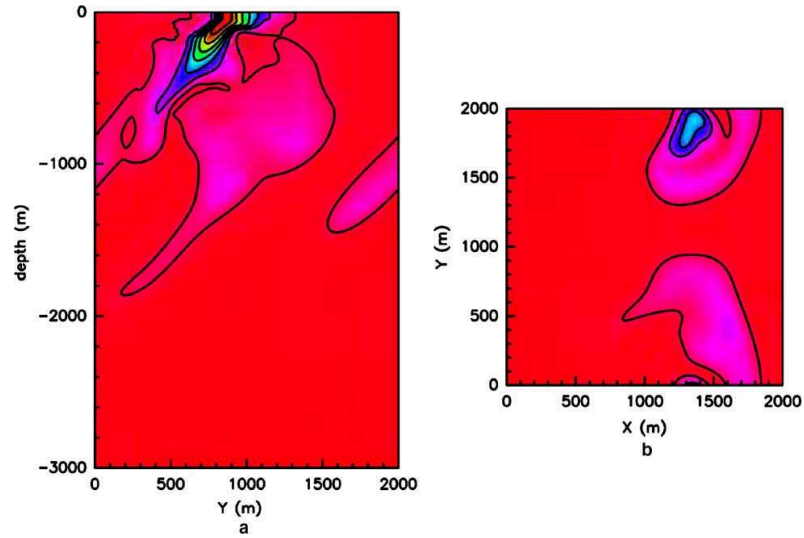


Fig. 3. GL case ($\theta = 45^\circ$ N): (a) south–north cut through the center of the domain and (b) horizontal cut at 1500 m depth, temperature contour lines every $\Delta T = 5.0 \times 10^{-4}$ K starting from $\Delta T = 3.1 \times 10^{-3}$ K at $t = 2$ days after the onset of cooling.

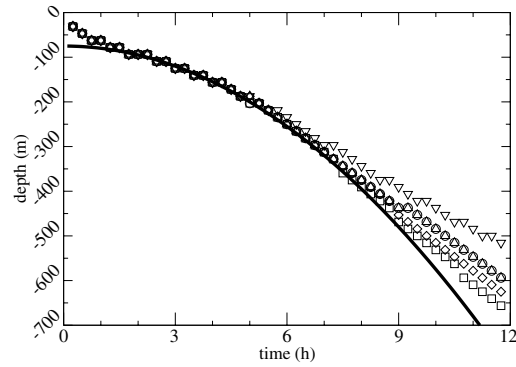


Fig. 4. Vertical displacement of plumes for the first 12 h: (—) fit (const. acceleration), (\square) NP, (\diamond) LS, (\triangle) GL, (∇) EG, (\circ) NR.

of the buoyant water front is observed. In Fig. 4 this initial behavior is fitted to a constant acceleration of $g' = 7.72 \times 10^{-7} \text{ m/s}^2$, this corresponds to a temperature difference of $\Delta T = g'/(g\alpha) = 3.93 \times 10^{-4} \text{ K}$, which is slightly less than half the maximal temperature after 1 h into the experiment. At this early time all five experiments show almost identical behavior as rotation

has a vanishing influence. After that initial state the acceleration reduces. This behavior agrees very well with laboratory experiments that showed a decrease of acceleration after $t \approx 2.4/\Omega$ (Sheremet, 2004; Fernando et al., 1998). The plume displacement in the EQ case deviates first from the constant acceleration regime as it exhibits the slowest vertical displacement of all cases, the horizontal rotation vector organizes the plume into horizontal rolls stretched in the north–south direction strongly inhibiting the convection process. In the other extreme case (NP) the rotation only inhibits lateral spreading of the plume making the downward convection process most efficient, as a consequence this case is the last to leave the constant acceleration process of all cases considered. The cases LS and GL are in between these two extremes and more representative of what happens in the ocean. In the early stage the case of no rotation is almost identical to the GL case when the vertical plume displacement is considered, suggesting that for the GL case the retarding effect of the horizontal component of the rotation vector is almost balanced by the accelerating effect of the vertical component of the rotation vector. In other aspects of the dynamics, these two cases are completely different as can be easily seen by comparing Fig. 1(a) and (d).

In the case of an alignment of rotation and gravity (NP) the behavior agrees well with the laboratory results of Fernando et al. (1998), although our plume is laminar: the plume evolves into a cylindrical fluid column (see Fig. 1) with a radius given by approximately $R_{NP} = 1.4(F_0/\Omega^3)^{1/4} = 472$ m.

Maxworthy and Narimousa (1994) determined in laboratory experiments that the vertical speed of convective plumes is constant after an initial adjustment and given by

$$w = (1.0 \pm 0.1)\sqrt{B/f} \quad (6)$$

when gravity and rotation vector are aligned and when the buoyancy forcing at the surface is homogeneous, B representing the buoyancy flux per surface area. In our numerical experiments we also determined the vertical plume displacement after the initial adjustment. The results are given in Fig. 5(a). After about 6–8 h the vertical plume displacement proceeds at almost constant

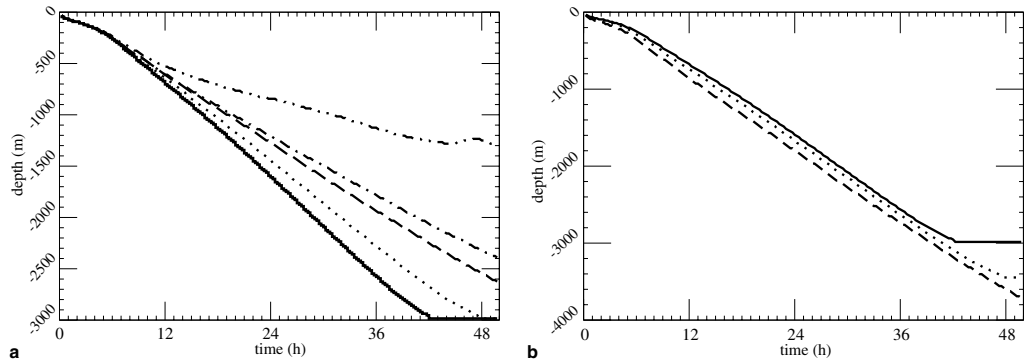


Fig. 5. Vertical displacement of plumes (a) and vertical displacement of plumes divided by the sine of the latitude (b): (—) NP, (···) LS, (---) GL, (-·-·) NR and (- - -) EQ.

velocity, except for the case with no rotation and the equatorial case. The magnitude of the velocity is also in good agreement with Eq. (6). Deviations from the constant velocity regime are also observed some 300 m before the plume reaches the floor, a length scale that corresponds to the horizontal dimension of the plume. This comes at no surprise as in flows dominated by rotation, the variation of the velocity vector along the axis of rotation is inhibited (Taylor–Proudman theorem). In Fig. 5(b) the displacement of the plume is divided by the sine of the latitude and it is clearly visible that the renormalized vertical velocity agrees for all three cases considered. Based on this findings we can thus extend the formula (6) of Maxworthy and Narimousa (1994) to cases of tilted convection and obtain:

$$w = \sqrt{B/f} \sin(\theta) = \sqrt{\frac{B \sin(\theta)^3}{f_{\perp}}} \quad (7)$$

where $f = 2\Omega$, $f_{\perp} = 2\Omega \sin(\theta)$. The best fit for the normalized velocities gives $w(\theta = 90^\circ) = 2.25 \times 10^{-2}$ m/s.

The plume dynamics at the equator (EQ) is different from all other cases in many aspects. No coherent plume is formed the heavy water sinks and spirals around the horizontal axis of rotation extending in the north–south direction. The extension in this direction is not inhibited as the vertical component of the rotation vector vanishes. No coherent plume speed can be obtained in this case.

Another important point is the increased mixing in tilted convection already mentioned in Sheremet (2004). Fig. 1(c)–(e) show indeed smaller size features than Fig. 1(b) which shows a single coherent axis-symmetric structure. In the case of tilted convection the axis-symmetry is broken and the plume evolves in a more chaotic way. The presence of the fine structures as for example thin “Taylor ink walls” in the cases LS and GL increase the mixing as compared to the NP or NR case. The horizontally averaged temperature one-and-a-half days into the convection experiment are shown in Fig. 6. It can be clearly seen that in the experiments involving a vertical and a

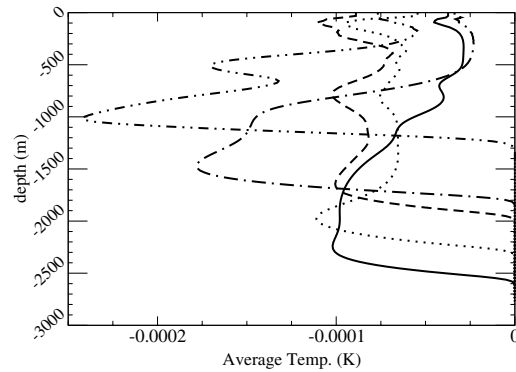


Fig. 6. Horizontally averaged temperature 1.5 days into the experiment: (—) NP, (···) LS, (---) GL, (-·-) NR and (- - -) EQ.

horizontal component of the rotation axis the mean temperature at each level is decreased (more negative temperature!) after the passage of the plume head as compared to the case with a vertical axis of rotation, the average temperature in the NR and NP cases is only about half of the value in the LS and GL cases. In the case corresponding to the Labrador Sea and the Gulf of Lions the water column above the tip of the front is almost perfectly homogenized.

4. Conclusions and perspectives

Based on direct numerical simulations, we have demonstrated that the horizontal component of the rotation vector has significant qualitative and quantitative consequences on the dynamics of a single convective plume at time scales longer than about a quarter of a day. Our here presented numerical calculations are in close agreement with laboratory experiments of Sheremet (2004). The convection is composed of a sinking in the direction of buoyancy force combined with a stretching along the axis of rotation. The vertical speed of the plume is reduced by the horizontal component of the rotation, and the mixing is increased. We furthermore extend an existing formula for the vertical plume speed in the case of aligned gravity and rotation vectors to the case of an arbitrary angle.

The here presented case was restricted to the dynamics of a single plume in an isothermal ocean leading to deterministic convection laws. At convection sites stratification is generally weak as the water masses are well mixed by previously occurred convection events and, as the restratification process is slow (seasonal time scale). The analysis of the important case of convection by an ensemble of plumes in an isothermal and stably stratified ocean is of stochastic nature. Such investigation, possibly leading to improved parameterizations of open-ocean convection, is presently in progress. An improved parameterization of convection in the Greenland Sea (75° N), Labrador Sea (60° N) and the Gulf of Lions (45° N), including “non-traditional” effects, is likely a key to improving hydrostatic ocean global circulation models (OGCMs), especially when problems on climate time scales are considered.

Acknowledgments

We are grateful to T. Gerkema, Y. Morel, T. Penduff and C. Staquet for discussions. Help from P. Begou with using the visualisation software is highly appreciated. The work was funded by EPSHOM-UJF No. 00.87.070.00.470.29.25. Calculations were performed at IDRIS (project 40727), France.

References

- Busse, F.H., Hartung, G., Jaletzky, M., Sommermann, G., 1998. Experiments on thermal convection in rotating systems motivated by planetary problems. *Dyn. Atmos. Oceans* 27, 161–174.
- Fernando, H.J.S., Clien, R.-r., Ayotte, A., 1998. Development of a point plume in the presence of background rotation. *Phys. Fluids* 10, 2369–2383.

- Goldstein, D., Handler, R., Sirovich, L., 1993. Modeling a no-slip flow boundary with an external force field. *J. Comput. Phys.* 105, 354–366.
- Killworth, P.D., 1983. Deep convection in the world ocean. *Rev. Geophys.* 21, 1–26.
- Marshall, J., Schott, F., 1999. Open-ocean convection: observations, theory, and models. *Rev. Geophys.* 37, 1–64.
- Marshall, J., Hill, C., Perelman, L., Adcroft, A., 1997. Hydrostatic, quasi-hydrostatic, and nonhydrostatic ocean modeling. *J. Phys. Oceanogr.* 27, 5733–5752.
- Maxworthy, T., Narimousa, S., 1994. Unsteady, turbulent convection into a homogeneous, rotating fluid, with oceanographic applications. *J. Phys. Oceanogr.* 24, 865–887.
- Peskin, C.S., 1977. Flow patterns around heart valves: a numerical method. *J. Comput. Phys.* 25, 220–252.
- Schott, F., Leaman, K.D., 1991. Observation with moored acoustic Doppler current profiles in the convection regime in the Gulf de Lion. *J. Phys. Oceanogr.* 21, 558–574.
- Send, U., Marshall, J., 1995. Integral effects of deep convection. *J. Phys. Oceanogr.* 25, 872–885.
- Sheremet, V., 2004. Laboratory experiments with tilted convective plumes on a centrifuge: a finite angle between the buoyancy force and the axis of rotation. *J. Fluid Mech.* 506, 217–244.
- Willebrand, J., Barnier, B., Böning, C., Dietrich, C., Killworth, P.D., LeProvost, C., Yia, Y., Molines, J.-M., New, A.L., 2000. Circulation characteristics in three eddy-permitting models of the North Atlantic. *Prog. Oceanogr.* 48, 123–161.
- Wirth, A., 2004. A non-hydrostatic flat-bottom ocean model entirely based on Fourier Expansion. *Ocean Mod.* 9, 71–87.
- Wood, R.A., Keen, A.B., Mitchell, J.F.B., Gregory, J.M., 1999. Changing the spatial structure of the thermohaline circulation in response to atmospheric CO₂ forcing in a climate model. *Nature* 372, 572–575.

4.5 Mean Circulation and Structures of Tilted Ocean Deep Convection

Mean Circulation and Structures of Tilted Ocean Deep Convection

A. WIRTH AND B. BARNIER

MEOM/LEGI, Grenoble, France

(Manuscript received 4 January 2007, in final form 17 April 2007)

ABSTRACT

Convection in a homogeneous ocean is investigated by numerically integrating the three-dimensional Boussinesq equations in a tilted, rotating frame (f - F plane) subject to a negative buoyancy flux (cooling) at the surface. The study focuses on determining the influence of the angle (tilt) between the axis of rotation and gravity on the convection process. To this end the following two essential parameters are varied: (i) the magnitude of the surface heat flux, and (ii) the angle (tilt) between the axis of rotation and gravity. The range of the parameters investigated is a subset of typical open-ocean deep convection events.

It is demonstrated that when gravity and rotation vector are tilted with respect to each other (i) the Taylor–Proudman–Poincaré theorem leaves an imprint in the convective structures, (ii) a horizontal mean circulation is established, and (iii) the second-order moments involving horizontal velocity components are considerably increased.

Tilted rotation thus leaves a substantial imprint in the dynamics of ocean convection.

1. Introduction

Most of the World Ocean is known to be in hydrostatic balance at large scales. However, ocean dynamics at scales smaller than about 10 km, convection, circulation in coastal areas, surface mixed layer dynamics, the breaking of internal waves, and the dynamics of overflows in straits are instances of ocean dynamics where nonhydrostatic effects are essential. These instances of nonhydrostatic ocean dynamics are important dynamical problems in their own right, but they also influence the large-scale dynamics of the World Ocean and the climate system of our planet. A detailed discussion of nonhydrostatic effects in the ocean dynamics can be found in Marshall et al. (1997).

A striking feature of open-ocean deep convection is that, although it governs a substantial part of the poleward heat transport of the atmosphere–ocean system through its influence on the thermohaline circulation, it is nevertheless extremely localized in space and time. In fact, convection chimneys account only for a tiny fraction of the World Ocean, and a convection event typically lasts for only about 1 week. A substantial part of

the large-scale and long-time ocean and climate dynamics is thus slaved to what happens at these almost space–time singularities. For a detailed discussion of open-ocean convection from an observational, theoretical, and modeling perspective, we refer the reader to the review of Marshall and Schott (1999). For a recent study of the impact of the convection process on the large- and mesoscale dynamics in the Labrador Sea, we refer the reader to Straneo (2006) and Chanut et al. (2008, hereafter ChBa).

Convection chimneys, being by themselves an ensemble of many convection plumes, typically measure about 100 km in the horizontal directions. They thus barely span the area of a single horizontal grid point in ocean global circulation models (OGCMs) employed in today's climate models. Even when much higher resolutions were computationally feasible, most models will not be able to explicitly represent the convection process because they integrate the hydrostatic primitive equations, neglecting vertical momentum. Numerical ocean models based on the hydrostatic approximation are, and will be in the foreseeable future, the major tools in entangling the ocean dynamics at the global or basin scale. Such models, however, have to be supplemented at certain locations to account for the influence of the nonhydrostatic processes, as, for example, convection. This can be achieved in two ways: first, by locally nesting a nonhydrostatic model at the critical

Corresponding author address: A. Wirth, MEOM/LEGI, BP 53, 38041 Grenoble CEDEX 9, France.
E-mail: achim.wirth@hmg.inpg.fr

regions, or second, by parameterizing the nonhydrostatic effects.

The present work is an attempt toward the second approach for the case of open-ocean convection. If such parameterization is used, its implementation is most likely to consume less computer power than a nested nonhydrostatic model. Detailed research on the influence of external parameters, such as, for example, magnitude and direction of rotation, is integral to developing and improving such parameterization and adjusting the parameter values in existing parameterization.

Existing parameterizations of open-ocean convection can be put into two categories. The first consists of schemes that are driven by the necessity to remove the convective instability with no reference to the physics of convection. The second type includes some of the physics of convection borrowed from atmospheric observations, models, and convection schemes. They thus exclude qualitative differences resulting from the different Rossby numbers involved in the ocean and atmosphere. Convection in the atmosphere takes only a few hours, while it takes a few days in the ocean. We will demonstrate that the corresponding difference in Rossby number is essential for the convection process and its parameterization. Oceanic convection is in a dynamically interesting regime because vertical velocities are large enough so that nonhydrostatic terms cannot be ignored, but are small enough so that rotation cannot be ignored either. Nonlinearity is strong enough so that the dynamics are in a three-dimensional turbulent regime, as opposed to quasi-two-dimensional heicon dynamics [see Klinger and Marshall (1995) for a detailed discussion of the three-dimensional versus heicon regimes]. Furthermore, the results published in Klinger and Marshall (1995) and those of the present work indicate that away from the surface boundary layer the convection process creates a vertical density structure that has the characteristic that the influence of (unstable) stratification is comparable to that of rotation.

We furthermore show that not only is the magnitude of the rotation vector (as expressed in the Rossby number) of importance, but so too is its direction. More precisely, in the majority of numerical calculations considering ocean dynamics, the traditional approximation (see, e.g., Marshall et al. 1997) is employed, which completely neglects the horizontal component of the rotation vector, and thus its "tilt." One exception is the large-eddy simulation (LES) by Wang (2006). Rotation is thus supposed to be collinear with gravity, which is strictly only the case at the poles. The traditional approximation may be justified in instances where vertical velocities are small compared to their horizontal coun-

terparts, that is, when nonhydrostatic terms can be neglected. However, when nonhydrostatic terms are essential for the dynamics, as in the case of convection, the horizontal component of the rotation vector (the tilt) has to be included.

The important part of the tilt in the rotation vector for the dynamics of a single convective plume in an oceanic context was demonstrated experimentally by Sheremet (2004) and numerically by Wirth and Barnier (2006). The dynamics of a collection of plumes generated by homogeneous forcing (cooling) at the surface cannot be deduced from the dynamics of a single plume due to the nonlinear interaction between the plumes with the turbulent background and the density stratification. It is thus of paramount importance to investigate the possible changes of ocean convection when subject to a homogeneous forcing at the surface.

The important consequences of two buoyant tracers (temperature and salinity) and a nonlinear equation of state are the subject of future research and are not considered here.

To summarize: open-ocean convection is a dynamically very involved process, where rotation (magnitude and direction), vertical acceleration, stratification, and three-dimensional turbulence (nonlinearity) each play a role of almost equal importance. That is, none of the terms in the Boussinesq equations can be neglected and none are dominant.

In the next section we discuss some basic facts of open-ocean convection with an emphasis on its integral effects, which are important when a parameterization is to be constructed. We then proceed by explaining the physics of our experiment, followed by a description of the mathematical model and its numerical implementation used for our investigations of deep convection in section 3. Results of our numerical experiments are presented in section 4. In section 4a, the imprint of the Taylor–Proudman–Poincaré (TPP) theorem on the structures of the turbulent convection process is shown, and in section 4b the horizontal mean temperature structure is discussed and the generation of mean horizontal velocities is demonstrated analytically and experimentally. The values of second-order moments essential to many parameterization schemes are determined and discussed in section 4c. We conclude in section 5 by discussing the implications of the here-presented results on the large-scale ocean dynamics.

2. Open-ocean deep convection

a. Basic facts

The entire deep-ocean convection process is usually divided into the following three phases: (i) precondi-

tioning, (ii) deep convection (vertical exchange of water masses), and (iii) lateral exchange between the (homogenized) convection site and the ambient fluid (see, e.g., Marshall and Schott 1999 for a review). The first and last process happen on scales of a few tens of kilometers to the order of a few hundreds of kilometers, and are usually well represented in hydrostatic models of ocean convection with sufficient resolution (ChBa). It is the second process—deep convection—that involves plumes of 100 m–1 km in diameter and is intrinsically nonhydrostatic. This process has thus to be parameterized in hydrostatic large-scale ocean models. The reminder of this work will be dedicated to only this part of the total convection process and will be named “convection” for brevity. Its spatial pattern consists of a convection chimney spanning several tens of kilometers in the horizontal direction. The chimney itself is composed of plumes. These “atoms of convection” perform the actual (negative) buoyancy transport and mixing.

In their work, Send and Marshall (1995) use observational data, numerical data, and theoretical considerations to determine that there is no substantial net downward motion in the interior of a chimney, with associated inflow at the surface and outflow at the bottom; but that the downward transport in the plumes is compensated for by strong upward transport in the area between the plumes, which cancel each other almost perfectly. This also means that there is no large-scale horizontal transport associated with the convection process. It follows that the integral effect of convection in a chimney is that of an efficient vertical mixing of the superposed water masses.

The statement of Send and Marshall (1995)—that the convection process is statistically homogeneous in the horizontal direction at scales larger than the plume scale—is of great importance for the reminder of our investigation because it ensures the statistical homogeneity of the convection process within a convection chimney, that is, the characteristics of the convection process in the interior of a chimney do not depend on nonlocal quantities like the chimney size or the location within the chimney. This finding allows us to effectively study the convection process by imposing periodic boundary conditions in the horizontal directions as long as the horizontal size of the entire domain is superior to several times the plume scale.

b. Scaling

We did check, by numerical experiments, that the large-scale quantities considered in this publication vary only slightly with the Rayleigh number (the friction parameters) once they are below a limit allowing for three-dimensional turbulent dynamics. This finding

is in agreement with published research from both laboratory and numerical experiments (Boubnov and Golitsyn 1995; Klinger and Marshall 1995), which show either no or only weak dependence of the dynamics on the friction parameters. The two nondimensional parameters evaluating the importance of friction are the flux Rayleigh number $Ra_f = (B_0 H^4)/(\kappa^2 \nu)$ and the Prandtl number $Pr = \nu/\kappa$, which represent friction. Here B_0 is the buoyancy flux, H is the vertical extent (depth) at the convection site, κ is diffusivity, and ν represents viscosity. This weak dependence is in contrast to “classical” Rayleigh–Benard-type convection, where the friction parameters determine the scaling of the heat transport, due to their domination of the boundary layer dynamics. In our experiments heat flux is imposed in a well-mixed surface layer, mimicking the effects of mixed layer turbulence and steering by surface waves. We thus avoid a thin thermal boundary layer at the top. From this mixed layer (negative) buoyancy is transferred into the deeper ocean, and the details of this transport are supposed to not depend on the friction parameters if the Péclet number $Pe = lw_{rms}/\kappa$, based on the mixed layer thickness l , the vertical root-mean-square velocity w_{rms} at the base of the mixed layer, and the diffusivity κ (larger than unity). This inertial character of convection has recently confirmed by numerical simulation (Lohse and Toschi 2003) and laboratory experiments (Gibert et al. 2006).

When the governing Eqs. (1)–(3) and (6) are used (provided below), and if we furthermore suppose that the actual value of dissipation parameters (viscosity and diffusivity) do not affect the large-scale dynamics outside the boundary layers, it follows that the dynamics are governed by the following four parameters: the rotation rate $|f|$, the angle of rotation described by the latitude θ , the buoyancy flux at the surface B_0 , and the ocean depth H . Three of these parameters are combined to form a nondimensional parameter of the natural Rossby number $Ro^* = \sqrt{B_0/(f^3 H^2)}$. We are thus left with only two independent nondimensional parameters, Ro^* and θ .

When rotation has no effect on the dynamics, the velocity scales as $u_{3D} = (B_0 H)^{1/3}$, and when the dynamics are dominated by rotation, the important length scale is given by $H_{rot} = (B_0/f^3)^{1/2}$ and $u_{rot} = (B_0/f)^{1/2} = u_{3D}(Ro^*)^{1/3}$. In laboratory experiments Maxworthy and Narimousa (1994) found that the critical value $Ro^* = 0.078$ separates the two regimes, whereas Klinger and Marshall (1995) found, using numerical experiments, that the transition depends also on the friction parameters. Following the criteria of Klinger and Marshall (1995) the herein-considered values are all within the three-dimensional turbulent regime (a finding that is

confirmed by our results presented in section 4), as are the values of real oceanic deep convection. Below we will thus only consider the case of three-dimensional scaling.

The scaling for reduced gravity $g'_{3D} = B_0/u_{3D} = (B_0^2/H)^{1/3}$ leads to a scaling for temperature anomalies, given by $T'_{3D} = (B_0^2/H)^{1/3}/(g\alpha)$.

The values for the parameters considered in this work are a subset of those observed in actual convection processes in the World Ocean (see section 3a).

3. The model

In section 3a, we start by describing how the above-mentioned scientific results and questions guided our choice of the physical problem adapted to explore the dynamics of tilted convection. In section 3b we then give a detailed explanation of the mathematical model best suited to investigate this physical problem. The numerical implementation employed to solve the mathematical model is described in section 3c.

a. The physical experiment

The aim of this paper is the investigation of the open-ocean deep convection process, which is the violent vertical exchange of water masses when rotation and gravity are not aligned. In the case of an alignment of rotation and gravity, this process is local at the plume scale, with either no or only a negligible effect on larger scales (see the previous section). This important finding allows us to consider a bi-periodic horizontal slice of the ocean, measuring only a few times the plume size in the horizontal directions. The typical plume size with such forcing is several hundreds of meters and descends at a speed of a few tenths of a centimeter per second (see, e.g., Wirth and Barnier 2006). We found in numerical experiments that a domain spanning 8 km in each horizontal direction allows for a sufficient space for a few plumes, spanning a few hundreds of meters in the horizontal direction, to descend independently. The atmospheric forcing varies on horizontal scales of 100–1000 km so that it is adapted to use a homogeneous cooling on the surface. An integration representing a few days of dynamics is necessary to account for the descent of several plumes and to obtain a statistically stationary dynamics. The domain size of 8 km in both horizontal directions is, however, far too small to obtain statistically significant results for even the lowest-order quantities. We thus continued the experiment after a statistically stationary state was obtained for a couple of days and used the (supposed) ergodicity of the dynamics by averaging over space and time to obtain converged statistical estimates.

Furthermore, the model domain spans exactly what we intend to parameterize, that is, the convective dynamics at a single grid point in a high-resolution OGCM [$O(10\text{ km})$]. Such a domain size is clearly too small to investigate the restratification process that follows the convection regime, which can be studied by significantly coarser hydrostatic ocean models (see ChBa).

To obtain information about the scaling behavior, we performed calculations for three different values of cooling (1000, 500, and 250 W m^{-2}) for the case of nontilted (North Pole) and tilted (Gulf of Lions, 45°) convection.

b. The mathematical model

To study the convection process a nonhydrostatic ocean model is essential. The mathematical model of the herein-presented ocean convection experiments are the Boussinesq equations [Eq. (1)] of an incompressible flow [Eq. (2)] in a rotating frame, supplemented by boundary conditions. The flow field is given by \mathbf{u} and the scalar (temperature) field by T . The buoyant scalar is transported by the flow [Eq. (3)] and diffuses at the rate κ :

$$\partial_t \mathbf{u} + \mathbf{u} \cdot \nabla \mathbf{u} + 2\boldsymbol{\Omega} \times \mathbf{u} + \nabla P = \alpha g T \mathbf{e}_\perp + \nu \nabla^2 \mathbf{u}, \quad (1)$$

$$\nabla \cdot \mathbf{u} = 0, \quad (2)$$

$$\partial_t T + \mathbf{u} \cdot \nabla T = \kappa \nabla^2 T + G. \quad (3)$$

The source term G ensures the prescribed heat fluxes through the upper boundary, the equation of state is linear with the expansion coefficient α , and $g = 9.81\text{ m s}^{-2}$ denotes gravity. The ocean surface is modeled by a free-slip rigid-lid boundary condition, while the ocean floor is modeled by a no-slip boundary condition. By using a no-slip boundary condition to model the ocean floor we introduce an additional numerical difficulty because we now have to resolve the thin Ekman layer on this boundary. The role of this Ekman layer is, however, of paramount importance to the convective dynamics because it helps to relax the Taylor–Proudman–Poincaré constraint, which inhibits all vertical motion; we refer the reader to Bush et al. (1992) for a detailed discussion of this point and to Wirth (2004) for a numerical investigation thereof.

Because we are considering only a small slice of the ocean (spanning 8 km in the horizontal directions), we can safely neglect the sphericity of the earth by using Cartesian geometry and we can also neglect the variation of the direction of the rotation vector with the latitudinal direction (θ). This geometry is called the f - F

TABLE 1. Physical parameters common in all experiments.

L_x	L_y	L_z	\mathbf{ff}	α	ρ	c_p
8 km	8 km	3.5 km	$1.45 \times 10^{-4} \text{ s}^{-1}$	$2 \times 10^{-4} \text{ K}^{-1}$	1000 kg m^{-3}	$3900 \text{ J K}^{-1} \text{ kg}^{-1}$

plane, where f and F are twice the normal and horizontal components of $\mathbf{\Omega}$, respectively; that is,

$$\mathbf{f} = \begin{pmatrix} 0 \\ F \\ f \end{pmatrix} = 2\mathbf{\Omega} \begin{pmatrix} 0 \\ \cos\theta \\ \sin\theta \end{pmatrix}. \quad (4)$$

The f - F plane allows for the implementation of periodic boundary conditions in both horizontal directions.

The source term,

$$G = (1 + \sigma\xi) \frac{G_0}{\sqrt{\pi D}} \exp[-(z/D)^2], \quad (5)$$

represents the surface cooling that decreases exponentially with depth on a characteristic scale $D = 90 \text{ m}$, mimicking the violent mixing in the upper ocean at convection sites due to high waves and mixed layer turbulence.

The white-in-time-and-space noise $\xi(\mathbf{x}, t)$, with small-amplitude σ , is added. The amplitude σ is chosen such that with a time step of 30 s the variance of the noise term $\sigma\xi$ equals 10^{-2} ; that is, $\sigma = 0.1 \times (30)^{-1/2}$. In the spatial dimensions the noise is chosen independently at every grid point using a pseudorandom number generator.¹

When the buoyancy density

$$\mathfrak{B} = \alpha g T \quad (6)$$

is used, rather than the temperature T , the constants α and g disappear from the governing equations. The surface forcing is written as a surface buoyancy flux $B_0 = \alpha g / (c_p \rho) \mathcal{H}_0$, where $c_p = 3900 \text{ J (K kg)}^{-1}$ is the heat capacity, $\rho = 1000 \text{ kg m}^{-3}$ is the density of water, and \mathcal{H}_0 denotes the surface heat flux, measured in watts per squared meter. We thus have $B_0 = \mathcal{H}_0 (5.031 \times 10^{-10} \text{ m}^4 \text{ W}^{-1} \text{ s}^{-3})$ and $G_0 = \mathcal{H}_0 / (c_p \rho)$. The values are listed in Tables 1 and 2.

¹ More precisely, $\xi(\mathbf{x}, t)$ is the time derivative of an ensemble of Wiener processes $W_{i,j,k}(t)$ indexed by the grid points (i, j, k) and $\langle [W_{i,j,k}(t)]^2 \rangle = t$. Different pseudorandom number generators of different complexities were used, ranging from a quasi-periodic function to the “Mersenne twister” (Matsumoto and Nishimura 1998); the herein-represented results are found not to depend on the actual generator employed.

The flux Rayleigh number is kept constant in all of the experiments [$\text{Ra}_f = (BH^4)/(\kappa^2\nu) = 6.04 \times 10^8$], the Prandtl number is one, and the natural Rossby numbers Ro^* are 0.0580, 0.0821, and 0.116 in experiments Ex1, Ex3, and Ex4, respectively (where $x = 1$ or 3).

We thus obtain the following numerical values for the scaling variables: $u_{3D} = (B_0 H)^{1/3} = 1.21 \times 10^{-1} \text{ m s}^{-1}$, $g'_{3D} = B_0 / u_{3D} = 4.17 \times 10^{-5} \text{ m}^2 \text{ s}^{-1}$, and $T'_{3D} = g'_{3D} / (g\alpha) = 2.12 \times 10^{-2} \text{ K}$.

c. The numerical implementation

The mathematical model is solved numerically using a pseudospectral scheme entirely based on Fourier expansion. The boundary conditions are implemented using a method inspired by the immersed boundary technique. For a detailed discussion of the model and the new boundary technique we refer the reader to Wirth (2004). Our model will forthwith be called the Harmonic Ocean Model (HAROMOD).

The coherent structures dominating the convective dynamics are known to have comparable horizontal and vertical scales, a fact that has to be reflected in the aspect ratio of the numerical grid. Because it is also important to numerically resolve the nonlinear dynamics of the plumes, a grid size of a few tenths of meters in all three dimensions is required. The need for resolving the bottom Ekman layer motivated the choice of a finer resolution in the vertical direction, and we thus have $\Delta x = \Delta y = 2\Delta z = 31.25 \text{ m}$, which corresponds to $256 \times 256 \times 224$ grid points. The friction coefficients are equal in the horizontal and vertical directions; they are chosen such that the flux Rayleigh number is equal in all experiments. The integration represents the dynamics of ocean convection during 168 h after the onset of cooling. Snapshots are stored every 3 h and data from the last 90 h are used to obtain time-averaged

TABLE 2. Physical parameters varied in the experiments.

Expt	Surface heat flux \mathcal{H}_0	Latitude
E01	1000 W m^{-2}	90°
E03	500 W m^{-2}	90°
E04	250 W m^{-2}	90°
E31	1000 W m^{-2}	45°
E33	500 W m^{-2}	45°
E34	250 W m^{-2}	45°

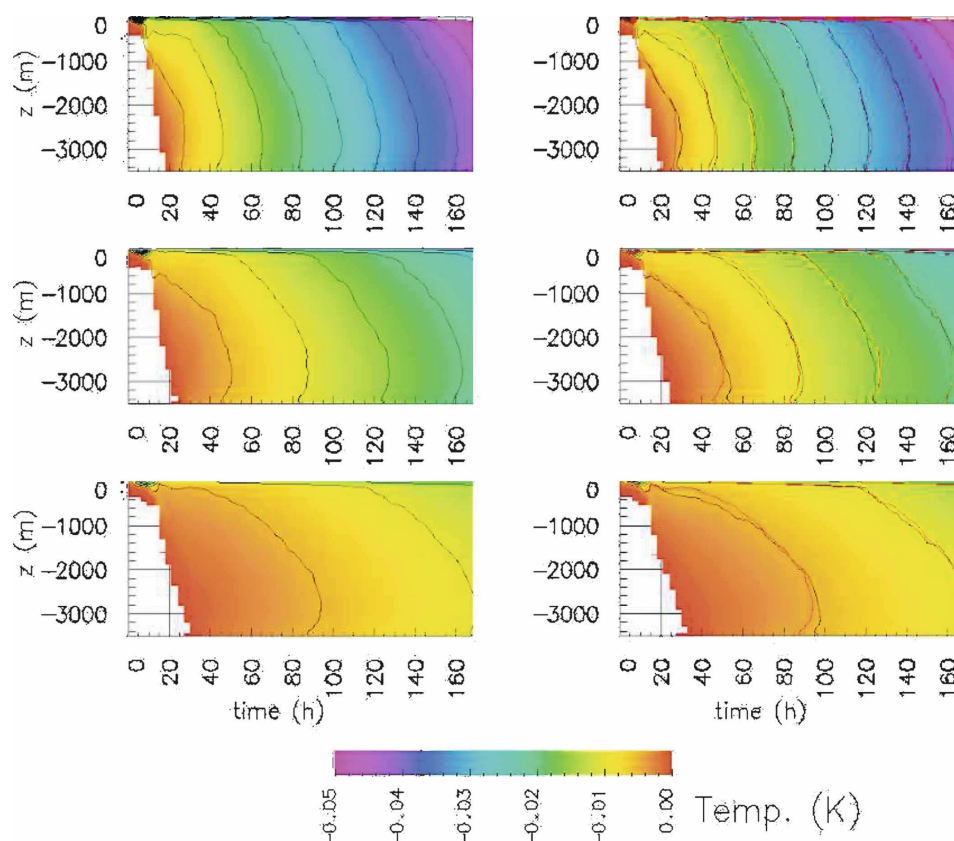


FIG. 1. Horizontally averaged temperature $\langle T \rangle_h$ as a function of depth (vertical scale, m) and time (horizontal scale, h) in the different experiments: (top left) E01, (top right) E31, (middle left) E03, (middle right) E33, (bottom left) E04, (bottom right) E34. Black lines are isotherm lines at every 5×10^{-3} K. The black lines in the left panels are the isolines corresponding to the red lines in the right panels (nontilted experiment).

quantities. We carefully checked that the last 90 h are in a statistically stationary state.²

4. Results

A detailed discussion on the dynamics of a single convective plume is published in Wirth and Barnier (2006), where a special emphasis was put on the influ-

ence of a nonvanishing angle between the directions of gravity and the rotation vector (tilted convection).

Here, we emphasize on the dynamics of the convection process in an ocean that is cooled homogeneously at its surface. The resulting dynamics are those of an ensemble of convective plumes. Because of the nonlinear character of the convection process, the dynamics of the turbulent plume ensembles cannot be derived from the behavior of a single plume. We again have to resort to numerical simulations to determine the basic features of turbulent convection.

The time evolution of the horizontally averaged temperature in all experiments is shown (in Fig. 1). After the onset of cooling, a negative temperature anomaly develops at the surface. In less than 12 h this unstable situation leads to convective motion, and a convective

² Temperature increases during the convection process, so it is not strictly speaking in a statistically stationary state; however, when the total mean temperature is continuously subtracted, which has no dynamical implications when using the Boussinesq approximation and a linear equation of state, such a state is obtained. For brevity we will thus call the entire process statistically stationary, once the convective front has reached the bottom of the domain.

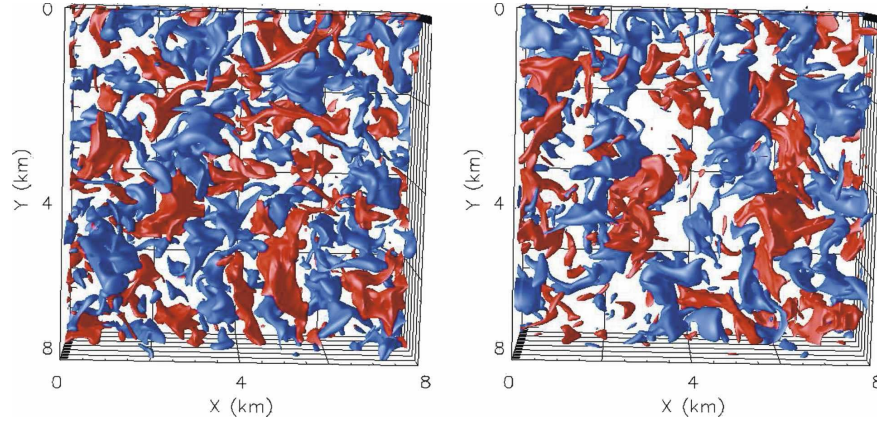


FIG. 2. Isosurfaces of vertical velocity $w = \pm 0.05 \text{ m s}^{-1}$ (+ red, - blue) looking upward from the ocean floor (x to the right, y downward) at the end of the experiments at $t = 168 \text{ h}$: (left) E04 and (right) E34. The elongation of structures in the y direction is conspicuous in experiment E34.

front descends into the unstratified ocean until it reaches the ocean floor after about 18–30 h, depending on the strength of the forcing and rotation.

The subject of this paper is the subsequent statistically stationary stage of convective dynamics in the entire water column. During this stage descending plumes surrounded by rising water mix the water column as can be seen in Fig. 2. A shallow boundary layer develops at the ocean surface. As in the case of a single plume, the influence of the (no slip) bottom slows down the front propagation 500 m (the typical horizontal plume scale) above the bottom, emphasizing once more the importance of the Ekman layer dynamics at the ocean floor. Figure 2 exposes that the differences in the horizontally averaged temperature structure between the tilted and nontilted dynamics are small.

a. The signature of the Taylor–Proudman–Poincaré theorem

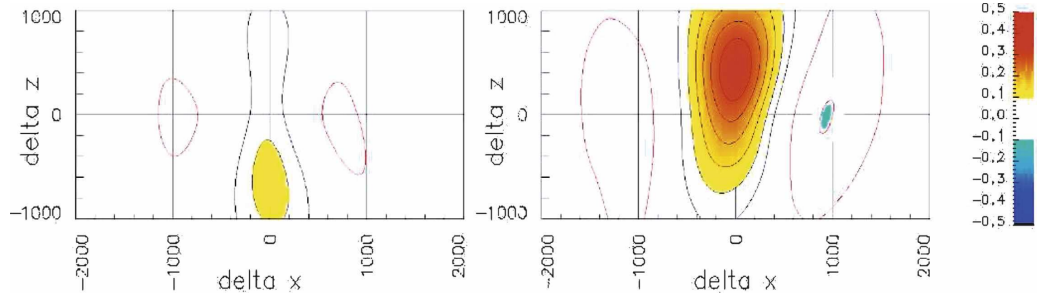
The analysis presented in this section is based on the discussion of the derivation, generality, and consequences of the Taylor–Proudman–Poincaré theorem by Colin de Verdière (2002).

When friction and nonlinearity are negligible the dynamics of a stratified Boussinesq fluid, subject to rotation, is governed by the TPP theorem:

$$2(\Omega_y \partial_y + \Omega_z \partial_z) \begin{pmatrix} u \\ v \\ w \end{pmatrix} = \frac{g}{\rho_0} \begin{pmatrix} \partial_x \rho \\ \partial_y \rho \\ 0 \end{pmatrix}. \quad (7)$$

The TPP theorem states that in the direction of the axis of rotation the velocity component aligned with gravity (w) does not change. While the constraint in the direction of the axis of rotation on the other two components of the velocity vector is influenced by changes in the density structure, the constraint of the TPP theorem on the horizontal components of the velocity vector is in fact the classical thermal wind relation in the case of a vertical rotation vector, and we will call it the generalized thermal wind relation for arbitrary directions of the rotation vector.

There are numerous discussions of the TPP theorem when applied to both large- and mesoscale ocean dynamics, that is, when the Rossby number associated with the dynamics is (very) small. In our case, however, the Rossby number $Ro = w_{rms}/(fL)$ is an order of unity or larger, and the dynamics are clearly in a three-dimensional regime. The TPP theorem nevertheless leaves an imprint in the turbulent dynamics. To investigate this imprint we calculate the correlation of a component of the velocity vector in two parallel planes that are separated in the y direction by a distance Δy . The southward plane, which spans the entire (periodic) domain in the x direction and 1 km in the z direction (from a depth of 2250 to 1250 m), is kept fixed, while the northward plane, which is of equal size, is shifted in the x and z direction by the amount $(\Delta x, \Delta z)$. The correlation between a velocity component in the two planes is then calculated. In mathematical terms (applied to the U component), we calculate the following correlations:

FIG. 3. Correlation $C_y(500 \text{ m}, W)$ for experiments (left) E04 and (right) E34.

$$\tilde{C}_y(\Delta y, U, y_0, t) = \left[\int_P U(x, y_0, z, t) U(x + \Delta x, y_0 + \Delta y, z + \Delta z, t) dx dz \right] / \left[\sqrt{\int_P U^2(x, y_0, z, t) dx dz} \right] \times \sqrt{\int_P U^2(x + \Delta x, y_0 + \Delta y, z + \Delta z, t) dx dz} \quad C_y(\Delta y, U) = \langle \tilde{C}_y(\Delta y, U, y_0, t) \rangle_{y_0, t} \quad (8)$$

where $\langle \cdot \rangle_{y_0, t}$ is an averaging over values y_0 separated by 1 km and 30 consecutive time instances separated by 3 h during the last 90 h of the experiment. The results of this analysis are presented in Figs. 3, 4, and 5. The predictions of Eq. (7) are nicely confirmed as follows: (i) The maximum correlation of the w component is displaced about 500 m and 1 km upward for a y distance Δy of the two planes of 500 m and 1 km, respectively, which demonstrates the high correlation along the axis of rotation; (ii) the same is approximately true for the u component, but the correlations are only about half, due to the decorrelation by the generalized thermal wind.

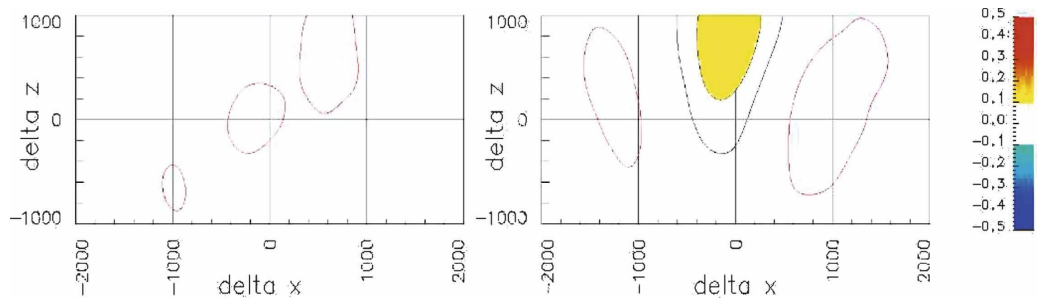
The cases with stronger forcing look qualitatively the same. Quantitative changes are due to the increased horizontal scales in the cases with stronger forcing [ro-

tation is less efficient in stopping the horizontal growth of plume structures; see Wirth and Barnier (2005)].

If we suppose that the convective motion is composed of descending plumes surrounded by upward-moving fluid and an isotropic turbulent component, we can build an analytical model of the convective process, based on the balance of rotation (f and F), turbulent friction (τ), and reduced gravity (g') acting on a convective parcel of fluid moving with the velocity (u, v, w). More precisely,

$$\begin{pmatrix} -\tau & f & -F \\ -f & -\tau & 0 \\ F & 0 & -\tau \end{pmatrix} \begin{pmatrix} u \\ v \\ w \end{pmatrix} = \begin{pmatrix} 0 \\ 0 \\ g' \end{pmatrix}. \quad (9)$$

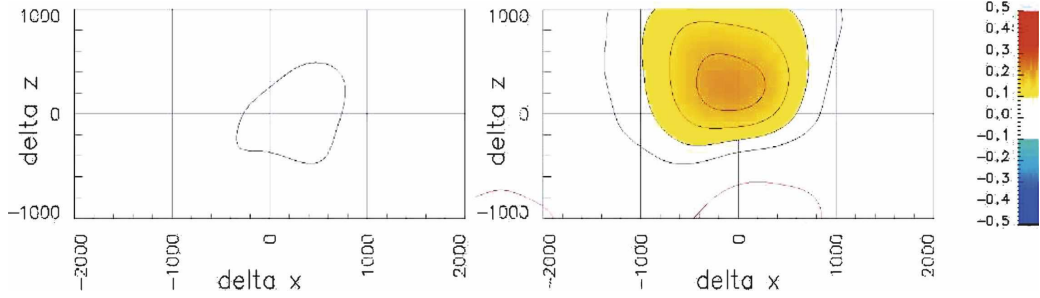
Solving the linear system leads to

FIG. 4. Correlation $C_y(1 \text{ km}, W)$ for experiments (left) E04 and (right) E34.

APRIL 2008

WIRTH AND BARNIER

811

FIG. 5. Correlation $C_y(500 \text{ m}, U)$ for experiments (left) E04 and (right) E34.

$$\begin{pmatrix} u \\ v \\ w \end{pmatrix} = \frac{g'}{f^2 + F^2 + \tau^2} \begin{bmatrix} F \\ -fF/\tau \\ -(\tau^2 + f^2)/\tau \end{bmatrix}, \quad (10)$$

$$= \tilde{c} \begin{pmatrix} \tau F/f^2 \\ F/f \\ -1 - \tau^2/f^2 \end{pmatrix}, \quad (11)$$

where $\tilde{c} = g' f^2 / [(f^2 + F^2 + \tau^2)\tau]$ is the unperturbed vertical plume speed and τ is the inverse friction time. We thus see that when friction is negligible (and \tilde{c} is finite) then the velocity vector is directed downward along the axis of rotation. By increasing the friction (while keeping \tilde{c} constant), we see that the rotation vector starts to tilt in the eastward (to first order in τ/f) and downward (to second order in τ/f) directions. A slight eastward tilt can be seen in Figs. 3, 4, and 5 because the correlation patterns are slightly shifted to the left. The shifts show that $\tau/f = O(10^{-1})$, but precise values cannot be obtained from our data. A downward shift is hard to detect because (i) it is only second order and (ii) it is countered by the correlation of isotropic turbulence (cf. to left part of Fig. 3). The higher correlations in the left panel of Fig. 3 for downward shifts are due to the increase of characteristic length scale with depth (see Fig. 9). The southward and eastward deviations have been observed and explained for the case of a single convective plume by Sheremet (2004) and Wirth and Barnier (2006).

b. Mean values

In this section we focus on the values of horizontal averages, because the problem is statistically homogeneous in both horizontal directions. The averages over a complete horizontal (periodic $8 \text{ km} \times 8 \text{ km}$) slice of the ocean are denoted by $\langle \cdot \rangle_h$. The typical size of a descending plume in the herein-presented experiments

is of the order of 1 km; horizontal averages are as such only averages over a few plumes and the significance of the statistics is limited. To decrease the statistical uncertainty of the averages we also used time averaging, by averaging over the last 30 snapshots of the integration separated by 3 h, that is, the last 90 h of the experiments. We carefully checked that the quantities considered have reached a statistically stationary state before the beginning of the sampling process. These averages are denoted by $\langle \cdot \rangle_{h,t}$, and their spatiotemporal evolution is what a perfect parameterization of the convective process should reproduce in an OGCM.

1) TEMPERATURE

The most important variable to consider is either the temperature or buoyancy density [both are linearly related, see Eq. (6)]. These quantities do not reach a statistically stationary state because their mean value varies linearly in time. The dynamics are, however, independent of the mean value (linear equation of state), and the derivatives of temperature reach a statistically stationary state. In Fig. 1 the temporal evolution of the horizontally averaged temperature $\langle T \rangle_h$ is presented. The qualitative behavior is an initial downward-propagating front of cold water. Above the front the average temperature is almost constant, except for a boundary layer at the surface. When the front has reached the ocean floor, the horizontally averaged temperature at every depth increases linearly in time at the same rate, leading to a stationary (inverse) stratification. The results shown in Fig. 6 indicate that stratification depends on the strength of forcing but not on the direction of the rotation vector.

Figure 6, as well as the isotherm lines in Fig. 1, shows clearly that the temperature gradient is not constant. The vertical temperature gradient can be well approximated by a linear behavior away from the top and bottom boundary (see Fig. 6). With a dependence

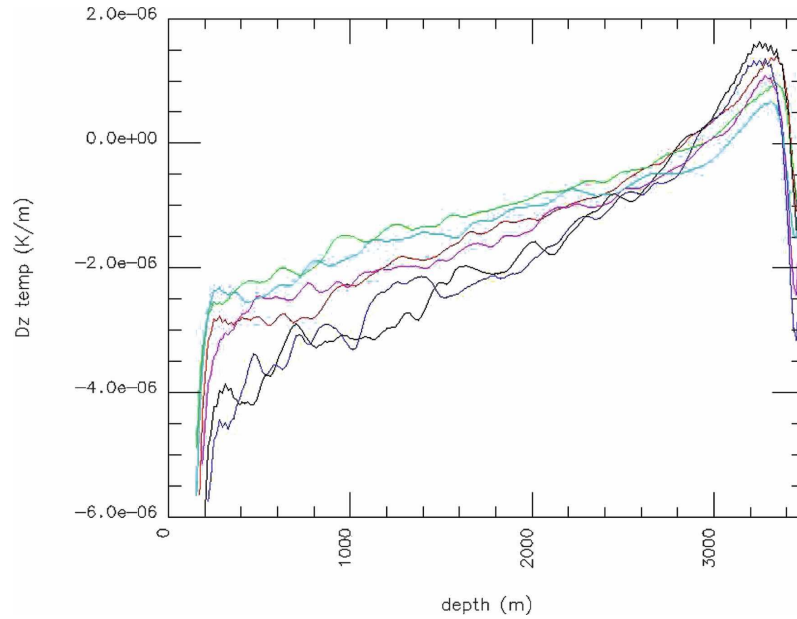


FIG. 6. Horizontally and temporally averaged temperature gradient $\langle \partial_z T \rangle_{h,t}$ (see Table 2 for experiments).

on the surface buoyancy flux (B_0), which is consistent with dimensional analysis, the second derivative of the mean temperature with respect to the vertical is thus constant, $\langle \partial_{zz} T \rangle_{h,t} = \tau \times B^{2/3} H^{-7/3} / (\alpha g)$, where we estimated the dimensionless constant $\tau = 10$.

In all of the results on temperature and its vertical gradients no significant difference between the non-tilted and tilted case could be detected, except for the differences in the bottom Ekman layer. Also of great importance is the observation that in the lower 500 m the temperature gradient is positive, which means that there is a countergradient flux of heat. This behavior is often named “nonlocal transport,” and it is caused by the buoyancy transport of the convective plumes that extend from the surface to the bottom of the domain. Fitting an affine law to the gradient of the depth-averaged temperature allows the buoyancy flux to be written as

$$\kappa_Z (\alpha g \partial_z T - \gamma) = -\frac{B_0 z}{H}, \quad (12)$$

where γ denotes the nonlocal part of the flux. Equation (12) is taken from the KPP parameterization (see Large et al. 1994), and the term on the right-hand side is a consequence of the stationarity of the dynamics. Dimensional analysis suggests $\kappa_Z = \kappa_0 (B_0 H^4)^{1/3}$, where

the dimensionless constant $\kappa_0 = \tau^{-1} = 0.1$ best fits our data, leading to $\kappa_Z = 40 \text{ m}^2 \text{ s}^{-1}$ for experiments E01 and E31, and a heat flux of only 250 W m^{-2} leads to an eddy diffusivity of about $\kappa_Z = 5 \text{ m}^2 \text{ s}^{-1}$ for a convection depth of 1 km. In OGCM calculations a constant eddy diffusivity of $\kappa_Z = 10 \text{ m}^2 \text{ s}^{-1}$, independent of depth and buoyancy forcing is often employed, which lies in between the values obtained here.

If we deduce from Fig. 6 that the temperature gradient is zero at about 500 m from the ground, we can obtain a nonlocal (countergradient) heat flux of about 1/7th of the heat flux at the surface. Dimensional analysis gives $\gamma = \gamma_0 (B_0 / H^2)^{2/3}$, with $\gamma_0 = 1/7$.

We would like to emphasize that the total vertical heat flux is always positive (negative temperature perturbations being transported downward), and decreases linearly from the maximum value at the surface to zero at the floor. In our calculations we cannot have an upward heat flux, which is often observed when convection into a stratified medium is considered, because in our experiment the lower boundary is the completely insulating ocean floor.

2) VELOCITY

Due to the top and bottom boundaries and the incompressibility of a Boussinesq fluid, the horizontally

averaged vertical velocity vanishes at every depth. No such constraint applies to the horizontal velocity components. For the case of an alignment of the rotation vector and gravity, the average horizontal velocity vanishes at every depth because the problem is invariant to rotations around the vertical axis. This is not the case for tilted convection. Indeed, Hathaway and Somerville (1983) noted that the tilted rotation vector can induce mean flows by producing correlations between the vertical and horizontal velocity components. The numerical calculations of Hathaway and Somerville (1983) are at very small Rayleigh and Taylor numbers and are not in a turbulent regime. They studied the influence of tilted rotation on the dynamics of convective rolls, and noted that when the Taylor number is increased, the averaged velocities and the correlations between the vertical and horizontal velocity components decrease. No quantitative estimate for the magnitude of the horizontal velocity in the case of oceanic tilted convection is thus possible from their calculations. Our calculations are at much higher Rayleigh and Taylor numbers and are tuned to investigate oceanic convection.

The equation for the horizontally averaged velocity is given by

$$\partial_t \langle u \rangle_h = -\partial_z \langle uw \rangle_h + f \langle v \rangle_h + \nu \partial_z^2 \langle u \rangle_h, \quad (13)$$

$$\partial_t \langle v \rangle_h = -\partial_z \langle vw \rangle_h + f \langle u \rangle_h + \nu \partial_z^2 \langle v \rangle_h. \quad (14)$$

These equations also reflect the fact that a vanishing total momentum (depth-averaged $\langle u \rangle_h$ and $\langle v \rangle_h$) is conserved at all times because the vertical integral of $\partial_z \langle uw \rangle_h$ and $\partial_z \langle vw \rangle_h$ vanish due to the vanishing vertical velocity at the top and bottom boundaries. If we suppose that the velocity variables are statistically stationary, the time derivative vanishes when time averages, denoted by $\langle \cdot \rangle_{h,t}$, are taken. If we further neglect the direct effects of viscosity in Eqs. (13) and (14), we obtain

$$f \langle v \rangle_{h,t} = \partial_z \langle uw \rangle_{h,t}, \quad (15)$$

$$f \langle u \rangle_{h,t} = -\partial_z \langle vw \rangle_{h,t}. \quad (16)$$

Because upward-moving fluid parcels are deflected north and westward and downward-moving fluid parcels are deflected south and eastward by rotation (conservation of angular momentum with a tilted rotation vector), this leads to a negative correlation of $\langle uw \rangle_{h,t}$ (see Fig. 7c) and a positive correlation of $\langle vw \rangle_{h,t}$ (see Fig. 7d). The vertical velocity component (w) vanishes at the lower and upper boundary, while the horizontal velocity components (u, v) vanish only on the lower (no

slip) boundary and have a local extreme at the upper boundary (vanishing first derivative). This leads to a positive velocity to a northeastward mean velocity in the upper kilometer of the ocean and an opposite velocity in the deeper part. In Fig. 8 it can be appreciated that Eqs. (15) and (16) are almost perfectly verified for an averaging over horizontal slices of the entire domain at 30 consecutive instances of time, separated by 3 h. Small differences are visible near the upper and lower boundaries. The neglected friction plays a nonnegligible role for the differences at the lower boundary. Other differences are caused by the incomplete elimination of the terms containing a time derivative due to a too short averaging period.

For experiment E31 the mean meridional velocity averaged over the upper 1 km of the ocean is about $8 \times 10^{-3} \text{ m s}^{-1}$, with the zonal velocity being much smaller (see Figs. 7a,b).

We would like to remark that the existence of a non-vanishing horizontal mean velocity does not contradict the assumption of locality of the convection process and the usage of bi-periodic geometry. The above clearly shows that the horizontal mean velocity is generated by a local balance between Coriolis force and turbulent Reynolds stress.

c. Second-order moments

In the previous subsection we clearly saw the importance of second-order moments as they are responsible for the generation of a mean horizontal velocity. It is the very nature of the turbulent closure problem that n th-order correlations are governed by $(n+1)$ th-order correlations.

We first reconsider the question of the right scaling for $w_{\text{rms}} = \langle w^2 \rangle_{h,t}$, and we see in Fig. 9a that $u_{\text{scal}} \sim B^{-3/8}$ is almost perfectly verified. This coefficient is close to, but significantly higher than, $1/3$ of the three-dimensional scaling. This might be the remnant of a $1/2$ scaling of the rotationally dominated case. [The flux Rayleigh number (Ra_f) is constant in all of the experiments.] With an increasing Rayleigh number the dynamics further converge toward the three-dimensional regime. It is thus reasonable to suppose that in the real ocean, where the Rayleigh number is many orders of magnitude higher, the dynamics are in the 3D regime, justifying our approach to using nonrotational scaling as the basis of our calculations.

When considering second-order moments of velocity components we see in Fig. 9b that the vertical component shows no considerable dependence on the latitude θ . The values in the experiments with a tilted rotation vector are mostly a little smaller than the nontilted

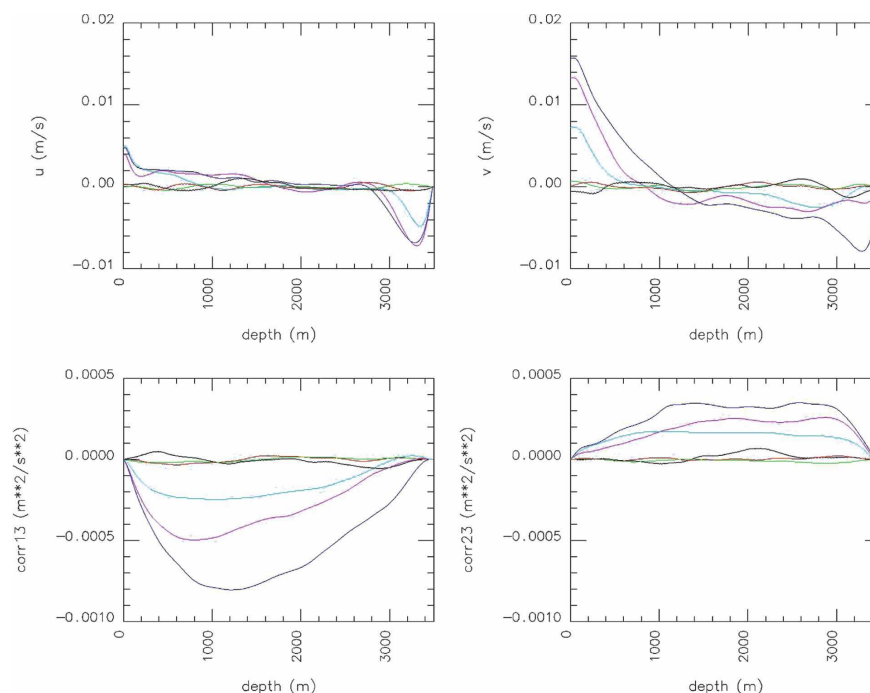


FIG. 7. Mean velocities (top left) $\langle u \rangle_{h,t}$ and (top right) $\langle v \rangle_{h,t}$, and correlations (bottom left) $\langle uw \rangle_{h,t}$ and (bottom right) $\langle vw \rangle_{h,t}$ (see Table 2 for experiments).

cases, but the difference never exceeds 5%. The situation is different for the horizontal components shown in Fig. 10. The values $u_{\text{rms}} = \langle u^2 \rangle_{h,t}$ and $v_{\text{rms}} = \langle v^2 \rangle_{h,t}$ are typically 20%–25% higher outside the top and bottom boundary layers.

The correlation $\langle wT \rangle_{h,t}$ is responsible for the downward heat transport; the stationarity of the dynamics

thus forces it to be a linear function of the distance above the ocean floor, with a gradient imposed by the surface heat flux divided by the total depth. There is thus no possible dependence on rotation, direction, and magnitude.

The correlation $\langle T'T' \rangle_{h,t}$ (not shown), where T' is the local temperature deviation from the horizontal mean,

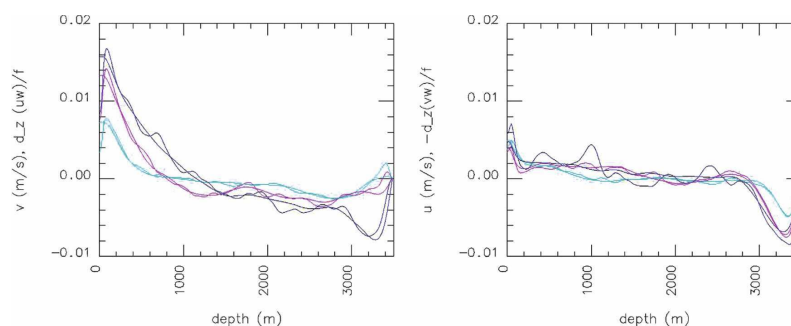


FIG. 8. Left- and right-hand sides of (left) Eq. (15) and (right) Eq. (16). The more wavy curves are the right-hand sides of the equations (see Table 2 for experiments).

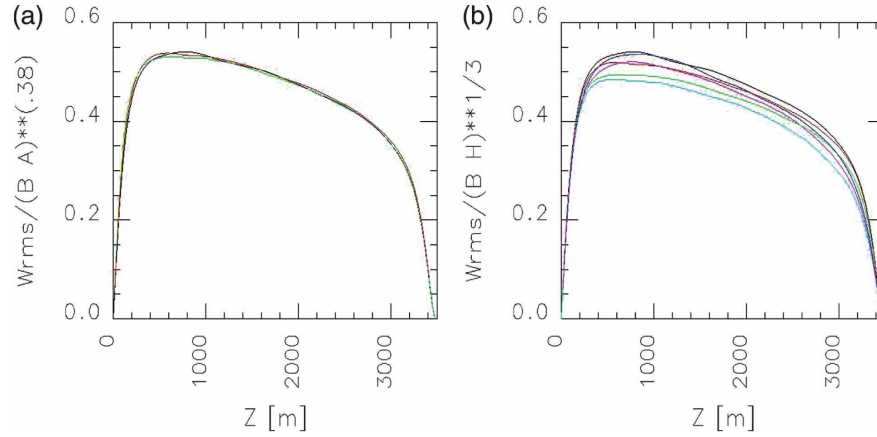


FIG. 9. The w_{rms} for (a) the nontilted experiments normalized by $B^{0.38}$, and (b) all of the experiments normalized by u_{3D} .

shows no significant dependence on the direction of the rotation axis.

5. Discussion

We have investigated the problem of tilted convection in an isothermal ocean. Although the dynamics are found to be in a regime where rotation plays no dominant role when the scaling of the dynamical variables are considered, the direction of the rotation vector leads to some important changes in the large-scale dynamics. We demonstrated that the following qualitative and quantitative changes occur when the traditional approximation is relaxed: (i) turbulent structures are aligned along the axis of rotation as predicted by the Taylor–Proudman–Poincaré theorem, (ii) the horizon-

tal component of the rotation vector enhances horizontal mixing, (iii) a horizontal mean circulation is established, and (iv) the inverse stratification, together with the horizontal mean circulation, leads to a equatorward heat transport as the coldest water at the surface moves northward.

These changes have important consequences in all instances where vertical transport of passive or active tracers is considered. The horizontal transport induced by a heat flux of 10^3 W m^{-2} at a latitude of $\theta = 45^\circ$ is equal to an Ekman transport induced by a wind field of $U_{10} = 75 \text{ km h}^{-1}$. The Ekman transport is confined to the upper tens of meters, whereas the horizontal transport induced by tilted convection spreads over the upper kilometer. The vertical extent is, however, not very important when vertical velocities due to divergences of

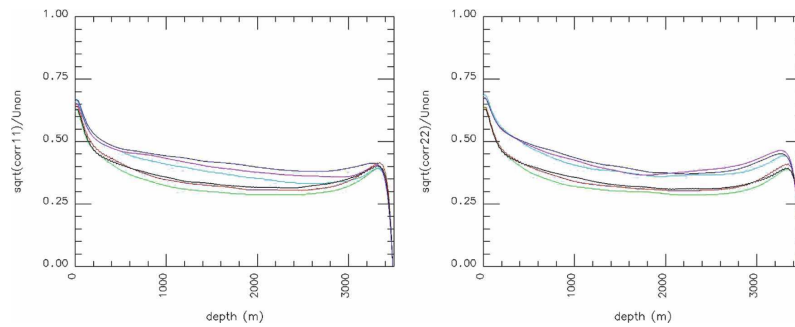


FIG. 10. The (left) u_{rms} and (right) v_{rms} for all of the experiments normalized by u_{3D} (see Table 2 for experiments).

the horizontal velocity field are considered. The similarity to the wind stress forcing that leads to horizontal divergence, Ekman pumping, and a large-scale circulation by Sverdrup balance can be taken further. Gradients in the heat flux at the ocean surface will lead to horizontal divergence, leading to vertical velocities and a large-scale circulation by Sverdrup balance, which is an effect that is completely neglected when the traditional approximation is employed.

Furthermore, the vertical shear induced by a tilted rotation vector will lead to tilted convective chimneys. This tilt in the chimney structure is likely to play an important role in the subsequent restratification of the convective area.

In the present paper we determined the influence of the horizontal component of the rotation vector on the convective dynamics. This influence should be reflected in parameterization schemes of the convective dynamics. The important, but somehow more controversial, discussion of the effect of the herein-presented results on existing parameterization schemes of the convection process and a construction of an improved parameterization scheme will be the subject of a forthcoming publication. The importance of the herein-presented effect on the ocean global circulation and, more precisely, on the thermohaline circulation can only be evaluated by implementing such improved parameterization in an ocean global circulation model (OGCM).

Acknowledgments. We are grateful to Theo Gerkema, Yves Morel, Chantal Staquet, Joel Sommeria, and two anonymous reviewers for their remarks, and to Pagode du Baron for discussion. The work was funded by EPSHOM-UJF 00.87.070.00.470.29.25 and EPSHOM-UJFCA2003/01/CMO. Calculations were performed at IDRIS (France) within Project 62037. This work is part of the COUGAR Project funded by ANR-06-JCJC-0031-01.

REFERENCES

- Boubnov, B. M., and G. S. Golitsyn, 1995: *Convection of Rotating Fluids*. Kluwer Academic, 224 pp.
- Bush, J. W. M., H. A. Stone, and J. Bloxham, 1992: The motion of an inviscid drop in a bounded rotating fluid. *Phys. Fluids*, **4A**, 1142–1147.
- Chanut, J., B. Barnier, W. Large, L. Debreu, T. Penduff, and J.-M. Molines, 2008: Mesoscale eddies in the Labrador Sea and their contribution to convection and restratification. *J. Phys. Oceanogr.*, in press.
- Colin de Verdière, A., 2002: Un fluide lent entre deux sphères en rotation rapide: Les théories de la circulation océanique. *Ann. Math. Blaise Pascal*, **9**, 245–268.
- Gibert, M., H. Pabiou, F. Chillà, and B. Castaing, 2006: High-Rayleigh-number convection in a vertical channel. *Phys. Rev. Lett.*, **96**, doi:10.1103/PhysRevLett.96.084501.
- Hathaway, D. H., and R. C. J. Somerville, 1983: Three-dimensional simulations of convection in layers with tilted rotation vectors. *J. Fluid Mech.*, **126**, 75–89.
- Klinger, B. A., and J. Marshall, 1995: Regimes and scaling laws for rotating deep convection in the ocean. *Dyn. Atmos. Oceans*, **21**, 227–256.
- Large, W. G., J. C. McWilliams, and S. C. Doney, 1994: Oceanic vertical mixing: A review and a model with a nonlocal boundary layer parametrization. *Rev. Geophys.*, **32**, 363–403.
- Lohse, D., and F. Toschi, 2003: Ultimate state of thermal convection. *Phys. Rev. Lett.*, **90**, doi:10.1103/PhysRevLett.90.034502.
- Marshall, J., and F. Schott, 1999: Open-ocean convection: Observations, theory, and models. *Rev. Geophys.*, **37**, 1–64.
- , C. Hill, L. Perelman, and A. Adcroft, 1997: Hydrostatic, quasihydrostatic, and nonhydrostatic ocean modeling. *J. Geophys. Res.*, **102**, 5733–5752.
- Matsumoto, M., and T. Nishimura, 1998: Mersenne twister: A 623-dimensionally equidistributed uniform pseudorandom number generator. *ACM Trans. Model. Comput. Simul.*, **8**, 3–30.
- Maxworthy, T., and S. Narimousa, 1994: Unsteady, turbulent convection into a homogeneous, rotating fluid, with oceanographic applications. *J. Phys. Oceanogr.*, **24**, 865–887.
- Send, U., and J. Marshall, 1995: Integral effects of deep convection. *J. Phys. Oceanogr.*, **25**, 855–872.
- Sheremet, V. A., 2004: Laboratory experiments with tilted convective plumes on a centrifuge: A finite angle between the buoyancy force and the axis of rotation. *J. Fluid Mech.*, **506**, 217–244.
- Straneo, F., 2006: Heat and freshwater transport through the central Labrador Sea. *J. Phys. Oceanogr.*, **36**, 606–628.
- Wang, D., 2006: Effects of the earth's rotation on convection: Turbulent statistics, scaling laws and Lagrangian diffusion. *Dyn. Atmos. Oceans*, **41**, 103–120.
- Wirth, A., 2004: A non-hydrostatic flat-bottom ocean model entirely based on Fourier expansion. *Ocean Modell.*, **9**, 71–87.
- , and B. Barnier, 2006: Tilted convective plumes in numerical experiments. *Ocean Modell.*, **12**, 101–111.

4.6 Estimation of friction parameters and laws in 1.5D shallow-water gravity currents on the f-plane by data assimilation

Estimation of friction parameters and laws in 1.5D shallow-water gravity currents on the f-plane, by data assimilation

Achim Wirth · Jacques Verron

Received: 11 June 2008 / Accepted: 15 September 2008
 © Springer-Verlag 2008

Abstract A 1.5-dimensional, 1.5-layer shallow water model and an ensemble Kalman filter are used to evaluate the feasibility of estimating friction parameters and determining friction laws of oceanic gravity currents. The two friction laws implemented are a linear Rayleigh friction and a quadratic drag law. We demonstrate that the assimilation procedure rapidly estimates the total frictional force, whereas the distinction between the two laws is evolving on a slower time scale. We also demonstrate that parameter estimation can, in this way, choose between different parametrisations and help to discriminate between physical laws of nature by estimating the coefficients presented in such parametrisations.

Keywords Ocean dynamics · Gravity current · Friction laws · Parameter estimation · Data assimilation

1 Introduction

Buoyancy forces caused by density differences of fluids are a major source of fluid motion in nature. When these forces act adjacent to topography, gravity cur-

rents are created. The major part of the deep and intermediate waters of the world ocean and marginal seas have done at least part of their voyage to the deep in the form of a gravity current. Oceanic gravity currents play a role of paramount importance in the formation of the water masses of the deep ocean and are thus key to understanding the oceanic component in the earth climate system. For the major part of oceanic gravity currents, the earth's rotation plays an important role, as they evolve on a timescale much larger than the rotation period of the planet earth. The dominant force balance is, thus, between gravity and the Coriolis force, that is geostrophic. Indeed, when the turbulent fluxes of water masses and momentum are neglected, such gravity currents flow along the inclined ocean floor, changing neither depth nor composition. Turbulent fluxes of tracers, that is mixing, entrainment and/or detrainment, determine the change of the water mass. Together with the turbulent fluxes of momentum at the floor and interface of the gravity current, they determine the change in position of the gravity current. The answer to the question of the evolution of a gravity current lies, thus, in the determination of the laws and parameters of its turbulent fluxes.

The inter-comparison study of several ocean general circulation models (OGCMs) (DYNAMO Group 1997; Willebrand et al. 2001) clearly determined the high sensitivity of the meridional heat transport (in the North Atlantic) to the representation of the (Denmark Strait and Faroe Bank Channel) overflows. The meridional heat transport is very sensitive to small-scale details and turbulence in the overflow regions not explicitly resolved in OGCMs and the numerical representation (the grid) of the overflow regions in the OGCMs. Dedicated research on these sub-grid-scale processes is key

Responsible Editor: Tal Ezer

A. Wirth (✉) · J. Verron
 LEGI / MEOM, CNRS, BP 53,
 38041 Grenoble Cedex 9, France
 e-mail: achim.wirth@hmg.inpg.fr

J. Verron
 e-mail: jacques.verron@hmg.inpg.fr

to improving the representation of the global ocean climate variability.

For an introduction to the dynamics of oceanic gravity currents, we refer the reader to Griffiths (1986). A large number of experimental studies of gravity currents on an inclined plane have contributed to our understanding of their dynamics (see, e.g. Whitehead et al. 1990; Sutherland et al. 2004). Most of these studies focus on the large-scale instability and eddy formation in such flows.

The understanding of the dynamics of gravity current has profited largely from the study of simplified stream-tube models. In stream-tube models, only average (bulk) values of the dynamical variables are considered at every cross section along the path of the gravity current (see Smith 1975, 1977; Killworth 1977, 2001; Price and Baringer 1994; Baringer and Price 1997). Due to their linear nature, the integrated buoyancy and Coriolis force can be calculated. The nonlinear frictional forces and the turbulent fluxes, perturbing the geostrophic equilibrium, have to be parametrised. The evolution of the gravity current can then be studied as a function of the parametrisations and parameter values employed. Integrations of these semi-analytical stream-tube models along a path of varying topographic slope were performed, and the parameter values are adjusted in such a way that the pathway and water mass characteristics compare favourably to observations. In this way, stream-tube models have contributed substantially to understanding the physics of oceanic gravity currents. This adjustment procedure, however, does not always lead to a deeper understanding of the physical processes involved (see Emms 1998). The implementation of stream-tube models or their physics in today's large-scale OGCMs is difficult. Although progress has been made in better representing gravity currents in large-scale OGCMs through bottom boundary layers (see e.g. Killworth and Edwards 1999), their dynamics is still a weak point of today's numerical models of the ocean circulation.

We focus here on the small-scale turbulent fluxes in gravity currents. A variety of parametrisations of the turbulent fluxes are proposed in the literature, but there is no agreement on which parametrisation should be favoured, not even to speak about the numerical values of the parameters present in such parametrisation. Pioneering work to systematically test various of such parametrisations and determine parameter values has recently been performed (see, e.g. Xu et al. 2006 for the non-rotating case and Ezer 2005 and Legg et al. 2006 for a case with rotation).

We expose here the first step of a pragmatic approach to obtaining the laws and parameter values of

turbulent fluxes using data assimilation. More precisely, it is not clear if the effect of bottom and interfacial friction in a gravity current is more likely to follow a linear Rayleigh friction law or a quadratic turbulent drag law (Chézy law); and what are the values of the corresponding friction coefficients? This is a question that has been considered, e.g. for the ocean by Moonn and Tang (1984) and for the case of the atmospheric boundary layer over the ocean by Stevensen et al. (2002), without using data assimilation. Both laws, the linear and quadratic, are implemented in all major ocean models. We therefore implement the two commonly used parametrisations of the same physical process, bottom and interfacial friction, in a numerical model that does not explicitly resolve this process, and we estimate the parameters in the parametrisations by assimilating data into the model. The data assimilation experiment will then not only tell us the optimal parameter values but also allows for an evaluation of the parametrisations by providing the error bars and/or the spread of the ensemble (when an ensemble method is considered). Even more striking, by allowing different parametrisation laws, the data assimilation experiment will actually tell us which law is the most appropriate in parametrising turbulent fluxes. The data are provided by either observations of oceanic gravity currents, laboratory experiments or numerical data from a model that explicitly resolves the process to be parametrised. However, in the present work, we perform identical twin experiments, where the “data” are provided by the same model as used for the parameter estimation experiments, to study the feasibility and the problems connected to estimating parameters of parametrisations describing the same physical process. For an introduction into parameter estimation, we refer the reader to Evensen et al. (1998).

In the next section, we give a detailed description of the physical problem and consider its mathematical formulation and numerical implementation. In Section 3, we discuss the assimilation method, that is, the ensemble Kalman filter (EnKF), and its numerical implementation. The twin experiments and results are presented in Sections 4 and 5. Discussion, physical interpretation of the results and perspectives are given in Section 6.

2 Idealised oceanic gravity current on the f-plane

2.1 The physical problem considered

In the experiments presented here, we use an idealised geometry, considering an infinite gravity current on an inclined plane with constant slope, and we do not allow for variations in the long-stream direction. We thus

neglect the long-stream variation of the gravity current and consider only the dynamics of a vertical slice. Please note that such simplified geometry inhibits large-scale instability and the formation of the large cyclones and other large-scale features, which is beneficial to our goal of studying the friction laws due to only small-scale dynamics.

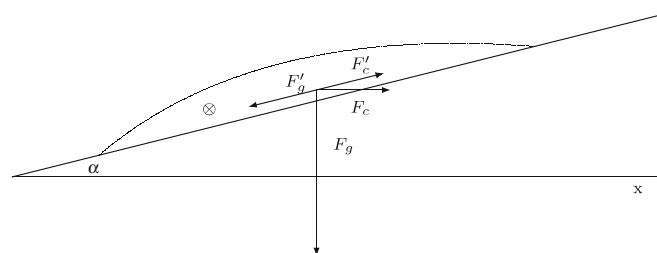
The gravity current transfers potential energy to kinetic energy, by sliding down the incline, and loses energy by friction (dissipation). The down-slope movement is, thus, “indirectly” determined by friction. This is exactly what happens to a gravity current in nature, and it is this dynamic that we like to entangle here. The difference is, of course, that our gravity current descends in time and not in space, as in the ocean. This setup is also used in laboratory experiments and other numerical simulations (see, e.g. Shapiro and Hill 1997 and Sutherland et al. 2004).

The gravity currents considered here are on an inclined plane of slope of one degree; the initial profile of its vertical extension above the inclined ocean floor $z = h(x) = \max(H - x^2/\lambda, 0)$ has a parabolic shape with $H = 200$ m and $\lambda = 5 \cdot 10^5$ m, leading to a gravity current that is 200 m high and 20 km large. The values used in the experiment are typical for oceanic gravity currents (see, e.g. Price and Baringer 1994). If the gravity current is initially geostrophically adjusted, the velocity components are given by:

$$v_G = g'/f(\partial_x h + \tan \alpha); \quad u_G = 0. \quad (1)$$

This geostrophic velocity is due to the balance between the Coriolis force and the buoyancy force in the direction parallel to the slope, as shown in Fig. 1. The Coriolis parameter is $f = 1.0313 \cdot 10^{-4} \text{ s}^{-1}$, corresponding to the Earth's rotation at mid-latitude. The reduced gravity $g' = g(\rho_{gc} - \rho_0)/\rho_0 = 9.8065 \cdot 10^{-4}$, where $g = 9.80665 \text{ m s}^{-2}$, ρ_{gc} the density of the gravity current and ρ_0 the density of the surrounding fluid corresponding to a temperature difference of 0.5K between the gravity current and the surrounding water with a linear expansion coefficient $\alpha = 2 \cdot 10^{-4} \text{ K}^{-1}$.

Fig. 1 Cross section of gravity current. The figure gives the force balance between the projection of the Coriolis force and the projection of the buoyancy force onto the topographic slope for a gravity current on a inclined plane when dissipative processes are neglected



These values lead to an average geostrophic speed of $\bar{v} = 1.66 \cdot 10^{-1} \text{ m s}^{-1}$.

2.2 The mathematical model

The mathematical model for the gravity current dynamics is a 1.5-dimensional, reduced-gravity, shallow-water model on an inclined plane. The shallow-water model first proposed by de Saint Venant (1871) and its various versions adapted for specific applications is one of the most widely used models in environmental and industrial fluid dynamics. For the derivation of the reduced gravity shallow-water equations in a geophysical context, we refer the reader to the text book by Gill (1982) and references therein.

As stated in the introduction, we here specialise to a gravity current with no variation in the y-direction, the horizontal direction perpendicular to the down-slope direction. That is, we have three scalar fields $u(x, t)$, $v(x, t)$ and $h(x, t)$ as a function of the two scalars x and t . In this case, the shallow-water equations on an inclined plane are given by:

$$\partial_t u + u \partial_x u - f v + g'(\partial_x h + \tan \alpha) = -D u + \nu \partial_x^2 u, \quad (2)$$

$$\partial_t v + u \partial_x v + f u = -D v + \nu \partial_x^2 v, \quad (3)$$

$$\partial_t h + u \partial_x h + h \partial_x u = \nu \partial_x^2 h. \quad (4)$$

The left-hand-side terms include the reduced gravity $g' = g \Delta \rho / \rho$, the slope α and the Coriolis parameter f . On the right-hand side, we have the terms involving dissipative processes. The parametrised vertical dissipative effects are represented in the first term involving

$$D = D(x, t) = (\tau + c_D \sqrt{u^2 + v^2})/h. \quad (5)$$

There is a linear friction constant τ parametrising dissipative effects that can be represented by vertical Rayleigh friction and a quadratic friction drag, the term with the drag constant c_D . The term involving the viscosity/diffusivity ν represents horizontal dissipative processes; its value is chosen to provide numerical stability of the calculations (see Subsection 2.3). Clearly,

the geostrophic speed (Eq. 1) is a solution of Eqs. 2–4 when $D(x, t) = 0$ and $v = 0$. The estimation of D or, more precisely, of the parameters τ and c_D is the subject of the present work. By using data assimilation, we plan to obtain the friction constants τ and c_D and, thus, determine if the friction is dominated by a linear or a quadratic law.

The parameters of the two most observed and employed friction laws, Rayleigh friction and the drag law, are estimated here. The methodology is not restricted to these two laws; these linear and quadratic laws can also be seen, pragmatically, as the beginning of a Taylor series.

The domain spans 100 km in the x -direction and the calculations performed represent 7 days of dynamics of the gravity current. The time of integration is limited due to the descending gravity current leaving the domain of integration when sliding down the slope.

This model can be seen as being more involved than stream-tube models (see Smith 1975, 1977; Killworth 1977, 2001; Price and Baringer 1994; Baringer and Price 1997) which do not include variations in the cross-stream direction but are less complex than primitive equations or non-hydrostatic models of the ocean dynamics. This model is also more complex than the one used by Shapiro and Hill (1997), who did not use an evolution equation for the velocity, assuming that it is slaved to the layer thickness.

2.3 Numerical implementation of dynamical model

The shallow-water model is implemented with a first-order, finite-difference scheme in space and time; the simplicity of the model is chosen to facilitate the implementation of various assimilation schemes and their comparison in future work. There are 500 points in the x -direction, leading to a resolution of 200 m; the time step is 5 s. The value of the horizontal viscosity/diffusivity is a function of the resolution and provides for the numerical stability of the code. We verified that the results presented here show only a negligible dependence when the value of the horizontal viscosity/diffusivity was halved and doubled; the actual value used is $\nu = 10 \text{ m}^2 \text{ s}^{-1}$.

3 Ensemble Kalman filter and its implementation

The EnKF is the main tool of our experiments performing the parameter estimation and providing us with the actual parameter values. The EnKF was introduced by Evensen (1994) and is used in data assimilation and parameter estimation experiments (see Evensen

2003; Brusdal et al. 2003). We refer the reader not familiar with the EnKF and the employed notation to the above-mentioned publications.

Every hour in time and every 1 km in the x -direction, the vertical extension of the gravity current, that is $h(x, t)$, is assimilated. Choosing a horizontal resolution for the assimilation five times sparser than the dynamical model does not only reduce the size of the assimilation experiment, but is also consistent with the fact that the grid-scale dynamics of the numerical model is dominated by dissipation and has only negligible dynamical information. We are only assimilating the vertical extension of the gravity current as it is the variable most easily measured in the ocean and in laboratory experiments. The measurement of the vertically integrated velocity within the gravity current, the other dynamical variable of the shallow water model, is more difficult to measure in the ocean and in laboratory experiments.

The assimilation is performed on the augmented state vector consisting of the vertical extension, the two velocity components and the two constant-in-time friction parameters:

$$\mathbf{x}(\bar{x}, \bar{t}) = (h(\bar{x}, \bar{t}), u(\bar{x}, \bar{t}), v(\bar{x}, \bar{t}), \tau, c_D)^t, \quad (6)$$

where \bar{x} and \bar{t} is the discretised version of x at assimilation grid-points and t at assimilation times, respectively, and t denotes transposition. The only (observed) variable assimilated is the vertical extension (h) of the gravity current. The analysis step for the EnKF reads:

$$\mathbf{x}_i^a = \mathbf{x}_i^f + \mathbf{K} (h^{\text{obs}} + \epsilon_i - \mathbf{H}\mathbf{x}_i^f) \quad (7)$$

$$\mathbf{K} = \mathbf{P}\mathbf{H}^T(\mathbf{H}\mathbf{P}\mathbf{H}^T + \mathbf{W})^{-1}, \quad (8)$$

where the index $i = 1, \dots, m$ runs over the realisations. The observation operator \mathbf{H} projects the state vector in the space of observations. The noise vectors ϵ_i represent the independent Gaussian-distributed zero-mean and σ -standard-deviation noise added to every observed value (see Burgers et al. 1998) and $\mathbf{W} = \sigma^2 \mathbf{I}$, where \mathbf{I} is the unity matrix. The error covariance matrix is given by

$$\mathbf{P} = \frac{1}{m-1} \sum_{i=1}^m (\mathbf{x}_i^f - \langle \mathbf{x}^f \rangle) (\mathbf{x}_i^f - \langle \mathbf{x}^f \rangle)^T, \quad (9)$$

where m is the size of the ensemble and $\langle \cdot \rangle$ denotes an ensemble average. The covariance matrix is truncated to a tridiagonal form to avoid spurious correlations between distant correlations, caused by under-sampling. This is also consistent with the dynamics at hand, as the maximum velocities (see Subsection 2.1) and wave speeds, given by $\sqrt{g'h}$, are of the order of 0.2 m s^{-1} . This means that, in the assimilation period of 1 h,

information can travel to the next assimilation point 1 km away, but it cannot reach over the distance of two assimilation grid points. In between assimilation points, h is interpolated linearly.

In general, the observed value of the vertical extension of the gravity current $h^{\text{obs}}(x, t)$ includes measurement errors $\eta(x, t)$ and is related to the true value by $h^{\text{obs}}(x, t) = h^{\text{true}}(x, t) + \eta(x, t)$. For consistency, the measurement error $\eta(x, t)$ has the same first- (zero mean) and second-order moments ($\bar{\sigma}^2$) as the noise vectors $\epsilon_i(x, t)$, but it does not depend on the actual realisation, that is, i . When assimilating data, σ has to be provided prior to the experiment, whereas $\bar{\sigma}$ is usually not known and can only be estimated.

In our parameter estimation experiments, the ensemble size is $m = 100$; this is much larger than the number of parameters to estimate, that is, two, equal to the number of observations at each assimilation time, but smaller than the dimension of the augmented state vector $\mathbf{x} = (\mathbf{h}, \mathbf{u}, \mathbf{v}, \tau, c_D)$, that is, 302. Using an ensemble size an order of magnitude larger did not improve the convergence significantly, reducing the ensemble size an order of magnitude leads to a frequent divergence of the assimilation.

Another important point is that the parameter values are set to be constant in time. This allows us to iterate our estimation experiment, that is, once we performed an entire estimation run, we could take the analysed values of the parameters after the last assimilation and use them for the first guess of a new experiment, iterating, thus, the same gravity current dynamics several times, always keeping the same data.

The values of the friction parameters are clearly non-negative, so every time the assimilation scheme provides a negative value of one of these parameters, which is possible due to the linearity of the analysis step and the statistical nature of the EnKF, the value is put to zero.

4 Twin experiments

The goal of our data assimilation experiment is to determine the friction law acting on the gravity extension (h) of the gravity current. The vertical extension, that is, the density structure of a gravity current, is the variable that is easiest to measure and observe in the ocean and in laboratory experiments. In our twin experiments, the data from observations or laboratory experiments are replaced by data from a control run (dynamics not subject to data assimilation) using the same numerical model as in the data assimilation experiments (see Section 2). In some experiments, the

initial conditions in the control runs differ from those of the assimilation runs. In Fig. 2, the vertical extension is shown for the control runs of three different sets of the friction parameters. The differences in the shapes of these curves are a prerequisite for the possible success of our experiments. It is a time series of these shapes, and only these, which is provided to the assimilation run and which has to determine the friction parameters on their basis. The observed variables must be sensitive to the parameters to be controlled. By performing twin experiments, we thus evaluate the feasibility of the data assimilation strategy by assimilating data that were produced by the very same model that is used for the assimilation experiment with the actual parameter values fixed. We thus explore the prerequisites under which the parameter estimation scheme is able to come up with the right set of parameters under these favourable conditions.

To explore the feasibility of the parameter estimation, we performed a series of experiments, which are summarised in Table 1, where σ gives the standard deviation of the noise added to the “observation” of the vertical extension of the layer. When the perturbed layer thickness is smaller than 10^{-6} m, it is put to 10^{-6} m. The initial distribution of the ensemble of parameters $(\tau^i, c_D^i)_{i=1, \dots, 100}$ has a normal distribution, with a mean of $(8 \cdot 10^{-3}, 7 \cdot 10^{-4})$ and a standard variation of $(5 \cdot 10^{-3}, 3.5 \cdot 10^{-4})$. Please note that the initial ensemble has a mean that is significantly different from the true values (τ_0, c_{D0}) (values used in the control run). The evaluation of the assimilation procedure is based on the convergence of the ensemble mean to the true values together with the decrease of the ensemble dispersion.

All pseudo-random numbers were generated by a “Mersenne Twister” (Matsumoto and Nishimura 1998). Other experiments, not shown here, with different mean values and standard deviations of the initial dis-

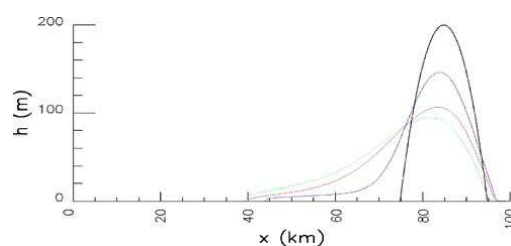


Fig. 2 Vertical extension of the gravity current (control runs) for experiments G0001 (blue), G0011 (red) and G0021 (green). At $t = 0$ (all curves superpose on black line), at $t = 96$ h, shapes in the three experiments are different

Table 1 Parameters varied in the assimilation experiments: linear friction parameter τ_0 , quadratic drag c_{D0} , noise σ and geostrophic adjustment γ ($\gamma = 0$ no initial velocity; $\gamma = 1$ current initially in geostrophic equilibrium)

Exp.	τ_0 (5.10^{-4} m s $^{-1}$)	c_{D0} (5.10^{-3})	σ (m)	$\tilde{\sigma}$ (m)	γ
A00001	1.0	0.0	10	0.0	1.0
A00011	0.0	1.0	10	0.0	1.0
G00001	1.0	0.0	10	0.0	1.0
G00011	0.0	1.0	10	0.0	1.0
G00021	1.0	1.0	10	0.0	1.0
G00121	1.0	1.0	5	0.0	1.0
G00221	1.0	1.0	20	0.0	1.0
G00321	1.0	1.0	2.5	0.0	1.0
G00421	1.0	1.0	40	0.0	1.0
G01021	1.0	1.0	10	0.0	0.0
G02021	1.0	1.0	10	0.0	0.8
G02221	1.0	1.0	20	0.0	0.8
G10021	1.0	1.0	10	10	1.0

tribution of the parameter values show qualitatively the same behaviour. One has to take care, however, that the true value (the one used in the control run) is a likely member of the initial ensemble to avoid slow convergence. The initial v component of the velocity in the control run is given by $v = \gamma v_g$, only for $\gamma = 1$, the control run starts from geostrophic equilibrium. The assimilation runs always start from a geostrophically adjusted state, as an unperturbed gravity current is close to such a state.

5 Results

5.1 Estimating one parameter

We started, in Exp. A0001 and A0011, to estimate the parameters τ and c_D , respectively, keeping the other parameters equal to zero. In Fig. 3, a convergence to the true value is seen in both cases. As stated in the previous section, the gravity dynamics spans 7 days (168 h) and the ensemble of the $(\tau^i, c_D^i)_{i=1\dots m}$ at the end of a 7-day assimilation experiment is then reused as the first guess of a new data assimilation run, with the same control run. By this, we are able to iterate the assimilation experiment many times to improve the values for (τ, c_D) . This explains why we present results for times larger than 7 days.

Reusing the data might seem, at a first glance, contradictory to the concept of the Kalman filter, which uses all data in an optimal way at the first passage. This is, however, only true if the problem is linear (parabolic cost-function), the initial ensemble of the parameter values are perfectly chosen (mean and variance), the ensemble size is infinite and the covariance matrix is complete. Iterating the procedure provides for a better first guess of the initial ensemble of the parameter values and increases the ensemble size. A possible

consequence of the iteration is that the variance of the ensemble is underestimated due to the fact that the procedure supposes the data to be independent, which it is not. This can be seen in Fig. 3, where the mean value converges rapidly to the correct value and the subsequent iterations mostly reduce the variance. The situation is different in the other experiments where the non-linearity is increased due to the interplay of two different friction laws and we see a continued convergence to the exact values in subsequent iterations. The ensemble of parameter values could be resampled after each iteration to avoid the artificial decrease in variance, but it is a result of our research that this was not necessary to do so in the here-presented experiments

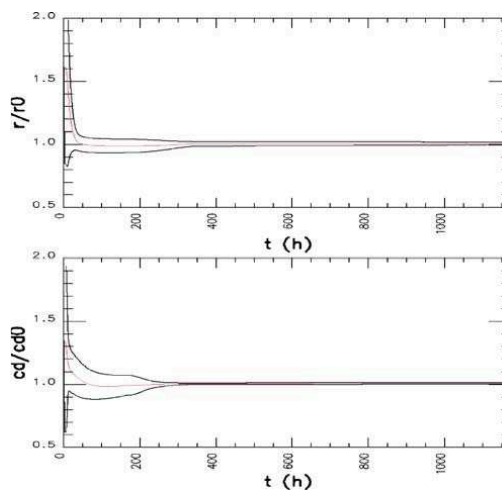


Fig. 3 Mean value (red) and standard deviation (black) normalised by the true value for the estimated parameter in experiment A0001 (upper) and A0011 (lower)

when considering the estimation of the parameter values (see below).

5.2 Discriminating between laws

In the previous subsection, we demonstrated that the assimilation procedure manages to estimate the right parameter values in the case of linear and quadratic friction. The type of the friction law was, however, imposed before the estimation procedure, a feature that we relax now. That is, we still use the same data but the assimilation procedure does not know with which kind of friction law the data were produced and what the corresponding parameter value is. We investigate in experiments G00001 and G00010 if the assimilation scheme obtains the parameter values and, in this way, manages to determine the friction law. We emphasise that the difference to experiments A00001 and A00010 is that, now, the assimilation scheme does not know that the other parameter is vanishing, but it has to establish it.

The results are presented in Fig. 4. The initial ensemble of the parameter values is the same for both experiments. In both cases, we see a good convergence to the right values and, thus, a clear determination of the right friction law.

5.3 Estimating both parameters

The next step is to consider dynamics which include both friction laws. The procedure is identical to that

of the previous subsection, only that now, both parameter values are non-vanishing. There are indeed a large number of examples where the friction law passes from linear to quadratic and where both laws coexist (see Schlichting and Gertsen 2000 pp. chap 1.3). In cases where one friction law is established, the friction coefficient (weakly) depends on the Reynolds number. By allowing for two, or more, friction laws, not only the optimal value of the friction parameter is estimated but also its variation with the Reynolds number (see Section 6). The case of estimating both τ and c_D at the same time is more challenging, as they both include friction in the model dynamics and have, to the first order, the same effect on the gravity current, that is, make it move down-slope. Furthermore, we choose, in experiments G0021, G0121, and G0221, values for τ and c_D such that they have a similar magnitude of the friction force, that is $\tau \approx c_D |\mathbf{u}|$ and $|\mathbf{u}| = \sqrt{u^2 + v^2}$, which is the most challenging case. A large number of experiments have been performed with different values of the friction parameters, the results show no qualitative differences. In Fig. 5, the convergences of the parameter values are shown. In general, one notices a good convergence in τ - c_D -space of all members of the ensemble towards the true values. A better convergence for runs with lower perturbations σ (noise level) is noticed. A further reduction of the variance of the noise added to the observations (necessary to make the EnKF consistent; see Burgers et al. 1998) leads to a divergence of the EnKF. A conspicuous feature of Fig. 5 is the fact that the ensemble is aligned along a straight line, which corresponds to a space-time-mean absolute velocity of the gravity current of

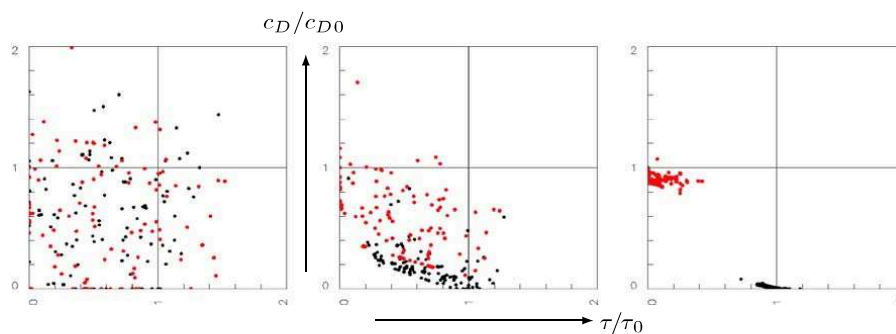


Fig. 4 Distribution of the ensemble in τ (horizontal direction) and c_D (vertical direction) space for the two experiments: G0001 (black dots) and G0011 (red dots), at different times: Initial distribution (left) (some initial values lie outside the area shown), after 7 days (middle) and after seven iterations of the 7-day dynamics

(right). The values of τ and c_D are normalised by the true value used in the control run (see Table 1). The experiment shows a successful convergence towards the true values. The black dots converge to $(\tau, c_D) = (\tau_0, 0)$ and the red dots to $(\tau, c_D) = (0, c_{D0})$

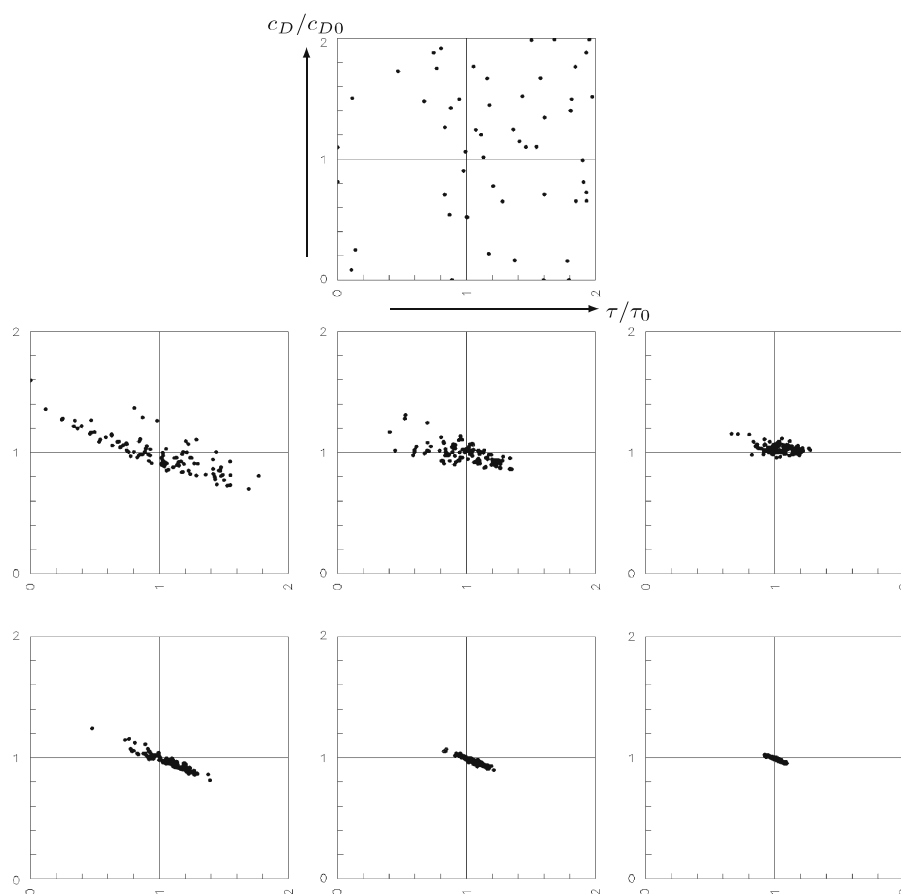


Fig. 5 Distribution of the ensemble in τ (horizontal direction) and c_D (vertical direction) space for the three experiments: G0221 (left column), G0021 (middle column) and G0121 (right column), for different times: Initial distribution (upper line)

(same in all experiments; some initial values lie outside the area shown), after 7 days (middle line) and after seven iterations of the 7-day dynamics (lower line). The values of τ and c_D are normalised by the true value used in the control run

$|\bar{\mathbf{u}}| \approx 0.2 \text{ m s}^{-1}$. The space time mean absolute velocity of the gravity current is defined by:

$$|\bar{\mathbf{u}}| = \frac{1}{AT} \int_0^T \int_L h |\mathbf{u}| dx dt \quad (10)$$

where $A = \int_L h dx$ is the cross-section of the gravity current, L is the extension in the x -direction and T is the duration of the experiment (7 days). Indeed, the total friction is given by $c_D |\mathbf{u}| + \tau$, which is constant along a line of slope $-|\mathbf{u}|$ in τ - c_D -space. The fast convergence onto the line of slope $-|\bar{\mathbf{u}}|$ (forthwith called manifold of slow convergence) followed by a slow convergence along the line means that the estimation of

the total friction is easily done whereas the distinction between the nature of the friction, linear or quadratic, is more complex, takes a longer amount time and requires for smaller noise levels in the observed variable. The dynamics in τ - c_D parameter-space thus happen on two time-scales, a fast convergence onto the manifold of slow convergence followed by a slow convergence within it.

It is, however, interesting to note that there is a rather good convergence to the correct values with a rather high noise level, which is actually larger than the thickness of the gravity current itself. This feature of fast convergence onto a manifold of slow conver-

gence in parameter space followed by a slow convergence within the manifold of slow convergence is not a peculiarity of the here-presented investigations but a general feature when estimating non-independent parameters.

In all the estimation experiments considered so far, we only considered gravity currents which were initially in a geostrophic equilibrium, a condition we like to relax in the sequel. We remind the reader that the control run replaces the observations of an actual gravity current, and by allowing it to differ from geostrophy, we evaluate the parameter estimation when applied to gravity currents not in a geostrophic equilibrium. The data assimilation experiment is, however, unchanged and based on the assumption that the current is in geostrophic equilibrium, which means that it is ignoring not only the friction parameters but also the initial velocity distribution. This creates an inconsistency especially in the early evolution before the gravity current adjusts to geostrophy. We found that the difficulty arises not so much from inertial oscillations of the not-adjusted gravity current (the control run), but from the fact that the kinetic energy in the non-adjusted runs is smaller. The assimilation reacts by imposing high values of the drag coefficient (c_D) to drain energy from the

assimilation runs. The drag coefficient, rather than the linear friction constant, increases as the fastest down-slope motion of the only partially adjusted gravity current is at locations with the largest slope, where the geostrophic velocities are also highest. The increase in the drag coefficient is so large that all members of the ensemble actually leave the parameter square shown in Fig. 6 for experiment G1021, but they come back later in the assimilation experiment. Once the energy levels are comparable and the control run is geostrophically adjusted, we observe a fast convergence onto the manifold of slow convergence. The guess for c_D , however, is too high (and τ correspondingly small) in all realisations so that the true value is not a likely candidate of the ensemble and subsequent assimilation has a very slow convergence, on the manifold of slow convergence, to the true value. It is no surprise that opting for a larger value of the observation error, as done in G02221, gives better results due to the lower confidence of the model in the observations; the initial increase is slowed down and the subsequent convergence to the true value is helped by the fact that the spread of the ensemble is larger and the true value is a likely candidate of the ensemble (Fig. 6). Again, we see a fast convergence onto the manifold of slow

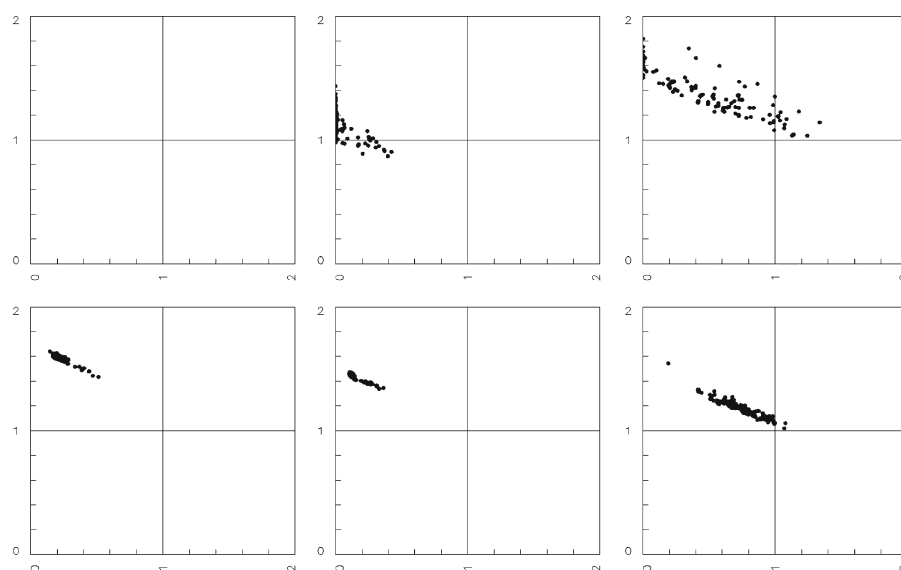


Fig. 6 Distribution of the ensemble in τ/τ_0 (horizontal direction) and c_D/c_{D0} (vertical direction) space, both normalised by the values of the control run, for the three experiments: G01021 (left row), G02021 (middle row) and G02221 (right row), for different times: After 7 days (upper line) and after seven iterations of the

7-day dynamics (lower line). The values of τ and c_D are normalised by the true value used in the control run. The initial distribution is the same as Fig. 5. After 7 days, all members of the ensemble in G01021 are outside the area shown

convergence followed by a slow convergence on the manifold of slow convergence.

In the experiments discussed so far, we had a vanishing observation error $h^{\text{obs}} = h^{\text{true}}$, that is, $\tilde{\sigma} = 0$. This is not consistent with the EnKF, as it requires $\tilde{\sigma} = \sigma$. It is, however, consistent with the fact that, in our twin experiments, we do not have observation errors. Furthermore, when performing parameter estimation experiments with observational or laboratory data, $\tilde{\sigma}$ is unknown. To determine the dependence of the experiment on the observation error, we performed experiment G10021, which is identical to G00021 except that it includes an observational error $\eta(x, t)$ with $\tilde{\sigma} = \sigma$. The results have no significant differences, demonstrating again the robustness of the EnKF.

6 Discussion

The EnKF has once more proved to be a robust tool for data assimilation. We established the possibility of estimating the parameters in friction laws in gravity currents by only observing its thickness. We showed convergence to the true values in almost all examples, even for values of the (Gaussian zero-mean) observation error that are comparable to the thickness of the gravity current. The speed of the convergence is very much dependent on the parameters (ensemble size, observation error and initial spread). In all cases, the convergence can clearly be decomposed into two steps: a fast convergence onto the manifold that corresponds to the total friction followed by a slow convergence on the manifold, corresponding to a discrimination between the two friction laws.

It is also made clear that the implementation of the EnKF is not straightforward but has to be guided by physical, mathematical and numerical insight to adjust and change the various parameters like the degrees of freedom in the model, ensemble size (m), the observation error, the initial spread of the ensemble and the space-time resolution of the assimilation. All these parameters are linked together in some non-linear manner, and it is impossible to rigorously establish the optimal values even when considering a rather simple model, as it is done here. This makes data assimilation an art founded in exact science.

The here-presented behaviour, as, for example, the distinction between a fast and slow convergence, is likely a general feature of parameter estimation when several parametrisations are put in competition to mimic the same physical process, and it is easy to estimate the total action of the process but it needs more specific information to distinguish between them.

The present work is the first step towards using data assimilation to estimate the turbulent fluxes in gravity currents. Moving beyond identical twin-experiments and assimilating the data from a non-hydrostatic model of the gravity current dynamics (HAROMOD, see Wirth 2004 and Wirth and Barnier 2006, 2008) and from laboratory experiments performed on the Coriolis turn table at LEGI (Grenoble) is a subject of current research which aims to evaluate types of parametrisations and values of parameters to represent friction in gravity currents. A better representation of gravity currents in today's numerical models of the dynamics of the global ocean will improve their representation of the abyssal water masses, the overturning circulation and, thus, the global heat transport of the world ocean, leading to better understanding of climate dynamics of planet earth.

As already briefly mentioned in Section 5, by estimating two or more parameters, one not only determines the friction values but also the dependence of the parameter on the Reynolds number. Indeed, we can rewrite Eq. 5 as:

$$D = (\tau + c_D|\mathbf{u}|)/h = \tilde{c}_D|\mathbf{u}|/h. \quad (11)$$

where $\tilde{c}_D = \tau/|\mathbf{u}| + c_D$ decreases with the Reynolds number, as it usually does over a solid surface (see Schlichting and Gertsen 2000 pp. chap 1.3). Equation 11 can also be seen as the beginning of a Taylor series for the friction coefficient as a function of the Reynolds number. Including higher-order terms in the present investigation would be against the empirical finding that the drag coefficient decreases with the Reynolds number. This is, however, not the case for the drag coefficient at the ocean-atmosphere interface, which is known to grow for large wind speeds due to the increased roughness of the interface (waves) at large wind speeds. The extension of the here-presented research to such applications is straightforward. The here-presented methodology is, thus, not restricted to the dynamics of gravity currents. Key observations in the ocean may help identify parametrisations of important phenomena which are poorly parametrised so far (overflows, friction, diapycnal mixing, mixing induced by internal wave breaking, turbulent fluxes, etc.)

Using data from the non-hydrostatic numerical simulations allows us to estimate not only the difficulties expected when passing to real observations but demonstrates that data assimilation is a systematic tool to connect models of different complexity in a hierarchy. Model hierarchies will play an increasing role in future earth system research (see IPCC Fourth Assessment Report 2007). Ongoing research aims at employing the here-presented technique and tools to estimate

the bottom friction of a gravity current on the Coriolis platform, a variable that has so far evaded direct measurement. The complexity of the estimation of the friction parameters in the real ocean depends on the spatial variability of the roughness of the ocean floor.

Finally, we would like to emphasise that this research actually goes beyond the technical problem of estimating parameters. By allowing the assimilation scheme to choose between different parametrisations, as shown above, we actually answer the scientific question about the nature of the underlying physical process. Parameter estimation can in this way choose between different parametrisations and help discriminate the physical laws of nature by estimating the coefficients presented in such parametrisations.

Acknowledgements Comments from and discussions with Jean-Michele Brankart and Emmanuel Cosme were key in writing this paper. We are grateful to Bernard Barnier, Yves Morel and Joel Sommeria for their remarks and to Pagode du Baron for discussion. This work is part of the COUGAR project funded by ANR-06-JCJC-0031-01 and by LEFE/INSU/CNRS.

References

- Baringer MO, Price JF (1997) Momentum and energy balance of the Mediterranean outflow. *Phys J Oceanogr* 27:1678–1692
- Brusdal K, Brankart JM, Halberstadt G, Evensen G, Brasseur P, van Leeuwen PJ, Dombrowsky E, Verron J (2003) A demonstration of ensemble-based assimilation methods with a layered OGCM from the perspective of operational ocean forecasting systems *Marine. J Syst* 40–41:253–289
- Burgers G, van Leeuwen P, Evensen G (1998) Analysis scheme in the ensemble Kalman filter. *Mon Weather Rev* 126:1719–1724
- DYNAMO Group (1997) Dynamics of North Atlantic models: simulation and assimilation with high resolution models. *Ber Inst Meereskd Kiel* 294:333
- Emms PW (1998) Stream-tube models of gravity currents in the ocean. *Deep-Sea Res* 44:1575–1610
- Evensen G (1994) Sequential data assimilation with a nonlinear quasi-geostrophic model using Monte Carlo methods to forecast error statistics. *Geophys J Res* 99:10143–10162
- Evensen G, Dee DP, Schröter J (1998) Parameter estimation in dynamical models. In: Chassignet EP, Verron J (eds) *Ocean modeling and parametrization NATO sciences series*. Kluwer, Dordrecht, pp 373–398
- Evensen G (2003) The ensemble Kalman filter: theoretical formulation and practical implementation. *Ocean Dyn* 53:343–367
- Ezer T (2005) Entrainment, diapycnal mixing and transport in three-dimensional bottom gravity current simulations using the Mellor-Yamada turbulence scheme. *Ocean Mod* 9:151–168
- Gill AE (1982) *Atmosphere and ocean dynamics*, International Geophysics series. Academic, London
- Griffiths RW (1986) Gravity currents in rotating systems. *Ann Rev Fluid Mech* 18:59–89
- IPCC Fourth Assessment Report, Climate Change (2007) The physical science basis, Chapter 1.5.1
- Killworth PD (1977) Mixing on the Weddell Sea continental slope. *Deep-Sea Res* 24:427–448
- Killworth PD (2001) On the rate of descent of overflows. *Geophys J Res* 106:22267–22275
- Killworth PD, Edwards NR (1999) A turbulent bottom boundary layer code for use in numerical ocean models. *Phys J Oceanogr* 29:1221–1238
- Legg S, Hallberg RW, Giron JB (2006) Comparison of entrainment in overflows simulated by z-coordinate, isopycnal and non-hydrostatic models. *Ocean Mod* 11:69–97
- Matsumoto M, Nishimura T (1998) Mersenne twister: a 623-dimensionally equidistributed uniform pseudorandom number generator. *ACM Trans Model Comput Simul* 8:3–30
- Moore W, Tang R (1984) Ocean bottom friction study from numerical modelling of sea surface height and SEASAT-ALT data. *Mar Geophys Res* 7:73–76
- Price JF, Baringer MO (1994) Outflows and deep water production by marginal seas. *Prog Oceanogr* 33:161–200
- de Saint Venant B (1871) *Théorie du mouvement non permanent des eaux, avec application aux crues des rivières et à l'introduction des marées dans leur lit*. C.R. A.S. 73:147–154
- Schlichting H, Gertsken K (2000) *Boundary-layer theory*. Springer, Heidelberg
- Shapiro GI, Hill AE (1997) Dynamics of dense water cascades at the shelf edge. *Phys J Oceanogr* 27:2381–2394
- Smith PC (1975) A stream tube model for bottom boundary currents in the ocean. *Deep-Sea Res* 22:853–873
- Smith PC (1977) Experiments with viscous source flows in rotating systems. *Dyn Atmos Ocean* 1:241–272
- Stevenson B, Duan J, McWilliams JC, Münnich M, Neelin JD (2002) Entrainment, Rayleigh friction, and boundary layer winds over the tropical Pacific. *J Climate* 15:30–44
- Sutherland BR, Nault J, Yewchuk K, Swaters GE (2004) Rotating dense currents on a slope. Part 1. Stability. *Fluid J Mech* 508:241–264
- Whitehead JA, Stern ME, Flierl GR, Klinger BA (1990) Experimental observations of baroclinic eddies on a sloping bottom. *Geophys J Res* 95:9585–9610
- Willebrand J, Barnier B, Böning C, Dieterich C, Killworth P, Le Provost C, Jia Y, Molines JM, New AL (2001) Circulation characteristics in three eddy-permitting models of the North Atlantic. *Prog J Oceanogr* 48:123–162
- Wirth A (2004) A non-hydrostatic flat-bottom ocean model entirely based on Fourier expansion. *Ocean Mod* 9:71–87
- Wirth A, Barnier (2006) Tilted convective plumes in numerical experiments. *Ocean Mod* 12:101–111
- Wirth A, Barnier (2008) Tilted convective plumes in numerical experiments. *Phys J Oceanogr* 38:803–816
- Xu X, Chang YS, Peters H, Özgökmen TM, Chassignet EP (2006) Parametrization of Gravity current entrainment for ocean circulation models using a high-order 3D nonhydrostatic spectral element model. *Ocean Mod* 14:19–44

4.7 On the basic structure of oceanic gravity currents

Ocean Dynamics (2009) 59:551–563
DOI 10.1007/s10236-009-0202-9

On the basic structure of oceanic gravity currents

Achim Wirth

Received: 2 February 2009 / Accepted: 27 April 2009 / Published online: 15 May 2009
© Springer-Verlag 2009

Abstract Results from numerical simulations of idealised, 2.5-dimensional Boussinesq, gravity currents on an inclined plane in a rotating frame are used to determine the qualitative and quantitative characteristics of such currents. The current is initially geostrophically adjusted. The Richardson number is varied between different experiments. The results demonstrate that the gravity current has a two-part structure consisting of: (1) the vein, the thick part that is governed by geostrophic dynamics with an Ekman layer at its bottom, and (2) a thin friction layer at the downslope side of the vein, the thin part of the gravity current. Water from the vein detrains into the friction layer via the bottom Ekman layer. A self consistent picture of the dynamics of a gravity current is obtained and some of the large-scale characteristics of a gravity current can be analytically calculated, for small Reynolds number flow, using linear Ekman layer theory. The evolution of the gravity current is shown to be governed by bottom friction. A minimal model for the vein dynamics, based on the heat equation, is derived and compares very well to the solutions of the 2.5-dimensional Boussinesq simulations. The heat equation is linear for a linear (Rayleigh) friction law and non-linear for a quadratic drag law. I demonstrate that the thickness of a gravity

current cannot be modelled by a local parameterisation when bottom friction is relevant. The difference between the vein and the gravity current is of paramount importance as simplified (streamtube) models should model the dynamics of the vein rather than the dynamics of the total gravity current. In basin-wide numerical models of the ocean dynamics the friction layer has to be resolved to correctly represent gravity currents and, thus, the ocean dynamics.

Keywords Ocean dynamics · Gravity current

1 Introduction

Buoyancy forces caused by density differences in fluids are a major source of fluid motion in nature. When these forces act adjacent to topography, gravity currents are created. The major part of the deep and intermediate waters of the world ocean and marginal seas have done at least part of their voyage to the deep in the form of a gravity current. Oceanic gravity currents play a role of paramount importance in the formation of the water masses and the ventilation of the deep ocean and are thus key to understanding the oceanic component in the earth's climate system.

For most oceanic gravity currents, the earth's rotation plays an important role, as they evolve on a timescale much larger than the rotation period of the planet earth. The dominant force balance is thus between gravity and the Coriolis force, that is, geostrophic. Research on non-rotating gravity currents cannot be extrapolated to the rotating case, as it ignores this leading order balance. When the turbulent (and the neglectable molecular) fluxes of water masses and

Responsible Editor: Eric Deleersnijder.

A. Wirth (✉)
LEGI / MEOM, CNRS, BP 53, 38041
Grenoble Cedex 9, France
e-mail: achim.wirth@hmg.inpg.fr

momentum are neglected, rotating gravity currents flow along the inclined ocean floor changing neither depth nor composition. Turbulent fluxes of tracers, that is mixing, entrainment and/or detrainment, determine the change of the water mass. Together with the turbulent fluxes of momentum at the floor and interface of the gravity current, they govern the pathway and the composition of the gravity current. Oceanic gravity currents are thus subject to three forces: (1) the buoyancy force pointing downslope, (2) the Coriolis force directed at a right angle to the direction of motion and (3) frictional forces due to dissipative fluxes of mass and momentum (see Fig. 7 in the [Appendix](#)). The first two forces are linear, the total buoyancy force depends linearly on the total buoyancy anomaly and the total Coriolis force is a linear function of the transport of the gravity current. The above shows that the answer and problem of the evolution of a gravity current lies in the determination of the laws and parameters of its dissipative fluxes of momentum and mass. For an introduction to the dynamics of oceanic gravity currents, I refer the reader to Griffiths (1986).

In the past 30 years, the study of streamtube models has greatly increased our understanding of the dynamics of oceanic gravity currents. In streamtube models, only average (bulk) values of the dynamical variables are considered at every cross section along the path of the gravity current (see Smith 1975, 1977; Killworth 1977, 2001; Price and Baringer 1994; Baringer and Price 1997; Emms 1998). Due to their linear nature, the integrated buoyancy and Coriolis force can be calculated. The nonlinear frictional forces and the turbulent fluxes, perturbing the geostrophic equilibrium, have to be parametrised. The evolution of the gravity current can then be studied as a function of the parametrisations and parameter values employed. Integrations of these semi-analytical streamtube models along a path of varying topographic slope are performed and the parameter values are adjusted in such a way that the pathway and water mass characteristics compare favourably to observations. This adjustment procedure, however, does not always lead to a deeper understanding of the physical processes involved (see Emms 1998). The implementation of streamtube models or their physics in large-scale ocean general circulation models is difficult. Although progress has been made in better representing gravity currents in large-scale ocean general circulation models through bottom boundary layers (see, e.g. Killworth and Edwards 1999; Price and Young 1998; Wu et al. 2007), their dynamics is still a weak point of today's numerical models of ocean circulation.

Many efforts have been undertaken to determine the turbulent fluxes from observations, laboratory experiments and numerical simulations, but no definite conclusion has been reached, no generally accepted parametrisation is available and no generally accepted parameter values have been obtained so far. As an example, a key parameter is the entrainment rate; there is, however, no definite answer even about its sign in rotating gravity currents (Ezer 2005; Legg et al. 2006). Killworth (2001) states that “entrainment should only occur over limited regions, with detrainment elsewhere”, and MacCready notes that “[...] the majority of entrainment with overlying waters occurs close to the overflow sill [...], and is largely negligible there after”. Furthermore, Ermanyuk and Gavrilov (2007) found in laboratory experiments on non-rotating gravity currents that the dissipative processes at the interface have a negligible role compared to those due to bottom friction.

The purpose of the present work is to determine the basic processes and structure of oceanic gravity currents in an idealised configuration as a testing ground for present and future models and parametrisations in basin scale models. To this end, I will numerically integrate the (nonhydrostatic) Navier–Stokes equations. With respect to streamtube models, I will not try to adjust parameter values so that they compare favourably to observation, but I will instead test the hypotheses they are based on by comparing their assumptions with our results from the Navier–Stokes model of highly idealised gravity currents. I show that gravity currents actually consist of two parts and that this two-part structure is key to understanding and modelling their dynamics.

In his pioneering paper on the dynamics of viscous-rotating-gravity currents, Smith (1977) stated, concerning their structure, “[...] a complete solution remains inaccessible” (Section 3, lines 7–8). I will here demonstrate that the structure, evolving in time, of idealised gravity currents can be obtained by solving a one-dimensional heat equation. Results on the basic structure of idealised oceanic gravity currents are also the starting point for the large-scale, three-dimensional instability analysis leading to the formation of coherent cyclonic structures (Meacham and Stephens 2001). The important dynamics of large-scale instability is not considered in this work.

The model is introduced in the next section, results are presented in Section 3 and they are discussed in Section 4, where I also consider the consequences of our results for the representation of oceanic gravity currents in ocean general circulation models (OGCMs).

2 Idealised oceanic gravity current

2.1 The physical problem considered

In the experiments presented here, I use an idealised geometry, considering an infinitely long gravity current on an inclined plane with constant slope, and I do not allow for variations in the long-stream direction. A similar geometry was investigated by Ezer and Weatherly (1990). I thus consider only the dynamics of a vertical slice perpendicular to the geostrophic flow direction of the gravity current. Please note that such simplified geometry inhibits large-scale instability and the formation of cyclones and other large-scale features. This is beneficial to our goal of studying the small-scale fluxes in gravity currents. The simplified geometry also filters out small-scale processes and instabilities in the y direction. Instead of a gravity current descending in space, along the direction of propagation, it descends in time (this strategy was also used by MacCready 1994 and others). Such descent is also investigated when the gravity current is initially homogeneous in the long-slope direction, as in laboratory experiments where the dense fluid is injected axisymmetrically on a cone structure (Shapiro and Zatspein 1997; Sutherland et al. 2004); semi-analytical calculations of the instability of a rotating gravity current (Meacham and Stephens 2001). The results can be compared to the observations of the transverse structure of a oceanic gravity current by Umlauf et al. (2007). The local dynamics will not differ from gravity currents descending in space as long as the large-scale descent is slow in space and time compared to the local turbulent dynamics, which is definitely the case when the dynamics is close to a geostrophic equilibrium. Such type of model is referred to as 2.5-dimensional, as it is three-dimensional, but the variables have no dependence on the stream-wise direction (the y direction in this case). I like to emphasise that none of the three components of the velocity vector are trivial and that the main (geostrophic) transport is in the y direction.

In observations and laboratory and numerical experiments, large-scale instabilities are observed for a wide range of parameter values. All the studies, that I am aware of, include a geostrophic adjustment process, which also destabilises the current. In laboratory experiments where the gravity current was injected close to a geostrophically adjusted state, these large-scale instabilities developed only very slowly (Wirth and Sommeria, unpublished manuscript), long time after the 2.5-dimensional dynamics, studied here, had started evolving. A geostrophically adjusted state also forms

the starting point of investigations concerning the stability of oceanic gravity currents and the dynamics of streamtube models.

The gravity currents considered here are on an inclined plane of a constant slope of one degree, the initial profile of its vertical extension above the inclined ocean floor $z = h(x) = \max\{H - x^2/\lambda, 0\}$ has a parabolic shape with $H = 200$ m and $\lambda = 5 \cdot 10^5$ m leading to a gravity current that is 200 m high and $L = 20$ km large. The values used in the experiment are typical for oceanic gravity currents (see, e.g. Smith 1977; Price and Baringer 1994; Killworth 2001). If the gravity current is initially geostrophically adjusted, the velocity components are given by:

$$u_G = 0; \quad v_G = \frac{g'(\partial_x h + \tan \alpha)}{f}; \quad w_G = 0. \quad (1)$$

This geostrophic velocity, also called the Nof speed (Nof 1983), is due to the balance between the Coriolis force and the buoyancy force in the downslope direction. Outside the gravity current, the water is initially at rest. Multiplying Eq. 1 by the thickness and integrating across the gravity current shows that the average geostrophic speed of the gravity current is given by $\bar{v}_G = (g'/f) \tan \alpha$. The Coriolis parameter is $f = 1.0313 \cdot 10^{-4} \text{ s}^{-1}$ corresponding to the earth rotation at mid-latitude. The reduced gravity is $g' = g(\rho_{gc} - \rho_0)/\rho_0 = \Delta T \cdot 2 \cdot 10^{-4} \text{ K}^{-1} 9.8065 \text{ m s}^{-2}$, where ΔT is the temperature difference between the ambient fluid and the gravity current, a constant thermal expansion coefficient of $2 \cdot 10^{-4} \text{ K}^{-1}$ and a gravitational acceleration of 9.8065 m s^{-2} are used. The temperature difference between the gravity current and the surrounding water ranges from 0.25 to 1.5 K. The values of the average geostrophic speed are given in Table 1. The vertical friction coefficient is $\nu_v = 10^{-3} \text{ m}^2 \text{ s}^{-1}$, leading to an Ekman layer thickness $\delta = \sqrt{2\nu_v/f} \approx 4.4$ m.

The dynamics depends on the six independent parameters $(\alpha, g', f, H, L, \nu_v)$; four independent non-dimensional numbers can be obtained: (1) the slope of the inclined plane $\tan \alpha$, (2) the Richardson number $Ri = g'H/\bar{v}_G^2 = Hf^2/(g' \tan^2 \alpha)$, (3) the Ekman number $Ek = (\delta/H)^2 = 2\nu_v/(fH^2) = 4.84 \cdot 10^{-4}$ comparing the frictional to the Coriolis force and (4) the ratio L/L_D , the width of the gravity current divided by the Rossby radius $L_D = \sqrt{g'H}/f$. In the experiments presented here, I choose to systematically vary the Richardson number, identified as a key parameter (see, e.g. Price and Baringer 1994; Killworth 2001), by varying the density (temperature) difference. The Froude number, $F = Ri^{-1/2}$, gives the geostrophic speed divided by the speed of the shallow water gravity wave.

I used the maximal height $H = 200$ m for the definition of the vein Richardson number and a vein Froude number. A vertical Reynolds number is given by $Re = 2(Ek Ri \tan \alpha)^{-1}$ and depends on the Ekman number, the Richardson number and the slope. This Reynolds number is the geostrophic velocity multiplied by the layer thickness and divided by the vertical viscosity. The influence of a second scalar, salinity and a nonlinear equation of state, leading to, e.g. the thermobaric effect (see Emms 1998), is not considered here.

2.2 The mathematical model

The mathematical model for the gravity current dynamics are the Navier–Stokes equations in a rotating frame with a buoyant scalar (temperature). I neglect variations in the stream wise (y) direction of all the variables but include the temperature difference and all the three components of the velocity vector, this type of model is usually revered to as 2.5 dimensional. This leads to a four-dimensional state vector depending on two space and the time variable, $(\Delta T(x, z, t), u(x, z, t), v(x, z, t), w(x, z, t))$.

The domain is a rectangular box that spans 51.2 km in the x direction and is 492 m deep (z direction). On the bottom, there is a no-slip and on the top a free-slip boundary condition. The horizontal boundary conditions are periodic. The initial condition is a temperature anomaly which has a parabolic shape, which is 200 m high and 20 km large at the bottom, as described in the previous subsection. The magnitude of the temperature anomaly is varied in the experiments. The initial velocities in the gravity current are geostrophically adjusted, the fluid outside the gravity current is initially at rest. The buoyancy force is represented by an acceleration of strength $g' \cos(\alpha)$ in the z direction and $g' \sin(\alpha)$ in the negative x direction to represent the inclination of angle $\alpha = 1^\circ$. This geometry represents a rectangular box that is tilted by an angle of one degree. Such implementation of a sloping bottom simplifies the numerical implementation and allows for using powerful numerical methods (see next subsection).

2.3 Numerical implementation of mathematical model

The numerical model used is HAROMOD (Wirth 2005). HAROMOD is a pseudo-spectral code, based on Fourier series in all the spatial dimensions, that solves the Navier–Stokes equations subject to the Boussinesq approximation, a no-slip boundary condition on the floor and a free-slip boundary condition at the rigid

surface. The time stepping is a third-order, low-storage, Runge–Kutta scheme. A major difficulty in the numerical solution is due to the large anisotropy in the dynamics and the domain, which is roughly 100 times larger than deep. There are 896 points in the vertical direction. For a density anomaly larger than 0.75 K, the horizontal resolution had to be increased from 512 to 2,048 points (see Table 1) to avoid a pile up of small-scale energy caused by an insufficient viscous dissipation range, leading to a thermalised dynamics at small scales as explained by Frisch et al. (2008). The horizontal viscosity is $\nu_h = 5 \text{ m}^2 \text{ s}^{-1}$ and the horizontal diffusivity is $\kappa_h = 1 \text{ m}^2 \text{ s}^{-1}$. The vertical viscosity is $\nu_v = 10^{-3} \text{ m}^2 \text{ s}^{-1}$ and the vertical diffusivity is $\kappa_v = 10^{-4} \text{ m}^2 \text{ s}^{-1}$. The anisotropy in the turbulent mixing coefficients reflects the strong anisotropy of the numerical grid. I checked that the results presented here show only a slight dependence on ν_h, κ_h and κ_v by doubling these constants in a control run. This is no surprise as the corresponding diffusion and friction times are larger than the integration time of the experiments. There is a strong dependence on ν_v , as it determines the thickness of the Ekman layer and the Ekman transport, which governs the dynamics of the gravity current as will be shown in Section 3. The vertical extension of the Ekman layer is a few metres, while the horizontal extension of the gravity current is up to 50 km. In a fully turbulent gravity current, the turbulent structures within the well mixed gravity current will be isotropic and will therefore measure only a few metres in size. To simulate a fully turbulent gravity current, 10^5 grid points would be necessary in the horizontal direction to obtain an isotropic grid. This is far beyond our actual computer resources.

2.4 Experiments performed

The density anomaly was varied in the experiments. The integration was stopped when the downslope side

Table 1 Physical and numerical parameters varied in the numerical experiments

Exp.	ΔT (K)	$\overline{v_G}$ (10^{-2}) ms^{-1}	Ri	N_x	Integration time (h)
G00	0.25	8.30	14.2	512	360
G01	0.5	16.6	7.12	512	192
G03	0.75	24.9	4.75	512	132
G12	1.0	33.2	3.56	2,096	96
G14	1.1	36.5	3.24	2,096	86
G15	1.25	41.5	2.85	2,096	76
G17	1.5	49.8	2.37	2,096	66

of the friction layer attained the boundary of the domain. All the experiments discussed in this publication are listed in Table 1, which includes information concerning the physics of the experiments: temperature anomaly ΔT , mean geostrophic velocity \bar{v}_G and Richardson number Ri , as well as numerical values: horizontal resolution and time of integration.

3 Results

I start with a qualitative description of the dynamics of the gravity current before quantitatively determining the key parameters.

3.1 Qualitative description

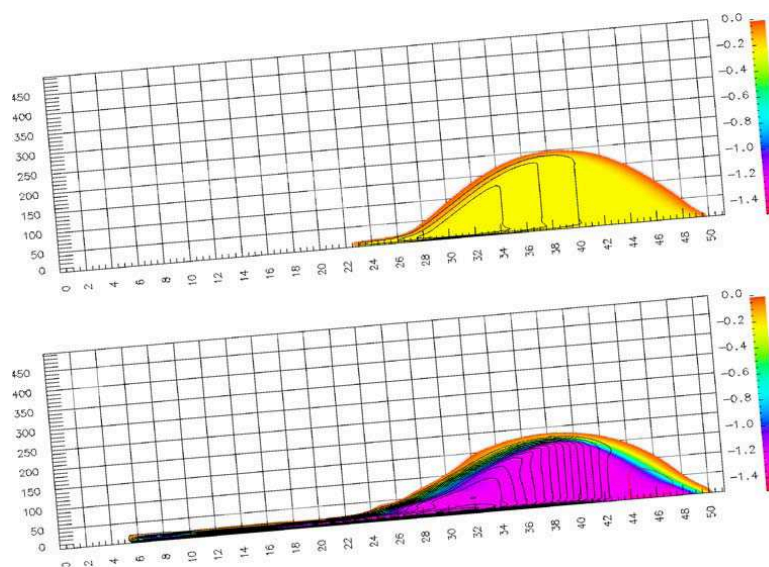
The gravity current is initially in a geostrophic state as expressed by Eq. 1. The velocity near the boundary is rapidly reduced due to friction. This rapid decrease of the velocity leads to inertial oscillations throughout the gravity current. Near the ocean floor, in the bottom Ekman layer, frictional forces reduce the long-slope velocity so the flow is no longer geostrophically adjusted, as the Coriolis force no longer balances the hydrostatic pressure gradient and the water in the Ekman layer

flows down the pressure gradient. At the downslope border of the vein, a friction layer forms, which consists of gravity current water moving downslope (see Fig. 2). This feature is observed in laboratory experiments by Smith (1977) and Lane-Serf and Baines (1998) (and references therein) and measured by Wirth and Sommeria (unpublished manuscript).

In Fig. 1, one sees a typical result of our numerical integrations for two experiments with different density and temperature differences. In the interior of the gravity current, the isolines of the y component are vertical due to geostrophy, which says that this velocity component is determined by hydrostatic pressure gradient, that is, the angle of the surface of the gravity current to the horizontal. In the upslope part of the gravity current, the y component of the velocity is negative due to the negative angle of the surface of the gravity current to the horizontal.

Figure 1 clearly shows that the gravity current consists of two parts, a “vein” which is the thick part of the gravity current (thicker than about 20 m) and a “friction layer”, the thin layer of dense fluid that extends downstream of the vein. The vein of the gravity current water detrains through the Ekman layer into the friction layer, which is responsible of the major part of the downslope transport of gravity current water. Please

Fig. 1 Structure of the gravity current after 60 h in exp. G00 (*top*) and G15 (*bottom*), see Table 1 for details. The inclination of the floor is exaggerated in the figure, for pedagogical reasons only; the real angle is only 1° . Please note that the vertical extension is given in metres and the horizontal extension in kilometres. The temperature anomaly, with respect to the ambient water, is shown (given in Kelvin). Isolines of the y component of the velocity (positive into the plane) are given every 0.05 ms^{-1} in *black* for positive values and *red* for negative values, zero line is omitted



note that the thickness of the friction layer is about two times the Ekman layer thickness $\delta = \sqrt{2\nu_v/f}$, confirming the results of Shapiro and Hill (1997). The friction layer typically contains a bottom and an interfacial Ekman layer, which match at its interior.

The Ekman layer extends through the entire width of the gravity current, friction layer and vein, and is most conspicuous when looking at the u component of the velocity vector, which is strongly negative (upslope is the positive direction) in the Ekman layer and small in the interior of the vein. Interfacial Ekman layers between the surrounding fluid and the gravity current are also observed, but the gradients involved are smaller than at the ocean floor.

In the vein away from the boundaries, the current is close to a geostrophic equilibrium, where the pressure gradient due to the interface of the gravity current is balanced by the Coriolis force due to the velocity of the vein. Near the boundaries, the speed of the gravity current is reduced and the Coriolis force can no longer balance the pressure gradient, which leads to fluid moving down the pressure gradient in the friction layer, that is, on average, down the slope. The variation in the Ekman layer transport creates convergence and divergence and the gravity current water is vertically pumped out and into the vein at the interface of the vein and the Ekman layer (see Fig. 2). These vertical velocities then affect the dynamics in the vein by vortex stretching in the same way as the vertical velocities at the wind induced Ekman layer influence the geostrophic Sverdrup dynamics in the interior ocean (see, e.g. Pedlosky 1998). The influence of friction on the dynamics of the vein

is, thus, via the vertical velocities at the base of the vein. Figure 1 also shows that the vein detrains via the friction layer. This detrainment, or Ekman drainage, depends on the (turbulent or eddy) vertical viscosity, which is a key parameter in the gravity current dynamics. In our calculations, the vertical viscosity is constant (see Subsection 2.3); in nature, the vertical eddy viscosity is, however, not constant but varies in space and time. The Ekman drainage has already been found to play an important role in laboratory experiments (Lane-Serf and Baines 2000).

In the interior of the vein, inertial oscillations are superposing the slow evolution of the gravity current in all calculations. In the calculations with higher values of the reduced gravity ($\Delta T > 0.75$ K), nonlinear behaviour is observed as can be seen in Fig. 3, where the vertical velocity outside and inside the gravity current shows an involved spatio-temporal variability. The sparse horizontal resolution of our calculations does not allow for the representation of turbulence in the unstratified interior of the gravity current.

3.2 Velocity, angle of descent and broadening

Before proceeding with a qualitative analysis of the data, I have to give a precise definition of the gravity current: water parcels having at least half the initial density anomaly are said to be within the gravity current. I verified that the results presented here vary only slightly when this threshold is varied around the value of one-half. The total volume of the gravity current

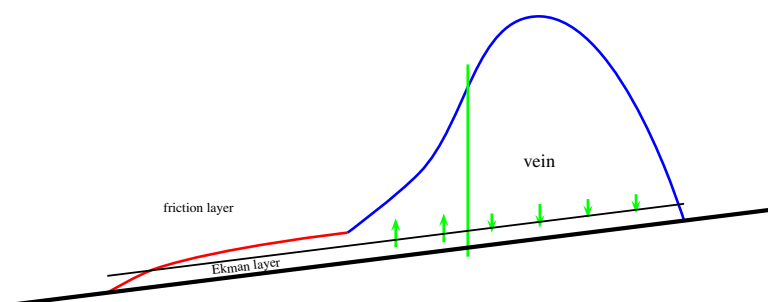


Fig. 2 Schematic of a cross section through a gravity current on an inclined plane as considered in this manuscript. The total gravity current consists of two distinct parts, the vein (the fluid under the blue line) and the friction layer (the fluid under the red line). In both parts, there is an Ekman layer close to the inclined

plane (under the thin black line). The green line separates the concave ($\partial_{xx}h > 0$) from the convex ($\partial_{xx}h < 0$) part of the vein. The small green arrows show the direction of vertical velocity out of or into the Ekman layer

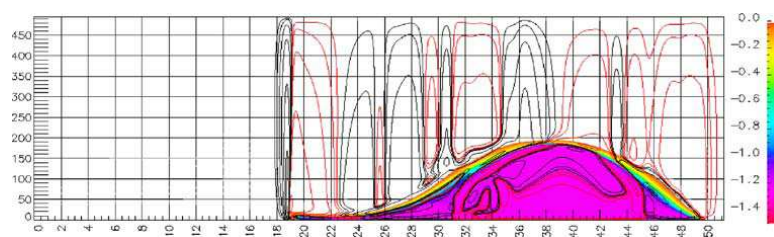


Fig. 3 Structure and vertical velocity field at 24 h in exp. G15. The temperature anomaly, with respect to the ambient water, is shown (given in Kelvin). Isolines of the w component of the velocity are given in *black* for positive values (upward) and *red* for negative values; the contour lines shown are $\pm 10^{-5}$, $3 \cdot 10^{-5}$, 10^{-4} , $3 \cdot 10^{-4}$, 10^{-3} , $3 \cdot 10^{-3}$; the logarithmic scale was chosen due to the large intermittency of the vertical velocity. Vertical velocities outside the vein are due to wave-like motion of the interface

shows only a small variation during the evolution of the gravity current. This shows that there is no substantial entrainment or detrainment for the total gravity current.

The density anomaly and the along-slope velocity (y component) both decrease in the experiments. To leading order, the dynamics is supposed to be given by the geostrophic equilibrium as discussed in Subsection 2.1. To verify this, I calculate the along-slope velocity component in the vein divided by the geostrophic speed of its reduced gravity, given by: $\bar{v}_G = (g'/f) \tan \alpha$, for each density class within the vein. When the average for all parcels in the vein which are at least 20 m above ground is analysed, the average along-slope velocity decreases to about 95% the geostrophic velocity after 2 days. This shows that the gravity current progresses along the slope at almost geostrophic speed, in agreement with previous findings of Price and Baringer (1994) and others.

Friction leads to a downslope transport of gravity current water. The dynamics of the vein differs completely from the dynamics of the total gravity current, and so does their rate of descent and their spreading, as can be verified in Fig. 4. The spread and descent of the gravity current, which includes the friction layer, is much larger than that of the vein alone.

Figure 4 shows that the depth of the upper bound of the vein stays almost constant, a feature that is well documented (see Price and Baringer 1994 and references therein), while the downslope sides of the vein and the friction layer descend. At the upslope side, the y component of the velocity vector is negative, as noted above, the fluid in the Ekman layer should, thus, move upslope. This leads to an arrested Ekman layer, as explained by Garrett et al. (1993), and no friction layer forms at the upslope side of the gravity

current. The speed of descent of the downslope front of the friction layer slightly decreases with time due to the decrease of its density anomaly. Indeed, there is a no-slip boundary condition at the ocean floor, the water right above it cannot keep up with the downward speed of the front of the gravity current and gravity current water superposes surrounding water near the downward progressing front. This surrounding water becomes mixed into the friction layer near the front and dilutes the gravity current water near the downward progressing front, a feature common to all gravity currents.

The descent of the centre of gravity of the vein is well fitted by a linear law (see Fig. 4). The rates of descent are given in Table 2. The angle of descent of the vein compares well to the theoretically predicted value of $1.2 \cdot 10^{-2}$, based on a linear force balance

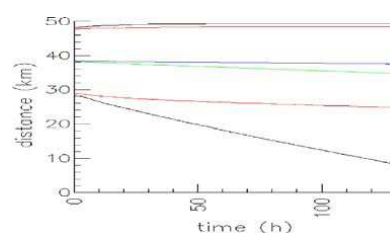


Fig. 4 The lower and upper bounds along the slope of the gravity current (*black curves*) and the vein (*red curves*) are shown. That is, the gravity current evolves (in time) between the *black lines* and the vein between the *red lines*. The vein is defined to be the part of the gravity current more than 20 m above ground. The path of the centre of gravity of the total gravity current (*green line*) and the vein only (*blue line*) are also shown. All the results are from exp. G03; other experiments show the same qualitative behaviour

Table 2 The speed of descent and the inverse rate of descent θ^{-1} , that is, the mean geostrophic speed divided by the speed of descent, are given for the vein of the gravity current and the total gravity current (gc) in the table, for all the experiments discussed

Exp.	Ri	Descent vein (10^{-3} m/s)	Rate of descent vein (10^{-2})
G00	14.2	0.82	1.0
G01	7.12	1.7	1.0
G03	4.75	2.7	1.1
G12	3.56	3.8	1.2
G14	3.24	4.6	1.2
G15	2.85	4.8	1.2
G17	2.37	6.1	1.2

between the Coriolis force and the friction force; please see the [Appendix](#) for the derivation of this value. This balance was already employed by Price and Baringer (1994) (they use a different definition of the Ekman number), but they did not make a distinction between the total gravity current and the vein. The angle of descent slightly increases with the Froude number as the Ekman layer dynamics becomes more nonlinear, leading to an increased effective (eddy-) viscosity.

The rate of the descent of the total gravity current increases with time as the volume of the friction layer increases, and, thus, so does the average downslope velocity. It is worth mentioning that, even in the beginning, the descent of the centre of gravity of the total gravity current is about three times the descent of the centre of gravity of the vein. This emphasises once more the fundamental difference between the dynamics of the vein and the gravity current.

Both the friction layer and the vein broaden in time (see Fig. 4), as their upslope sides stay almost level, while the downslope sides of the vein and the friction layer descend. The downslope side of the vein descends roughly at a constant speed which is about twice that of the centre of gravity of the vein (as noted by Price and Baringer 1994), given in Table 2. The descent of the downslope side of the friction layer is much faster than that of the vein. I emphasise, once more, that the spread of the vein is much slower than the spread of the total gravity current, as the major part of the spreading of the gravity current is performed by the friction layer (see Fig. 4).

Another point I like to emphasise, and I am not aware that it has been explicitly mentioned elsewhere, is that the downward progressing front of the friction layer does not have a thick and growing “head” as is the case for non-rotating gravity currents, but has a wedge-shape structure. In gravity current dynamics dominated by rotation, the water in a thick head would not feel the direct influence of friction and would turn

to move along the slope rather than downslope. This large difference is due to the fact that, in rotating gravity currents, friction makes the water flow downward, whereas, in their non-rotating counterparts, friction opposes the downward movement.

3.3 A minimal model for the vein dynamics

It is most important to notice that the descent of the vein, the thick part of the gravity current, is at least three times slower than that of the total gravity current, but why does the vein descend at a slower rate? The part of the vein above the Ekman layer is almost unaffected by the direct influence of friction, and I can thus apply the concept of conservation of potential vorticity to its dynamics, which states that the spreading of the vein, decrease of its thickness, should lead to a decrease of the total vorticity $\partial_x v + f$, which means that $(-\partial_x v)$ should increase ($\partial_x v < 0$). Geostrophy then states that $-\partial_{xx} h$ should increase, which means that the vein should narrow, which is the opposite of what I started with. So the better question is: why does the vein spread at all and how does it do it? As I have just shown, conservative dynamics forbids it, so it can only happen with the help of friction, that is, the Ekman layer. Close inspection of the dynamics actually shows that the vein does not spread but is inflated and deflated by the Ekman layer. At this downslope side, the surface of the gravity current is actually concave, as explained in Fig. 2. In this region, geostrophic speed increases (with the positive x direction being upslope), so downslope Ekman transport increases. Whenever the downslope Ekman transport increases, water is pumped out of the Ekman layer, and vice versa. This means that, when the surface of the gravity current is convex, water is pumped into the Ekman layer, as shown in Fig. 2, and vice versa, because of mass conservation. The thickness of the vein in the convex upper part, to the right of the green line in Fig. 2, decreases, while it increases in the concave part, to the left of the green line. Inspection of all our numerical results confirm the above behaviour, which allows us to construct a simple model for the vein dynamics.

If we put the above into mathematical language, we get:

$$\partial_t h = -\partial_x U_{\text{Ek}} = \frac{\delta}{2} \partial_x v_{\text{geo}} = \frac{\delta g'}{2f} \partial_{xx} h = \partial_x (\kappa_H \partial_x h), \quad (2)$$

where U_{Ek} is the Ekman transport in the x direction (negative in our experiments). This suggests that, to leading order, the evolution of the thickness h within the vein (not the friction layer) is given by the heat equation with a thickness diffusivity of $\kappa_H =$

$\sqrt{vg^2/(2f^3)}$). The boundary conditions at the lower and upper ends of the vein are important. At the downslope side end of the vein (point A), which is moving downward, the boundary condition is $\partial_x h(A) = 0$, which is automatically satisfied for the freely evolving height. At the upper end (point B), there is no flux if the surface is level, that is, $\partial_x h(B) = -\tan \alpha$, which I impose at the upper end of the vein. This leads automatically to the right detrainment of the integrated thickness $\int_A^B h dx$, through the friction layer, which is

$$\kappa_H \partial_x h(B) = -\kappa_H \tan \alpha = -\frac{\delta g'}{2f} \tan \alpha \quad (3)$$

Please note that there is no free parameter in the simple model, so no adjustment is possible! The finding that geostrophic dynamics subject to Ekman bottom friction can be described by a heat equation is also used by Gill (1982, Chap. 9.12, Eq. 9.12.8), MacCready (1994) and others. To the best of my knowledge, it has, so far, not been applied to gravity current dynamics. In Fig. 5, I see that the simple heat-equation model reproduces the shape of the vein very well from the integration of the Navier–Stokes equations for the runs

G00, G01 and G03. The differences at the upslope side of the gravity current suggest that the dynamics of the arrested Ekman layer is not completely captured by the idealised boundary condition. In Fig. 5, I show results after 24 and 60 h. At later times, the decrease in the reduced gravity g' , leading to a decreasing thickness diffusivity κ_H , has to be taken into account. It is most important to note that a variable thickness diffusivity does not change anything in the shape of the gravity current, the shape only evolves at a reduced speed. A heat equation with time-variable diffusivity can be transformed into a heat equation with a time-constant diffusivity by rescaling the time. It follows that the shape of a gravity current does not depend on the parameters; as long as the above calculations apply, the parameters only determine the speed of the evolution of the shape. Furthermore, the heat equation has self-similar solutions to which all initial distributions converge. This means that, even when two gravity currents differ initially, they converge to the same universal shape. So I have shown that there is one shape (a stable law) to which all 2.5-dimensional gravity currents converge, when the Ekman layer dynamics is linear!

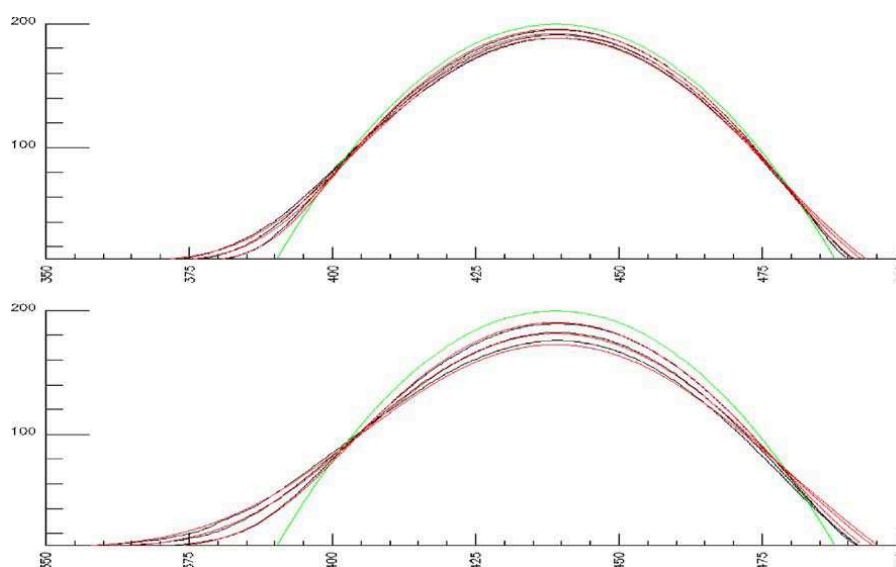


Fig. 5 Structure of the vein (thickness scale, vertical, starts from the thickness of the friction layer, 8 m) after 24 h (*upper figure*) and 60 h (*lower figure*) for the experiments G00 (least expanded), G01 and G03 (most expanded). Results from the Navier–Stokes

equation model (*black*) and the simple heat-equation model (*red*) are given. *Green line* shows the initial condition, which is identical in all experiments

In the case of a nonlinear friction law with a quadratic drag $\tau = c_D |\mathbf{u}| \mathbf{u}$ added to the linear friction, the heat (Eq. 3) transforms into:

$$\partial_t h = \partial_x \left[\frac{c_D g^2}{\sqrt{2} f^3} (\partial_x h + \tan \alpha)^2 + \kappa_H \partial_x h \right] = \partial_x (\kappa_H^{nl} \partial_x h) \quad (4)$$

Which is a non-linear heat equation with a diffusivity given by

$$\kappa_H^{nl} = \frac{c_D g^2}{\sqrt{2} f^3} (\partial_x h + 2 \tan \alpha) + \kappa_H. \quad (5)$$

Please note that, for Eq. 4 to be well defined, the nonlinear diffusivity κ_H^{nl} has to be always positive.

In our calculations, the transition to a weak nonlinear regime happens for a reduced gravity of around $2 \cdot 10^{-3} \text{ ms}^{-2}$ (exp. G12 is in a weakly non-linear regime). Supposing that, for such a parameter value, the linear and nonlinear diffusivity have equal magnitude, I obtain:

$$c_D = \frac{\sqrt{v f^3}}{2 g' \tan \alpha} \approx .5 \cdot 10^{-3}. \quad (6)$$

It is within measured values of the geostrophic drag coefficient over a smooth surface (Stull 1988). It is lower than the measured drag coefficients over the rough ocean floor, for which the value of $c_D = 3 \cdot 10^{-3}$ is often cited (Baringer and Price 1997; Killworth 2001). The estimation of friction parameters and laws is best performed using data assimilation techniques; the

convergence of such a method for the case of gravity currents is shown by Wirth and Verron (2008).

3.4 Detrainment through the frictional boundary layer

In the literature, there is no real agreement if water in oceanic gravity currents: (1) detrains, that is, the gravity current loses water to the surrounding, its volume decreases, but its density difference with the surrounding water stays constant; (2) entrains, that is the gravity current is diluted by surrounding water the density difference decreases and the volume increases (3) or if the gravity current mixes with the surrounding leading to a constant volume and a decrease in density anomaly. This question is of paramount importance for the evolution of the gravity current.

Initially, the experiment consists of two water masses separated by a sharp interface. The turbulent diffusivities κ_v and κ_h represent the vertical and horizontal mixing due to small scale dynamics (small in size compared to H in the vertical and L in the horizontal), not explicitly resolved by the numerical model. The vertical and horizontal turbulent diffusion times associated with the structures of the gravity current are estimated by: $t_{\text{diff}}^v = \kappa_v / H^2$ and $t_{\text{diff}}^h = \kappa_h / L^2$, where L is a typical horizontal and H a typical vertical scale of the gravity current. The value of the diffusivities depend on numerical variables as the numerical resolution. In the case presented here, $L = 20 \text{ km}$, this leads to a horizontal diffusion time at least ten times longer than the time of the experiments. The same is true if the vertical diffusion and scale of the vein is considered. This shows that, for the dynamics of the vein, the explicit mixing is negligible, as long as turbulent dynamics does not generate medium and large turbulent structures leading to turbulent diffusion across the stretched interface. The explicit impact of the diffusion on smaller size structures, such as the friction

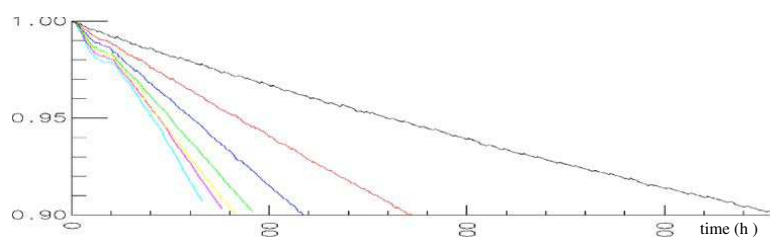


Fig. 6 The part of the gravity current in the vein. One sees a decrease in the volume of the vein differing between the experiments. The curves are, from left to right, for experiments

G17, G15, G14, G12, G03, G01 and G00, that is, decreasing temperature difference. The initial adjustment process (first 30 h) is clearly visible and followed by an almost linear behaviour

Table 3 Detrainment velocity

Exp.	ΔT (K)	w_{detr} (10^{-5} ms^{-1})	γ (10^{-4})
G00	0.25	1.1	1.4
G01	0.5	2.1	1.3
G03	0.75	3.2	1.3
G12	1.0	4.2	1.3
G14	1.1	4.6	1.3
G15	1.25	5.3	1.3
G17	1.5	6.2	1.2

layer ($H_{\text{fric}} \approx 10 \text{ m}$) cannot be neglected in the present experiments. I also checked that the results presented here show no significant dependence on the diffusivities by doubling their value in a control run.

The evolution of the volume of the vein, presented in Fig. 6, shows that the dominant dynamics of matter of the gravity current is a detrainment from the vein of the gravity current into the friction layer. It is then in the friction layer where the water moves down the slope. This detrainment, the loss of water in the vein, is measured in Fig. 6, which gives the temporal evolution of the surface of the cross section of the vein normalised by the total cross section of the gravity current (A/A_0 where $A_0 = 8/3 \cdot 10^6 \text{ m}^2$). In Table 3, the detrainment speed $w_{\text{detr}} = (dA/dt)/L$ and the detrainment parameter $\gamma = w_{\text{detr}}/\bar{v}_G$ is given for the experiments. I have shown in Subsection 3.2 that the horizontal extension of the gravity current varies only slightly from its initial value $L = 20 \text{ km}$, and will be taken as constant in the following analysis (see also Fig. 4).

One clearly sees that the detrainment rate γ has no significant change with the Richardson number. This comes as no surprise as, in the calculations presented here, the dynamics in the Ekman layer stays (close to) linear, and it is this dynamics that is responsible for the detrainment. Having said this, a comparison to linear theory imposes. The average transport in the bottom Ekman layer is $\bar{v}_G \delta/2$; this has to equal $w_{\text{detr}} L$ as the water comes out of the vein, and I obtain:

$$\gamma = \frac{w_{\text{detr}}}{\bar{v}_G} = \frac{\delta}{2L} = 1.1 \cdot 10^{-4}, \quad (7)$$

which compares very well to the values obtained in our experiments. It is also no surprise that the value obtained from linear theory is lower than the values obtained from the experiments as I did not consider the smaller transport added by the interfacial Ekman layer.

The detrainment values can be used to calculate the distance after which the vein of the gravity current has disappeared; as the detrainment rate does not depend on the Richardson number, to first order, this distance is equal for all the cases considered here and is given

by: $D_{\text{disappear}} = A_0/(L\gamma) \approx 10^6 \text{ m}$. This large distance demonstrates the persistence of the gravity current, when large-scale instabilities are excluded.

4 Discussion

I have demonstrated that rotating gravity currents consist of two parts, the vein and the friction layer. This two-part structure was also found in observations of Weatherly and Kelley (1982) and numerical simulations by Ezer and Weatherly (1990). The water in the vein above the Ekman layer travels along isobaths close to a geostrophic equilibrium descending only slowly into the deep ocean. The dynamics of the gravity current can be explained by Ekman layer theory. The vein detrains water to the friction layer. In the friction layer, the water progresses in the downslope direction. Although our simulations allow for a nonlinear chaotic dynamics, parts of the large-scale behaviour are well described by linear theory.

It is not the total gravity current that is important for the large-scale circulation but the vein, the thick part, that travels in an almost geostrophic dynamics along the isobaths descending slowly into the deep ocean. The vein can only maintain its reduced rate of descent by detraining water downstream at its lower boundary into the friction layer. In the friction layer, the water travels downslope and mixes with the surrounding water masses. It is water that is lost by the vein and does not take part in the large-scale propagation along the boundary. Streamtube models should, thus, model the dynamics of the vein and not the total gravity current, which has a different dynamics, as demonstrated above.

A key question I have not discussed so far is about the thickness of the Ekman layer, if it is negligible compared to the thickness of the vein, the dynamics of the friction layer can be truly neglected in the two-part structure and the dynamics of a gravity current is that of the vein sliding frictionless and being subject to large-scale instability. The Ekman transport, governing the evolution of the gravity current, is proportional to the Ekman layer thickness. In the calculations presented here, I choose a moderate value of less than 5 m for the Ekman layer thickness and, nevertheless, its dynamics is important. The true value of its thickness, being influenced by bottom roughness and the turbulence in the bottom layer, is likely to be of the same order or larger, amplifying the importance of the two-part structure of oceanic gravity currents and the results presented here. Ezer (2005) showed that the Ekman transport is responsible for roughly 20% of the

downslope transport in his simulations using a Mellor–Yamada parametrisation of vertical mixing.

The vertical resolution in today's OGCMs is too sparse to explicitly resolve the two-layer structure of the gravity current dynamics. The friction layer is, at best, a few metres thick, and its explicit representation asks for a resolution of the order of 1 m at the bottom, a resolution that is a few hundred times smaller than the actually employed vertical resolution at depth in OGCMs. General circulation models are, thus, not able to correctly predict the two-part structure of gravity currents, underestimate the detrainment and overestimate the descent of the vein (when neglecting other difficulties which inhibit the descent of the vein). Or, even worse, the detrained water will be found diluted in the grid-box downstream of the vein; as the thickness of the grid-box is much larger than that of the Ekman layer, the water will continue to move with the vein, and the diluted water will be counted as entrained rather than detrained. Following these arguments, it seems difficult to correctly represent the dynamics of a gravity current when the vertical extension of the bottom grid-box is smaller than the Ekman layer thickness.

Large-scale instabilities are explicitly suppressed in the research presented here by choosing a 2.5-dimensional geometry. Our results are, however, key to the research concerning the evolution of such instability as it gives the basic state from which large-scale instabilities will grow. So far, in the research on the instability of the vein of a gravity current, the basic state was conjectured or chosen to simplify the calculations (Meacham and Stephens 2001). The stable law of the shape of a gravity current, presented in Subsection 3.3, can now be used as the basis of analytical or numerical three-dimensional stability analysis.

In the experiments presented here, the Ekman number (the vertical viscosity ν_v) was fixed, leading to a laminar Ekman layer dynamics in our experiments, when a low value of the reduced gravity is considered. I exploited this dynamics and obtained that the evolution of the shape of the vein is governed by the heat equation with a diffusion coefficient, which can be calculated from the external parameters of the problem. For higher values of the reduced gravity, or lower values of the Richardson number, the vertical velocity within the Ekman layer leads to a change in its dynamics, and the linear friction laws are no longer applicable but are replaced by a quadratic drag law. I showed that, when a quadratic drag law applies, the dynamics is governed by a nonlinear heat equation.

It would be desirable to perform the 2.5-dimensional Boussinesq simulations with an explicitly resolved turbulent Ekman layer, which requires resolutions in the

centimetre scale in the vertical and horizontal direction, but this is beyond our actual computer resources. In the ocean, the vertical turbulent viscosity or even the friction law depends on unobserved quantities as the bottom roughness. Ongoing research is directed towards the determination of the friction laws and coefficients by data assimilation (Wirth and Verron 2008); by doing so, I hope to be able to avoid the explicit resolution and determination of small-scale processes and, nevertheless, obtain solid estimates for the small-scale turbulent fluxes, which will allow us to concentrate on the study of large-scale features.

This work is complementary to the theories of Killworth (2001) and others, who suppose that the thickness of the gravity current is determined locally by the entrainment or detrainment at the upper interface through a local Froude number criteria. The theory presented here determines the thickness non-locally by the convergences and divergences of the Ekman fluxes at the lower boundary and determines non-locally the evolution of the overall shape of the gravity current, using a (non-local) heat equation. This proves that there cannot be a purely local parametrisation of gravity current thickness. In realistic gravity currents, the two mechanisms are likely to act simultaneously. Furthermore, it was found in laboratory experiments on non-rotating gravity currents that the dissipative processes at the interface have a negligible role compared to those due to bottom friction (Ermanyuk and Gavrilov 2007). In oceanic gravity currents, the mixing and entrainment is enhanced by the roughness of the ocean floor, the change of slope and large-scale instabilities, features which are not considered here and which are the subjects of future research.

Acknowledgements I am grateful to Bernard Barnier, Yves Morel, Joel Sommeria and Jacques Verron for discussion and to two anonymous reviewers for their remarks which have greatly improved the paper. This work is part of the COUGAR project funded by ANR-06-JCJC-0031-01.

Appendix: Force balance in a rotating gravity current

In the x direction (upslope), the dominant force balance is between the Coriolis force and reduced gravity. In the y direction, the reduced gravity vanishes and the dominant force balance is between friction and the Coriolis force (Fig. 7). Using linear Ekman layer theory, I obtain:

$$fH \frac{v}{\cos \theta} \sin \theta - \frac{\nu \sqrt{2}}{\delta} \frac{v}{\cos \theta} \cos(\theta + \pi/4) = 0. \quad (8)$$

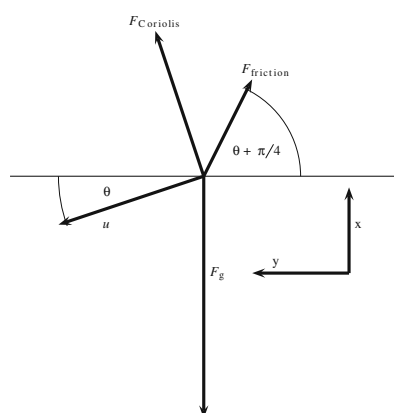


Fig. 7 Force balance in a gravity current descending at an angle θ to the horizontal at a constant speed u . The Coriolis force is at an angle of $3\pi/2$ to the direction of propagation and the frictional force at an angle of $5\pi/4$. In a stationary state, these two forces balance the gravitational force: $F_{\text{Coriolis}} + F_{\text{friction}} + F_g = 0$. Please note the turned coordinate system

As the angle of descent is small to leading order $\sin \theta \approx \theta$ and $\cos(\theta + \pi/4) \approx 1/\sqrt{2}$, Eq. 8 then gives:

$$\theta = \frac{v}{Hf\delta} = \sqrt{\frac{v}{2fH^2}} = \sqrt{\frac{Ek}{4}} \approx 1.1 \cdot 10^{-2}. \quad (9)$$

Please note that this result depends only on the Ekman number and is independent of the velocity of the gravity current. The analysis presented here does not apply to the friction layer as the Ekman spiral is not complete and θ is not small in this case, but can be extended to cases with a turbulent Ekman layer using a quadratic drag law.

References

- Baringer MO, Price JF (1997) Momentum and energy balance of the mediterranean outflow. *J Phys Oceanogr* 27:1678–1692
- Emms PW (1998) Streamtube models of gravity currents in the ocean. *Deep-Sea Res* 44:1575–1610
- Ezer T (2005) Entrainment, diapycnal mixing and transport in three-dimensional bottom gravity current simulations using the Mellor–Yamada turbulence scheme. *Ocean Model* 9:151–168
- Ezer T, Weatherly GL (1990) A numerical study of the interaction between a deep cold jet and the bottom boundary layer of the ocean? *J Phys Oceanogr* 20:801–816
- Ermanyuk EV, Gavrilov NV (2007) A note on the propagation speed of a weakly dissipative gravity current. *J Fluid Mech* 574:393–403
- Frisch U, Kurien S, Pandit P, Pauls W, Ray SS, Wirth A, Zou J-Z (2008) Hyperviscosity, Galerkin truncation, and bottlenecks in turbulence. *Phys Rev Lett* 101:144501
- Garrett C, MacCready P, Rhines P (1993) Boundary mixing and arrested Ekman layers: rotating stratified flow near a sloping boundary. *Annu Rev Fluid Mech* 25:291–323
- Gill AE (1982) *Atmosphere-ocean dynamics*. Academic, London, pp 662
- Griffiths RW (1986) Gravity currents in rotating systems. *Annu Rev Fluid Mech* 18:59–89
- Killworth PD (1977) Mixing on the Weddell Sea continental slope. *Deep-Sea Res* 24:427–448
- Killworth PD (2001) On the rate of descent of overflows. *J Geophys Res* 106:22267–22275
- Killworth PD, Edwards NR (1999) A turbulent bottom boundary layer code for use in numerical ocean models. *J Phys Oceanogr* 29:1221–1238
- Lane-Serf GF, Baines PG (1998) Eddy formation by dense flows on slopes in a rotating fluid. *J Fluid Mech* 363:229–252
- Lane-Serf GF, Baines PG (2000) Eddy formation by overflows in stratified water. *J Phys Oceanogr* 30:327–337
- Legg S, Hallberg RW, Girtton JB (2006) Comparison of entrainment in overflows simulated by z-coordinate, isopycnal and non-hydrostatic models. *Ocean Model* 11:69–97
- MacCready P (1994) Frictional decay of abyssal boundary currents. *J Mar Res* 52:197–217
- Meacham SP, Stephens JC (2001) Instabilities of currents along a slope. *J Prog Oceanogr* 31:30–53
- Nof D (1983) The translation of isolated cold eddies on a sloping bottom. *Deep-Sea Res* A 30:171–182
- Pedlosky J (1998) *Ocean circulation theory*. ISBN: 978-3-540-60489-1. Springer, Berlin Heidelberg New York, p 453
- Price JF, Baringer MO (1994) Outflows and deep water production by marginal seas. *Prog Oceanogr* 33:161–200
- Price JF, Yang J (1998) Marginal sea overflows for climate simulations. In: Cassignat E, Verron J (eds) *Ocean modeling and parameterization*. Kluwer, Dordrecht, pp 155–170
- Shapiro GI, Hill AE (1997) Dynamics of dense water cascades at the shelf edge. *J Phys Oceanogr* 27:2381–2394
- Shapiro GI, Zatsepin AG (1997) Gravity current down a steeply inclined slope in a rotating fluid. *Ann Geophys* 15:366–374
- Smith PC (1975) A stream tube model for bottom boundary currents in the ocean. *Deep-Sea Res* 22:853–873
- Smith PC (1977) Experiments with viscous source flows in rotating systems. *Dyn Atmos Ocean* 1:241–272
- Stull RB (1988) *An introduction to boundary layer meteorology*. Kluwer, Dordrecht
- Sutherland BR, Nault J, Yewchuk K, Swaters GE (2004) Rotating dense currents on a slope. Part 1. Stability. *J Fluid Mech* 508:241–264
- Umlauf L, Arneborg L, Burchard H, Fiekas V, Lass HU, Mohrholz V, Prandke H (2007) Transverse structure of turbulence in a rotating gravity current. *Geophys Res Lett* 34:L08601. doi:10.1029/2007GL029521
- Weatherly GL, Kelley Jr EA (1982) Too cold bottom layers at the base of the Scotian Rise. *J Mar Res* 40:985–1012
- Wirth A (2005) A non-hydrostatic flat-bottom ocean model entirely based on Fourier expansion. *Ocean Model* 9:71–87
- Wirth A, Verron J (2008) Estimation of friction parameters and laws in 1.5D shallow-water gravity currents on the f-plane, by data assimilation. *Ocean Dyn* doi:10.1007/s10236-008-0151-8
- Wu W, Danabasoglu G, Large WG (2007) On the effects of parameterized Mediterranean overflow on North Atlantic ocean circulation and climate. *Ocean Model* 19:31–52

4.8 Estimation of friction laws and parameters in gravity currents by data assimilation in a model hierarchy

<p>Noname manuscript No. (will be inserted by the editor)</p>

Estimation of Friction Parameters in Gravity Currents by Data Assimilation in a Model Hierarchy

A. Wirth

Received: date / Accepted: date

Abstract This paper is the last in a series of three investigating the friction laws and their parametrisation in idealised gravity currents in a rotating frame. Results on the dynamics of a gravity current (Wirth, *Ocean Dyn.* **59**, 551, 2009) and on the estimation of friction laws by data assimilation (Wirth & Verron *Ocean Dyn.* **58**, 247, 2008) are combined to estimate the friction parameters and discriminate between friction laws in non-hydrostatic numerical simulations of gravity current dynamics, using data assimilation and a reduced gravity shallow water model.

I demonstrate, that friction parameters and laws in gravity currents can be estimated using data assimilation. The results clearly show that friction follows a linear Rayleigh law for small Reynolds numbers and the estimated value agrees well with the analytical value obtained for non-accelerating Ekman layers. A significant and sudden departure towards a quadratic drag law at an Ekman layer based Reynolds number of around 800 is shown, in agreement with classical laboratory experiments. The drag coefficient obtained compare well to friction values over smooth surfaces. I show that data assimilation can be used to determine friction parameters and discriminate between friction laws and that it is a powerful tool in systematically connection models within a model hierarchy.

Keywords ocean dynamics · gravity current · friction laws · parameter estimation · data assimilation

PACS 65N35 · 76M22 · 86A05

1 Introduction

The realism today's and tomorrow's numerical models of the ocean dynamics is and will be governed by the accuracy of the parametrisations of the processes not explicitly

A. Wirth
LEGI / MEOM
CNRS
BP 53, 38041 Grenoble Cedex 9, France
E-mail: achim.wirth@hmg.inpg.fr

resolved and resolvable in these models. A typical example is the thermohaline circulation of the world ocean, a basin-scale long-time circulation. It is key to the climate dynamics of our planet and it is governed by small scale processes. The thermohaline circulation starts with the convective descent of dense water masses at high latitudes, a process performed by plumes smaller than a kilometre (Wirth & Barnier 2006 and Wirth & Barnier 2008). When the dense water touches the ocean floor and/or passes through a strait, a gravity current is created, which is governed by the friction forces at the ocean floor (Wirth 2009). The bottom friction is influenced by the dynamics at scales of the order of one meter and less. Similar small scale processes are likely to determine the subsequent deep western boundary current and the upward transport and the mixing in the interior and coastal regions of the ocean. These small scale processes will not be explicitly resolved in ocean general circulation models (OGCMS) even in a far future. The understanding and parametrisation of these processes is of paramount importance to the progress in modelling the dynamics of the climate.

In the present work I focus on bottom friction determined by small scale three dimensional turbulence. This process has much smaller spacial scales and faster time scales than the large scale circulation above. This scale separation in space and time is the prerequisite of an efficient parametrisation of bottom friction. Two types of bottom friction laws are commonly employed in engineering and geophysical fluid dynamics applications: a Rayleigh friction with a friction force per unit area $F = \rho h \tau u$ depending linearly on the fluid speed u at some distance of the boundary and a quadratic drag law $F = \rho c_D |u|u$, where τ and c_D are the linear friction parameter and the drag coefficient, respectively, h is the thickness of the fluid layer and ρ the density of the fluid. In todays ocean general circulation models a mixture of both laws is commonly employed, where the friction force per unit area is given by

$$F = \rho c_D \sqrt{u^2 + c^2} u. \quad (1)$$

The velocity c represents unresolved velocity due to tidal motion and other unresolved short time-scale processes. Typical values for c are a few tenths of centimetres per second. Such friction law leads asymptotically to a linear friction law for small velocities $u \ll c$ and to a quadratic drag law for $u \gg c$.

The precise determination of friction laws and parameters are also fundamental to the understanding of the large scale dynamics in the ocean. Gryanik *et al.* 2004, showed that the energy-containing scales of the large scale ocean dynamics is determined by the friction laws and parameters.

Bottom friction has also been identified as an important process acting as a sink of kinetic energy. Kinetic energy is principally injected into the ocean by the surface wind-stress at the basin scale. It can only be dissipated at scales where molecular viscosity is acting, that is below the centimetre scale. The pathway of the energy from the basin scale to the dissipation scale is currently to large parts unexplored. The turbulent bottom boundary layer dissipates energy at a rate proportional to $c_D V^3$ where c_D is the (local) drag coefficient and V the (local) flow speed near the boundary. The fact that the energy dissipation is proportional to the third power of the speed emphasises the importance of high speed events and processes in the vicinity of the ocean floor. The determination of the precise value of the drag coefficient which varies over an order of magnitude depending on the roughness of the boundary (see *e.g.* Stull 1988) is, therefore, key to determining the energy fluxes and budget of the worlds ocean.

In the present work I focus on the dynamics of oceanic gravity currents which is governed by bottom friction, as it was shown in Wirth (2009). Gravity currents are

clearly high-speed events at the ocean floor with speeds of over 1ms^{-1} . Friction laws and parametrisations at solid boundaries have been a major focus of research in fluid dynamics for the last century, due to their paramount importance in engineering applications. Although large progress has been made in determining the friction over rough boundaries (see *e.g.* Jiménez 2004) the friction depends of a variety of properties of the ocean floor which are undetermined, as for example: the roughness type, the roughness scales, the multi-scale properties of its roughness, the sediment suspension, the orientation of the roughness elements and the variability of the roughness, to mention only a few. Furthermore, these properties will not be available to ocean modellers in the foreseeable future. In the present work I determine the friction laws and parameters by observing the time evolution of the thickness of a gravity current. In the absence of a sufficient density of data from oceanic observations or laboratory experiments, the data is taken from nonhydrostatic numerical simulations of gravity current dynamics. Once the friction laws and parameters determined, they can be used in future integrations of ocean general circulation models (OGCM). To solve the inverse problem of determining the friction laws and parameters from the evolution of the gravity current, I use data assimilation. The formalism of estimating friction laws in oceanic gravity currents has been introduced and discussed in Wirth & Verron (2008).

I am here interested in the dynamics that governs the thick part of the gravity current, called the vein (see Wirth 2009). The friction layer, the thin part at the down-slope side of the vein, represents a water mass that is lost for the gravity current, does not contribute to its further evolution, and is mixed into the surrounding water in a short time. The dynamics of the friction layer, which is less than 20m thick, is also likely to be determined by small scale structures of the ocean floor.

This paper is the last in a series of three. In the first (Wirth & Verron 2008) we determined the feasibility and convergence of estimating friction parameters while observing only the thickness of the gravity current. In the second (Wirth 2009), I studied the dynamics of an idealised gravity current using a non-hydrostatic numerical model. I showed that such a gravity current has a two part structure consisting of a vein, the thick part, which is close to a geostrophic dynamics mostly perturbed by the influence of the Ekman pumping caused by bottom friction. At the down-slope side of the vein is the friction layer, the other part, completely governed by frictional dynamics. In the present work the two approaches are combined. The data is taken from non-hydrostatic numerical simulations of Wirth 2009 and provided to the assimilation scheme introduced in Wirth & Verron 2008. For the self-containedness of the present paper an overlap to the two previous papers is unavoidable.

The methodology presented here, although developed for the case of idealised gravity currents, is not restricted to such, but can be generalised to other processes investigated by a model hierarchy. Conceptually, I show how to systematically connect models of different complexity in a model hierarchy. The same methodology can be employed when parameters are to be estimated using data from observations or laboratory experiments.

In the next section I introduce the physical problem considered and the two mathematical models employed to study its dynamics, followed by a discussion of their numerical implementations. The data assimilation algorithm connecting the two models is discussed in section 3. A detailed presentation of the experiments performed is given in section 4, results are presented in section 5 and discussed in section 6.

2 Idealised Oceanic Gravity Current on the f-Plane

2.1 The Physical Problem Considered

In the numerical experiments I use an idealised geometry, considering an infinite gravity current in a rotating frame on an inclined plane with a constant slope, and I do not allow for variations in the long-stream direction. As discussed in Wirth (2009) a gravity current dominated by rotation is, to leading order, in a geostrophic equilibrium where the downslope acceleration due to gravity is balanced by the Coriolis force. Such gravity current flows along-slope, not changing its depth (see fig. 1). It is friction that makes a rotating gravity current flow downslope. This is the opposite in non-rotating gravity currents, where friction opposes the downslope movement and results from studies of non-rotating gravity currents can not be applied to rotating gravity currents. In the geometry considered here, I neglect the long-stream variation of the gravity current. Such a dynamics is usually referred to as 2.5 dimensional as it includes the fully three dimensional velocity vector but depends on only two space dimensions. Please note, that such simplified geometry inhibits large scale instability, the formation of the large cyclones and other large-scale features, which is beneficial to our goal of studying the friction laws due to only small scale dynamics.

The initial condition is a temperature anomaly which has a parabolic shape which is 200m high and 20km large at the bottom. The velocity is initially geostrophically adjusted (see subsection 2.2 for details).

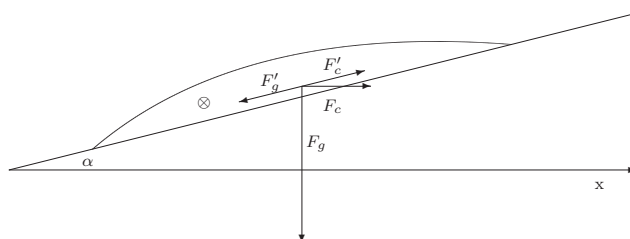


Fig. 1 Cross section of a gravity current with an average geostrophic velocity into the plane. The Coriolis force F_c and the buoyancy force F_g are shown. The fig. establishes the force balance between the projection of the Coriolis force F'_c and the projection of the buoyancy force F'_g onto the topographic slope, for a gravity current on a inclined plane, of angle α , when dissipative processes are neglected.

The physical problem is considered with the help of two mathematical models of different complexity. The first are the Navier-Stokes equations with a no-slip boundary condition on the ocean floor, subject to the Boussinesq approximation. The second is a single layer reduced gravity shallow water model. The bottom friction is explicitly resolved in the first while it has to be parametrised in the second.

2.2 The Navier-Stokes Model

The mathematical model for the gravity current dynamics are the Navier-Stokes equations subject to the Boussinesq approximation in a rotating frame with a buoyant scalar (temperature). The state vector is formed by the temperature anomaly of the gravity current water with respect to the surrounding water and all the three components of the velocity vector. I neglect variations in the stream wise (y -) direction of all the variables. Such type of model is usually referred to as 2.5 dimensional. The x -direction is upslope (see fig. 1). This leads to a four dimensional state vector depending on two space and the time variable, $(\Delta T(x, z, t), u(x, z, t), v(x, z, t), w(x, z, t))$.

The domain is a rectangular box that spans 51.2km in the x -direction and is 492m deep (z -direction). On the bottom there is a no-slip and on the top a free-slip boundary condition. The horizontal boundary conditions are periodic. The initial condition is a temperature anomaly which has a parabolic shape which is 200m high and 20km large at the bottom, as described in the previous subsection. The magnitude of the temperature anomaly ΔT is varied between the experiments. The reduced gravity is $g' = g \cdot 2 \cdot 10^{-4} \text{K}^{-1} \cdot \Delta T$ with $g = 9.8066 \text{ ms}^{-2}$. The Coriolis parameter is $f = 1.03 \cdot 10^{-4} \text{ s}^{-1}$. The initial velocities in the gravity current are geostrophically adjusted:

$$u_G = 0; \quad v_G = \frac{g'(\partial_x h + \tan \alpha)}{f}; \quad w_G = 0. \quad (2)$$

the fluid outside the gravity current is initially at rest. The buoyancy force is represented by an acceleration of strength $g' \cos(\alpha)$ in the z -direction and $g' \sin(\alpha)$ in the negative x -direction to represent the slope of an angle $\alpha = 1^\circ$. This geometry represents a rectangular box that is tilted by an angle of one degree. Such implementation of a sloping bottom simplifies the numerical implementation and allows for using powerful numerical methods (see next subsection).

2.3 Numerical Implementation of the Navier-Stokes Model

The numerical model used is HAROMOD (Wirth 2004). HAROMOD is a pseudo spectral code, based on Fourier series in all the spatial dimensions, that solves the Navier-Stokes equations subject to the Boussinesq approximation, a no-slip boundary condition on the floor and a free-slip boundary condition at the rigid surface. The time stepping is a third-order low-storage Runge-Kutta scheme. A major difficulty in the numerical solution is due to the large anisotropy in the dynamics and the domain, which is roughly 100 times larger than deep. There are 896 points in the vertical direction. For a density anomaly larger than .75K the horizontal resolution had to be increased from 512 to 2048 points (see table 1), to avoid a pile up of small scale energy caused by an insufficient viscous dissipation range, leading to a thermalized dynamics at small scales as explained by Frisch *et al.* (2008). The horizontal viscosity is $\nu_h = 5 \text{ m}^2 \text{ s}^{-1}$, the horizontal diffusivity is $\kappa_h = 1 \text{ m}^2 \text{ s}^{-1}$. The vertical viscosity is $\nu_v = 10^{-3} \text{ m}^2 \text{ s}^{-1}$, the vertical diffusivity is $\kappa_v = 10^{-4} \text{ m}^2 \text{ s}^{-1}$. The anisotropy in the turbulent mixing coefficients reflects the strong anisotropy of the numerical grid. I checked that the results presented here show only a slight dependence on ν_h, κ_h and κ_v by doubling these constants in a control run. This is no surprise as the corresponding diffusion and friction times are larger than the integration time of the experiments. There is a strong dependence on ν_v as it determines the thickness of the Ekman layer and the Ekman

transport, which governs the dynamics of the gravity current as I have shown in Wirth 2009. The vertical extension of the Ekman layer is a few meters while the horizontal extension of the gravity current is up to fifty kilometres. In a fully turbulent gravity current the turbulent structures within the well mixed gravity current will be isotropic and will therefore measure only a few meters in size. To simulate a fully turbulent gravity current 10^5 grid points would be necessary in the horizontal direction to obtain an isotropic grid. This is far beyond our actual computer resources.

The time of integration is limited due to the descending gravity current leaving the domain of integration when sliding down the slope, which depends on the initial density anomaly. The actual integration times in all experiments are given in table 1.

2.4 The Shallow Water Model

The second, and less involved, mathematical model for the gravity current dynamics is a 1.5 dimensional reduced gravity (1.5 layer) shallow water model on an inclined plane. The shallow water model, first proposed by Barré de Saint Venant (1871), and its various versions adapted for specific applications is one of the most widely used models in environmental and industrial fluid dynamics. For the derivation of the reduced gravity shallow water equations in a geophysical context, I refer the reader to the text book by Vallis (2006), and references therein.

As stated in the introduction I here specialise to a gravity current with no variation in the y -direction, the horizontal direction perpendicular to the down-slope direction. That is I have three scalar fields $\tilde{u}(x, t)$, $\tilde{v}(x, t)$ and $h(x, t)$ as a function of the two scalars x and t . The thickness of the gravity current is given by h . The velocities $\tilde{u}(x, t) = \int_0^h u(x, z, t) dz/h$ and $\tilde{v}(x, t) = \int_0^h v(x, z, t) dz/h$ represent the vertical averages over the whole layer thickness $h(x, t)$ of the local velocity components $u(x, z, t)$ and $v(x, z, t)$. I further suppose that the dynamics within the gravity current is well described by a two-layer structure: an Ekman layer with a thickness scale $\delta = \sqrt{2\nu_v/f}$ at the bottom and the rest of the gravity current above. To take into account several features of the gravity current dynamics discovered with the non-hydrostatic model (see Wirth 2009), the shallow-water model employed in Wirth & Verron (2008) had to be refined. Results presented in Wirth (2009) show, in agreement with Ekman layer theory, that the x -component of the velocity is concentrated in the Ekman layer. This confinement of u to the Ekman layer is included in the shallow water equations through the Coriolis-Boussinesq variable:

$$\beta = \frac{\int_0^h u^2 dz}{(\int_0^h u dz)^2} > 1 \quad (3)$$

If there is no vertical shear $\beta = 1$. If there is no bottom friction, the shear in a homogeneous fluid layer is small and $\beta \approx 1$. When Ekman layers are present there is substantial shear and $\beta > 1$. Ekman layers are a conspicuous feature in all geophysical flows subject to bottom friction and this has to be reflected in the mathematical model employed. In a shallow water model this can be done by explicitly *via* the Coriolis-Boussinesq variable. The Coriolis-Boussinesq variable is a function of the variation of the velocity profile in the vertical. When using the linear Ekman spiral, I obtain to first order $\beta = h/(2\delta)$ when $h \gg \delta$ which depends on the layer thickness h and is thus a function of space and time. Please see the appendix A for details concerning the calculations of the Coriolis-Boussinesq parameter.

The governing equations for the velocities vertically averaged over the whole thickness of the dynamic layer h , Ekman layer plus the rest above, are given by:

$$\partial_t \tilde{u} + \beta \tilde{u} \partial_x \tilde{u} - f \tilde{v} + g' (\partial_x h + \tan \alpha) = -D_u \tilde{u} + \nu \partial_x^2 \tilde{u}, \quad (4)$$

$$\partial_t \tilde{v} + f \tilde{u} = -D_v \tilde{v} + \nu \partial_x^2 \tilde{v}, \quad (5)$$

$$\partial_t h + \tilde{u} \partial_x h + h \partial_x \tilde{u} = \nu \partial_x^2 h. \quad (6)$$

The left hand side terms include the reduced gravity $g' = g\Delta\rho/\rho$ the slope α and the Coriolis parameter f . The non-linear term in the \tilde{v} -equation, that is $\tilde{u}\partial_x\tilde{v}$, is absent as the u velocity is concentrated in the Ekman layer and

$$\left| \frac{\int_0^h uv \, dz}{(\int_0^h u \, dz)(\int_0^h v \, dz)} \right| \ll 1. \quad (7)$$

On the right hand side I have the terms involving dissipative processes. Please note that this includes the bottom friction as well as the friction at the interface, in numerical experiments with the non-hydrostatic model (Wirth 2009) the latter is found to be smaller than the former. The parametrised friction is represented in the first term on the left hand side, involving:

$$D_u = D_u(x, t) = 4\beta (\tau + r/h^2 + c_D \sqrt{(4\beta \tilde{u})^2 + \tilde{v}^2})/h. \quad (8)$$

$$D_v = D_v(x, t) = (\tau + r/h^2 + c_D \sqrt{(4\beta \tilde{u})^2 + \tilde{v}^2})/h. \quad (9)$$

There are three free parameters τ , r and c_D . There is a linear friction constant parametrising dissipative effects that can be represented by linear Rayleigh friction. This linear friction is represented by two parameters τ and r , the first represents the part that is independent of the thickness and the second is divided by the square of the thickness. Usually the thickness of laminar boundary layers grows in time, when the dynamics is influenced by rotation, this growth is halted creating the well known Ekman layer dynamics (see *e.g.* Vallis 2006). Using only the term containing the parameter τ represents well the dynamics when an Ekman layer is developed, that is, when the thickness of the gravity current is larger than a few times the Ekman layer thickness. For smaller thicknesses, smaller than a few times the Ekman-layer thickness, a term involving the thickness of the gravity current should be included. I found heuristically that adding a friction force that depends quadratically on the layer thickness fits the data reasonably well for the gravity currents with a low density anomaly. In this publication I am, however mostly interested in the friction forces acting on the vein as stated in the introduction. In the results presented below the friction force due to the depth dependent term is a negligible part of the total friction, in the vein. The quadratic friction drag c_D , models the turbulent friction between the ground and the gravity current. The Coriolis-Boussinesq parameter is given by $\beta = h/(2\delta)$ for large values of the layer thickness, as derived in appendix A. If β is smaller than 2 it is put equal to 2 in the advection term and if it is smaller than 1/4 it is put to 1/4 in the friction terms. The first choice is consistent with the fact that in the advection term the Coriolis-Boussinesq parameter is by definition always larger than unity. Concerning the friction terms: for large layer thickness, β agrees with the value calculated in the appendix A and for a very small layer thickness, $\beta = 1/4$ agrees with the fact that the friction in the x and y direction in eqs. (8) and (9) should have the same form in the absence of an Ekman spiral. I checked that the choices for these thresholds have only a negligible influence

on the results. The term involving the viscosity/diffusivity ν represents horizontal dissipative processes, its value is chosen to provide numerical stability of the calculations (see subsection 2.5).

Clearly, the geostrophic velocity:

$$\tilde{u} = 0, \quad \tilde{v} = \frac{g'}{f}(\partial_x h + \tan \alpha), \quad (10)$$

is a solution of eqs. (4 – 6) when $D_u = D_v = 0$ and $\nu = 0$. The estimation of D or more precisely of the parameters τ , r and c_D are the subject of the present work. By using data assimilation I plan to obtain the friction constants τ and c_D and thus determine if the friction acting on the vein is dominated by a linear or a quadratic law.

2.5 Numerical Implementation of the Shallow Water Model

The shallow water model is implemented with a first order finite difference scheme in space and time. There are 500 points in the x -direction, leading to a resolution of 200m, the time step is 5s. The value of the horizontal viscosity/diffusivity is a function of the resolution and provides for the numerical stability of the code. I verified that the here presented results show only a negligible dependence when the value of the horizontal viscosity/diffusivity was halved and doubled, the actual value used is $\nu_H = 5\text{m}^2\text{s}^{-1}$, it is identical to the corresponding value ν_h in the non-hydrostatic model.

3 Ensemble Kalman Filter and its Implementation

For the self containedness of this publication the implementation of the Ensemble Kalman filter is explained here, the reader familiar with Wirth & Verron (2008) is invited to skip the section.

The ensemble Kalman filter (EnKF) is the main tool of our experiments performing the parameter estimation and providing us with the actual parameter values. The EnKF was introduced by Evensen (1994) and is used in data assimilation and parameter estimation experiments (see Evensen (2003) and Brusdal *et al.* 2003). I refer the reader not familiar with the EnKF and the employed notation to the above mentioned publications.

Every hour in time and every 1 km in the x -direction, the vertical extension of the gravity current, that is $h(x, t)$, is assimilated. Choosing a horizontal resolution for the assimilation 5 times sparser than the dynamical model does not only reduce the size of the assimilation experiment, but is also consistent with the fact, that the grid-scale dynamics of the numerical model is dominated by dissipation and has only negligible dynamical information. I am only assimilating the vertical extension of the gravity current as it is the variable most easily measured in the ocean and in laboratory experiments. The measurement of the vertically integrated velocity within the gravity current, the other dynamical variable of the shallow water model, is more difficult to measure in the ocean and in laboratory experiments.

The assimilation is performed on the augmented state vector consisting of the vertical extension, the two velocity components and the three constant-in-time friction parameters:

$$\mathbf{x}(\bar{x}, \bar{t}) = (h(\bar{x}, \bar{t}), \tilde{u}(\bar{x}, \bar{t}), \tilde{v}(\bar{x}, \bar{t}), \tau, r, c_D)^t. \quad (11)$$

Where \bar{x} and \bar{t} is the discretized version of x at assimilation grid-points and t at assimilation times, respectively and t denotes transposition. The only (observed) variable assimilated is the vertical extension (h) of the gravity current. The analysis step for the EnKF reads,

$$\mathbf{x}_i^a = \mathbf{x}_i^f + \mathbf{K} \left(h^{obs} + \epsilon_i - \mathbf{H} \mathbf{x}_i^f \right) \quad (12)$$

$$\mathbf{K} = \mathbf{P} \mathbf{H}^T (\mathbf{H} \mathbf{P} \mathbf{H}^T + \mathbf{W})^{-1} \quad (13)$$

Where the index $i = 1, \dots, m$ runs over the realisations. The observation operator \mathbf{H} projects the state vector in the space of observations. The noise vectors ϵ_i represents the independent Gaussian-distributed zero-mean and σ -standard-deviation noise added to every observed value (see Burgers *et al.* 1998) and $\mathbf{W} = \sigma^2 \mathbf{I}$ where \mathbf{I} is the unity matrix. The estimated error covariance matrix is given by

$$\mathbf{P} = \frac{1}{m-1} \sum_{i=1}^m (\mathbf{x}_i^f - \langle \mathbf{x}^f \rangle) (\mathbf{x}_i^f - \langle \mathbf{x}^f \rangle)^t, \quad (14)$$

where m is the size of the ensemble and $\langle \cdot \rangle$ denotes an ensemble average. The covariance matrix is truncated to a tridiagonal form to avoid spurious correlations between distant correlations, caused by under sampling. This is also consistent with the dynamics at hand as the maximum velocities (see subsection 2.1) and wave speeds, given by $\sqrt{g'h}$ are of the order of 0.2ms^{-1} . This means that in the assimilation period of 1 hour information can travel to the next assimilation point one kilometre away, but it can not reach over the distance of two assimilation grid points. In between assimilation points h is interpolated linearly.

In general the observed value of the vertical extension of the gravity current $h^{obs}(x, t)$ includes measurement errors $\eta(x, t)$ and is related to the true value by $h^{obs}(x, t) = h^{true}(x, t) + \eta(x, t)$. For consistency the measurement error $\eta(x, t)$ has the same first (zero mean) and second order moment ($\tilde{\sigma}^2$) as the noise vectors $\epsilon_i(x, t)$, but does not depend on the actual realisation, that is i . When assimilating data, σ has to be provided prior to the experiment whereas $\tilde{\sigma}$ is usually not known and can only be estimated.

In our parameter estimation experiments, the ensemble size is $m = 100$, this is much larger than the number of parameters to estimate, that is three, equal to the number of observations at each assimilation time, but smaller than the dimension of the augmented state vector $\mathbf{x} = (\mathbf{h}, \mathbf{\tilde{u}}, \mathbf{\tilde{v}}, \tau, r, c_D)$, that is 303. Using an ensemble size an order of magnitude larger did not improve the convergence significantly, reducing the ensemble size an order of magnitude leads to a frequent divergence of the assimilation.

It is important to note that not only the parameter values are estimated, but the entire state vector is updated every time data is assimilated. This allows to perform parameter estimation in the case where the shallow-water model is unable, even with perfectly adjusted parameters, to reproduce some aspects of the Navier-Stokes dynamics. Entrainment is a typical example, it happens in the Navier-Stokes dynamics, there is no reliable parametrisation available for the shallow-water model and friction parameters can not account for all the impacts of entrainment on the evolution of the layer-thickness. Trying to estimate the friction parameters without correcting the other values of the state vector frequently leads to a divergence of the estimation procedure in experiments where mixing, entrainment or detrainment is present (experiments with high values of the density anomaly).

Another important point is, that the parameter values are supposed to be constant in time. The values of the friction parameters are clearly non-negative, so every time the assimilation scheme provides a negative value of one of these parameters, which is possible due to the linearity of the analysis step and the statistical nature of the EnKF, the value is put to zero.

All pseudo-random-numbers were generated by a “Mersenne Twister” (Matsumoto & Nishimura 1998).

4 Experiments

The goal of our data assimilation experiment is to determine the friction laws acting on the vein of a gravity current, linear versus quadratic, and the corresponding friction parameters, by only observing the vertical extension (h) of the gravity current. The vertical extension, that is the density structure of a gravity current is the variable that is easiest to measure and to observe in the ocean and in laboratory experiments. Velocities, even their average values are hard to determine as they are highly variable in space and intermittent in time. The thickness h is extracted from the runs of the Navier-Stokes model, it is determined by the position above ground of the thermocline that corresponds to half the initial maximum temperature anomaly in the gravity current at the assimilation points x , every 1km, and the assimilation times t , every hour. It is the time series of these shapes $h(x, t)$, and only these, which are provided to the assimilation run to determine the friction parameters. Please note that the space integral of h , the total volume, is not conserved but has some slight variation due to mixing, entrainment and detrainment, whereas in the shallow water model without assimilation it is conserved. The data assimilation procedure corrects the total state vector, including the h -value and the method can thus deal consistently with variations in the total gravity current fluid volume (or area in our 2.5D case).

A series of seven experiments was performed. The density anomaly ΔT is the only parameter varied between the experiments. A list of all experiment performed, the duration of the experiment, the average geostrophic velocity \bar{v}_g and the Reynolds number,

$$Re_{Ek} = \frac{v_g \delta}{\nu_v} = \frac{\Delta T \cdot 2 \cdot 10^{-4} \text{K}^{-1} g \tan(\alpha) \sqrt{2}}{\sqrt{f^3 \nu}} = \Delta T \cdot 1.5 \cdot 10^3 \text{K}^{-1}, \quad (15)$$

based on the Ekman layer thickness, given by $\delta = \sqrt{2\nu/f}$, are shown in table 1. The Reynolds number based on the Ekman layer thickness, is the determining parameter for laminar flow. When vertical velocities develop (absent in the homogeneous linear Ekman layer), the now turbulent Ekman layer increases in thickness and the actual Reynolds number is larger than calculated by eq. (15) and given in table 1. Results shown in the next section show that vertical velocities become significant for temperature anomalies of about one Kelvin. When vertical velocities are important the flow is characterised by the surface Rossby number,

$$Ro = \frac{v_g}{f z_0} = \frac{v_g u_*}{f \nu_v} = \frac{\sqrt{c_D} v_g^2}{f \nu_v}, \quad (16)$$

where z_0 is the roughness length, which for smooth surfaces is given by $z_0 = \nu_v/u_*$. The friction velocity $u_* = \sqrt{c_D} v_g$ and the surface Rossby number are results of our

numerical calculations, rather than an initial parameter, and is therefore presented in table 2 of the Results section. In the turbulent boundary layer vertical velocities of order u_* develop. The typical length scale is now formed by a balance between rotation effects and vertical velocity $\delta_{turb} \approx u_*/f$, rather than the balance between viscosity and rotation for the laminar case. Observations show that the actual thickness of the turbulent Ekman layer is $\approx \delta_{turb}/4$, including a log-layer of thickness $\approx \delta_{turb}/10$. The above teaches us, that the surface Rossby number is the equivalent to the Ekman-scale Reynolds number with a turbulent Ekman layer thickness δ_{turb} replacing the laminar Ekman layer thickness δ . The former characterises turbulent flow and the latter laminar flow. To avoid confusion I continue to discriminate between the experiments in terms of temperature anomaly rather than Reynolds or surface Rossby number. The surface Rossby number is also a measure of the thickness of the turbulent Ekman layer (or the log-layer) to the thickness of the viscous sub-layer $\delta_{sub} = \nu/u_*$ (Please see McWilliams 2006 chapter 6 for a concise introduction to planetary boundary layer dynamics).

Exp.	ΔT (K)	integration time (h)	\bar{v}_g (m s ⁻¹)	Re_{Ek}
G00	0.25	360	.0830	$.38 \cdot 10^3$
G01	0.5	192	0.166	$.75 \cdot 10^3$
G03	0.75	132	0.249	$.88 \cdot 10^3$
G12	1.0	96	0.332	$1.5 \cdot 10^3$
G14	1.1	86	0.365	$1.7 \cdot 10^3$
G15	1.25	76	0.415	$1.9 \cdot 10^3$
G17	1.5	66	0.498	$2.3 \cdot 10^3$

Table 1 Estimated parameter values in the numerical experiments

In the data assimilation experiment the observation error for the layer thickness was set to $\sigma = 10\text{m}$. I checked that the results presented in the next section do not depend significantly on the actual value of σ when chosen within reasonable limits. The ensemble of the initial values for the parameters was chosen randomly, with an ensemble mean value at the order of magnitude of the expected values. The procedure was iterated by using the ensemble at the end of a assimilation experiment as the initial ensemble for the consecutive experiment. I also tried inflation of the ensemble values, the distance from the ensemble mean was increased by a constant factor for every ensemble member at every assimilation time, to avoid spurious decrease of the ensemble variance. Inflation did not change significantly the results. All results reported here were done without inflation.

5 Results

In the case of a (linear stationary) Ekman dynamics, the linear Rayleigh friction can be calculated analytically, as already explained in Wirth (2009):

$$\tau = \frac{\nu}{\delta} = \sqrt{\frac{\nu f}{2}} \quad (17)$$

with an Ekman layer thickness $\delta = \sqrt{2\nu/f}$. The value for the calculations presented here is: $\tau = 2.27 \times 10^{-4} \text{ms}^{-1}$.

I started by performing parameter estimation experiments using the shallow water model used in Wirth & Verron (2009), that is, without the Coriolis-Boussinesq parameter and the thickness dependent parameter r , results were poor. The results for the vein improved significantly when the non-linear term was multiplied by the Coriolis-Boussinesq parameter. A free evolution of the shallow water model (without data assimilation) with the estimated values of τ and c_D showed results that compare poorly with the data for the thickness h from the non-hydrostatic calculations in friction layer, where the thickness is small. This problem improved when the parameter space was augmented by the thickness dependent parameter r . In the words of data assimilation: without the calculated Coriolis-Boussinesq parameter and the estimated friction parameter r the assimilation converged to a (local) minimum of the cost function which has a value that is not small enough. In the words of a dynamicist: without the Coriolis-Boussinesq parameter and the parameter r an important physical process is missing and the dynamics can not be understood without it. I like to emphasise that without using data assimilation one might have thought that one just did not find the right minimum in parameter space, with data assimilation one can be more confident, so not certain, that the minimum was found but the model had major deficiencies so that it is not capable to represent well enough the dynamics. Anyhow, adding the Coriolis-Boussinesq parameter and the thickness dependent friction leads to an improvement of the representation of the dynamics, especially for the cases with a high temperature anomaly (ΔT).

The experiments are listed in table 1 and results are presented in table 2. The results for the Rayleigh friction parameter (τ) compare well to the analytical value of equation (17) for small values of the temperature anomaly. The impact of the thickness dependent friction parameter r is negligible in the thick part of the gravity current in all the experiments performed (see table 2). The drag coefficient is small in these cases with a small temperature anomaly but increases abruptly with the temperature anomaly and represents a substantial part of the total friction in the experiments with a larger temperature anomaly. I also calculated for all experiments an effective drag coefficient:

$$\tilde{c}_D = c_D + \frac{\tau}{v_g}, \quad (18)$$

and the surface Rossby number Ro . It is the effective drag coefficient that is usually represented in diagrams like fig. 2 by the engineering community (Schlichting & Gertsen 2000), as it is difficult to separate the two friction laws without using data assimilation.

Exp.	$\tau \cdot 10^{-4} \text{ms}^{-1}$	$r \cdot 10^{-2} \text{m}^2 \text{s}^{-1}$	$c_D \cdot 10^{-4}$	$\tilde{c}_D \cdot 10^{-4}$	Ro
G00	1.9	3.2	.01	23.	$6.7 \cdot 10^1$
G01	2.4	2.4	.2	15.	$0.12 \cdot 10^4$
G03	2.0	2.3	1.6	9.6	$0.77 \cdot 10^4$
G12	2.1	1.5	1.2	7.5	$1.2 \cdot 10^4$
G14	2.1	1.0	1.2	7.0	$1.4 \cdot 10^4$
G15	1.7	.6	1.4	5.5	$2.0 \cdot 10^4$
G17	1.4	.4	1.5	4.3	$3.0 \cdot 10^4$

Table 2 Estimated parameter values in the numerical experiments

The sudden appearance of a drag law at Reynolds numbers $Re_{Ek} \approx 8 \cdot 10^2$ is shown. The values of the effective drag coefficient are shown in fig. 2. Another interesting feature of the assimilation procedure is, that I not only obtain effective drag coefficient as is usually the case but I clearly manage to separate the friction process in a linear and a quadratic part, gaining further insight in the dynamics.

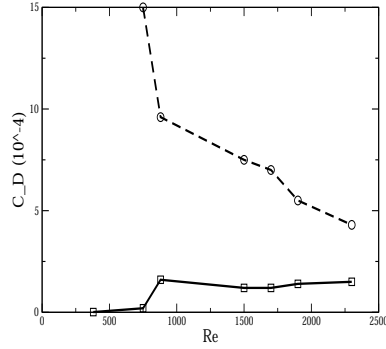


Fig. 2 The drag coefficient c_D (straight line) and the effective drag coefficient \bar{c}_D (dashed line), are presented as a function of the Reynolds number (based on the laminar Ekman layer thickness) Re_{Ek}

When comparing the dynamics of a free run of the shallow-water model, without data assimilation to the dynamics of the Navier-Stokes model, the agreement is generally satisfactory, but deteriorates with increasing temperature anomaly of the gravity current. I have to emphasise that a difference between a free run with adjusted parameters to the data, does not *a priori* devaluate the parameter estimation. The difference might originate from a process not represented, neither directly nor parametrised, in the shallow-water model. During the data assimilation this difference is corrected by the update of the whole state vector, in the free run this correction is absent. More precisely: entrainment, detrainment and mixing changes the layer thickness h and the overall volume of the gravity current, the importance of these processes increase with the Reynolds number. The corresponding parameters are not estimated in the shallow-water model. A change of the total volume can not be obtained by changing the friction parameters, as they do not affect the volume of the gravity current. The layer thickness is corrected at every data assimilation as it is part of the state vector. The free run and the data do therefore not necessarily agree, even when the total volume of the gravity current is considered.

As stated in section 3 I supposed the parameters to be constant, a variability in time is clearly detected in all three parameters. Their variability is however small compared to their absolute value.

6 Discussion

I have demonstrated, that friction parameters and laws in gravity currents can be estimated using data assimilation. The results clearly show that friction follows a linear Rayleigh law for small Reynolds numbers and the estimated friction coefficient agrees well with the analytical value obtained for non-accelerating Ekman layers. A significant and sudden departure towards a quadratic drag law at Reynolds number of around 800 is shown, roughly in agreement with laboratory experiments (Nikuradse 1933, Schlichting & Gertsen 2000). Although the quadratic drag law is dominated by the linear friction at the Reynolds numbers considered in this study, the assimilation procedure clearly manages to detect its appearance and consistently estimate its value. The drag coefficient obtained $\approx 1.5 \cdot 10^{-4}$ (see table 2) is on the lower end of classical values over smooth surfaces (see Stull 1988, Schlichting & Gertsen 2000). This comes at no surprise as only part of the turbulent small scale motion, responsible for the turbulent viscosity, is explicitly resolved in the non-hydrostatic model, due to the strong anisotropy in the numerical grid (see subsection 2.3). The experiments were performed for moderate surface Rossby numbers as: (i) the numerical resolution in the Navier-Stokes model does not allow for an explicit representation of the fully turbulent Ekman layer (see subsection 2.3) and (ii) with increasing Rossby number non-hydrostatic effects become important, neither explicitly resolved nor implicitly included (parametrised) in the shallow water model used for the assimilation.

Comparison of free runs of the shallow-water model with the estimated parameter values clearly show that the shallow-water model performs well in the vein, whereas it deteriorates in the friction layer with increasing temperature anomaly. In these areas the local Froude number is larger than unity and the oscillations of the interface and its breaking starts to develop. These non-hydrostatic processes are neither explicitly included in the (hydrostatic) shallow-water model nor are they parametrised. The parametrisation of the dynamics at the interface, including the mixing, entrainment and detrainment, is subject to current research, using higher resolution three dimensional non-hydrostatic simulations of only a small part of the gravity current. Furthermore, to represent the bottom friction in the shallow water model I supposed that unaccelerated linear Ekman layer theory applies to leading order. This assumption is questionable when non-linear effects, leading to a drag law, become dominant. I demonstrated that the linear dynamics and the nonlinear departure from it are well captured in the present work. I also showed that data assimilation is a powerful tool in systematically connection models in a model hierarchy.

The parameters of the two most observed and employed friction laws, Rayleigh friction and the drag law, are estimated here. The methodology is not restricted to this two laws, this linear and quadratic laws can also be seen, pragmatically, as the beginning of a Taylor series.

Friction forces are difficult to observe directly or to determine in laboratory experiments, as forces exerted on the boundary are small, inhomogeneous in space and intermittent in time. I have also performed laboratory experiments on rotating gravity currents on the Coriolis platform in Grenoble (France) and measured its thickness. The quantity of data measured was not sufficient to determine the friction parameters and laws. Further laboratory experiments with a substantially increased number of observations are planned.

A Appendix: Calculation of the Coriolis-Boussinesq parameter for linear Ekman layers

The Solution for the Ekman spiral of a fluid moving with a constant geostrophic speed of V_G in the y-direction is given by:

$$\bar{u} = V_G \exp(-z/\delta) \sin(z/\delta) \quad (19)$$

$$\bar{v} = V_G (1 - \exp(-z/\delta) \cos(z/\delta)), \quad (20)$$

where I have denoted \bar{u} the variable that has a dependence in the z -direction as opposed to vertically averaged value $u = \langle \bar{u} \rangle = \frac{1}{h} \int_0^h \bar{u} dz$. The vertical average of the velocity component in the x-direction and its square, using eq. (19), are:

$$u = \langle \bar{u} \rangle = \frac{1}{h} \int_0^h \bar{u} dz = \frac{V_G}{h} \int_0^h \exp(-z/\delta) \sin(z/\delta) dz = \frac{V_G \delta}{2h} = \frac{V_G}{4\beta} \quad (21)$$

$$u^2 \neq \langle \bar{u}^2 \rangle = \frac{V_G^2}{h} \int_0^h \exp(-2z/\delta) \sin^2(z/\delta) dz = \frac{V_G^2 \delta}{8h} = \frac{V_G^2}{16\beta} \quad (22)$$

$$\beta = \frac{\langle \bar{u}^2 \rangle}{\langle \bar{u} \rangle^2} = \frac{h}{2\delta} \quad (23)$$

Please note that equation (21) shows that the mean velocity in the x-component is only one quarter of geostrophic velocity divided by β . Linear Ekman layer theory shows, that the frictional force is equal in both directions, so that in the friction term the u value has to be multiplied by 4β . The non-linear term in the v -equation is $u \partial_x v$ is vanishing to leading order of β^{-1} as the u -velocity is concentrated in the Ekman layer, whereas the bulk of the v -momentum is above it.

I used:

$$\int \exp(-z/\delta) \sin(z/\delta) dz = \frac{-\delta}{2} (\sin(z/\delta) + \cos(z/\delta)) \quad \text{and} \quad (24)$$

$$\int \exp(-2z/\delta) \sin^2(z/\delta) dz = \frac{-\exp(-2z/\delta)}{8} (2 \sin^2(z/\delta) + \sin(z/\delta) \cos(z/\delta) + 1). \quad (25)$$

I emphasise that these calculations are only valid for the unaccelerated laminar Ekman layer.

References

1. K. Brundal, J.M. Brankart, G. Halberstadt, G. Evensen, P. Brasseur, P.J. van Leeuwen, E. Dombrowsky, & J. Verron (2003) A demonstration of ensemble-based assimilation methods with a layered OGCM from the perspective of operational ocean forecasting systems *J. Marine Systems*. **40-41**, 253–289.
2. G. Burgers, P. van Leeuwen & G. Evensen (1998) Analysis scheme in the ensemble Kalman filter *Mon. Weather Rev.* **126**, 1719–1724.
3. G. Evensen (1994), Sequential data assimilation with a nonlinear quasi-geostrophic model using Monte Carlo methods to forecast error statistics. *J. Geophys. Res.* **99**, 10,143–10,162.
4. G. Evensen (2003), The ensemble Kalman filter: theoretical formulation and practical implementation. *Ocean Dyn.* **53**, 343–367.
5. Frisch U., S. Kurien, R. Pandit, W. Pauls, S. Sankar Ray, A. Wirth, and J.-Z. Zhu, “Hyperviscosity, Galerkin Truncation, and Bottlenecks in Turbulence” *Phys. Rev. Lett.*, **101**, 144501, 2008.
6. N. Gryanik, I. M. Held, K. S. Smith & G. K. Vallis (2004) The effects of quadratic drag on the inverse cascade of two-dimensional turbulence, *Phys. Fluids* **16**, 73; doi:10.1063/1.1630054.
7. J. Jiménez (2004), Turbulent flows over rough walls, *Ann. Rev. Fluid Mech* **36**, 173–196.

-
8. M. Matsumoto and T. Nishimura (1998), Mersenne twister: a 623-dimensionally equidistributed uniform pseudorandom number generator. *ACM Trans. Model. Comput. Simul.* **8**, pp., 3–30.
 9. J.C. McWilliams (2006), *Geophysical Fluid Dynamics*, Cambridge University Press.
 10. J. Nikuradse (1933), Stromungsgesetze in rauhen Rohren, *Verein deutscher Ingenieure Forschungsheft* **361**, 1–22.
 11. B. de Saint Venant (1871), Théorie du mouvement non permanent des eaux, avec application aux crues des rivières et à l'introduction des marées dans leur lit. *C. R. A. S.* **73**, 147–154.
 12. Schlichting & Gertsen(2000), *Boundary-Layer Theory*, Springer Verlag.
 13. G. Vallis 2006, *Atmospheric and Oceanic Fluid Dynamics*, Cambridge University Press.
 14. A. Wirth (2004), A non-hydrostatic flat-bottom ocean model entirely based on Fourier expansion, *Ocean Mod.* **9**, pp. 71–87.
 15. irth, A (2009), “On the basic structure of oceanic gravity currents” *Ocean Dynamics* **59**, 551–563. DOI 10.1007/s10236-009-0202-9
 16. A. Wirth & Barnier (2006), “Tilted convective plumes in numerical experiments,” *Ocean Mod.* **12**, pp. 101–111.
 17. A. Wirth & Barnier (2008), “Mean circulation and structures of tilted ocean deep convection”, *J. Phys. Oceanogr.*, **38**, 803 – 816, 2008.
 18. Wirth, A & J. Verron (2008), “Estimation of Friction Parameters and Laws in 1.5D Shallow-Water Gravity Currents on the f-Plane, by Data Assimilation” *Ocean Dynamics* **58**, 247–257. DOI 10.1007/s10236-008-0151-8

4.9 On the numerical resolution of the bottom layer in simulations of oceanic gravity currents

Manuscript prepared for J. Name
with version 3.2 of the L^AT_EX class copernicus.cls.
Date: 8 February 2010

On the numerical resolution of the bottom layer in simulations of oceanic gravity currents

N. Laanaia, A. Wirth, J.M. Molines, B. Barnier, and J. Verron

LEGI / MEOM / CNRS (France)

Abstract.

The role of an increased numerical vertical resolution, leading to an explicit resolution of the bottom Ekman layer dynamics, is investigated. Using the hydrostatic ocean model NEMO-OPA9, we demonstrate that the dynamics of an idealised gravity current (on an inclined plane), is well captured when a few (around five) sigma-coordinate levels are added near the ocean floor. Such resolution allows to considerably improve the representation of the descent and transport of the gravity current and the Ekman dynamics near the ocean floor, including the important effect of Ekman veering, which is usually neglected in today's simulations of the ocean dynamics.

Results from high resolution simulations (with σ and z -coordinates) are compared to simulations with a vertical resolution commonly employed in today's ocean models. The latter show a downslope transport that is reduced by almost an order of magnitude and the decrease in the along slope transport is reduced six-fold. We strongly advocate for an increase of the numerical resolution at the ocean floor, similar to the way it is done at the ocean surface and at the lower boundary in atmospheric models.

1 Introduction

The realism of numerical models of the ocean dynamics depends on their capability to correctly represent the important processes, at large and also at small scales. The dynamics of gravity currents was identified as a key process governing the strength of the thermohaline circulation and its heat transport from low to high latitudes (Willebrand *et al.* 2001). Oceanic gravity currents are small scale processes, only about 100km

wide and a few hundred meters thick, that have a substantial impact on the global climate dynamics.

A conspicuous feature of today's numerical simulations of the ocean circulation is their increased vertical resolution at the ocean surface. It is the physics of the near surface processes and their importance for the large scale ocean circulation that imposes the grid refinement near the surface. More precisely, the ocean is forced predominantly by fluxes of inertia and heat at its surface. These fluxes give rise to the so called planetary boundary layer dynamics (PBL). It is through this boundary layer, that the surface forcing propagates to the interior ocean. The quality of a simulation of the ocean dynamics is thus governed by the representation of the PBL dynamics. The important dynamical processes in the surface PBL have a smaller vertical scale than the dynamics in the interior ocean and this fact has to be represented in the grid of the numerical model, leading to the above mentioned refinement near the surface.

At the ocean floor a similar PBL develops. This feature is, however, rarely reflected in the structure of the vertical resolution. To the contrary, the grid size is usually an increasing function of depth, leading to the sparsest resolution at the ocean floor. The PBL dynamics at the ocean floor can not be explicitly represented with such a vertical grid. Please note, that in numerical models of the dynamics of the atmosphere, a grid refinement near the earth's surface is commonly employed to resolve explicitly a large part of the important processes at this boundary. The dynamics at the ocean floor is however similarly important and involved, as the dynamics at the ocean surface and at the lower boundary of the atmosphere. A large part of the kinetic energy is supposed to be dissipated at the ocean floor representing a major sink of kinetic energy and an important player in the global energy cycle of the ocean dynamics.

Furthermore, a misrepresentation of the PBL dynamics is worse in the bottom layer than in the surface layer, when the momentum balance is considered. Indeed, at the surface

Correspondence to: A. Wirth
achim.wirth@hmg.inpg.fr

the wind shear is imposed and thus also the corresponding Ekman transport, which means, that even with a bad representation of the PBL dynamics the overall Ekman transport is correct in magnitude and direction. In the bottom layer, to the contrary, the shear is a function of the velocity field near the bottom. Getting the velocity field wrong also means, that the Ekman transport is wrong in magnitude and direction. It is through the divergence of the Ekman layer transport that the momentum fluxes at the boundaries are communicated to the ocean interior (see *e.g.* Pedlosky 1998). The need is especially important when the dynamics of gravity currents are considered. It was demonstrated by Willebrand *et al.* 2001 that the thermohaline circulation of the North Atlantic in numerical models is strongly influenced by the local representation of the gravity current dynamics in the Denmark Strait.

Many efforts have been made during the last thirty years to parametrise the effect of the bottom PBL on the large-scale ocean dynamics. Parametrisations of varying complexity have been developed to represent various features of the dynamics of gravity currents (see *e.g.* Killworth & Edwards 1999, Xu *et al.* 2006 and Legg *et al.* 2006 and 2008). Today there is no generally accepted parametrisation and the representation of gravity currents is considered a major flaw in today's state-of-the-art ocean models. Developing a parametrisation of the Ekman layer dynamics, based on linear homogeneous stationary Ekman layer theory might be of limited use in cases where neither of the conditions are met. Indeed, inertial oscillations and a rapid evolution of the gravity current, make the validity of such parametrisations questionable.

In the present work we explore another direction. Rather than parametrising the total PBL dynamics on the bottom we resolve some of it explicitly, by increasing the resolution near the bottom in the very same way as it is commonly done near the surface. This refinement can easily be implemented in a σ -coordinate grid, available in several numerical models of the ocean circulation. This idea has, so far to the best of our knowledge, not been explored in detail. The importance of the vertical resolution in gravity current dynamics has already been emphasised by various authors. A fine grid or a grid refinement near the ocean floor was already employed, for example, in Ezer & Weatherly 1990 and Jungclaus 1999. But we like to mention that in these publications, although having a high vertical resolution, the Ekman layer dynamics in the PBL is usually not sufficiently resolved and the effect of vertical resolution on the gravity current dynamics has not been explored in detail. Most recently Legg *et al.* 2008, varying the vertical viscosity over more than three orders of magnitude rather than the grid resolution, noted that resolving the Ekman layer has a dominant role in determining the descent of the gravity current and favours its downslope movement. Their paper also gives a very nice introduction to, and a review of, recent results using numerical simulations of gravity current dynamics.

In this work we suggest a vertical resolution in ocean models that represents a compromise between calculation time

and representation of the important processes. We focus on the importance of vertical resolution in the representation of the dynamics of gravity currents as: (i) they are affected by the PBL dynamics on the ocean floor, (ii) gravity currents are important features of the large scale circulation, (iii) they represent a difficult problem to simulate numerically and (iv) they have and are thoroughly studied in observations, laboratory experiments, numerical models and analytical calculations and the results are discussed in a large number of publications.

The present work is dedicated to the importance of Ekman layer dynamics and its vertical resolution numerical simulations of gravity currents. This vertical resolution is shown to be of paramount importance for the process considered here. The important problem of errors in the horizontal pressure gradient in σ -coordinate models, a subject discussed in a large number of publications, is not considered here.

2 Dynamics and Representation of the Oceanic Bottom Boundary Layer

The dynamics in the PBL at the ocean floor is turbulent. The key parameter of its dynamics is the friction velocity:

$$u^* = \sqrt{\frac{\tau}{\rho}}, \quad (1)$$

where τ is the friction force per unit area exerted by the ocean floor and ρ is the density of the sea water.

The PBL in the ocean can be roughly decomposed into four layers. The first, counting upward from the bottom, is the viscous sub-layer which is only a few millimetres thick $\delta_v \approx 5\nu/u^*$ and which is governed by laminar viscous dynamics. Above this layer the dynamics transits in the buffer layer towards the log-layer, which is a few meters thick and governed by turbulent transfer of inertia. The thickness of the buffer-layer is a function of the roughness of the ocean floor. The transfer of inertia is supposed constant throughout the log-layer and its magnitude also depends on the roughness of the ocean floor. In the fourth layer, at even further distance $\delta_f \approx 0.2u^*/f$, of a few tenths of metres above ground, rotation influences the dynamics and a turbulent Ekman layer develops (see Coleman *et al.* 1990 and McWilliams 2009).

The dynamics in the first three layers can not be explicitly resolved in ocean models even in a far future. The viscous sub-layer is only a few millimetres thick and the buffer- and log-layer are governed by turbulent structures of only a few metres in size in the vertical and horizontal directions. An explicit resolution asks for grid cells of less than one meter in all three spatial directions and a time step smaller than one second, requirements which are far from being feasible for basin-scale ocean models, with today's and tomorrow's computer resources. The characteristic time scale of the dynamics in the first three boundary layers is faster than

:

3

the inverse of the Coriolis parameter, which is a prerequisite for an efficient parametrisation in ocean models. The dynamics in the first three bottom layers, viscous-, buffer- and log- layer, is usually parametrised by implementing either: (i) a no slip boundary condition together with an increased vertical turbulent viscosity or (ii) a drag force at the lowest grid cell, which depends linearly or quadratically on the velocity at the first grid point from the wall. The actual drag force per unit area in today's ocean models is often given by $\mathbf{F} = (c_D/\rho)(|\mathbf{u}| + c)\mathbf{u}$, where \mathbf{u} is the fluid velocity near the ocean floor, c_D the drag coefficient depending on the roughness of the ocean floor and c is a velocity representing processes not explicitly included, as for example the tidal dynamics. This leads to a linear friction force for $u \ll c$ and a quadratic friction force for $u \gg c$. The problem of parametrising the influence of these three layers lies in the determination of the corresponding friction parameters (see Wirth & Verron 2009 and Wirth 2010).

We prefer to resolve explicitly a part of the dynamics in the Ekman layer rather than to totally parametrise its influence on the dynamics above. The parametrisation of the Ekman layer dynamics is more subtle due to the veering (turning) of the velocity vector in the Ekman layer. When this effect is omitted, as it is currently done in most ocean general circulation models, the friction force is not only wrong in magnitude but also in direction. The focus of the present work is on the numerical resolution of the Ekman layer dynamics at the ocean floor.

3 Idealised Oceanic Gravity Current on the f-Plane

3.1 The Physical Problem Considered

In the experiments presented here we use an idealised geometry, considering an infinite gravity current on an inclined plane with constant slope of 1° in a rotating frame with a constant Coriolis parameter $f = 1.0313 \cdot 10^{-4} \text{s}^{-1}$. The water in the gravity current is $\Delta T = 0.2 \text{K}$ colder than the surrounding water, gravity is $g = 9.8065 \text{ms}^{-2}$ and the thermal expansion coefficient equals $2.0 \cdot 10^{-4} \text{K}^{-1}$. This leads to a reduced gravity $g' = 3.9226 \cdot 10^{-4} \text{ms}^{-2}$. In the initial condition the thickness $h(y)$ has a parabolic shape that is 20km wide and has a maximum value of 200m. Initially the velocity is in a geostrophic equilibrium.

When dissipative effects and instability of the gravity current are ignored the gravity current is stationary and travels in the along-slope direction with an average geostrophic velocity of $u = (g'/f) \tan 1^\circ$. It is the friction, transmitted by the PBL dynamics, that is responsible for the evolution of the gravity current. Please note that in the rotating case it is friction that makes the gravity current move down-slope, whereas in the non-rotating gravity current friction opposes the down slope movement. This dynamics has been studied numerically in Wirth 2009 using the non-hydrostatic model

HAROMOD introduced in Wirth 2004. We are here concerned with the representation of the dynamics in hydrostatic ocean models.

3.2 The Mathematical Model

In the present research we consider two configurations to study the physical problem described above. The first configuration is 2.5 dimensional and the second 3 dimensional. In the 2.5D configuration we only consider the dynamics within a 2 dimensional vertical slice perpendicular to the geostrophic velocity. We do not allow for variations in the long-stream direction. Although the geometry is 2D all three components of the velocity vector are retained. The 2.5D configuration has two advantages. First, it suppresses large scale instability of the gravity current and the formation of large scale eddies, which is beneficial to our goal of looking at the influence of small scale processes in the PBL. Second, a detailed study of the influence of resolution is numerically more feasible in the less costly 2.5D configuration. The 3D configuration is then used to verify how the results found in the 2.5D configuration transfer, qualitatively and quantitatively, to the full 3D case. That is, we check if the presence of 3D instabilities and other structures alter the results found in the 2.5D case.

The domain spans 50km in the y-direction (upslope), its maximal depth is 1250m. The 3D configuration spans 200km in the x-direction which is ten times the initial width of the vein (see below).

The mathematical model used to study the physical configuration introduced above are the hydrostatic (primitives) equations subject to a no slip boundary condition at the bottom and a rigid lid at the surface. The vertical eddy viscosity is $4 \cdot 10^{-3} \text{m}^2 \text{s}^{-1}$ leading to a thickness of the laminar Ekman layer of $\delta_{Ek} = \sqrt{2\nu/f} = 8.8 \text{m}$ and the vertical diffusivity is $1 \cdot 10^{-4} \text{m}^2 \text{s}^{-1}$. The horizontal viscosity is $\nu_h = 10 \text{m}^2 \text{s}^{-1}$ and the horizontal diffusivity is $\kappa_h = 1 \text{m}^2 \text{s}^{-1}$.

3.3 The Numerical Model and its Vertical Resolution

The above introduced mathematical models are numerically integrated with the numerical model NEMO-OPA9. The horizontal resolution ($\Delta y = 143 \text{m}$) in the direction of the slope is, with one exception ($\Delta y = 3125 \text{m}$ in G04), the same in all experiments (please see tabs. 1 and 2 for details). The horizontal resolution of exp. G04 is typical for high resolution regional models. In the three dimensional experiments $\Delta x = 400 \text{m}$

The purpose of our research is to evaluate the effect of a vertical grid refinement near the ocean floor and determine the grid structure that is an optimal compromise between accuracy and the cost of calculation. Two types of grid geometries are employed here, both are standard options in the NEMO-OPA9 model. One is the conventional z-coordinate, where all grid-points of a certain level lie at the same depth.

The grid structure has a regular orthogonal form. Usually the vertical resolution is a function of depth, with a refinement near the surface and a sparse grid at the bottom. For the case considered here, a high resolution at the topography, the refinement has to extend over the total depth, leading to a uniform grid structure with many grid points in areas where they are not necessarily needed.

The second type of grid geometry is the σ -coordinate, which is terrain following. In a σ -coordinate model the number of levels is equal everywhere so that no grid point is wasted in the vertical. In a σ -coordinate model grid points of the same level are situated at the same depth relative to the total depth at each horizontal location. This type of grid structure allows for an efficient refinement of the grid near the topography. Except for two experiments all our experiments are performed with a σ -coordinate system. No 3D reference experiments (high resolution) experiments have been performed to the inhibitive computer requirements.

We want to emphasise here that the mathematical model presented in the previous subsection has a well defined solution which is, of course, independent of the numerical model employed to approach it. As the numerical models with both types of grids are consistent their solutions will both converge to the mathematical solution when the grid resolution and the corresponding time step are reduced. The question is, however, which of the grids has a faster convergence when numerical costs are equal. The case considered here is clearly in favour of the σ -coordinate model.

In our numerical simulations we distinguish three zones in the vertical direction (see fig. 3). the first zone, called Z1, includes the PBL and is about 40m thick. The second, called Z2, extends from about 40 to 200m from the ocean floor and includes thus the upper part of the vein. The third zone, called Z3, extends from about 200m above the ocean floor to the surface and contains no gravity current water. It, nevertheless, has an influence on the dynamics of the gravity current. The vertical resolution is varied between experiments in the three zones to explore its effect on the representation of the gravity current dynamics.

4 Experiments

We performed two sets of experiments the first are 2.5D and the second 3D. Both sets are explained in the following two subsections, the results of the experiments are given in the next section. The initial conditions, identical for both sets of experiments, can be seen in fig. 1, the temperature is constant within the gravity current which has a parabolic shape and the long-slope velocity is geostrophically adjusted, please note that it reverses within the gravity current.

4.1 Experiments 2.5D

We started by performing two reference experiments of the 2.5D configuration at very high vertical resolution with 500 levels for the z -coordinate and 200 the σ -coordinate calculations. Please see table 1 for a concise presentation of all the 2.5D experiments performed. The first reference experiment (G01), one of two experiments using a z -coordinate, and the second (G02) with a σ -coordinate, are performed to establish results to which the other experiments can be compared to. In experiment G01 the vertical resolution is 2.5m everywhere. Whereas in exp. G02 the first level is at only 0.3m from the ocean floor (measured at the upslope side of the domain). Experiment G02 is thus of higher quality than G01 due to the grid refinement near the ocean floor. The other experiments the resolution is varied in the vertical zones defined above (Z1, Z2 and Z3) to evaluate the lack of resolution in the different zones, each one being representative of different physical processes. For the grids with three levels in the zone Z1 the first three horizontal-velocity grid points are at 2.5m, 10m and 22.5m from the ocean floor resolution (on the up slope side of the domain). A typical σ -coordinate grid with three levels in the zone Z1 is given in fig. 3

In experiment G04 the horizontal resolution is increased to $\Delta y = 3.125\text{km}$ a value typical for today's state-of-the-art regional GCM calculations. A second experiment, G09, with a z -coordinate system is performed. It has half the resolution (in x and z) of G01 and the convective adjustment is used. Such scheme is usually employed in ocean global circulation models (OGCM) integrations to parametrise convective processes at the ocean surface. The convective adjustment procedure used, increases the vertical viscosity and diffusivity may orders of magnitude, to $1\text{m}^2\text{s}^{-1}$, when a static instability is detected. This mimics convection and is beneficial near the surface, but destroys the gravity current dynamics as we will demonstrate in the next section.

4.2 Experiments 3D

In the 3D experiments a reference experiment, as performed for the 2.5D case, is prohibited by the size of the calculation. We therefore used the resolution which was found to give good results in the 2.5D case, exp. G03 (see table 1 and section 5) as the resolution of our 3D reference experiment G11 (see table 2). The resolution of G11 is shown in fig. 3.

The effect of a non resolved Ekman layer was studied in exp. G12, its vertical resolution is similar to G05. Exp. G13 at an even sparser resolution is close to what is used in classical high vertical-resolution calculations of gravity current dynamics and OGCM calculations. The higher resolution in the zone Z3 as compared to the 2.5D experiments is required for the numerical stability of the calculation. Indeed, the eddy dynamics due to large scale instability of the flow, which are suppressed in the 2.5D calculations ask for a higher resolution in Z3 (see section 5).

:

5

5 Results

5.1 Results 2.5D

The two reference simulations (G01 and G02) produce very similar results for the temperature structure, compared in fig 2 and the velocity field, showing the consistency of the numerical scheme on both numerical grids. The shapes compare very well to the results of non-hydrostatic calculations of Wirth 2009 and to laboratory experiments made on the Coriolis platform in Grenoble (Wirth & Sommeria 2007), validating the use of a hydrostatic model to numerically simulate gravity current dynamics. The conspicuous feature, common in all the laboratory experiments and high resolution numerical simulations, is a vein, the thick part of the gravity current and a thin “friction layer” at its down slope side. The vein descends only slowly in time, but detains water at its down-slope side through the friction layer. This two part structure is key to the dynamics of oceanic gravity currents. It is discussed in detail in Wirth (2009).

The first point we like to emphasise is the disastrous effect that the convective adjustment implemented in most ocean models has on the dynamics of gravity currents. When heavier water overlies lighter water a convective dynamics mixes the two water masses in a short time (see *e.g.* Wirth 2009). In hydrostatic OGCMs this process is absent and a convective adjustment procedure is used that mixes the two water masses and their inertia. The convective adjustment used in our simulations does this by artificially augmenting the vertical diffusivity and viscosity to the value of $1m^2s^{-1}$. Increasing only the diffusivity and leaving the viscosity unchanged is contrary to the fact that the turbulent Prandtl number is order unity. This procedure is found to mimic very well the convective dynamics at the ocean surface but has a disastrous effect on the dynamics of gravity currents. Indeed, at the downslope front of the gravity current the down-slope velocity decreases in the vicinity of the floor and heavy gravity current water superposes lighter ambient water, which triggers convective adjustment. The high vertical viscosity then inhibits a downslope movement of the gravity current and a vertical wall of dense water develops at the down-slope side of the gravity current as shown in fig. 4, this is an artifact of the convective adjustment procedure. A comparison to fig. 2 shows clearly the completely different dynamics due to the convective adjustment and demonstrates that it should not be used in gravity current calculations. The experiment involving convective adjustment will not be further discussed in the sequel.

The rate of descent of the gravity current is the most important property, its time evolution is given in fig. 5. The rate of descent is defined by the movement of the x -component of the centre of gravity c_x of the gravity current. It is defined as:

$$c_x = \frac{\int x(T - T_0)dA}{\int (T - T_0)dA}, \quad (2)$$

where T_0 is the temperature of the surrounding water and the whole area, in the 2.5D case, or the whole volume, in the 3D case, is denoted by A .

A conspicuous feature is the strong resemblance between the experiments having at least three levels in the zone Z1 (G01, G02, G03, G04, G06) showing a stronger descent than the experiments with a feeble resolution and proofing the importance of the PBL dynamics (already emphasised in Wirth & Verron 2008 and Wirth 2010). It is striking that: (i) the resolution in zones Z2 and Z3 have only a negligible influence, that (ii) only three layers in the zone Z1 are sufficient, and that (iii) the horizontal resolution is not key (see exp. G04). Simulations with only one level in the zone Z1 are clearly insufficient, they all lead to a descent rate that is smaller by at least a factor of two as compared to the reference calculation. The higher descent rate of the z -coordinate experiment (G01) is due to the increased thickness of the friction layer, increased by spurious numerical diffusion along the horizontal direction (see fig. 2).

We like to mention however, that it is not the rate of descent alone that is key but also the distribution of the descent is of paramount importance. In fact as we see in fig. 2 most of the fluid descends in the friction layer at the down-slope side of the vein, whereas the bulk of the gravity current descends only slowly. This dynamics was explored in detail in Wirth 2009. This double-structure of the gravity current is key to the evolution of the density structure at the slope and can, of course, only be represented when the resolution at the topography is fine enough. Please see section 6 for a discussion of the implications of the descent on the large scale circulation.

Another important parameter, although less important than the descent rate, is the along-slope transport of temperature. It is defined by:

$$V_T = \int v(T - T_0)dA. \quad (3)$$

Contrary to the downslope transport, which is performed in the PBL, the along-slope transport is done by the gravity current water above the vein, asking for a good resolution also in the zone Z2. This increased resolution is provided in exp. G01, G02 and G03 and the good agreement of the along-slope transport in these experiments can be verified in fig. 6.

When the Ekman layer is not resolved the veering (turning) of the velocity vectors in the vicinity of the wall is absent. The friction force exerted by the ocean floor is thus not only wrong in magnitude but also in direction. In the calculations with only 3 levels in the zone Z3 a correct Ekman veering is observed (not shown).

5.2 Results 3D

The dynamics in the 3D case can clearly be divided in two phases. An early behaviour somehow resembling the 2.5D

dynamics, but with the appearance of wave like disturbances on the gravity current that favour the downslope movement. The wave length of the instability is a little over 5km in all experiments, which is very close to predicted value of $L = \sqrt{g'H}/f$. As in the 2.5D experiments, the downslope dynamics in the first phase is strongly dependent on the resolution in the PBL, with an increased down-slope movement with a better resolution (see fig. 7). The three dimensionality increases the downslope movement by about 30% in this early phase. The down-slope movement with a sufficient resolution (G11) of the PBL is found to be about 8-times larger than that of the case with a classical resolution (G13). The along slope movement in this early phase is very similar to the 2.5D experiments as can be verified in fig. 8. An increased resolution leads to a smaller along slope transport. The dynamics similar to the corresponding 2.5D experiments is followed, after a little more than 5 to 7 days (depending on the experiment), by a generation of strong eddies leading to a fully 3D dynamics with an over three fold increase of the downslope movement in the reference experiment (G11). The generation of eddies in gravity currents is a conspicuous feature and is explored in observations (Jungclauss *et al.* 2001), laboratory experiments (Whitehead *et al.* 1990) and numerical simulations (Legg *et al.* 2006). The cross over from one dynamics to the other is conspicuous in all the variables. In the experiments some of the gravity current water reached the boundary on the lower side of the domain after only a little more than five days and the dynamics of the downslope and along slope dynamics is altered. Furthermore, our resolution in the zone Z3 is too sparse in all experiments to allow for a detailed evaluation of the eddy dynamics. These two reasons prevent an analysis of the eddy regime.

6 Discussion

Our results demonstrate, that a better grid resolution in the PBL is key to the representation of the dynamics of oceanic gravity currents in numerical models. Our study shows, that only a few (≈ 5) additional σ -levels are necessary to obtain a large improvement in the representation of the PBL dynamics. Such increase represents a raise of only 10% of calculation time in a typical state-of-the-art ocean model. The research presented here concentrates on the laminar dynamics of gravity currents and the development of its instability. The early phase, before the generation of large scale eddies after more than 5 days, is important as it represents the initial downslope movement and influences the subsequent generation of the eddies. Furthermore, we see no reason why the here presented results for the dynamics of gravity currents can not be extrapolated to other processes near the ocean floor and to the interaction of ocean dynamics with topography in general.

The finding, that convective adjustment procedure destroys gravity current dynamics, blocking the downslope movement, is key to the representation of gravity currents and numerical simulations of ocean dynamics in high latitudes in general, which is strongly influenced by the descent of dense water.

Our results come at no surprise, the importance of the friction layer is already emphasised in Wirth (2009). It has a thickness a little larger than the Ekman layer thickness. If the numerical resolution does not allow for its resolution the dynamics of the gravity current can not be correctly represented. Most important, it is not the increase of the vertical viscosity, that enables the downslope movement of the gravity current, as put forward in recent publications, but the resolution of the Ekman layer dynamics. Such resolution can be obtained by either: increasing the vertical viscosity or the vertical resolution near the ocean floor. The latter is the sensible way to go. It is not the physics that has to be adjusted to the numerics, but the numerics should respect the physics. We like to emphasise, that an increase of the vertical viscosity, leading to a thicker PBL, instead of increasing the vertical resolution, both leading to a better resolved PBL dynamics is not a solution to the problem for still another reason. The Ekman transport in a laminar PBL is a function of the vertical viscosity ($\propto \sqrt{\nu_v}$) and the dynamics of the gravity current above the PBL is governed by vertical Ekman pumping due to the divergence in the Ekman transport. Artificially increasing the vertical viscosity is clearly the wrong thing to do. Please note that the situation is very different to the increase of the horizontal viscosity to allow for a resolution of the horizontal boundary layer, the Munk-layer. The transport in the Munk layer is, however, imposed by the interior Sverdrup dynamics and does, to leading order, not depend on the horizontal viscosity.

It is not only the rate of descent of the centre of gravity that is important. The descent in a fine layer changes the density all along the slope but less massively than a descent of the gravity current as a bulk, the latter leading to a larger density anomaly but more locally. It is the density structure at the boundary that determines the baroclinic transport in geostrophic theory. The density structure is in large areas of the world's oceans determined by gravity current dynamics. An example are gravity currents all along the coast of Antarctica. Getting the gravity current dynamics wrong means getting the geostrophic large scale dynamics wrong, that means getting it wrong to leading order.

Acknowledgements.

References

- Coleman, G.N., J.H. Ferziger & P.R. Spalart (1990), A numerical study of the turbulent Ekman layer, *J. Fluid. Mech.* **213**, 313–348.

:

7

- Ezer T, Weatherly GL(1990) A numerical study of the interaction between a deep cold jet and the bottom boundary layer of the ocean? *J. Phys Oceanogr* **20**, 801–816.
- R.W. Griffiths (1986), Gravity currents in rotating systems, *Ann. Rev. Fluid Mech* **18**, 59–89.
- J.H. Jungclaus (1999), A three-dimensional simulation of the formation of anticyclonic lenses (meddies) by the instability of an intermediate depth boundary current, *J. Phys. Oceanogr.* **29**, 1579–98.
- J.H. Jungclaus, J. Hauser & R.H. Käse(2001), Cyclogenesis in the Denmark Strait overflow plume, *J. Phys. Oceanogr.* **31**, 3214–3229.
- P.D. Killworth & N.R. Edwards (1999), A turbulent bottom boundary layer code for use in numerical ocean models, *J. Phys. Oceanogr.* **29**, 1221–1238.
- S. Legg, R.W. Hallberg & J.B. Girton (2006), Comparison of entrainment in overflows simulated by z-coordinate, isopycnal and non-hydrostatic models, *Ocean Mod.* **11**, 69–97.
- S. Legg, L. Jackson & R.W. Hallberg (2008), Eddy resolving modeling of overflows, *Geophysical Monograph Series* **117**, 63–81.
- Pedlosky, J.(1998), *Ocean Circulation Theory*, Springer 453 ps. ISBN: 3-540-60489-8.
- Whitehead, J.A., M.E. Stern, G.R. Flierl & B.A. Klinger 1990, Experimental observations of baroclinic eddies on a sloping bottom, *J. Geophys. Resea.* **95**, 9585–9610.
- Willebrand J., Barnier B., Böning C., Dieterich C., Killworth P., Le Provost C., Jia Y., Molines J.M. & New A.L. (2001), Circulation characteristics in three eddy-permitting models of the North Atlantic. *J. Progress in Oceanography* **48**, 123–162.
- A. Wirth, (2004), A non-hydrostatic flat-bottom ocean model entirely based on Fourier expansion, *Ocean Mod.* **9**, pp. 71–87.
- A. Wirth, (2009) “On the basic structure of oceanic gravity currents” *Ocean Dynamics* **59**, 551–563. DOI 10.1007/s10236-009-0202-9
- A. Wirth, (2010) “Estimation of Friction Parameters in Gravity Currents by Data Assimilation in a Model Hierarchy” sousmis *Ocean Dynamics*.
- A. Wirth & J. Verron, (2008) “Estimation of Friction Parameters and Laws in 1.5D Shallow-Water Gravity Currents on the f-Plane, by Data Assimilation” *Ocean Dynamics* **58**, 247–257, 2008. DOI 10.1007/s10236-008-0151-8
- A. Wirth & J. Sommeria, (2007) “Gravity current experiments on the Coriolis platform” *Technical report EPSHOM*

Exp.	Resolution (nx,ny,nz)	Coord. type	Z1	Z2	Z3
G11	(500,350,12)	σ	3	4	4
G12	(500,350,10)	σ	1	4	4
G13	(500,350,14)	σ	0	3	10

Table 2. List of the 3D exps. (see tab. 1 for details).

Exp.	Resolution (ny,nz)	Coord. type	Z1	Z2	Z3	Rem.
G01	(350,200)	z	16	64	120	reference
G02	(350,500)	σ	98	278	124	reference
G03	(350,10)	σ	3	4	2	
G04	(16,10)	σ	3	4	2	
G05	(350,8)	σ	1	4	2	
G06	(350,7)	σ	3	1	2	
G07	(350,5)	σ	1	1	2	
G08	(350,4)	σ	1	1	1	
G09	(250,250)	z	49	139	62	convect. adj.

Table 1. List of the 2.5D exps. The domaine spans 50km in the y -direction. The number of levels in the vertical zones Z1, Z2 and Z3 (as explained in the text) are given.

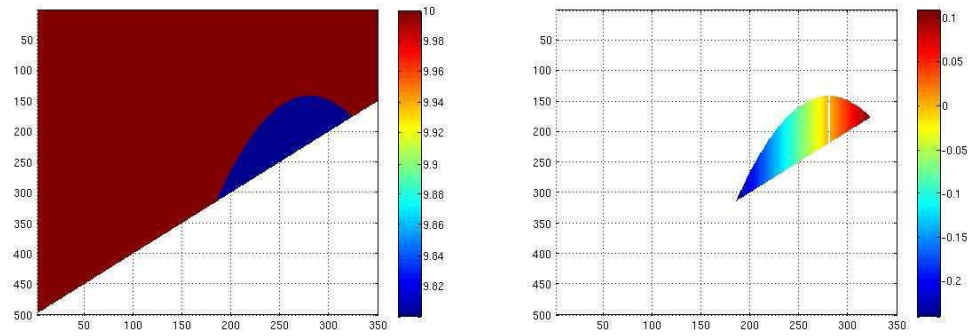


Fig. 1. Initial condition: temperature (left) and geostrophically adjusted velocity u (cross stream component; y-direction is upslope).

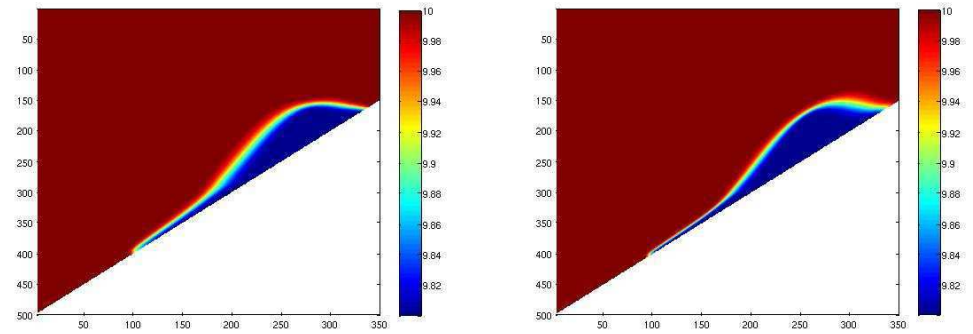


Fig. 2. Temperature structure (in $^{\circ}\text{C}$) in the reference simulations after 2 days; left: z-coordinate (G01) and right: σ coordinate (G02). Coordinates give grid in the x -direction and the z -direction for the z-coordinate grid. For the σ -coordinate results are interpolated to the z-coordinate grid (in the z -direction)

:

9

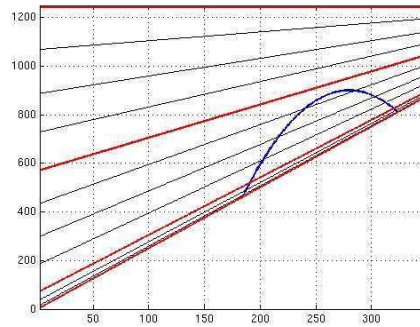


Fig. 3. σ -coordinates of G11 shown (black lines). Red-lines mark the boundaries of the zones Z1, Z2 and Z3 (bottom to top). Blue line gives initial profile of gravity current.

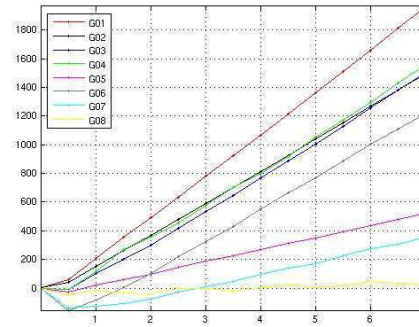


Fig. 5. Down-slope displacement of the centre of gravity of the gravity current in the 2.5D experiments during the first 7 days of the experiments. Vertical axis in metres and horizontal axis in days.

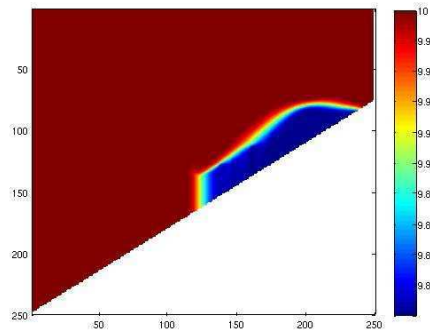


Fig. 4. Temperature structure (in C°) in the simulation with convective adjustment (G09). Coordinates give grid levels.

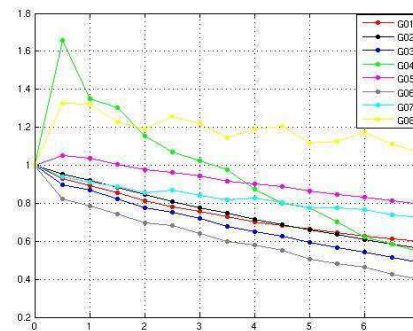


Fig. 6. Along-slope transport of the gravity current (normalised by the initial geostrophic value) in the 2.5D experiments during the first 7 days of the experiments.

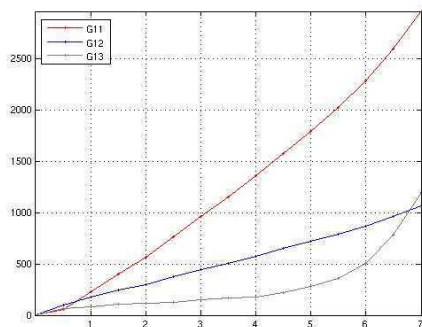


Fig. 7. Down-slope displacement of the centre of gravity of the gravity current in the 3D experiments during the first 7 days of the experiments. Vertical axis in metres and horizontal axis in days.

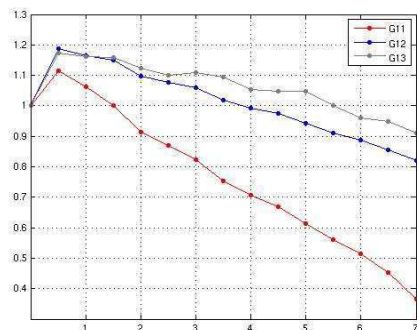


Fig. 8. Along-slope transport of the gravity current in the 3D experiments during the first 7.5 days of the experiments.

Quatrième partie

Cours d'Océanographie Physique

A Guided Tour Through Physical Oceanography

Achim Wirth

May 10, 2010

Il libro della natura è scritto in lingua matematica

(The book of nature is written in the language of mathematics)

Galileo Galilei

Contents

1	Preface	5
2	Observing the Ocean	7
2.1	Geometry of the Ocean	7
2.2	Variables measured	7
3	Physical properties of sea water	9
3.1	Salinity	9
3.2	Temperature and Potential Temperature	10
3.3	θ -S Diagrams	11
3.4	Pressure	11
3.5	Density and σ	12
3.6	Heat Capacity	13
3.7	Conservative Properties	15
3.8	Water Masses in the Ocean	15
3.9	Sea Ice and Ice Bergs	15
4	Surface fluxes, the forcing of the ocean	17
4.1	Heat Flux	17
4.1.1	Radiative Fluxes	17
4.1.2	Sensible Heat Flux	18
4.1.3	Latent Heat Flux	18
4.1.4	Other Heat Fluxes	19
4.2	Fresh Water Flux	19
4.3	Wind Shear	19
4.4	What about tides?	20
5	Dynamics of the Ocean	21
5.1	From the Navier-Stokes to the Shallow Water Equations	21
5.2	The Linearized One Dimensional Shallow Water Equation \mathcal{S}	23
5.3	Reduced Gravity	24
5.4	Two Dimensional Stationary Flow	25
5.5	Rotation	26
5.6	The Coriolis Force	26
5.7	The Shallow Water Equations in a Rotating Frame	28
5.8	Geostrophic Equilibrium	29
5.9	Energetics of flow in Geostrophic Equilibrium	30
5.10	Linear Potential Vorticity and the Rossby Adjustment Problem	30
5.11	Potential Vorticity (non-linear)	32

5.12	The Beta-plane	32
5.13	A few Words About Waves	33
6	Gyre Circulation	35
6.1	Sverdrup Dynamics in the SW Model (the math)	35
6.2	The Ekman Layer	38
6.2.1	Ekman Transport (one layer)	38
6.2.2	The Ekman Spiral	39
6.3	Sverdrup Dynamics in the SW Model (the physics)	41
7	Multi-Layer Ocean dynamics	43
7.1	The Multilayer Shallow Water Model	43
7.2	Conservation of Potential Vorticity	44
7.3	Geostrophy in a Multi-Layer Model	44
7.4	Barotropic versus Baroclinic	46
7.5	Eddies, Baroclinic instability	46
7.6	Continuous Stratification	48
8	Equatorial Dynamics	49
9	Abyssal and Overturning Circulation	51
9.1	The Stommel Arons Theory	52
9.2	Multiple Equilibria of the Thermohaline Circulation	53
9.3	What Drives the Thermohaline Circulation?	55
10	Penetration of Surface Fluxes	57
10.1	Molecular Transport	57
10.2	Turbulent Transport	58
10.3	Convection	60
10.4	Richardson Number	60
10.5	Entrainment	61
10.6	Gravity Currents	62
11	Solution of Exercises	63

Chapter 1

Preface

This course deals with the aspects of physical oceanography which are important to understand the dynamics and role of the ocean in the climate system of our planet earth. There are outstanding and very comprehensive books on the dynamics of the world's ocean, and the purpose of this *Guided Tour Through Physical Oceanography* is not to rival them, but rather to provide for a concise, self-contained and systematic introduction to the field, emphasizing the basic questions. While teaching an introductory class of physical oceanography to graduate students, I found no concise introduction to the subject that deals with the matter on an advanced and modern level. By modern I mean oriented “[...] toward the understanding of physical processes which control the hydrodynamics of oceanic circulation.” (H. Stommel, *The Gulfstream*, 1958). More precisely, when considering such physical process we first assume that such process can be modeled by the Navier-Stokes equations, an assumption that is surely satisfied to a very high degree of accuracy. We then proceed in four steps: (i) formulate assumptions about the process that simplify the problem; (ii) use these assumptions to derive simplified (mathematical) models; (iii) study the thus obtained simplified models; and (iv) compare the results to observations (if available) to validate or reject the results. If the results have to be rejected when confronted with observations, laboratory experiments or results from more complete models, we have to formulate new assumptions, that is, restart with (i). It is the first point, the choice of the important assumptions which is key to scientific progress and asks for a deep scientific insight.

Today's research on ocean dynamics is guided by the power of increasingly complex numerical models. These models are, however, so involved, that simpler models are needed to comprehend them and the study of a phenomenon of ocean dynamics passes by the study of a hierarchy of models of increasing complexity.

The prerequisites for this guided tour is a course in calculus and some knowledge of elementary fluid dynamics. I try to present the subject “as simple as possible but not simpler” (A. Einstein). It is indeed my conviction that some introductory courses of ocean dynamics are over-simplified and are thus impossible to really understand or are plainly wrong.

Many important aspects of the ocean circulation are omitted, which is permitted in a *guided tour* but not so much in a text book. The most important are waves (surface, Poincaré, Kelvin and Rossby), which are not visited by this *guided tour*. The justification that we are here mostly concerned with the behavior of the ocean on long time scales, relevant to climate dynamics, much longer than the typical time scale of the above mentioned waves, is weak. Including oceanic waves in a self-contained and systematic way would easily double the length of this course.

I choose not to present figures of observations and data in this course as they are subject to rapid improvement and as their latest version can easily be retrieved from the Internet. The

search for such data and figures are given as exercises.

Chapter 2 is a short account of the observations of the worlds oceans in the past and present. In Chapter 3 we discuss the composition and thermodynamic properties of oceanic water. The forces acting on the ocean are discussed in Chapter 4. Chapter 5 is the key part of this *guided tour through physical oceanography*, where the basic concepts of oceanic circulation theory are derived. In chapter 6 we will see how the forcing put the water masses of the ocean into motion. An important question is: how can the forcing, which acts on the surface of the ocean influence the motion in the deep ocean? Indeed, over 250 years ago the famous mathematician L. Euler wrote: “La raison nous assure, et l’expérience nous confirme, que les courants pénètrent rarement jusqu’au fond de la mer.” (Recherche sur la découverte des courants de mer, Leonhard Euler). (Reason insures us and experience confirms, that the currents penetrate rarely to the ocean floor (my translation)), and we will see which processes are responsible for generating and sustaining ocean currents down to the very bottom of the ocean.

Chapter 7 is dedicated to baroclinic phenomena, dynamics that can not be described by a single horizontal layer.

The overturning or thermohaline circulation, discussed in chapter 9, deals with the sinking of dense water masses in the high latitudes, their circulation in the abyssal ocean and their upward motion in the worlds ocean. This thermohaline circulation is important for the climate dynamics as it transports large amounts of heat, carbon dioxide and as it varies on climatic (long) time scales.

At the equator the Coriolis parameter, representing the effect of terrestrial rotation, vanishes. Chapter 8 discusses the consequences for the dynamics of the equatorial ocean.

This guided tour would not be complete without discussing the, small scale, three dimensional turbulent fluxes in the ocean. To model this processes the quasi two dimensional models used in the previous chapters are no longer adapted and different models, based on different assumptions have to be derived from the Navier-Stokes equations, this is accomplished in chapter 10.

Chapter 2

Observing the Ocean

A systematic determination of the bathymetry (depth structure) of the world ocean and its observation started with the *HMS Challenger* expedition (1872–1876). Besides biological and geological observations, the temperature was measured at different depths and locations of the world's ocean and water samples were taken which were then analysed to determine the salinity and the composition of seawater. Current measurements in the open sea were more difficult to perform from a ship subject to current and wind-forces and could only be estimated.

Today the ocean is observed from research vessels which take measurements along a well defined trajectory and at given depth, from moorings which are attached to the ocean floor and take observations at one location during a certain period of time, usually a few years, and from floating buoys which are transported by the current but change their depth following a predefined schedule and communicate the measurements by satellite. These devices measure the velocity, temperature and chemical and biological composites of the oceanic water and provide us with a spatio-temporal, that is, a four dimensional picture of the dynamics and the composition of the world's ocean. This picture is, however very patchy. At every instance in time large areas of the ocean go unobserved. Starting from the 1980's satellite observations measure the height of the sea surface, the sea surface temperature, the sea surface salinity and the ocean color of the sea surface at a spacial and temporal density and continuity unknown from previous observations. Satellites can, however, only provide us with data from the sea surface as electro-magnetic waves do not penetrate into the deep ocean. Much of today's knowledge of the world's oceans is due to satellite observations and many efforts go to extrapolating this surface measurements into the deep ocean.

2.1 Geometry of the Ocean

The world ocean has a surface of $361 \times 10^6 \text{ km}^2$, and an average depth of 3.8km. The average depth is approximately the same in the Pacific, Atlantic and Indian Ocean.

Exercise 1: Search the Internet for maps of the bathymetry (depth) of the world's ocean.

2.2 Variables measured

Using oceanic currents to accelerate and facilitate sea voyages is a concept as old as navigation itself. On the open sea ocean currents were however hard to detect. Sea men using the gulf stream to travel from the east coast of the US, realised quite early that the gulf-stream water was warmer than the surrounding waters and they used temperature measurements to determine

their position with respect to the gulf stream. During the cold war, Russian submarines used the same trick to approach the east coast of the US along the northern border of the Gulf Stream, where they could hide due strong density gradients and turbulent ocean dynamics deflecting the sonar signal.

Scientists were then interested in measuring other properties of sea water to determine the path ways of water masses in the ocean. Salinity measurements are easy to perform due to the strong relation to the electric conductivity of the sea water. Today a variety of constituents of the oceanic water masses are measured including: oxygen, carbon-dioxide, freon, radioactive tracers and the concentration of biological constituents. Freon gases, were released to the atmosphere starting from the first part of the 20th century and was stopped when it was found that they are responsible for the destruction of the atmospheric ozone layer, are dissolved in the ocean. By measuring their concentration in oceanic waters the age of the water masses, that is the time since their last contact with the atmosphere, can be obtained. The same applies to some radioactive traces which were released to the atmosphere during atomic bomb explosions in the atmosphere during the mid twentieth century.

Tracers as temperature and salinity which change the density of the water masses are called *active tracers* as they act on the dynamics through their buoyancy, tracers that have no substantial impact on density of the water mass and thus on the dynamics are named *passive tracers*. The measurement of passive tracers is nevertheless important as they provide information about the movement of water masses.

Exercise 2: Search the Internet for maps of sea surface temperature (SST) and sea surface salinity (SSS).

Chapter 3

Physical properties of sea water

Sea water has many physical properties: temperature, salinity, pressure, density, electric conductivity, thermal conductivity, viscosity, diffusivity of temperature, diffusivity of salt, compressibility, thermal expansion, thermal capacity, speed of sound, optical refraction index and many more. If we like to characterize a probe of sea water we do not have to measure all of these quantities as they are not all independent. Indeed thermodynamics teaches us that sea water is described by only three independent variables¹. That means, if we have measured three of this properties say temperature, salinity and pressure all the other variables can be calculated (or looked up in a table) and do not have to be measured. The best known relation between physical properties is the function that allows to calculate the density of sea water from temperature, salinity and pressure it is called the *equation of state*.

$$\rho = \rho(T, S, P). \quad (3.1)$$

Density, or more precisely density differences, are of primary importance as they act due to the earths gravitational force on the dynamics of the ocean and is a primary source of motion in the ocean. We will thus further investigate the four properties appearing in the equation of state.

3.1 Salinity

Salinity is the easiest to comprehend, its concentration is given in grams of salt dissolved in one kilogram of sea water and is measured in practical salinity units (psu). If one kilogram of sea water contains 34.7 grams of salt, the sea water has a salinity of 34.7 psu. Since the 1980s this is not exactly true as salinity is determined by the conductivity of the water sample: the mass of dissolved salt in 1kg of sea water is actually around 1.005g times the salinity, depending on pressure and temperature. Typical values of salinity in the world ocean range from 33 to 37 psu. In marginal seas they differ from these typical values as these basins are often shallow and have higher fresh water fluxes per volume. In the Mediterranean Sea (average depth of 1500m) they vary between 37 and 39 psu, in the Red Sea (average depth of 490m) they typically measure between 40 and 42 psu, while in the Baltic Sea (average depth of 55m) they range from 10 to 20 psu. Marginal basins play an important role in the global ocean dynamics due to their role as “factories” of extreme water mass properties (salinity and temperature).

The sea salt is composed of different sorts of salt, although the salinity varies in the world ocean the ratio of the different salts is rather constant, an observation called *Dittmar’s law*,

¹We neglect the influence of: dissolved gases, chemical substances other than salt, variations in the composition of the sea salt and biology.

named after William Dittmar who, in 1884, analysed the waters collected by the scientific expedition of the British corvette, HMS Challenger (1872–1876). The major constituents of sea salt are shown in table 3.1. Small regional variations of the composition of sea salt are however present in the ocean and will probably to be included in the determination of a future equation of state with a higher degree of accuracy.

Salt	percentage
Chloride	54
Sodium	31
Sulfate	8
Magnesium	4
Calcium	1
Potassium	1
others	1

Table 3.1: Major constituents of sea salt

3.2 Temperature and Potential Temperature

Temperature is measured in degrees Celsius ($^{\circ}\text{C}$) and temperature differences in Kelvin (K), oceanographers are however slow in adapting to the SI unit Kelvin to measure temperature differences.

The temperature of the world ocean typically ranges from -2°C (-1.87°C freezing point for $S = 35$ at surface) (freezing temperature of sea water) to 32°C . About 75% of the world ocean volume has a temperature below 4°C . Before the opening of the Drake Passage 30 million years ago due to continental drift, the mean temperature of the world ocean was much higher. The temperature difference in the equatorial ocean between surface and bottom waters was about 7K compared to the present value of 26K. The temperature in the Mediterranean Sea is above 12°C even at the bottom and in the Red Sea it is above 20°C .

If one takes a mass of water at the surface and descends it adiabatically (without exchanging heat with the environment) its *in situ* (latin for: in position; the temperature you actually measure if you put a thermometer in the position) temperature will increase due to the increase of pressure. Indeed if you take a horizontal tube that is 5km long and filled with water of salinity $S = 35\text{psu}$ and temperature $T = 0^{\circ}\text{C}$ and put the tube to the vertical then the temperature in the tube will monotonically increase with depth reaching $T = 0.40^{\circ}\text{C}$ at the bottom. To get rid of this temperature increase in measurements oceanographers often use *potential temperature* θ (measured in $^{\circ}\text{C}$) that is the temperature of a the water mass when it is lifted adiabatically to the sea surface. It is always preferable to use potential temperature, rather than *in situ* temperature, as it is a conservative tracer (see section 3.7). Differences between temperature and potential temperature are small in the ocean $< 1.5\text{K}$, but can be important in the deep ocean where temperature differences are small.

3.3 θ -S Diagrams

If one mixes the mass m_1 (measured in kg) of sea water of salinity S_1 with the mass m_2 of sea water of salinity S_2 one obtains the mass $m_1 + m_2$ of sea water of salinity

$$S_3 = \frac{m_1 S_1 + m_2 S_2}{m_1 + m_2}. \quad (3.2)$$

This follows from the definition of the salinity and the mass conservation.

If one mixes the mass m_1 of sea water of temperature θ_1 with the mass m_2 kg of sea water of temperature θ_2 one obtains the mass $m_1 + m_2$ of sea water of temperature (see fig. 3.3)

$$\theta_3 = \frac{m_1 \theta_1 + m_2 \theta_2}{m_1 + m_2}. \quad (3.3)$$

The above is only strictly true if the heat capacity does not vary with temperature and salinity, which is approximately true if we restrict ourselves to oceanic values (errors are typically smaller than 1%), and when the (negligible) heat of mixing is neglected.

The analysis of water masses are performed with the help of θ -S *diagrams* as shown in fig. 3.3

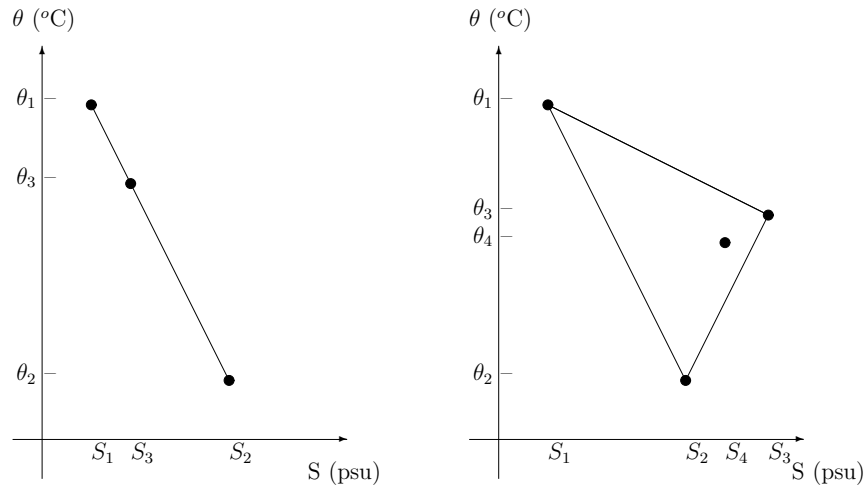


Figure 3.1: θ -S-diagram. Left: mixing of two water masses, the mixture of two water masses lies on a line between water masses. Right: mixing of three water masses, the mixture of 3 water masses lies within the triangle formed by the three water masses. The exact location can be obtained by eqs. 3.2 and 3.3.

3.4 Pressure

Pressure is measured in Pascal ($1 \text{ Pa} = 1 \text{ N m}^{-2}$). When pressure is considered, oceanographers usually mean hydrostatic pressure:

$$p(x, y, z) = p_{\text{atmos}} + g \int_z^0 \rho(z') dz', \quad (3.4)$$

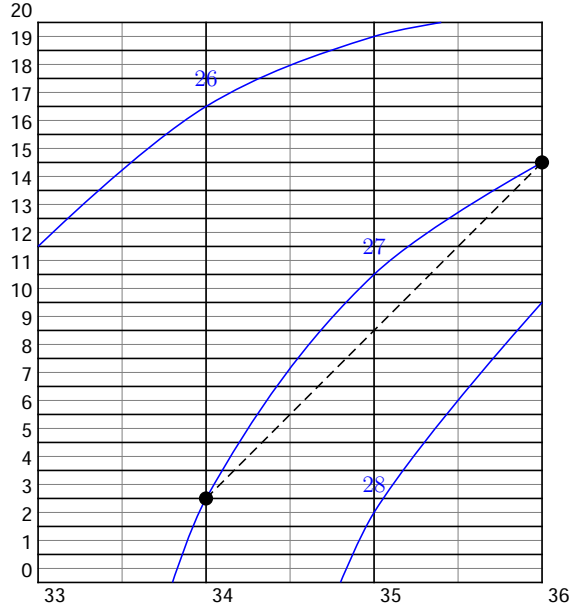


Figure 3.2: θ -S-diagram, potential density 0 dbar lines and σ -values are shown in blue. It is clearly seen that the mixture of two watermasses (dots) of equal density, which lies on the dashed line, is always denser than the initial water masses.

due to the atmospheric pressure p_{atmos} and the product of density ρ and gravitational acceleration of the overlaying fluid. Please note that also for oceanographers the upward direction is the positive direction, although they mostly speak of depth, this often leads to confusion. When using the hydrostatic pressure we neglect the usually small variations of pressure due to the fluid motion (acceleration of fluid). In the equations of motion (see 5.1 – 5.3), it is not the pressure, but its gradient that matters, which means, that only changes in pressure but not the absolute values are of importance to the dynamics. This allows oceanographers to furthermore neglect the atmospheric pressure and define that at the ocean surface $p = 0$. Other units of pressure are bars (1 bar = 10^5 Pa), or decibar (1 dbar = 10^4 Pa) which is roughly the increase of pressure when the ocean depth increases by 1m.

Attention: pressure is a scalar quantity, that is, has no direction!

3.5 Density and σ

Density is measured in kg/m^3 and typical values for sea water range from $1020 - 1050 \text{ kg/m}^3$ the density of sea water is usually given in sigma-values $\sigma_T(T, S) = (\rho(T, S, 0) - 1000 \text{ kg/m}^3) / (1 \text{ kg/m}^3)$, that is a water of $\rho(10^\circ, 35, 0) = 1031.0 \text{ kg/m}^3$ has $\sigma(10^\circ, 35) = 31.0$ (no units!). The σ_T (sigma-sub-T) value refers to the density a water mass at temperature T and Salinity S has at the ocean surface.

3.6. HEAT CAPACITY

13

Density depends on temperature, salinity and pressure in a non-linear way and these non linearities lead to many interesting phenomena. The actual dependence, for values typical to the ocean, is given by the *UNESCO 1981 formula* which is a best fit to laboratory measurements. A numerical version of this formula is implemented in all numerical models of the ocean dynamics.

The non linearity of the equation of state leads to interesting and important phenomena in oceanography. One is *cabbeling* which means that by mixing of two water masses the resultant water mass has a density which is superior than the weighted mean density. As shown in fig. 3.2 if the two water masses have the same density their mixture, somewhere on the dashed line, has a larger density.

It is the difference in density that is dynamically important. We have seen in section 3.2 that two which are at different depth might have the same temperature but different potential temperature. As it is the potential temperature that is conserved by a water mass when move adiabatically it seems more natural to measure sigma values in terms of potential temperature. To compare densities of water masses oceanographers introduced the notion of potential density, where $\sigma_0(\theta, S)$ is the “sigma value” of a water mass of potential temperature θ and salinity S when brought adiabatically (no exchange of heat) to the sea surface. Potential density is, unfortunately, not the answer to all the problems, as two water masses which have the same σ_0 might have different densities at depth. This is again a consequence of the non-linearity in the state equation called *thermobaricity* which is due to the fact that warmer water is less compressible than colder water. This can be seen in fig. 3.3 where the sigma density of two water masses is given at the pressure of 0 dbar (at the surface) and at 4000 dbar. The water mass which is heavier at the surface is actually lighter at 4000 dbar. This lead to the definition of not only the potential density at the surface σ_0 but also for example to σ_{4000} , which gives the sigma value of a water parcel when transported adiabatically to a pressure of 4000dbar \approx 4000m depth.

Locally the dependence can be written:

$$\rho(T + \delta T, S + \delta S, p + \delta p) = \rho(T, S, p)(1 - \alpha\delta T + \beta\delta S + \gamma\delta p), \quad (3.5)$$

where α is the thermal expansion coefficient, β is the saline contraction coefficient and γ the compressibility of sea water. The non-linearity of the state equation arises from the fact that all these coefficients are themselves functions of temperature, salinity and pressure.

3.6 Heat Capacity

The dynamics of the ocean is important for our climate due to its transport of heat from the low to the high latitudes. The heat capacity of sea water is around $4.0 \times 10^3 \text{ J (K kg)}^{-1}$, about four times the value of air. At the sea surface air is almost 770 times less dense than water. At equal volume water contains approximately 3000 times more heat than air.

Exercise 3: Suppose that the atmosphere above the ocean has a constant temperature (independent of height) and that the ocean underneath is at the same temperature. What is the depth of the ocean if it contains the same amount of heat as the atmosphere above? ($C_p(\text{seawater}) = 4.0 \times 10^3 \text{ J/(kgK)}$ and $C_p(\text{air}) = 1.0 \times 10^3 \text{ J/(kgK)}$). Do not use the thickness of the atmosphere in your calculations.

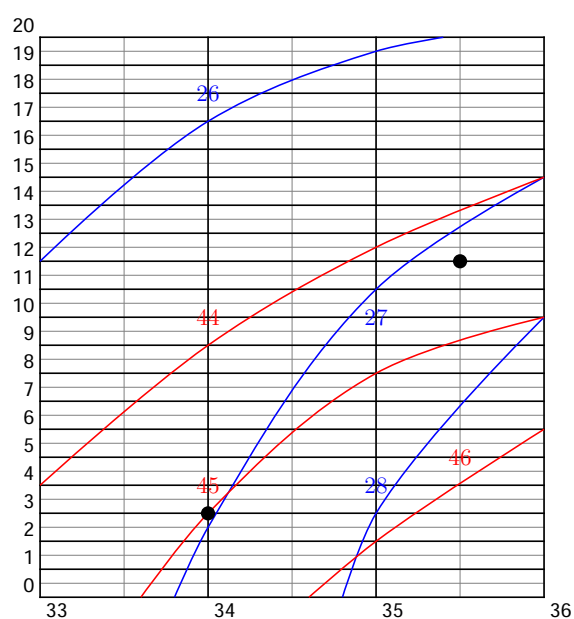


Figure 3.3: θ -S-diagram; potential density 0 dbar lines and σ_0 -values are shown in blue; potential density 4000 dbar lines and σ_{4000} -values are shown in red. The figure illustrates the phenomenon of thermobaricity. The hotter and saltier water mass is heavier at the surface and lighter at 4000m depth than the other water mass. This happens because hot water is less compressible than colder water.

3.7 Conservative Properties

The dynamics of a tracer S transported by an incompressible fluid of velocity field \mathbf{u} , diffused with the diffusion κ and subject to sources and sinks Q is governed by the advection diffusion equation:

$$\partial_t S + \mathbf{u} \cdot \nabla S - \nabla \cdot (\kappa \nabla S) = Q. \quad (3.6)$$

A scalar is said to be conservative if $Q = 0$.

Besides their important influence on the density there is another reason why salinity and potential temperature play such an important role in oceanography they are conservative. Away from the boundaries these properties can only be changed by mixing with water masses of different characteristics. Please note, that temperature is not conservative as it changes when a water parcel is transported up or down in the ocean, when pressure changes. This is equivalent to say, that there are no sources or sinks of salinity and potential temperature in the ocean interior.

Other scalars like dissolved oxygen nutrients and biological concentrations are not conservative as they have sinks and sources.

3.8 Water Masses in the Ocean

Water in the ocean mixes due to molecular diffusion and turbulent stirring (see section 10.2). In large parts of the ocean, away from the boundaries, the mixing is small. Water parcels thus conserve their conservative characteristics, salinity and potential temperature, when transported over long distances and a mean large scale transport velocity of water masses and the velocity field in the ocean can be determined by measuring potential temperature and salinity. Furthermore, water mass characteristics change only slowly in the deep ocean and show only small variations over the years. These changes can be used as important indicators of climate (long-time-large-space) variability.

3.9 Sea Ice and Ice Bergs

Fresh water freezes at 0°C and sea water with a salinity of 35psu freezes at -1.8°C , at atmospheric pressure. Fresh water has its maximal density at 4°C , when lakes cool below this temperature the cold water stays at the surface and freezing happens quickly near the surface while 4°C warm water is found in the deep lake. The ice formation of lakes mostly depends on the atmospheric temperature and the wind speed. For water with a salinity over 24.7psu the maximum density is at the freezing temperature. When the ocean is cooled the cold surface water descends and is replaced by warmer water from depth until the freezing temperature is reached. Sea water can only freeze when the cooling from the atmosphere is stronger than the convective warming from the deep ocean. So, for the formation of sea ice, besides atmospheric temperature and the wind speed, the water depth and the stratification of the ocean in temperature and salinity are important parameters. No such convective warming is present for fresh water lakes once the temperature is below 4°C , and indeed you can go ice-skating on lakes in northern Europe while the nearby sea is completely ice free. The vertical convection process is studied in section 10.3.

Ice cover are crucial to the ocean dynamics as it: (i) has a strong influence on the reflection of the incoming radiation, especially when they are covered by fresh snow (see section 4.1.1),

(ii) reduces the transfert of heat, isolating the ocean, (iii) actes as a thermal resevoir due to the latent heat associated with melting and freezing and (iv) changes the salinity and buoyancy, through melting and freezing. The first point is responsible for the fact that polar regions are very sensitive to global climate change. A little change in temperature can freeze or melt sea ice, the positive feed back of the albedo will then amplify the initial temperature change.

The Arctic Ocean is almost completely surrounded by land, while the Antarctic Ocean is completely open towards lower latitude. Arctic sea ice is thus hindered to travel towards lower latitude and typically survives several summer periods and has a typical thickness from two to three meters. Only about 10 % of the arctic ice travels south through the Fram Strait every year. Whereas the Antarctic ice is mostly seasonal, with 80 % disappearing by the end of the austral summer and has a typical thickness from one to two meters.

During freezing salt becomes trapped in the ice forming brine pockets which have a size around 10^{-4} m. The amount of salt trapped in the ice during freezing increases with the growth rate of the sea ice and the salinity of the seawater. Newly formed ice has a typical salinity around 14psu which is roughly half of the salinity of seawater. Within the sea ice the brine moves downward and leaves the ice at its lower boundary. The overall salinity of sea ice decreases with its age, leading to different salinities of the seasonal ice in the Antarctic and the multi-year ice in the Arctic. The salinity of ice has important influence on its thermal properties such as heat capacity, thermal conductivity and latent heat content. Sea ice also contains air bubbles, their volume typically increases with age, reducing the ice density. A typical value for air bubble volume of multi-year ice is 15%. Sea ice is a multi-component multi-phase material. The fraction of each component and phase is subject to change due to exterior forcings.

Ice bergs are broken off (calved) parts of land glaciers and ice shelves, land glaciers that have migrated into the ocean, and do not contain significant amounts of salt. Ice bergs calved from ice shelves can have a horizontal extent of 100km.

Chapter 4

Surface fluxes, the forcing of the ocean

The principal source of the ocean dynamics are the fluxes through the ocean surface. The principal fluxes at the surface of the ocean are:

- heat flux
- fresh water flux
- momentum flux
- other chemical fluxes

The major source of ocean currents is the momentum flux provided by the wind-shear at the ocean surface. The first two of these fluxes, provided by heating-cooling and precipitation-evaporation at the ocean surface, create density differences influencing the ocean dynamics. The primary source of all these energy fluxes is the sun.

4.1 Heat Flux

The heat flux can be decomposed in four major contributions:

$$Q = Q_{\text{shortwave}} + Q_{\text{infrared}} + Q_{\text{sensible}} + Q_{\text{latent}} + \epsilon \quad (4.1)$$

Where we define $Q > 0$ if the ocean receives energy.

The first two are radiative fluxes which will be discussed in the next subsection, followed by sections discussing the sensible heat fluxes due to molecular exchange of heat and latent heat fluxes due to evaporation (and condensation of moist air).

4.1.1 Radiative Fluxes

The wave length of irradiation of a black body depends on its temperature (law of Wien). The radiation from the sun which has an average temperature around 6000K has a wave length around $\lambda = 0.48\mu m$ (short wave) ($1\mu m = 10^{-6}m$), which is in the short wave (visible) spectra. The radiation of the ocean and atmosphere, with an average surface temperature of 283K has a wave length around $\lambda = 10\mu m$, which is in the infrared spectra. The energy radiated is proportional to the fourth-power of the temperature (law of Stefan-Boltzmann)

The short wave heat flux of the sun just above the atmosphere is given by the solar-(NON)-constant which has an average value of 1.37kW m^{-2} , and varies $\pm 4\%$. Roughly two thirds of this variability is due to the varying distance between the sun and the earth and the reset

due to the variability of the solar radiation. The solar irradiance has a marked cycle of 11 years leading to a variability of only 0.1%. The effects of (small) shifts in the frequency of the solar irradiance on the earth's heat budget are unexplored. Due to geometry of the earth, its inclination of its rotation axis to the sun, and its rotation, the short wave heat flux at the top of the atmosphere during one day is a function of the day in the year and the latitude.

Part of the incoming short wave radiation is reflected back to space by the atmosphere, the amount strongly depends on the cloudiness.

The quantity of short wave heat energy absorbed by the earth depends also on the extent to which it reflects radiation. This is measured by the albedo which is the ratio of reflected energy to incident energy. The albedo is a dimensionless number between zero for a black body which absorbs all radiation, and one, for an object reflecting all light as, for example, a perfect mirror. Various values of albedo are given in table. 4.1.1.

Surface type	albedo
fresh snow	0.7 – 0.9
ice	0.3 – 0.4
ocean surface	0.05 – 0.15

Table 4.1: Albedo

The albedo of the ocean depends also on the roughness of the ocean (waves) and the angle of incidence of the radiation. The errors in the determination of the albedo of the sea surface present a major source of error in the estimation of the heat uptake of the ocean.

Exercise 4: Search the Internet for typical values of the albedo of the ocean.

Exercise 5: Search the Internet for a global map of the short-wave and long-wave radiative heat fluxes.

4.1.2 Sensible Heat Flux

The sensible heat flux, that is the heat fluxes between the ocean and the atmosphere due to molecular exchange of heat (not matter) is mostly negative, as the ocean surface, which is heated by the radiation of the sun, is on average warmer than the atmosphere just above. The sensible heat flux depends on the density of air $\rho_{\text{air}} = 1.3 \text{ kg m}^{-3}$ its heat capacity $C_p = 1.3 \times 10^3 \text{ J (K kg)}^{-1}$, the wind speed usually measured at the reference level of 10 meters above the ocean surface $|\mathbf{u}_{10}|$ and the local temperature difference between the sea surface temperature (SST) and the atmosphere 10 meters above the ocean.

The bulk formula to calculate the sensible heat flux is

$$Q_{\text{sensible}} = \rho_{\text{air}} C_p C_s |\mathbf{u}_{10}| (T_{\text{atmos}} - SST), \quad (4.2)$$

where the sensible heat transfer coefficient $C_s = 900$ is empirically determined.

Exercise 6: Search the Internet for a map of the sensible heat flux of the world ocean.

4.1.3 Latent Heat Flux

Evaporation is the major loss of heat by the ocean. The most energetic water molecules have enough energy to escape the water reducing this way the average temperature of the remaining

4.2. FRESH WATER FLUX

19

water. The thus produced latent heat flux (which is almost always negative; except in the rare cases when hot moist air overlies the ocean and energetic fluid molecules enter the ocean) depends on the latent heat coefficient $L_E = 2.5 \times 10^6 \text{ J kg}^{-1}$, the wind speed measured at the reference level 10 meters above the ocean surface $|\mathbf{u}_{10}|$ and the relative humidity of the atmosphere 10m above the ocean q_a which is measured in kg of water vapour by kg of air and q_s is the saturation value which is a function of the sea surface temperature (SST), where it is supposed, that the air just above the ocean is saturated with water vapor.

The flux is approximated by a bulk formula:

$$Q_{\text{latent}} = \rho_{\text{air}} L_E C_L |\mathbf{u}_{10}| (q_s - q_a), \quad (4.3)$$

where the latent heat transfer coefficient $C_L = 1.35 \times 10^{-3}$ is empirically determined.

Exercise 7: Search the Internet for a map of the latent heat flux of the world ocean.

Exercise 8: Why is 10m chosen as the reference level?

4.1.4 Other Heat Fluxes

There are other sources of heat fluxes to the ocean which are however much smaller than the fluxes discussed above. Bio-chemical processes heat the ocean, as do naturally occurring radioactive processes, geothermal energy from the interior of our planet and internal friction of the fluid motion. Although the total energy fluxes of these processes are small they might be important locally in the ocean, an example are underwater volcanoes which heat up the ocean locally.

4.2 Fresh Water Flux

Fresh water fluxes are mainly due to rain, evaporation, condensation, melting of sea ice, freezing of sea water and river runoff. Recent research also suggests that a substantial amount of fresh water enters the oceans through ground water fluxes.

Exercise 9: Search the Internet for a map of the fresh water flux of the world ocean.

4.3 Wind Shear

The wind shear (a 2 dimensional vector quantity) is the major source of motion of the oceanic water masses. Many attempts have been made to obtain the exact shear as a function of the wind-velocity at the reference level of 10 meters above the ocean.

$$\tau = c_D \rho_{\text{air}} |\mathbf{u}_{10}| \mathbf{u}_{10} \quad (4.4)$$

Where the drag coefficient c_D is also a function of the wind velocity measured 10m above the sea surface \mathbf{u}_{10m} and the density of air is around $\rho_{\text{air}} = 1.3 \text{ kg m}^{-3}$. The drag coefficient is often estimated to be $c_D = 1.3 \times 10^{-3}$. More recent research suggests:

$$c_D = (0.29 + \frac{3.1m/s}{u_{10m}} + \frac{7.7(m/s)^2}{u_{10m}^2})/1000 \text{ for } 3m/s < |u_{10m}| < 6m/s, \quad (4.5)$$

$$c_D = (0.6 + .070u_{10m})/1000 \text{ for } 6m/s < |u_{10m}| < 26m/s. \quad (4.6)$$

This empirical formulas can at best be seen as a sophisticated rule of thumb. Note that the drag coefficient increases with wind speed. This is due to the larger roughness (waves) of the ocean surface with higher winds.

Uncertainties in the determination of the wind stress are a major difficulty in modelling the ocean dynamics.

Exercise 10: Search the Internet for a map of the wind shear of the world ocean.

4.4 What about tides?

The tidal dynamics varies on time scales that are very short compared to the large scale circulation relevant for climate issues and has no direct dominant influence on the long-term large-scale dynamics of the ocean. Tides do however substantially affect the large scale circulation by increasing the vertical mixing of the ocean due to the interaction of tidal motion and topographic features of the ocean basin. The tidal energy used to vertically mix the ocean is however difficult to estimate, as are the locations where this mixing occurs. These questions are actually an important subject of research in physical oceanography.

Chapter 5

Dynamics of the Ocean

5.1 From the Navier-Stokes to the Shallow Water Equations

The dynamics of and incompressible fluid is described by the Navier-Stokes equations:

$$\partial_t u + u \partial_x u + v \partial_y u + w \partial_z u + \frac{1}{\rho_0} \partial_x P = \nu \nabla^2 u \quad (5.1)$$

$$\partial_t v + u \partial_x v + v \partial_y v + w \partial_z v + \frac{1}{\rho_0} \partial_y P = \nu \nabla^2 v \quad (5.2)$$

$$\partial_t w + u \partial_x w + v \partial_y w + w \partial_z w + \frac{1}{\rho_0} \partial_z P = -g \frac{\rho}{\rho_0} + \nu \nabla^2 w \quad (5.3)$$

$$\begin{aligned} & \partial_x u + \partial_y v + \partial_z w = 0 \\ & + \text{boundary conditions} \end{aligned} \quad (5.4)$$

where u is the zonal, v the meridional and w the vertical (positive upward even in oceanography) velocity component, P the pressure, ρ density, ρ_0 the average density, ν viscosity of seawater, g gravity, and $\nabla^2 = \partial_{xx} + \partial_{yy} + \partial_{zz}$ is the Laplace operator.

The equation of a scalar transported by a fluid is:

$$\partial_t T + u \partial_x T + v \partial_y T + w \partial_z T = \kappa_T \nabla^2 T \quad (5.5)$$

$$+ \text{boundary conditions} \quad (5.6)$$

$$\partial_t S + u \partial_x S + v \partial_y S + w \partial_z S = \kappa_S \nabla^2 S \quad (5.7)$$

$$+ \text{boundary conditions} ,$$

where T is temperature, S is salinity and κ_T , κ_S are the diffusivities of temperature and salinity. The state equation:

$$\rho = \rho(S, T, P) \quad (5.8)$$

allows to obtain the density from salinity, temperature and pressure.

The above equations describe the motion of the ocean to a very high degree of accuracy, but they are much too complicated to work with, even today's and tomorrows numerical ocean models are and will be based on more or less simplified versions of the above equations.

These equations are too complicated because:

- Large range of scales; from millimeter to thousands of kilometers
- Nonlinear interactions of scales

- How is pressure P determined, how does it act?
- Complicated boundary conditions; coastline, surface fluxes ...
- Complicated equation of state (UNESCO 1981)
-

A large part of physical oceanography is in effect dedicated to finding simplifications of the above equations. In this endeavour it is important to find a balance between simplicity and accuracy.

How can we simplify these equations? Two important observations:

- The ocean is very very flat: typical depth ($H=4\text{km}$) typical horizontal scale ($L=10\,000\text{ km}$)
- Sea water has only small density differences $\Delta\rho/\rho \approx 3 \cdot 10^{-3}$

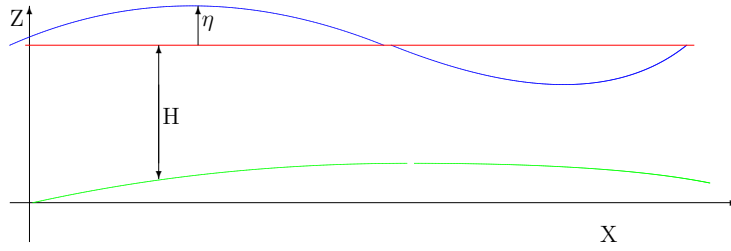


Figure 5.1: Shallow water configuration

Using this we will try to model the ocean as a *shallow homogeneous* layer of fluid, and see how our results compare to observations.

Using the shallowness, equation (5.4) suggests that w/H is of the same order as u_h/L , where $u_h = \sqrt{u^2 + v^2}$ is the horizontal speed, leading to $w \approx (Hu_h)/L$ and thus $w \ll u_h$. So that equation (5.3) reduces to $\partial_z P = -g\rho$ which is called the *hydrostatic approximation* as the vertical pressure gradient is now independent of the velocity in the fluid.

Using the homogeneity $\Delta\rho = 0$ further suggest that:

$$\partial_{xz}P = \partial_{yz}P = 0. \quad (5.9)$$

If we derive equations (5.1) and (5.2) with respect to the vertical direction we can see that if $\partial_z u = \partial_z v$ at some time this propriety will be conserved such that u and v do not vary with depth. (We have neglected bottom friction). Putting all this together we obtain the following equations:

$$\partial_t u + u\partial_x u + v\partial_y u + \frac{1}{\rho}\partial_x P = \nu\nabla^2 u \quad (5.10)$$

$$\partial_t v + u\partial_x v + v\partial_y v + \frac{1}{\rho}\partial_y P = \nu\nabla^2 v \quad (5.11)$$

$$\partial_x u + \partial_y v + \partial_z w = 0 \quad (5.12)$$

$$\text{with } \partial_z u = \partial_z v = \partial_{zz} w = 0 \quad (5.13)$$

+ boundary conditions

5.2. THE LINEARIZED ONE DIMENSIONAL SHALLOW WATER EQUATIONS § 23

What are those boundary conditions? Well on the ocean floor, which is supposed to vary only very slowly with the horizontal directions, the vertical velocity vanishes $w = 0$ and it varies linearly in the fluid interior (see eq. 5.13). The ocean has what we call a free surface with a height variation denoted by η . The movement of a fluid partical on the surface is govended by:

$$\frac{d_H}{dt}\eta = w(\eta) \quad (5.14)$$

where $\frac{d_H}{dt} = \partial_t + u\partial_x + v\partial_y$ is the horizontal Lagrangian derivation. We obtain:

$$\partial_t\eta + u\partial_x\eta + v\partial_y\eta - (H + \eta)\partial_z w = 0 \quad (5.15)$$

or

$$\partial_t\eta + u\partial_x(H + \eta) + v\partial_y(H + \eta) + (H + \eta)(\partial_x u + \partial_y v) = 0. \quad (5.16)$$

Using the hydrostatic approximation, the pressure at a depth d from the unperturbed free surface is given by: $P = g\rho(\eta + d)$, and the horizontal pressure gradient is related to the horizontal gradient of the free surface by:

$$\partial_x P = g\rho\partial_x\eta \text{ and } \partial_y P = g\rho\partial_y\eta \quad (5.17)$$

Some algebra now leads us to the shallow water equations (sweq):

$$\partial_t u + u\partial_x u + v\partial_y u + g\partial_x\eta = \nu\nabla^2 u \quad (5.18)$$

$$\partial_t v + u\partial_x v + v\partial_y v + g\partial_y\eta = \nu\nabla^2 v \quad (5.19)$$

$$\begin{aligned} \partial_t\eta + \partial_x[(H + \eta)u] + \partial_y[(H + \eta)v] = 0 \\ + \text{boundary conditions} \end{aligned} \quad (5.20)$$

All variables appearing in equations 5.18, 5.19 and 5.20 are independent of z !

5.2 The Linearized One Dimensional Shallow Water Equation

S

We will now push the simplifications even further, actually to its non-trivial limit, by considering the linearized one dimensional shallow water equations. If we suppose the dynamics to be independent of y and if we further suppose $v = 0$ and that H is constant, the shallow water equations can be written as:

$$\partial_t u + u\partial_x u + g\partial_x\eta = \nu\nabla^2 u \quad (5.21)$$

$$\begin{aligned} \partial_t\eta + \partial_x[(H + \eta)u] = 0 \\ + \text{boundary conditions.} \end{aligned} \quad (5.22)$$

if we further suppose that $u^2 \ll g\eta$ that the viscosity $\nu \ll g\eta L/u$ and $\eta \ll H$ then:

$$\partial_t u + g\partial_x\eta = 0 \quad (5.23)$$

$$\partial_t\eta + H\partial_x u = 0 \quad (5.24)$$

+boundary conditions,

which we combine to:

$$\begin{aligned} \partial_{tt}\eta &= gH\partial_{xx}\eta \\ &+ \text{boundary conditions.} \end{aligned} \quad (5.25)$$

This is a one dimensional linear non-dispersive wave equation. The general solution is given by:

$$\eta(x, t) = \eta_0^-(ct - x) + \eta_0^+(ct + x) \quad (5.26)$$

$$u(x, t) = \frac{c}{H}(\eta_0^-(ct - x) - \eta_0^+(ct + x)), \quad (5.27)$$

where η_0^- and η_0^+ are arbitrary functions of space only. The speed of the waves is given by $c = \sqrt{gH}$ and perturbations travel with speed in the positive or negative x direction. Note that c is the speed of the wave not of the fluid!

Rem.: If we choose $\eta_0^-(\tilde{x}) = \eta_0^+(-\tilde{x})$ then initially the perturbation has zero fluid speed, and is such only a perturbation of the sea surface! What happens next?

An application of such equation are Tsunamis if we take: $g = 10\text{m/s}^2$, $H = 4\text{km}$ and $\eta_0 = 1\text{m}$, we have a wave speed of $c = 200\text{m/s} = 720\text{km/h}$ and a fluid speed $u_0 = 0.05\text{m/s}$. What happens when H decreases? Why do wave crests arrive parallel to the beach? Why do waves break?

You see this simplest form of a fluid dynamic equation can be understood completely. It helps us to understand a variety of natural phenomena.

Exercise 11: does the linearized one dimensional shallow water equation conserve energy?

Exercise 12: is it justified to neglect the nonlinear term in eq. (5.21) for the case of a Tsunami?

5.3 Reduced Gravity

Suppose that the layer of fluid (fluid 1) is lying on a denser layer of fluid (fluid 2) that is infinitely deep. $H_2 \rightarrow \infty \Rightarrow c_2 \rightarrow \infty$, that is perturbations travel with infinite speed. This implies that the lower fluid is always in equilibrium $\partial_x P = \partial_y P = 0$. The lower fluid layer is passive, does not act on the upper fluid but adapts to its dynamics, so that $\eta_1 = \frac{\rho_1 - \rho_2}{\rho_1} \eta_2$. If we set $\eta = \eta_1 - \eta_2$ then $\eta = \frac{\rho_2}{\rho_2 - \rho_1} \eta_1$ and the dynamics is described by the same sw eqs. 5.18, 5.19 and 5.20 with gravity g replaced by the *reduced gravity* $g' = \frac{\rho_2 - \rho_1}{\rho_2} g$ ("sw on the moon").

Example: $g' = 3 \cdot 10^{-3}g$, $H = 300\text{m}$, $\eta_0 = .3\text{m}$ we get a wave speed $c = \sqrt{g'H} = 3\text{m/s}$ and a fluid speed of $u = 1\text{m/s}$.

Comment 1: when replacing η by $g'\eta$ it seems, that we are changing the momentum equations, but in fact the thickness equation is changed, as we are in the same time replacing the deviation of the free surface η (which is also the deviation of the layer thickness in not-reduced-gravity case) by the deviation of the layer thickness η , which is $(\rho_2 - \rho_1)/\rho_2$ times the surface elevation in the reduced gravity case. This means also that every property which is derived only from the momentum equations not using the thickness equation is independent of the reduced gravity.

Comment 2: fig. 5.3 demonstrates, that the layer thickness can be measured in two ways, by the deviation at the surface (η_1) or by density structure in the deep ocean (η_2). For ocean dynamics the surface deviation for important dynamical features, measuring hundreds of kilometers in the horizontal, is usually less than 1m whereas variations of (η_2) are usually

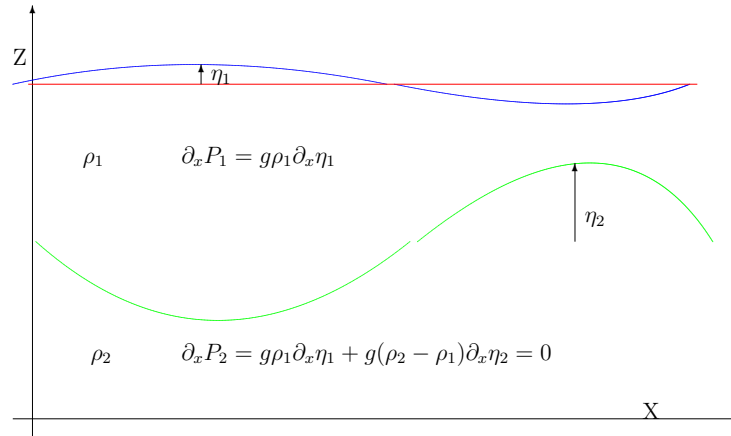


Figure 5.2: Reduced gravity shallow water configuration

several hundreds of meters. Historically the measurement of the density structure of the ocean to obtain η_2 are the major source of information about large scale ocean dynamics. Today's satellites measure the surface elevation of the ocean (altimetry) at a spatial and temporal density unknown before and are today our major source of information.

5.4 Two Dimensional Stationary Flow

We have seen in the previous sections, that the dynamics of a shallow fluid layer can be described by the two components of the velocity vector $(u(x, y, t), v(x, y, t))$ and the surface elevation $\eta(x, y, t)$. The vertical velocity $w(x, y, t)$ is, in this case, determined by these 3 variables. The vertical velocities in a shallow fluid layer are usually smaller than their horizontal counterparts and we have to a good approximation a two dimensional flow field. Important quantities in fluid mechanics are the divergence $d = \partial_x u + \partial_y v$ and the vorticity $\zeta = \partial_x v - \partial_y u$. If a variable does not depend on time it is called stationary. The trajectory of a small particle transported by a fluid is always tangent to the velocity vector and its speed is given by the magnitude of the velocity vector. In a stationary flow its path is called a stream line. If the flow has a vanishing divergence it can also be described by a stream function Ψ with $v = \partial_x \Psi$ and $u = -\partial_y \Psi$.

Exercise 13: show that every flow that is described by stream function has zero divergence.

Exercise 14: express the vorticity in terms of the stream function.

Exercise 15: draw the velocity vectors and streamlines and calculate vorticity and divergence. Draw the a stream function where ever possible:

$$\begin{pmatrix} u \\ v \end{pmatrix} = \begin{pmatrix} -x \\ -y \end{pmatrix}; \begin{pmatrix} y \\ 0 \end{pmatrix}; \begin{pmatrix} -y \\ x \end{pmatrix}; \begin{pmatrix} -x \\ y \end{pmatrix}; \frac{1}{x^2 + y^2} \begin{pmatrix} -y \\ x \end{pmatrix}; \begin{pmatrix} \cos y \\ \sin x \end{pmatrix}. \quad (5.28)$$

5.5 Rotation

When considering the motion of the ocean, at time scales larger than a day, the rotation of the earth is of paramount importance. Newton's laws of motion only apply when measurements are done with respect to an inertial frame, that is a frame without acceleration and thus without rotation. Adding to all measurements (and to boundary conditions) the rotation of the earth would be very involved (the tangential speed is around 400m/s and the speed of the ocean typically around 0.1m/s), one should then also have "rotating boundaries", that is the rotation would only explicitly appear in the boundary conditions, which then would be very involved. It is thus a necessity to derive Newton's laws of motion for a frame rotating with the earth, called *geocentric frame*, to make the problem of geophysical fluid dynamics treatable by calculation.

5.6 The Coriolis Force

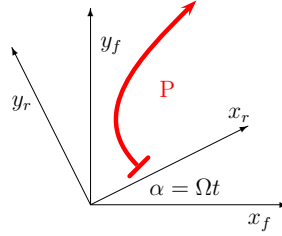


Figure 5.3: A moving point P observed by a fix and a rotating coordinate system

Let us start with considering a movement of a point P that is observed by two observers, one in an inertial frame (subscript $_f$) and one in a frame (subscript $_r$) that is rotating with angular velocity Ω . The coordinates at every time t transform following:

$$\begin{pmatrix} x_f \\ y_f \end{pmatrix} = \begin{pmatrix} x_r \cos(\Omega t) - y_r \sin(\Omega t) \\ x_r \sin(\Omega t) + y_r \cos(\Omega t) \end{pmatrix} \quad (5.29)$$

In a inertial (non-rotating) frame Newtons laws of motion are given by:

$$\partial_{tt} \begin{pmatrix} x_f \\ y_f \end{pmatrix} = \begin{pmatrix} F_f^x \\ F_f^y \end{pmatrix} \quad (5.30)$$

Where F_i are forces per mass, to simplify notation. So, in an inertial frame if the forces vanish the acceleration vanishes too. How can we describe such kind of motion in a rotating frame.

Combining eqs. (5.29) and (5.30), performing the derivations and neglecting the forces in eq. 5.30, we obtain:

$$\partial_{tt} \begin{pmatrix} x_f \\ y_f \end{pmatrix} = \begin{pmatrix} (\partial_{tt}x_r - 2\Omega\partial_t y_r - \Omega^2 x_r) \cos(\Omega t) - (\partial_{tt}y_r + 2\Omega\partial_t x_r - \Omega^2 y_r) \sin(\Omega t) \\ (\partial_{tt}x_r - 2\Omega\partial_t y_r - \Omega^2 x_r) \sin(\Omega t) + (\partial_{tt}y_r + 2\Omega\partial_t x_r - \Omega^2 y_r) \cos(\Omega t) \end{pmatrix} = 0 \quad (5.31)$$

This is only satisfied if:

$$\partial_{tt}x_r - 2\Omega\partial_t y_r - \Omega^2 x_r = 0 \quad \text{and} \quad (5.32)$$

$$\partial_{tt}y_r + 2\Omega\partial_t x_r - \Omega^2 y_r = 0. \quad (5.33)$$

5.6. THE CORIOLIS FORCE

27

Which is the analog of eq. (5.30) in a rotating frame.

The second and the third term in eqs. (5.32) and (5.33) look like (real) forces, especially if we write them on the right side of the equal sign and they are called the Coriolis and the centrifugal force, respectively. They also feel like real forces, when you experience them in a merry-go-round. They look like and feel like but they are no real forces. They are artifacts of a rotating coordinate system and are thus called apparent forces.

If we express this equation in terms of $u = \partial_t x$ and $v = \partial_t y$ we obtain:

$$\partial_t \begin{pmatrix} u_f \\ v_f \end{pmatrix} = \partial_t \begin{pmatrix} u_r \\ v_r \end{pmatrix} + 2\Omega \begin{pmatrix} -v_r \\ u_r \end{pmatrix} - \Omega^2 \begin{pmatrix} x_r \\ y_r \end{pmatrix}. \quad (5.34)$$

But what about the real forces (F_f^x, F_f^y) we neglected? Well forces are usually measured in the geocentric frame and so we do not have to worry how they transform from an inertial frame to a geocentric frame.

Other ways of deriving these equations can be found in literature, all leading to the same result. The equations are usually given in vector notation:

$$\partial_t \mathbf{u}_f = \partial_t \mathbf{u}_r + 2\boldsymbol{\Omega} \times \mathbf{u} + \boldsymbol{\Omega} \times \boldsymbol{\Omega} \times \mathbf{r}. \quad (5.35)$$

Here \times denotes the vector product (if you know what the vector product is: be happy!; if you do not know what the vector product is: don't worry be happy!). On our planet the rotation vector points northward along the south-north axis and has a magnitude of $|\boldsymbol{\Omega}| = 2\pi/T = 7.3 \cdot 10^{-5} \text{s}^{-1}$. Where $T \approx 24 \cdot 60 \cdot 60 \text{s}$ is the earth's rotation period.

For large scale oceanic motion the horizontal component of the rotation vector $\boldsymbol{\Omega}$ is usually neglected, this is called the *traditional approximation*. Twice the vertical component of the rotation vector is denoted by $f = 2|\boldsymbol{\Omega}| \sin \theta$ and called *Coriolis parameter*, here θ is latitude. In the calculations involving mid-latitude dynamics $f = 10^{-4} \text{s}^{-1}$ is a typical value.

Using the traditional approximation and restraining to the two dimensional case equation (5.35) reads:

$$\partial_t \begin{pmatrix} u_f \\ v_f \end{pmatrix} = \partial_t \begin{pmatrix} u_r \\ v_r \end{pmatrix} + f \begin{pmatrix} -v_r \\ u_r \end{pmatrix} - \frac{f^2}{4} \begin{pmatrix} x_r \\ y_r \end{pmatrix}. \quad (5.36)$$

Exercise 16: suppose $\partial_t(u_f, v_f) = (0, 0)$ (no forces acting) and $(x_r, y_r) = (R \cos(\omega t), R \sin(\omega t))$ calculate ω and give an interpretation of the solution.

From now on we will omit the the subscript “ r ”.

The most disturbing term on the right-hand-side of equation (5.34) is the last (centrifugal term) as it makes reference to the actual location of the particle (or fluid element) considered. This means that the laws of motion change in (rotating) space!?!

When considering the motion of a fluid we can however forget about the centrifugal term, why? For this look at figure (5.4), which shows a cylindrical tank in rotation with a fluid inside, that is rotating with the tank. What we see is, that the free surface of this fluid has a parabolic shape, which is exactly such that the pressure gradient, induced by the slope of the free fluid surface balances the the centrifugal force. If this were not be the case the fluid would not be at rest! If in our calculations we suppose that the zero potential is the parabolic surface rather than a flat horizontal surface the last term in equation (5.34) is perfectly balanced by the pressure gradient due to the slope of the free fluid surface, that is:

$$g \nabla \eta + \frac{f^2}{4} \mathbf{r} = 0. \quad (5.37)$$

In such situation the last term in equation (5.34) has to be dropped.

Exercise 17: suppose $(x, y) = (R \cos(\omega t), R \sin(\omega t))$ for a fluid particle in the fluid corresponding to fig. 5.4, without exterior forces acting. Calculate ω . Such kind of motion, that is, anti-cyclonic rotation with a period which is **half** the local rotation period, is indeed often observed in oceanic and atmospheric motion and is called *inertial oscillation* and their frequency $(-f)$ is called *inertial frequency*.

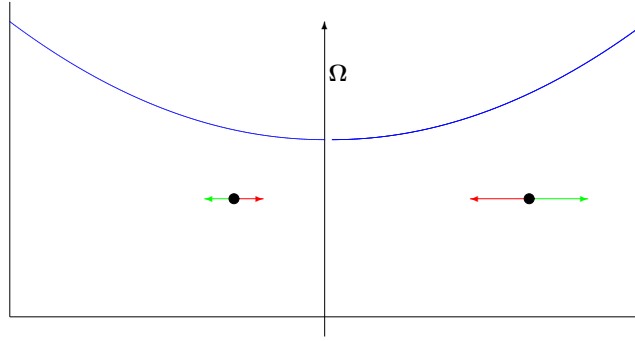


Figure 5.4: Cylinder in rotation with a free surface; two fluid particles with centrifugal force (green) and pressure gradient force (red).

On earth the same thing happens, the centrifugal force changes the geopotential of the earth, flattens it a little bit, makes it an ellipsoid.

5.7 The Shallow Water Equations in a Rotating Frame

If we take the results from the previous section we see that we only have to add the Coriolis force in the shallow water equations to obtain the shallow water equations in a rotating frame:

$$\partial_t u + u \partial_x u + v \partial_y u - f v + g \partial_x \eta = \nu \nabla^2 u \quad (5.38)$$

$$\partial_t v + u \partial_x v + v \partial_y v + f u + g \partial_y \eta = \nu \nabla^2 v \quad (5.39)$$

$$\partial_t \eta + \partial_x [(H + \eta)u] + \partial_y [(H + \eta)v] = 0 \quad (5.40)$$

+boundary conditions.

The nonlinear terms can be neglected if *Rossby number* $\epsilon = u/(fL)$ is small. The Rossby number compares the distance a fluid particle has traveled in the time f^{-1} to the length scale of the phenomenon considered. The linear (small Rossby number) version the shallow water equations in a rotating frame is:

$$\partial_t u - f v + g \partial_x \eta = 0 \quad (5.41)$$

5.8. GEOSTROPHIC EQUILIBRIUM

29

$$\partial_t v + f u + g \partial_y \eta = 0 \quad (5.42)$$

$$\partial_t \eta + H(\partial_x u + \partial_y v) = 0 \quad (5.43)$$

+boundary conditions.

Important: When approaching the equator f tends to zero, so rotation no longer dominates and most of the considerations following are not applicable. Equatorial dynamics is different!

In equations (5.41) and (5.42) we have neglected the viscous term which can be safely done as $\nu(\text{sea water}) \approx 10^{-6} \text{m}^2/\text{s}$.

Exercise 18: What is the Rossby number of the basin wide circulation in the North Atlantic when $u = 10^{-1} \text{m/s}$? What is the Rossby number of a Gulf Stream eddy when $u = 1 \text{m/s}$ and the radius $R = 30 \text{km}$?

5.8 Geostrophic Equilibrium

Large-scale ocean currents usually change on a time scale much larger than f^{-1} and are thus often well approximated by the stationary versions of eqs. (5.41) – (5.43) which are,

$$f v = g \partial_x \eta \quad (5.44)$$

$$-f u = g \partial_y \eta \quad (5.45)$$

this is called the *geostrophic equilibrium*. For a flow in geostrophic equilibrium all variables can be expressed in terms of the free surface, you can easily calculate that the vorticity is given by $\zeta = (g/f)\nabla^2 \eta$. Note that to every function $\eta(x, y)$ there is a unique flow in geostrophic equilibrium associated to it. In the case with no rotation ($f = 0$) the stationary solutions of the linearised equations have $\eta = 0$ and $\partial_x u + \partial_y v = 0$. In the case without rotation $\eta(x, y)$ does not determine the flow.

Exercise 19: What happened to the stationary version of equation (5.43)?

Exercise 20: Across the Gulf Stream, which is about 100km wide there is a height difference of approx. 1m. What is the corresponding geostrophic speed of the Gulf Stream.

Exercise 21: In a *sea surface height* (SSH) map, how can you distinguish cyclones from anti-cyclones? What happens on the southern hemisphere?

The function $\Psi = (gH/f)\eta$ is called the *geostrophic transport stream-function* as $\partial_x \Psi = H v$ and $\partial_y \Psi = -H u$ which means that: (i) isolines of Ψ , and also of η , are stream-lines of the geostrophic velocity field, and (ii) $\Psi(B) - \Psi(A)$ is the transport that passes between points A and B. In oceanography transport is usually measured in *Sverdrup* ($1 \text{Sv} = 10^6 \text{m}^3/\text{s}$), which corresponds to a cube of water of side length 100 meters passing in 1 second.

When the stationarity assumption is not made the eqs. (5.41) – (5.43) can be used to derive an equation for η only where u and v can be derived from η . This leads to:

$$\partial_t [\partial_{tt} \eta + f^2 \eta - gH \nabla^2 \eta] = 0 \quad (5.46)$$

$$\partial_{tt} u + f^2 u = -g(\partial_{tx} \eta + f \partial_y \eta) \quad (5.47)$$

$$\partial_{tt} v + f^2 v = -g(\partial_{ty} \eta - f \partial_x \eta) \quad (5.48)$$

Exercise 22: derive eqs. (5.46) – (5.48).

Exercise 23: show that the geostrophic equilibrium is a solution of eqs. (5.46) – (5.48).

Exercise 24: show that the only stationary solution of eqs. (5.46) – (5.48) is geostrophic equilibrium.

5.9 Energetics of flow in Geostrophic Equilibrium

For the shallow water dynamics the total energy is composed of kinetic and *available potential energy* (the part of the potential energy which is available in the layered model by reducing the surface anomaly η , if $\eta = 0$ everywhere the available potential energy vanishes):

$$E_{total} = E_{kin} + E_{pot} = \frac{\rho}{2} \int_A H(u^2 + v^2) dx dy + \frac{g\rho}{2} \int_A \eta^2 dx dy \quad (5.49)$$

$$= \frac{g^2 \rho}{2f^2} \int_A H((\partial_x \eta)^2 + (\partial_y \eta)^2) dx dy + \frac{g\rho}{2} \int_A \eta^2 dx dy \quad (5.50)$$

where we used (eqs. 5.44 and 5.45). If the surface perturbation has the simple form $\eta = \eta_0 \sin(x/L)$ then the energy is given by:

$$E_{total} = E_{kin} + E_{pot} = \frac{g\eta_0^2}{4} \int_A \left(\frac{Hg}{f^2 L^2} + 1 \right) dx dy \quad (5.51)$$

Where the first term is the kinetic and the second term the available potential energy. We see that in a geostrophic flow the kinetic energy is larger than the available potential energy when the structure is smaller than the *Rossby radius* $R = \sqrt{gH/f^2}$. So for large geostrophic structures most of the energy is in the potential part and for small structures in the kinetic part. The *Rossby radius* is of the order of a few thousands of kilometers for the shallow water dynamics of the ocean (the barotropic Rossby radius) but only several tenths of kilometers when the reduced gravity dynamics of the layer above the thermocline are considered (the baroclinic Rossby radius).

5.10 Linear Potential Vorticity and the Rossby Adjustment Problem

If we take ∂_x (eq. (5.42)) - ∂_y (eq. (5.41)) we see that:

$$\partial_t \zeta + f(\partial_x u + \partial_y v) = 0. \quad (5.52)$$

relating vorticity $\zeta = \partial_x v - \partial_y u$ to divergence $\partial_x u + \partial_y v$. Using eq. (5.43) we get:

$$\partial_t \left(\frac{\zeta}{f} - \frac{\eta}{H} \right) = 0. \quad (5.53)$$

One usually calls $Q_{sw}^{lin} = \frac{\zeta}{f} - \frac{\eta}{H^2}$ the linear shallow water potential vorticity. The above equations show, that at every location *linear shallow water potential vorticity* (PV) is conserved, when the dynamics is governed by the linearised shallow water equations.

The Rossby adjustment problem considers the adjustment of an initially step-like perturbation (see fig. 5.10), and we would like to know the final, geostrophically balanced state of this perturbation. To this end we use the conservation of potential vorticity and we further require the final state to be in geostrophic equilibrium. The initial potential vorticity is given by $sgn(x)(f\eta_0)/H^2$ the PV of the adjusted state is the same, we thus have,

$$g/(Hf)\partial_{xx}\eta_a - f\eta_a/H^2 = sgn(x)(f\eta_0)/H^2, \quad (5.54)$$

$$R^2\partial_{xx}\eta_a - \eta_a = \eta_0 sgn(x), \quad (5.55)$$

5.10. LINEAR POTENTIAL VORTICITY AND THE ROSSBY ADJUSTMENT PROBLEM 31

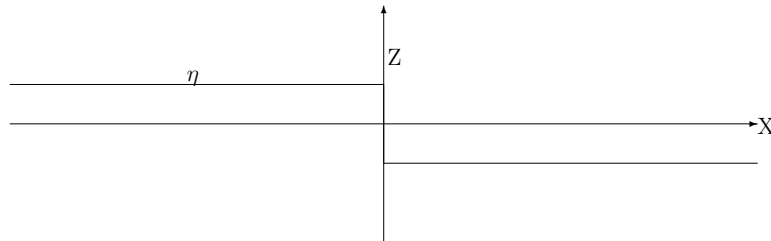


Figure 5.5: Initial condition

which has the solution:

$$\eta_a = \operatorname{sgn}(x)\eta_0(\exp(-|x|/R) - 1) \quad (5.56)$$

with $R = \sqrt{gH/f^2}$ is called the *Rossby radius* of deformation. It is the distance, a gravity wave travels in the time f^{-1} .

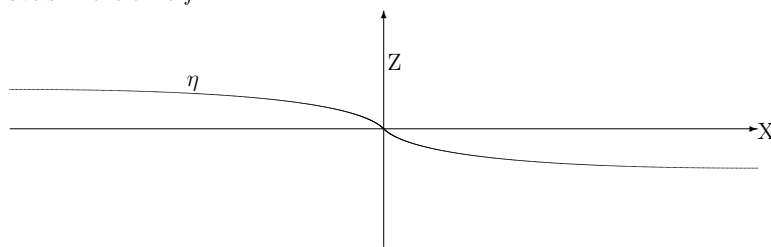


Figure 5.6: Adjusted state

We have calculated the final geostrophically adjusted state from an initial perturbation using geostrophy and conservation of linear PV, but we have not shown how this adjustment happens. For this a numerical integration of the linear shallow water equations are necessary, eqs. (5.41) – (5.43).

Exercise 25: calculate the final velocity field (u, v) .

Exercise 26: what happens when rotation vanishes?

Exercise 27: in section 5.2 we saw that if rotation is vanishing, an initial perturbation of the free surface moves away in both directions leaving an unperturbed free surface and a zero velocity behind. Does this contradict the conservation of linear potential vorticity?

Exercise 28: calculate the loss of available potential energy and compare it to the gain in kinetic energy during the adjustment process.

Exercise 29: calculate the (barotropic) Rossby radius of deformation ($H = 5\text{km}$), calculate the reduced gravity (baroclinic) Rossby radius of deformation ($H = .5\text{km}$, $g' = 3 \cdot 10^{-2}\text{m/s}^{-2}$)

5.11 Potential Vorticity (non-linear)

Similar calculations for the non-linear equations (5.38) – (5.40) lead to

$$\frac{d}{dt} \left(\frac{\zeta + f}{H + \eta} \right) = 0. \quad (5.57)$$

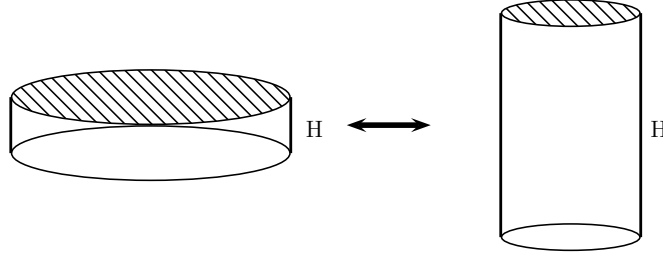
This means that every fluid parcel, or in this case every fluid column, conserves its potential vorticity $Q_{sw} = (\zeta + f)/(H + \eta)$, that is, potential vorticity is transported by the two dimensional flow. The part $f/(H + \eta)$ which does not depend explicitly on the velocity is called *planetary potential vorticity*, while $\zeta/(H + \eta)$ is called the dynamical part.

Example: Eddy over sea mount.

Exercise 30: derive eq. (5.57).

Exercise 31: If you make the assumption of linearity, can you obtain Q_{sw}^{lin} from Q_{sw} ?

Exercise 32: The moment of inertia of a cylinder of mass m , radius r and height H is given by $I = mr^2/2$ the angular momentum is given by $L = I\omega$. If a cylinder stretches or flattens without any forces acting from the outside its angular momentum is conserved:



Show, that during this process ω/H is conserved.

The previous exercise demonstrates, that the conservation of potential vorticity is nothing else than the conservation of angular momentum applied to a continuum in a rotating frame.

5.12 The Beta-plane

So far we supposed the earth to be flat! The dominant difference, induced by the spherical shape of the earth, for the large scale ocean dynamics, at mid- and low latitudes, is the change of the (locally) vertical component of the rotation vector.

For the large scale circulation a major source of departure from geostrophy is the variation of $f = f_0$ with latitude. So far we have considered f to be constant we will now approximate it by $f = f_0 + \beta y$, where $f_0 = 2|\mathbf{\Omega}| \sin(\theta_0)$ and $\beta = 2(|\mathbf{\Omega}|/R) \cos(\theta_0)$ are constant where R is the radius of the earth, it takes its maximum value $\beta_{max} = 2.3 \times 10^{-11} \text{m}^{-1} \text{s}^{-1}$ at the equator. The geometry with a linearly changing Coriolis parameter is called the β -plane. The change of f with latitude, the so called β -effect, compares to the effect of constant rotation for phenomena with horizontal extension $L \approx f/\beta = R \tan(\theta)$ or larger.

Replacing f by $f_0 + \beta y$ in equations (5.41), (5.42) and (5.43):

$$\partial_t(\partial_x v - \partial_y u) + f(\partial_x u + \partial_y v) + \beta v = 0 \quad (5.58)$$

leading to:

$$\partial_t \zeta - f \partial_z w + \beta v = 0. \quad (5.59)$$

which states, that the vorticity ζ is changed by the vertical gradient of the vertical velocity (vortex stretching) and the planetary change, due to β and the latitudinal velocity).

Exercise 33: what is the sign of f and β on the northern and southern hemisphere, respectively?

Exercise 34: what is the value of f and β on the equator, north and south pole?

Exercise 35: discuss the importance of f and β for equatorial dynamics.

5.13 A few Words About Waves

As mentioned in the preface we do not explicitly consider wave dynamics in this introductory text. I like to make, nevertheless, some “hand waving” arguments about the role of waves in the ocean.

The ocean and atmosphere dynamics at large scales are always close to a geostrophic balance. There are, however, different sources of perturbations of the geostrophically balanced state:

- variation of the Coriolis parameter f
- non-linearity
- topography
- instability
- forcing (boundary conditions)
- friction
- other physical processes (convection, ..)

As the geostrophic adjustment process happens on a much faster time scale than the geostrophic dynamics, these perturbations lead not so much to a departure from the geostrophic state but more to its slow evolution. In this adjustment process, discussed in section 5.10, (gravity) waves play an important role. It is an important part of research in geophysical fluid dynamics (*GFD*) (DFG, en français) to find equations that reflect the slow evolution of the geostrophic state, without explicitly resolving the geostrophic adjustment process. Such equations are called *balanced equations*, and are based on the evolution of PV. The best known system of balanced equations are the *quasi-geostrophic equations*. The problem in constructing such equations is how to calculate the velocity field from PV, a process usually referred to as inversion. The fast surface gravity waves influenced by rotation, *Poincaré waves* have no PV signature and thus do not appear in the balanced equations, which leads to a large simplification for analytical and numerical calculations. Balanced equations such rely on the assumption that the ocean dynamics can be separated into fast wave motion and slow vortical motion with no or negligible interactions between the two. They describe the dynamics on time-scales longer than the period of gravity waves, typically several inertial periods f^{-1} . The balanced equations are not valid when approaching the equator, as $f^{-1} \rightarrow \infty$. The dynamics described by the balanced equations is said to represent the slow dynamics or to evolve on the *slow manifold*.

Balanced equations explicitly resolve the *Rossby waves* which play a key role in the response of balanced dynamics to forcing and the adjustment to a geostrophic state. *Kelvin waves*, which are also explicitly resolved by the balanced equations, are important near boundaries and in the vicinity of the equator.

The very fast dynamics is the dynamics that happens at a time scale smaller than f^{-1} and it is usually three dimensional turbulent dynamics. To model it the full three dimensional Navier-Stokes equations have to be considered.

Chapter 6

Gyre Circulation

The ocean is forced at its surface by a wind-stress $\tilde{\tau}$ which is measured in Newton/m². A typical value for the ocean is in the order of 0.1N/m². In the present manuscript we work with $\tau = \tilde{\tau}/\rho$ which has units of m²/s².

6.1 Sverdrup Dynamics in the SW Model (the math)

In all the ocean basins an almost stationary large scale *gyre* circulation is observed. We suppose that this circulation is a consequence of the wind shear at the ocean surface. We thus add some (wind) forcing to the linearized stationary shallow water equations on the β -plane.

$$-fv + g\partial_x\eta = \tau_x/H \quad (6.1)$$

$$+fu + g\partial_y\eta = \tau_y/H \quad (6.2)$$

$$H(\partial_x u + \partial_y v) = 0 \quad (6.3)$$

+boundary conditions.

Adding $-\partial_y$ (6.1) and ∂_x (6.2) leads to:

$$H\beta v = (\partial_x\tau_y - \partial_y\tau_x) \quad (6.4)$$

So at every point the meridional component of the fluid transport (vH) is completely determined by the vorticity of the surface stress! Equation (6.4) is called the *Sverdrup relation*. It says that if vorticity is injected into the fluid parcel it can not increase its vorticity as this would contradict stationarity, so it moves northward where *planetary potential vorticity* (f/H) is larger. So the Sverdrup relation is a statement of conservation of potential vorticity in a forced and stationary situation.

When knowing the wind field, the Sverdrup relation gives v , using the zero divergence of geostrophic flow we can calculate $\partial_x u$. If we know u at one point in a ocean basin at every latitude we can determine u in the whole basin by integrating in the zonal direction,

$$u(x1, y1) = - \int_{x0}^{x1} \partial_y v(x, y1) dx + u(x0, y1). \quad (6.5)$$

But u is prescribed at the two boundaries of the ocean basin (as the velocity vector at the boundary is directed parallel to the boundary), which makes u over-determined. What does this mean in “physical terms?” Take a look at fig. 6.1, where a caricature of the North Atlantic with a simplified wind-stress (independent of longitude) is given. The corresponding v component of the velocity is also given. If we start by imposing a vanishing zonal velocity at

the eastern boundary the stream lines will look as in fig. 6.1 (if we impose it at the western boundary the picture will be flipped with respect to a vertical line). It is clearly seen that stream lines intersect the western boundary, which means, that there is flow through the western boundary. This is contrary to the concept of a boundary.

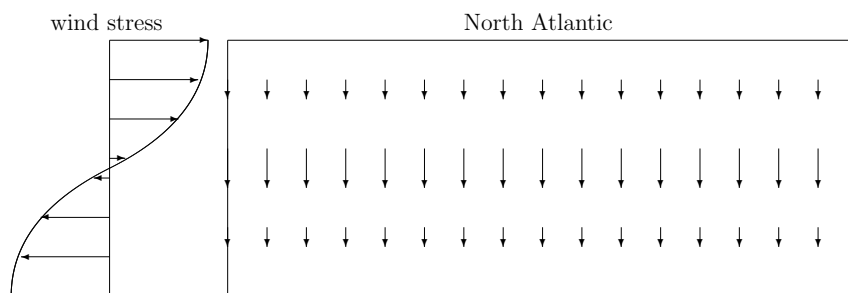


Figure 6.1: Sverdrup Balance: v-component only

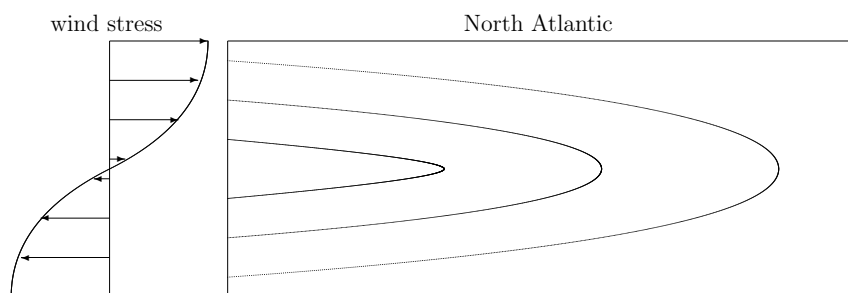


Figure 6.2: Sverdrup Balance: Stream function with $u=0$ on western boundary

How can we solve the problem? Why not, for a change, look at the real ocean. Measurements of the ocean indicate that the circulation is, after all, well represented by (6.1) with the only difference of a strong *western boundary currents* which we do not have in (6.1). The western boundary current, which closes the Sverdrup circulation, is dominated by friction (eddy viscosity effects). From a conceptual view point it is clear that such an area is necessary and that each stream line has to pass by such an area, as the wind constantly injects (negative) vorticity (and energy) in the ocean, that has to be dissipated somewhere. But let's be more quantitative. When including friction at the western or eastern boundary we have to change eq. (6.2) to:

$$fu + g\partial_y\eta = \tau_y/H + \nu_{eddy}\partial_{xx}v. \quad (6.6)$$

The term $\nu_{eddy}\partial_{xx}v$ represents the dominant contribution of friction as it is the meridional velocity component v that changes fastest in the zonal x -direction. The eddy viscosity ν_{eddy} is many orders of magnitude larger than the molecular viscosity of sea water. The concept of eddy viscosity is explained in section 10.2. Near the boundary we can neglect the wind forcing

6.1. SVERDRUP DYNAMICS IN THE SW MODEL (THE MATH)

37

and the dominant balance is then,

$$\beta v_B = \nu_{\text{eddy}} \partial_{xxx} v_B, \quad (6.7)$$

which has solutions of the form,

$$v_B = C_1 \exp(2x/r) + \exp(-x/r) (C_2 \cos(-x/\tilde{r}) + C_3 \sin(-x/\tilde{r})), \quad (6.8)$$

with $r = (\beta/\nu_{\text{eddy}})^{1/3}/2$ and $\tilde{r} = r/\sqrt{3}$. One condition of the boundary solution is, that it has to decrease away from the boundary, which means that $C_1 = 0$ if the boundary current develops on the western boundary and $C_2 = C_3 = 0$ if the boundary current develops on the eastern boundary. The boundary dynamics is there to insure that $u = v = 0$ on the boundary, these are two conditions. If the boundary current is on the eastern boundary we have only one constant to adjust, so it is usually not possible. So the frictional boundary current can do its job (satisfy the boundary conditions) only if it is on the western boundary.

There are still other dynamical arguments why the boundary current can not be on the eastern boundary: (i) in the situation in fig. 6.1 the wind injects negative vorticity in the flow, vorticity is conserved by the fluid column moving with the flow, not subject to any forcing. In a stationary state the vorticity extracted has to be re-injected during the cyclical path of a fluid column. A boundary layer at the western border does exactly this. A boundary layer at the eastern border would drain even more vorticity, which leads to a contradiction in terms of the vorticity balance. (ii) The dynamical adjustment in the ocean is performed by Rossby waves, which have a westward group velocity. This means that the dynamics at a point adjusts to the dynamics to its eastern side. That's what the boundary current does, so it has to be to the extreme western part of the basin to adjust to the entire interior dynamics.

On the southern hemisphere the boundary current is also on the western boundary as β (unlike f) has the same sign on both hemispheres! In the above derivation of the Sverdrup transport only β but not f was involved.

So the big picture is: (i) the ocean interior is well described by Sverdrup dynamics, (ii) which is complemented at the western boundary by a thin boundary current, which is dominated by friction.

Comment 1: The wind stress induces a transport (uH, vH) rather than a velocity (u, v) .

Exercise 36: which dynamics would we expect in fig. 6.1 when rotation vanishes?

Exercise 37: in the above calculations we have neglected the non-linear terms. This is only valid when the Rossby numbers are small. What is the Rossby number of the interior flow at mid latitudes when $v = .1\text{m/s}$, $L = 5000\text{km}$. What is the Rossby number of the boundary layer flow at mid latitudes when $v = 1.0\text{m/s}$, $L = 100\text{km}$.

Comment 2: For the Sverdrup relation to apply, it is not so much the Rossby number that has to be small but the two terms neglected, (i) the time derivative of the *relative vorticity* $\partial_t \zeta$ and (ii) the non-linear term $\mathbf{u} \nabla \zeta$, have to be small compared to the transport of *planetary vorticity* $v\beta$. Observations show that the mean wind forcing and thus the mean circulation changes only slightly during several years in large parts of the world's ocean. The total vorticity, measured from an inertial frame, of the fluid motion on our planet can be decomposed in the relative part, measured from a frame moving (rotating) with the surface of the earth, and the planetary part given by the Coriolis parameter f . In the boundary layer, however, the non-linear term is not smaller than the transport of planetary vorticity and there are non-linear phenomena in the western boundary currents, as for example the Gulf-Stream and the Kuroshio, which are not well explained by the above theory.

6.2 The Ekman Layer

Strictly speaking, this section belongs to chapter 10 because it deals with how wind forcing penetrates to the deep ocean, but it just happens that we need to know Ekman theory to continue our investigation of “Forced Dynamics.”

Ekman’s theory of the adjustment of a fluid in a rotating frame to an equilibrium when subject to wind forcing, is probably the most cited and most misunderstood theory of ocean dynamics. To elucidate this Ekman layer dynamics we will advance in small steps, emphasizing the physical understanding of the process, without neglecting the mathematical derivation.

Suppose we have an infinitely deep layer of a homogeneous fluid subject to wind forcing τ_x , constant in time and space, at its surface that is acting in the x -direction. The flow is independent of x, y as the forcing has no variations in these variables and as there are no boundaries. But the flow depends on the vertical coordinate z . In this case the vertical velocity w vanishes everywhere due to the divergence free condition, eq. (5.4). The Navier-Stokes equations (5.1) – (5.4), in a rotating frame, then simplify to:

$$\partial_t u(z, t) - f v(z, t) = \nu \partial_{zz} u(z, t) \quad (6.9)$$

$$\partial_t v(z, t) + f u(z, t) = \nu \partial_{zz} v(z, t) \quad (6.10)$$

with the boundary conditions:

$$\nu \partial_z u(0) = \tau_x; \quad \partial_z v(0) = 0, \quad (6.11)$$

$$\lim_{z \rightarrow -\infty} \partial_z u(z) = \lim_{z \rightarrow -\infty} \partial_z v(z) = 0. \quad (6.12)$$

The surface boundary condition (6.11) represents the vertical gradient of the horizontal velocity due to wind stress, while we suppose no frictional forces at the (far away) bottom of the Ekman layer.

6.2.1 Ekman Transport (one layer)

To further simplify the problem we consider the transport $U(t) = \int_{-H}^0 u(z, t) dz$ and $V(t) = \int_{-H}^0 v(z, t) dz$ of the whole fluid column. Please note, that these variables depend only on time and we have neglected all vertical structure in the problem. This can be easily done in the present problem as eqs. (6.9), (6.10) and the boundary conditions (6.11), (6.12) are linear. Integrating the right hand side of eq. (6.9) we have $\int_{-H}^0 \nu \partial_{zz} u(z, t) dz = \nu \partial_z u(0) = \tau_x$. When we further neglect friction at the bottom of the fluid layer eq. (6.9), (6.10) and boundary conditions (6.12) read:

$$\partial_t U(t) - f V(t) = \tau_x \quad (6.13)$$

$$\partial_t V(t) + f U(t) = 0 \quad (6.14)$$

We now like to consider the spin up of an Ekman transport initially at rest. In the non-rotating case ($f = 0$) we have the solution:

$$U(t) = \tau_x t \quad (6.15)$$

$$V(t) = 0, \quad (6.16)$$

so the fluid constantly accelerates in the x -direction and no stationary state is reached!

6.2. THE EKMAN LAYER

39

In the rotating case ($f \neq 0$) the solution is given by:

$$U(t) = \frac{\tau_x}{f} \sin(ft) \quad (6.17)$$

$$V(t) = \frac{\tau_x}{f} (\cos(ft) - 1) \quad (6.18)$$

Initially the solution behaves as in the non rotating case, that is, it accelerates in the x -direction with an acceleration given by τ_x . But in the rotating case eqs. (6.13) and (6.14) also have the stationary (time-independent) solution:

$$U = 0; \quad V = -\frac{\tau_x}{f}, \quad (6.19)$$

which has no counter part in the non-rotating case. This solution is a force balance between the Coriolis force and the wind stress. The depth averaged Ekman transport is at 90° to the right of the wind force as this is the only possibility for the Coriolis force to balance the wind stress.

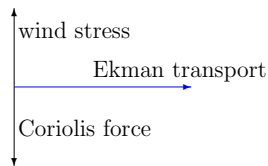


Figure 6.3: Depth averaged Ekman transport

The solutions for the rotating case given in eqs. 6.17 and 6.18 are in fact a sum of the stationary solution plus *inertial oscillation*. When friction is included the oscillations will be damped and the transport will converge towards a (modified) stationary solution.

Exercise 38: What is the energetics of the Ekman transport?

Exercise 39: Does the Ekman transport depend on the viscosity?

It is the Ekman transport, and only the Ekman transport, that determines the influence of the wind forcing on the deep ocean. For completeness we will discuss in the next subsection the vertical structure of the Ekman dynamics.

6.2.2 The Ekman Spiral

We start this section with two instructive exercises.

Exercise 40: What happens when we include bottom (Rayleigh) friction in eqs. 6.13 and 6.14? The stationary solution is governed by:

$$-fV = -rU + \tau_x \quad (6.20)$$

$$fU = -rV \quad (6.21)$$

and we obtain the solution:

$$U = \frac{r}{r^2 + f^2} \tau_x \quad (6.22)$$

$$V = \frac{-f}{r^2 + f^2} \tau_x. \quad (6.23)$$

We see that when including bottom friction the fluid motion is still deviated to the right (on the northern hemisphere) with respect to the wind stress but the angle is smaller than the 90 of the frictionless case. So the friction induces fluid motion in the direction of the wind stress.

Exercise 41: Two layers: We now suppose that the Ekman layer can be decomposed into two layers of thickness H_1 and H_2 . This “poor man’s vertical structure” does not correspond to any real situation but helps us to understand the physics of the Ekman spiral treated in the next subsection. The governing equations for the stationary solution are:

$$-fV_1 = r(U_2/H_2 - U_1/H_1) + \tau_x \quad (6.24)$$

$$fU_1 = r(V_2/H_2 - V_1/H_1) \quad (6.25)$$

$$-fV_2 = r(U_1/H_1 - U_2/H_2) \quad (6.26)$$

$$fU_2 = r(V_1/H_1 - V_2/H_2) \quad (6.27)$$

Where r times the velocity difference represents the linear friction between the two layers. You can write the linear system (6.24) – (6.27) in the form,

$$\mathbf{AU} = \mathbf{B}, \quad (6.28)$$

where $\mathbf{U} = (U_1, V_1, U_2, V_2)$. Verify that all solutions have: $U_1 + U_2 = 0$, and $f(V_1 + V_2) = \tau_x$, which is the Ekman transport already calculated above. You can use this to eliminate U_2 and V_2 from the problem and simplify eq. (6.28) to:

$$\tilde{\mathbf{A}}\tilde{\mathbf{U}} = \tilde{\mathbf{B}} \quad (6.29)$$

with $\tilde{\mathbf{U}} = (U_1, V_1)$. Find the solution and give an interpretation.

What is the vertical structure of the Ekman transport? We can approximate the vertical structure by including more and more layers in the vertical. The first layer being subject to wind forcing, the Coriolis force and the friction induced by the second layer. Every other layer is driven by the frictional force transmitted by its upper neighbour and feels the friction of its lower neighbour. All layers are subject to the Coriolis force. Using the results from subsection 6.2.1 we estimate that every layer will move to the right of the movement of its upper neighbour, at a smaller pace. Such motion will lead to a spiral motion in the vertical decaying with depth. To render this qualitative arguments into a quantitative theory we go back to eqs. (6.9), (6.9) and boundary conditions (6.11), (6.12). To simplify the problem we will only consider the time independent solution of these equations neglecting the inertial oscillations. Equations (6.9) and (6.10) can be combined to form a single equation of fourth order:

$$-f^2 u(z) = \nu^2 \partial_{zzzz} u. \quad (6.30)$$

If we suppose that the viscosity is independent z -component this equation is easily solved and the solution satisfying the boundary conditions 6.11 6.12 is:

$$u(z) = V_0 \exp(z/\delta) \cos(z/\delta + \pi/4) \quad (6.31)$$

$$v(z) = V_0 \exp(z/\delta) \sin(z/\delta + \pi/4) \quad (6.32)$$

where $\delta = \sqrt{2\nu/|f|}$ is the Ekman layer thickness and $V_0 = \tau_x \delta / (\nu\sqrt{2})$. The solution shows that the current at the surface is deviated 45° to the right with respect to the wind velocity (on the northern hemisphere, to the left on the southern hemisphere).

Exercise 42: What is the energetic balance of the Ekman spiral?

An Ekman spiral is clearly observed in the ocean where $\delta \approx 30\text{m}$, in laboratory experiments and in numerical experiments. Indeed the work of Vagn Walfrid Ekman (1905) was initiated by Fridtjof Nansen who observed that in the Arctic the ice drifts 20° to 40° to the right of the wind direction and who also had the physical intuition that rotation of the earth was the reason and that the resulting dynamics should be a spiral decreasing with depth. He then encouraged Vagn Walfrid Ekman (1905) to do the mathematics.

At large Reynolds numbers the dynamics in the Ekman layer is turbulent leading to an eddy viscosity that varies with depth and the spiral is distorted. We emphasize once more, that the Ekman transport however does not depend on the internal structure and details of the Ekman layer, as demonstrated in subsection 6.2.1. It is this transport that puts the deep ocean into motion.

It is no surprise that the Ekman spiral was discovered through measurements of the drift of sea ice and the currents underneath. First, it is much easier to perform current measurements by drilling a small hole in the ice and descending the current meter, than to perform the same kind of measurements from a drifting ship in a wavy ocean. Second, the damping of surface waves in the ocean, by ice cover, reduces small-scale dynamics (turbulence) that overlay or perturb the Ekman spiral, and which distorts the Ekman spiral. The deviation of the surface current to the wind direction is indeed smaller in the ice free ocean, usually around 30° .

We note that the Ekman transport does only depend on the shear (τ_x, τ_y) and the Coriolis parameter. The role of friction is to set the depth and the structure of the dynamics in the Ekman layer. An Ekman dynamics exists not only at the ocean surface but also at the ocean floor, that exerts a frictional force on the fluid.

The large difference between the Ekman and the geostrophic dynamics is its variation with depth. In the geostrophic dynamics the force is due to the horizontal pressure gradient, which has no variation with depth in a homogeneous ocean when the hydrostatic approximation is made. Whereas the Ekman dynamics relies on (turbulent; see Section 10.2) viscosity to penetrate the depth of the ocean. The Ekman dynamics is thus confined to the upper tenths of meters of the ocean.

6.3 Sverdrup Dynamics in the SW Model (the physics)

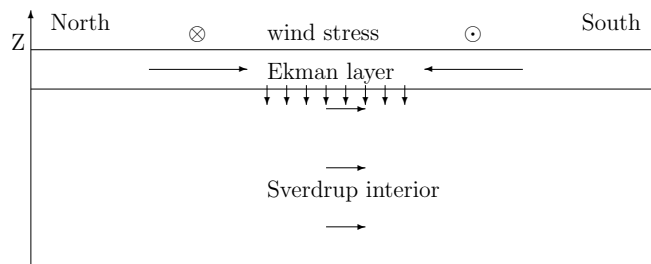


Figure 6.4: Sverdrup physics

In section 6.1 we have calculated the potential vorticity balance of the stationary large scale oceanic dynamics of a shallow fluid layer subject to wind forcing at the surface.

From what we learned in section 6.2 it seems, at first sight, unlikely that a fluid layer, that is forced by a wind stress at the surface will develop a velocity independent of depth. It seems much more likely that a substantial shear will develop in the upper-part (Ekman-layer) of the fluid, and that the main body of the fluid rests motionless. This is however not the case, the wind-stress is indeed transferred to the deep layers. How this happens is the subject of this section.

As we have seen in section 6.2 the transport in the Ekman layer ($H_{Ek} \approx 30\text{m}$) is given by,

$$u_{Ek}H_{Ek} = \tau_y/f \quad (6.33)$$

$$v_{Ek}H_{Ek} = -\tau_x/f \quad (6.34)$$

using the zero divergence we see that the Ekman dynamics leads to a vertical velocity

$$w_{Ek} = -\partial_x(\tau_y/f) + \partial_y(\tau_x/f), \quad (6.35)$$

In the geostrophic interior no direct action of the wind-stress is felt and eqs. 6.1 – 6.3 give,

$$\beta v = f \partial_z w, \quad (6.36)$$

which is called the Sverdrup relation. On the surface w_{Ek} has to be compensated by a vertical “geostrophic” velocity $w_G = -w_{Ek}$. Using eq. (6.4) we get,

$$\beta H v_G = f w_G = -f w_{Ek} = f H_{Ek} (\partial_x u_{Ek} + \partial_y v_{Ek}) = f [\partial_x(\tau_y/f) - \partial_y(\tau_x/f)]. \quad (6.37)$$

The total zonal (Sverdrup) transport is,

$$H v_S = H v_G + H_{Ek} v_{Ek} = f/\beta [\partial_x(\tau_y/f) - \partial_y(\tau_x/f)] - \tau_x/f \quad (6.38)$$

$$= (\partial_x \tau_y - \partial_y \tau_x)/\beta \quad (6.39)$$

which is identical to 6.4!

What do all this beautiful calculations tell us?

- The Sverdrup transport can be split up between an Ekman transport and a geostrophic interior transport.
- The Ekman transport is directly set into motion by the by the wind stress through (eddy) viscous friction.
- The interior dynamics is set up by the vertical velocity induced by the divergence of the Ekman transport
- The interior dynamics is put into motion by stretching of the water column and the conservation of planetary potential vorticity (f/H).

Chapter 7

Multi-Layer Ocean dynamics

7.1 The Multilayer Shallow Water Model

The models employed so far to study the ocean dynamics consisted of a single layer, which represented the dynamics of a single vertically homogeneous (in speed and density) layer above a solid bottom or above a infinitely deep inert layer of higher density (reduced gravity model). We also saw that these type of models are very successful in explaining the main features of the large scale ocean circulation. There are, however, important phenomena of the circulation which can not be explained by such one-layer models. We thus move on to the dynamics of several layers of homogeneous (in speed and density) fluid layers of different density and velocity, stacked one above the other. We will here restrict the analysis to a model with two active layers, the generalisation to more layers is strait forward. The equations governing the dynamics of such a hydrostatic two-layer shallow water model are:

$$\partial_t u_1 + u_1 \partial_x u_1 + v_1 \partial_y u_1 - f v_1 + g \partial_x (\eta_1 + \eta_2) = \nu \nabla^2 u_1 \quad (7.1)$$

$$\partial_t v_1 + u_1 \partial_x v_1 + v_1 \partial_y v_1 + f u_1 + g \partial_y (\eta_1 + \eta_2) = \nu \nabla^2 v_1 \quad (7.2)$$

$$\partial_t \eta_1 + \partial_x [(H_1 + \eta_1) u_1] + \partial_y [(H_1 + \eta_1) v_1] = 0 \quad (7.3)$$

$$\partial_t u_2 + u_2 \partial_x u_2 + v_2 \partial_y u_2 - f v_2 + g'' \partial_x (\eta_1 + \eta_2) + g' \partial_x \eta_2 = \nu \nabla^2 u_2 \quad (7.4)$$

$$\partial_t v_2 + u_2 \partial_x v_2 + v_2 \partial_y v_2 + f u_2 + g'' \partial_y (\eta_1 + \eta_2) + g' \partial_y \eta_2 = \nu \nabla^2 v_2 \quad (7.5)$$

$$\partial_t \eta_2 + \partial_x [(H_2 + \eta_2) u_2] + \partial_y [(H_2 + \eta_2) v_2] = 0 \quad (7.6)$$

+boundary conditions .

Where the index 1 and 2 denote the upper and the lower layer, respectively. It is interesting to note that the two layers interact only through the hydrostatic pressure force caused by the thicknesses of the layers. Indeed, the upper layer (layer 1) is subject to the hydrostatic pressure of the surface which has a total anomaly of $\eta_1 + \eta_2$. Whereas the the lower layer (layer 2) is subject to the same pressure plus the pressure at the interface $g' \eta_2$ due to the increased density in the lower layer, where $g' = g(\rho_2 - \rho_1)/\rho_2$ is the reduced gravity, that is, the weight of the lower-layer fluid in the upper layer environment and $g'' = g\rho_1/\rho_2$. In the *Boussinesq approximation* g'' is set equal to g , thus neglecting the density differences in the inertial mass but keeping it in the weight. Equations (7.1) – (7.6) are the mathematical model for the investigations of the present chapter.

Exercise 43: What happens to equations (7.1) – (7.6) if $\rho_1 = \rho_2$?

Exercise 44: Write down the linearised version of eqs. (7.1) – (7.6).

7.2 Conservation of Potential Vorticity

Exercise 45: Show that the linearised version of eqs. (7.1) – (7.6) conserve the linear potential vorticity at every horizontal location and for every layer.

Exercise 46: Show that eqs. (7.1) – (7.6) conserve the potential vorticity at every horizontal location and for every layer (when friction is neglected).

Wow! This means that if we describe our ocean by more and more layers, then potential vorticity is conserved for every fluid particle!

7.3 Geostrophy in a Multi-Layer Model

As we have seen in section 5.8 the geostrophic equilibrium is a balance between the pressure and the Coriolis force, neglecting time-dependence, non-linearity, friction and using the Boussinesq approximation, eqs. (7.1) – (7.6) then read:

$$fv_1 = g\partial_x(\eta_1 + \eta_2) \quad (7.7)$$

$$-fu_1 = g\partial_y(\eta_1 + \eta_2) \quad (7.8)$$

$$fv_2 = g\partial_x(\eta_1 + \eta_2) + g'\partial_x\eta_2 \quad (7.9)$$

$$-fu_2 = g\partial_y(\eta_1 + \eta_2) + g'\partial_y\eta_2 \quad (7.10)$$

$$(7.11)$$

It is now interesting to consider the differences between eqs. (7.7) – (7.9) and (7.8) – (7.10) which are:

$$v_1 - v_2 = -\frac{g'}{f}\partial_x\eta_2 \quad (7.12)$$

$$u_1 - u_2 = \frac{g'}{f}\partial_y\eta_2, \quad (7.13)$$

$$(7.14)$$

which are called the *thermal wind* relation, as they were first discovered in, and applied to, atmospheric dynamics. They show that in the geostrophic limit the horizontal gradient of the height of the interface is related to the velocity difference across the interface perpendicular to the gradient of the height of the interface.

This finding can of course be generalised to models with several layers and also to the limit of an infinity of layers, that is, to a continuous variation of density and velocity. Which then means in the geostrophic limit: if we know the density structure of the ocean, we know the vertical gradient of the horizontal velocity every where. If we knew the velocity at a certain depth we could use the thermal wind relation to calculate the velocity every where. As the geostrophic velocities in the deep ocean are usually smaller than near the surface, oceanographers conjecture a *level of no motion* which is set rather arbitrarily to, for example, 4000m depths, to calculate the geostrophic velocities every where.

The thermal wind relation was of paramount importance in the past, when it was difficult to measure velocities from a ship at open sea. The density structure on the contrary was much easier to determine precisely. Today with the help of satellites the measurements of velocities have become much more precise, and comparisons with the density structure show the good agreement with the thermal wind relations.

Exercise 47: Where would the velocities be directed in fig. 7.1 on the southern hemisphere?

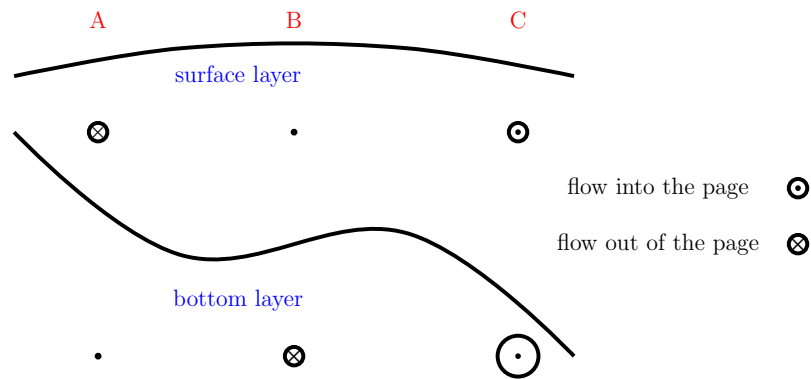


Figure 7.1: Geostrophy in a two layer model: in region **A** the pressure gradient of the inter-facial slope compensates the pressure gradient of the surface slope and the lower layer is inert; in region **B** the surface is level and there is no geostrophic motion in the surface layer, the inter-facial slope corresponds to a velocity in the bottom layer; in region **C** the slope of the surface and the interface lead to a higher velocity in the bottom layer. The slope of the surface is exaggerated with respect to the interface slope, the vertical variations of the interface are of the order of 1m, while the interface varies hundreds of meters. The situation presented corresponds to the northern hemisphere.

7.4 Barotropic versus Baroclinic

Barotropic flow means that iso-baric surfaces coincide with iso-density surfaces. This is the case if and only if $\eta_1 = \text{const.}$ in the two layer case or $\eta_i = \text{const.}$ for all $i = 1 \dots N - 1$ in the multi-layer case (index are counted from top to bottom, 1 being the surface layer and N the bottom layer). Geostrophy applied to (7.1) – (7.6), without using the Boussinesq approximation and the fact that $g' + g'' = g$, we see that the flow does not change with depth which is the case for barotropic flow. In oceanography the barotropic component of the flow is a component for which the horizontal velocity does not change in the vertical direction. Confusion often arises because sometimes the depth average velocity is called the barotropic component and sometimes it is the geostrophic flow corresponding to the surface elevation ($\sum_{i=1}^N \eta_i$). Anyway the differences between the flow and the barotropic flow is called the baroclinic flow. So there is vertical shear in the horizontal velocity field if and only if the baroclinic flow is not vanishing.

Exercise 48: Give an example to show that the two definitions of “barotropic component” differ.

7.5 Eddies, Baroclinic instability

There is one important phenomena that we can not explain from what we have learned so far and this is the abundance of oceanic eddies with the size of approximately the first baroclinic Rossby radius, that is around 100km. The maximum speed in these eddies is 1ms^{-1} . Indeed when the first satellite observations of the ocean were available the ocean looked like a “sea of eddies”, a feature that is well reproduced by today’s numerical models of the ocean circulation.

Observations and numerical simulations show that at many locations in the ocean the velocity fluctuations due to eddying motion are up to two orders of magnitude larger than the average velocity.

Exercise 49: Search the Internet for maps of sea surface height (SSH) from observations and numerical models. Where do you see the eddies?

Exercise 50: Estimate the vorticity ζ of an ocean eddy and its Rossby number $Ro = \zeta/f$. Are eddies well described close to a geostrophic equilibrium?

Comment: The *Rossby number* and the baroclinic *Rossby radius* are two different things with no direct connection, they are just named after the same person. The Rossby number compares the relative vorticity to the planetary vorticity, or the magnitude of the non-linear term to the Coriolis term. While the Rossby radius is the distance a gravity wave of speed $\sqrt{g'H}$ has traveled in the time f^{-1} .

Exercise 51: Estimate the SSH anomaly at the eddy center of a Gulf Stream eddy.

The process of formation of these eddies, which is called *Baroclinic instability*, is not only an oceanic phenomenon but the cyclones and anticyclones in the mid-latitudes which determine our weather are their atmospheric counterparts and are dynamically the same process. In the atmosphere the baroclinic Rossby radius is of the order of 1000km which explains the size of the cyclones and anticyclones in the atmosphere. It is clear that these “eddies” are key to our understanding of the atmospheric dynamics but in the ocean they are rather small, do they affect the large scale ocean dynamics? YES! they do! We have seen in section 5.8 that geostrophic dynamics at scales larger than the baroclinic Rossby radius has most of its energy stored as *available potential energy* which is constantly supplied by the wind-stress through Ekman pumping at a scale which is roughly 30 times the baroclinic Rossby radius.

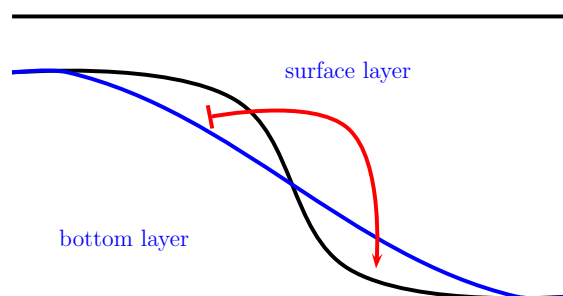


Figure 7.2: Baroclinic instability flattens the interfacial surface. The black line represents the surface before and the blue line after the baroclinic instability. This leads to a downward transport of heavy fluid, that is, a release of available potential energy, as indicated by the red arrow. It does so by forming eddies which mixes the interfacial layer thickness.

The available potential energy is thus $30^2 \approx 1000$ larger than the kinetic part, as the flow is close to a geostrophic equilibrium. This energy has to be drained somehow. That is what the baroclinic instability does by generating eddies at the scale of the baroclinic Rossby radius. We see that the energetics of the large scale circulation can not be understood without this important process. We remind the reader that in chapter 6 we did only consider the conservation of potential vorticity but did not mention energy.

The eddies, themselves not being far from geostrophy, about the same amount of energy as available potential energy and kinetic energy as they are of the size of the baroclinic Rossby radius. So baroclinic instability transfers large scale available potential energy to small scale kinetic and available potential energy. Where does the energy go from there? Eddies interact form smaller and smaller structures as, for example, filaments which are then dissipated away in a turbulent cascade process. Eddies also transport the water masses in the latitudinal direction and lose their temperature anomalies by surface fluxes. That is, for example: warm core Gulf Stream eddies travel north loose, their heat to the atmosphere and fade away, transporting substantial parts of heat from low to high latitudes.

The detailed discussion of the onset and evolution of baroclinic instability is beyond the scope of this *Guided Tour*.

7.6 Continuous Stratification

Observations of the ocean indicate, that there are over substantial parts of the ocean areas where the water mass properties and the velocities are almost constant in the vertical direction, separated by sudden jumps in these variables. So the ocean is often well described by layers and this is the basis of the success of layered models. Dividing the ocean in more and more layers that is $\lim N \rightarrow \infty$ one approaches a continuous stratification.

Chapter 8

Equatorial Dynamics

The ocean dynamics near the equator is different from other places on our planet as the Coriolis parameter $f = 2\Omega \sin \theta$, measuring the vertical component of the rotation vector, a key parameter in geophysical fluid dynamics, vanishes at the equator. We remind the reader that the ocean currents are mostly horizontal and we can thus to first order neglect the horizontal component of the rotation vector. The terms containing the horizontal component of the rotation vector always involve the vertical component of the velocity vector due to the orthogonal nature of the vector product $\boldsymbol{\Omega} \times \mathbf{u}$. Neglecting the horizontal component of the rotation vector is called the *traditional approximation*. This does not mean that the effects of rotation can be neglected when considering equatorial dynamics. Although the Coriolis parameter vanishes at the equator its change with the respect to the meridional direction, $\beta = 2(\Omega/R) \cos \theta$, where R is the earth's radius, is maximal at the equator. The equatorial dynamics is thus well described by what is called the *equatorial β -plane*. The reduced gravity shallow water equations for the equatorial β -plane are given by eqs. (5.38) - (5.40) with $f = \beta y$.

Another peculiarity of equatorial dynamics is the strong density stratification across the thermocline. At the equator radiative forcing is strongest leading to warm waters and there is also no cooling of the surface waters in winter time, a process important at high latitudes. Precipitation is also strong near the equator freshening the surface waters. Both phenomena lead to strong vertical density differences in the equator, which is responsible that the vertical velocity shear is also more pronounced than in other regions of the ocean.

The first question we have to address is of course about the latitudinal extension of the equatorial β -plane. If we compare the wave speed $c = \sqrt{g'H}$ to the value of β we obtain the equatorial Rossby radius $R_{eq} = \sqrt{c/\beta}$. For barotropic dynamics $H \approx 4\text{km}$ we obtain $R_{eq} \approx 3000\text{km}$. Due to the strong vertical density difference across the equatorial thermocline most phenomena are, however, baroclinic in the tropics (at low latitude). For such dynamics g has to be replaced by the reduced gravity $g' = g\Delta\rho/\rho$ and the relevant thickness is this of the layer above the thermocline. For this reduced gravity dynamics of the waters above the thermocline $c^{bc} = 0.5\text{ms}^{-1}$ which leads to $R_{eq}^{bc} \approx 300\text{km}$. This gives a band extending approximately 3° to the north and south of the equator, a rather large area.

The easterly winds (winds coming from east) drive the westward (to the west) *equatorial current*. These current causes a pileup of water at the western side of the basin, which leads to a eastward *equatorial undercurrent* just below the waters directly influenced by the wind-stress. The equatorial undercurrent is a band of eastward moving water at about 200m depth which is about 100m thick and 300km large and which has maximal velocities of up to 1.5ms^{-1} in the Pacific Ocean. The equatorial pile up of water at western side of the basin also leads to eastward (counter) currents at the surface north and south of the equator, which are called *north equatorial counter current* (NECC) and *south equatorial counter current* (SECC),

respectively. Due to the north south asymmetry of the wind forcing, the NECC is usually more pronounced than the SECC, which is often not observed. These currents exist in all three ocean basins, but their exact location and strength differs. In the Indian Ocean these currents reverse due to the reversing monsoon wind forcing.

Chapter 9

Abyssal and Overturning Circulation

The study of the deep circulation of the world ocean has historically relied on the analysis of water masses. The reasons are that: (i) in the deep water masses change very slowly in time as they are not subject to boundary forcing and as they give an integrated view of the velocity field which mostly weakens when descending into the depth of the ocean; (ii) it is technically difficult to measure the moderate but highly variable velocities in the deep ocean, especially from a ship that is transported by the stronger currents at the ocean surface.

In 1751 Stephen Hales constructed a “bucket sea-gage” and asked Henry Ellis, the captain of the *Earl of Halifax*, to perform temperature measurements in the deep North Atlantic. Ellis found that temperature decreases with depth and noted: “This experiment, which seemed at first but mere food for curiosity, became in the interim very useful to us. By this means we supplied our cold bath, and cooled our wines or water at pleasure; which is vastly agreeable to us in this burning climate.”

It was Count Rumford who noted in 1800 that this cold water can only originate from high latitudes and called it “[...] an inconvertible proof of the existing of cold water at the bottom of the sea, setting from the poles towards the equator.” This picture was then refined and the zones of formation of the deep waters were identified to lie in the high latitudes of the North Atlantic and the Antarctic Ocean. There is no formation of deep waters in the Indian and Pacific Ocean. The deep waters are upwelling in the rest of the ocean counter balancing the diffusion of heat into the deep ocean and thus forming the thermocline, that is a more or less sharp boundary between the warm surface waters and the cold deep waters in the mid and low latitudes. These processes are schematised in fig. 9.1.

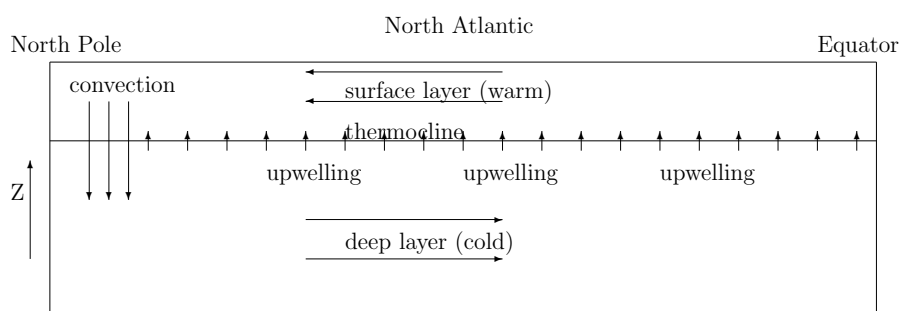


Figure 9.1: Overturning Circulation

Only in the beginning of the 20th century Chamberlain (1906) considered the possibility of variability or even a reversal of the deep ocean currents and its effects on climate. The vulnerability of the overturning circulation to changes in the freshwater forcing at the ocean surface is today seen as a likely candidat for the abrupt (several decades) *Dansgaard-Oeschger* climate change events.

9.1 The Stommel Arons Theory

The picture presented in the previous section led Stommel and Arons to consider the dynamics of the deep layer in the ocean, which is subject to a localized injection of water in the northern part and an upwelling, from the deep layer into the surface layer, through out the rest of the thermocline. In the simplest geometry our ocean is a slice of the earth confined between longitudes ϕ_w , ϕ_e and in the south by the equator. The injection happens at the North Pole and has a strength S_N (measured in Sv). As the total volume of the deep layer is conserved the upwelling velocity $w_{up} = S/A$ where A is the surface of our slice, $A = R^2(\phi_e - \phi_w)$. This positive vertical velocity leads to a stretching of the deep layer and thus by conservation of potential vorticity (eq. 5.57 or actually planetary potential vorticity) to a northward velocity which is given by $v_{sv} = fw_{up}/(H\beta) = w_{up}R \tan(\theta)/H$. But north-ward velocity means towards the source! Conservation of mass imposes a southward transport somewhere in the fluid, and knowing Sverdrup theory we suspect this transport to occur on the western boundary.

North Atlantic

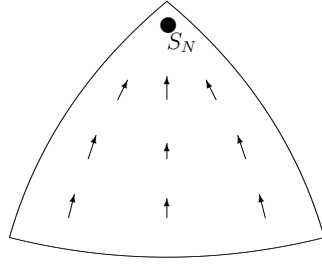


Figure 9.2: Stommel-Arons Model

The north-ward interior (Sverdrup) transport as a function of latitude is

$$T_{sv} = v_{sv}H(\phi_e - \phi_w)R\cos(\theta) = w_{up}R^2(\phi_e - \phi_w)\sin(\theta) = S_N\sin(\theta). \quad (9.1)$$

The vertical transport into the deep layer north of the latitude θ (it actually goes out of the deep layer it has a minus sign!) is equal to minus the upward velocity times the surface,

$$T_{up} = -w_{up}R^2(\phi_e - \phi_w) \int_{\theta}^{\pi/2} \cos(\theta')d\theta' = -w_{up}R^2(\phi_e - \phi_w)(1 - \sin(\theta)) = S_N(\sin(\theta) - 1) \quad (9.2)$$

For a slice north of θ we have,

$$S_N + T_{sv} + T_b + T_{up} = 0 \quad (9.3)$$

9.2. MULTIPLE EQUILIBRIA OF THE THERMOHALINE CIRCULATION

53

Which allows us to calculate the boundary transport:

$$T_b = -2S_N \sin(\theta), \quad (9.4)$$

this means, that at the apex the boundary current has twice the strength of the source.

There is clear evidence of the existence of an overturning circulation in the temperature structure of the world's ocean, as stated in the beginning of this section. The overturning circulation itself is, however, very difficult to observe as the velocities v_{sv} and w_{up} are small and such difficult to measure. The convection process is very localised in time and space and difficult to quantify. The boundary current such seems to be the only easily observable branch of the overturning circulation! All the branches of the overturning circulation are clearly observed in today's numerical models of the ocean circulation.

Exercise 52: What happens when the strength of the source is increased or decreased?

Exercise 53: What happens when the source is displaced southward?

Exercise 54: What happens when there are more sources?

Exercise 55: What happens when the source is at the equator?

Exercise 56: What happens when the ocean spans a slice from the North- to the South-Pole? What happens at the equator?

9.2 Multiple Equilibria of the Thermohaline Circulation

The here presented model was introduced by Stommel-Marotzke-Stocker. It represents the most simple model of the thermohaline circulation. There are only two boxes which are characterized by their respective temperature and salinity. The temperature in both boxes is held fix, while the salinity depends on precipitation, this is called: "mixed boundary conditions." Such boundary conditions are reasonable as sea surface temperature (SST) anomalies are damped by heat fluxes, whereas sea surface salinity (SSS) anomalies have no essential influence on precipitation or evaporation.

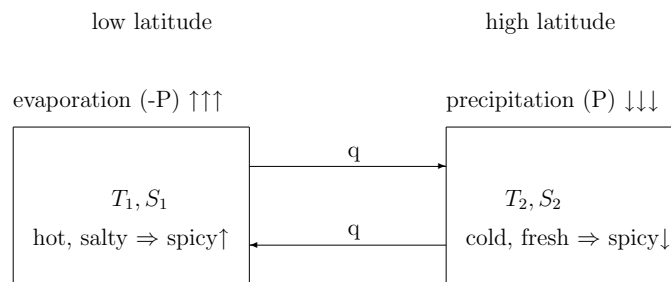


Figure 9.3: Stommel Box-Model (note: low latitude to right)

$$\dot{S}_1 = |q|(S_2 - S_1) + P \quad (9.5)$$

$$\dot{S}_2 = |q|(S_1 - S_2) - P \quad (9.6)$$

$$q = k\alpha(T_2 - T_1) + k\beta(S_2 - S_1) \quad (9.7)$$

Where $\alpha > 0$ and $\beta < 0$ are the expansion coefficients of temperature and salinity, respectively, and k is a coefficient that connects q to the density difference, and $P > 0$. For simplicity of the mathematics, and as we are only interested in qualitative results, we fix $\alpha = 1$, $\beta = -1$ and $k = -1$. The actual values can be adjusted based on observations. We then define $\Delta S = S_2 - S_1$ and $\Delta T = T_2 - T_1$ and note that $\Delta T < 0$ (and $\Delta S < 0$ if $P > 0$)!

$$\frac{1}{2}\Delta\dot{S} = -|q|\Delta S - P, \quad (9.8)$$

with $q = \Delta S - \Delta T$. Looking for stationary states ($\Delta\dot{S} = 0$) we obtain:

$$|\Delta S - \Delta T|\Delta S + P = 0. \quad (9.9)$$

We will call a THC with $q > 0$ forward and with $q < 0$ reverse. Solving these equations we obtain the following stationary states:

$$\Delta S = \frac{1}{2}(\Delta T \pm \sqrt{(\Delta T)^2 - 4P}) \text{ if } q > 0 \quad (9.10)$$

$$\Delta S = \frac{1}{2}(\Delta T - \sqrt{(\Delta T)^2 + 4P}) \text{ if } q < 0 \quad (9.11)$$

A fourth solution contradicts the $q < 0$ condition. We can now distinguish several cases (see also fig. 9.2):

(1) for $P < 0$ an unrealistic forcing, there is only one solution which is a strong forward THC, as salinity and temperature favor a positive q .

(2) $0 < P < (\Delta T)^2/4$ and we have three solutions, one unstable and two stable. The two stable solutions are

$$\Delta S = \frac{1}{2}(\Delta T + \sqrt{(\Delta T)^2 - 4P}) \text{ and } q = \frac{1}{2}(-\Delta T + \sqrt{(\Delta T)^2 - 4P}) > 0 \quad (9.12)$$

$$\Delta S = \frac{1}{2}(\Delta T - \sqrt{(\Delta T)^2 + 4P}) \text{ and } q = \frac{1}{2}(-\Delta T - \sqrt{(\Delta T)^2 + 4P}) < 0 \quad (9.13)$$

What is the physics of these two stationary solutions? The first is the usual fast and forward thermohaline circulation, this means that the THC is so fast that precipitation has no time to act and temperature effects dominate over salinity. The second solution is slower and reversed, the circulation is slow so precipitation can do its job and salinity dominates temperature differences.

(3) $P > (\Delta T)^2/4$ that is strong precipitation and we have only one stationary solution which is dominated by salinity and is an inverse THC (perhaps the Pacific Ocean and the North Atlantic at the end of glacial periods).

We have thus seen that using mixed boundary conditions for temperature and salinity, we can have two solutions for the same forcing! A nonlinear equation can have several solutions for the same set of parameters and boundary conditions.

Another important point is that such ocean model exhibits a hysteresis behaviour as a function of a control variable as for example the precipitation. When small perturbations are added, such model can give rise to abrupt changes between the two stable states followed by periods of stability of arbitrary length. The observed break down of the thermohaline circulation in the North Atlantic is often explained by such kind of model and multiple equilibria.

Exercise 57: We have written all the equations in non-dimensional form. Perform the calculations for a concrete example (for example: volume of the boxes 1m^3 , ...).

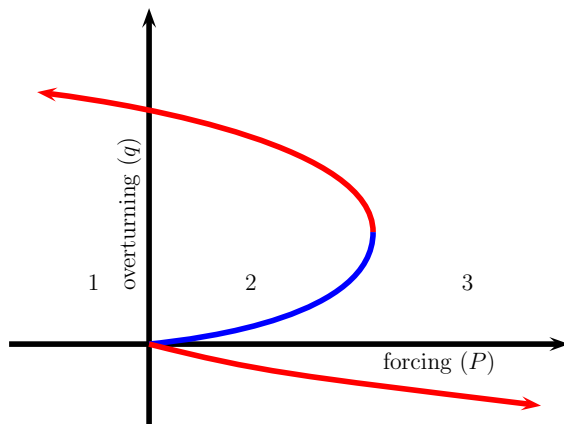


Figure 9.4: Hysteresis behaviour of the model as described by eqs. (9.12) and (9.13). The strength of the overturning circulation (q) is described as a function of the precipitation (P) for a fixed temperature difference (ΔT). Stable solutions are shown in red, the unstable solution in blue. There is one solution in the region 1 and 3. There are two stable solutions and one unstable solution in region 2.

9.3 What Drives the Thermohaline Circulation?

A key question we have not considered so far is where does the mechanical energy come from that drives the thermohaline circulation and transports the heat? A question we did not consider when discussing the Stommel-Aarons model, which is based on conservation of potential vorticity. The evaporation takes water from the surface which is then, at a different location, reintroduced in the ocean, by rain and river runoff. The important point is, however, that the mass is taken and put back at the ocean surface, that is at the same geopotential height! Which means that no net potential energy (mgh) is provided to the ocean as neither mass nor height is different at evaporation and precipitation points (see fig. 9.3). What about the mechanical work ($dW = -pdV$) done on the ocean by thermal expansion and contraction, that is change of volume dV . Again, both processes happen at the surface, at the same pressure p , and again: no net energy is provided to the ocean by thermal atmospheric forcing. Please note that the situation is completely different for the atmosphere, as shown in fig. 9.3, which is generally heated at a lower geopotential height, typically at the surface, than at which it is cooled, by radiating energy into space, and mechanical work is provided.

So what drives the THC? Originally it was thought that the forcing comes from the cooled water pushing the thermohaline circulation until Sandström, in 1908, asked the question about the energy balance discussed above. Sandström concluded that in a fluid heated and cooled at the surface the fluid below the cold source, should be homogeneous at the cold temperature and the fluid between the cold and warm sources would be stably stratified with only low fluid velocities. A result that bears the name of Sandström's Theorem.

Then the idea was put forward, that the diffusion of heat from the surface into the depth at low latitudes descends the effective heating into the ocean and provides thus for the missing energy to drive the THC, which meant that the THC is pulled rather than pushed. Recent research initiated by Munk & Wunsch in 1998 favors still another idea, which is that the driving force is the wind. This means that the low to high latitude heat flux of $2 \times 10^{15} \text{W}$ is a passive consequence of the wind driven circulation powered by only $2 \times 10^{12} \text{W}$, a thousand times less!

The picture they propose is, that the wind stress drives a conveyor belt that transports the heat.

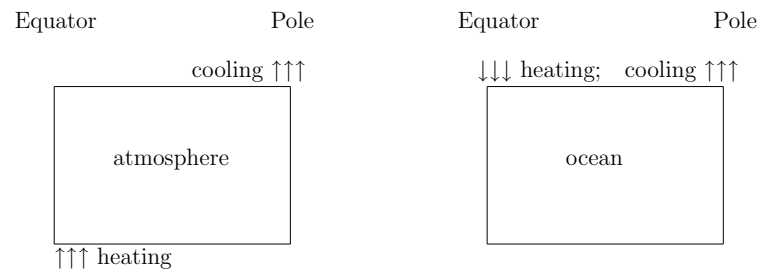


Figure 9.5: Energy Balance

Chapter 10

Penetration of Surface Fluxes

The ocean is mostly driven by the fluxes of heat, fresh water and momentum at its surface. The influence of these fluxes are, however, not only felt in a thin layer at the ocean surface, but influence the dynamics of the entire ocean. In this chapter we discuss how the forcing applied at the surface of the ocean penetrates into the depth of the ocean.

For the processes of vertical penetration, it is clear that we can no longer neglect the dynamics in the vertical direction, and the shallow water equations are not adapted for the processes studied here (with the exception of gravity currents). We thus have to look for other simplifications of the the full three-dimensional Navier-Stokes equations. A first guess might be to neglect the dynamics all together and pretend that the transport to the interior is due to molecular motions, that is viscosity and diffusivities (for heat and salt). This possibility is discussed and refuted in section 10.1.

In section 10.2 we show, using the Navier-Stokes equations and some “hand-waving” that the three dimensional dynamics at small scales creates some viscous and diffusive behavior at large scales. This idea is the basis of all realistic calculations not only in ocean dynamics but in fluid dynamics in general.

10.1 Molecular Transport

The molecular thermal diffusivity of sea water is $\kappa \approx 10^{-7} \text{m}^2 \text{s}^{-1}$. The diffusion equation in the vertical is given by,

$$\partial_t T = \partial_z (\kappa \partial_z T). \quad (10.1)$$

We further suppose that there is a periodic heat flux of magnitude Q at the surface (boundary condition), that is:

$$\partial_z T|_{z=0} = \frac{Q}{c_p \rho \kappa} \cos(2\pi t/\tau + \pi/4). \quad (10.2)$$

The linear equation (10.1) with the boundary conditions (10.2) has the solution:

$$T(z, t) = T_A e^{-z/L} \cos(2\pi t/\tau - z/L), \quad (10.3)$$

with:

$$T_A = \frac{Q}{c_p \rho} \sqrt{\frac{\tau}{2\pi\kappa}} \text{ and } L = \sqrt{\frac{\tau\kappa}{\pi}}. \quad (10.4)$$

Where $Q \approx 200 \text{ Wm}^{-2}$, $c_p = 4000 \text{ JK}^{-1} \text{ kg}^{-1}$, $\rho = 1000 \text{ kgm}^{-3}$ if we take τ to be one day get: $T_A \approx 20 \text{ K}$ and $L = 5.2 \text{ cm}$, this means that the surface temperature in the ocean varies by 40K in one day and the heat only penetrates a few centimeters. If τ is one year, considering the seasonal cycle, $T_A \approx 400 \text{ K}$ and $L \approx 1 \text{ m}$. This means that the surface temperature in the ocean varies by 800K in one year and the heat only penetrates about one meter. This does not at all correspond to observation!

When using the molecular viscosity, ν we can also calculate the thickness of the Ekman layer $\delta = \sqrt{2\nu/f}$ which is found to be a few centimeters. The observed thickness of the Ekman layer in the ocean is however over 100 times larger.

This shows that molecular diffusion can not explain the vertical heat transport, and molecular viscosity can not explain the vertical transport of momentum! But what else can?

10.2 Turbulent Transport

In the early 20th century fluid dynamicists as L. Prandtl suggested that small scale turbulent motion mixes scalars and momentum very much like the molecular motion does, only that the turbulent mixing coefficients are many orders of magnitude larger than their molecular counterparts. This is actually something that can easily be verified by gently poring a little milk into a mug of coffee. Without stirring the coffee will be cold before the milk has spread evenly in the mug, with a little stirring the coffee and milk are mixed in less than a second.

In this section we like to have a quantitative look at the concept of eddy viscosity in a very simplified frame work that nevertheless contains all the important pieces. The starting point of our investigation are the Navier-Stokes equations (5.1 –5.4). We start by considering the two dimensional motion in the $x - z$ -plane. Motion and dependence in the y direction are neglected only to simplify the algebra, and do not lead to important changes. We further suppose that the large scale velocity field is only directed in the x -direction and depends only on the z -direction $U(z)$. The x and z component of the small scale turbulent motion is given by u' and w' , respectively.

$$\begin{pmatrix} u \\ w \end{pmatrix} = \begin{pmatrix} U(z) + u' \\ w' \end{pmatrix} \quad (10.5)$$

with $U(z) = \langle u \rangle_x$.

The $\langle \cdot \rangle_x$ operator denotes the average over a horizontal slice:

$$A(y) = \langle a(x, y) \rangle_x = \frac{1}{L} \int_L a(x, y) dx \quad (10.6)$$

$$(10.7)$$

In the sequel we will use the following rules:

$$\langle \lambda(z)a \rangle_x = \lambda(z) \langle a \rangle_x \quad (10.8)$$

$$\langle \partial_z a \rangle_x = \partial_z \langle a \rangle_x \quad (10.9)$$

and

$$\langle \partial_x a(x, z) \rangle_x = \frac{1}{x_2 - x_1} \int_{x_1}^{x_2} \partial_x a(x, z) dx = \frac{a(x_2, z) - a(x_1, z)}{x_2 - x_1}, \quad (10.10)$$

which vanishes if $a(x, z)$ is bounded and we take the limit of the averaging interval $L = (x_2 - x_1) \rightarrow \infty$. But of course:

$$\langle ab \rangle_x \neq \langle a \rangle_x \langle b \rangle_x. \quad (10.11)$$

10.2. TURBULENT TRANSPORT

59

If we suppose $u' = w' = 0$, that is, no turbulence the Navier-Stokes equations (see eq. (5.1) – (5.4)) become:

$$\partial_t U + F = \nu \partial_{zz} U \quad (10.12)$$

where $F = (\partial_x P)/\rho$ is the pressure Force. If we allow for small scale turbulent motion we get:

$$\partial_t (U + u') + \partial_x ((U + u')(U + u')) + \partial_z (w'(U + u')) \quad (10.13)$$

$$+ F + \partial_x p' = \nu \partial_{zz} (U + u'). \quad (10.14)$$

Where we have used the identity

$$u \partial_x u + w \partial_z u = \partial_x (uu) + \partial_z (uw), \quad (10.15)$$

which is a direct consequence of the incompressibility ($\partial_x u + \partial_z w = 0$). Applying the horizontal averaging operator to eq. (10.14) we get:

$$\partial_t U + \partial_x \langle (U + u')(U + u') \rangle_x + \partial_z \langle w'(U + u') \rangle_x + F + \langle \partial_x p' \rangle_x = \nu (\partial_{xx} + \partial_{zz}) \langle (U + u') \rangle_x \quad (10.16)$$

which simplifies to:

$$\partial_t U + \partial_z \langle w' u' \rangle_x + F = \nu \partial_{zz} U \quad (10.17)$$

If we now compare eqs. (10.12) and (10.17) we see that the small scale turbulent motion adds one term to the large scale equations. The value of this term depends on the small scale turbulence and the large scale flow and is usually unknown. There are now different ways to parametrise this term, that is, express it by means of the large scale flow. The problem of finding a parametrisation is called closure problem.

None of the parametrisations employed today is rigorously derived from the underlying Navier-Stokes equations, they all involve some “hand-waving.” We will here only discuss the simplest closure, the so called K-closure.

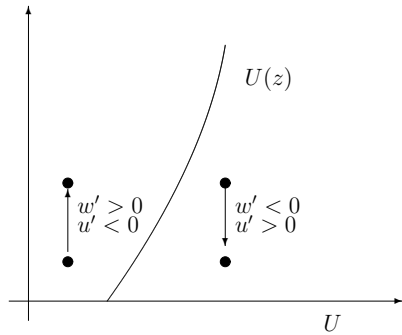


Figure 10.1: K-closure

The K-closure assumes the turbulent flux term to be proportional to the large-scale velocity gradient:

$$\langle w' u' \rangle_x = -\nu'_{eddy} \partial_z U \quad (10.18)$$

where $-\nu_{eddy}$ is the proportionality coefficient. Looking at fig. 10.1 this choice seems reasonable: firstly the coefficient should be negative as upward moving fluid transport a fluid parcel that originates from an area with a lower average velocity in the x -direction to an area with a higher average velocity in the x -direction, such that u' is likely to be negative. The reverse is true for downward transport. Such that $\langle w'u' \rangle_x$ is likely to be negative. Secondly, a higher gradient is likely to increase $|u'|$ and such also $-\langle w'u' \rangle_x$.

Using the K-closure we obtain:

$$\partial_t U + F = (\nu + \nu'_{eddy}) \partial_{zz} U, \quad (10.19)$$

which is identical to eq. (10.12) except for the increased effective viscosity $\nu_{eddy} = \nu + \nu'_{eddy}$ called the eddy viscosity

Exercise 58: perform the calculations without neglecting the motion and dependence in the y -direction.

Exercise 59: perform the calculations for a passive scalar (a scalar quantity that diffuses and is transported by the fluid without acting on the velocity field).

10.3 Convection

Oceanic convection is the buoyancy driven vertical mixing of water masses. Convection occurs when the water column is unstable, that is, heavier water is lying above lighter water. In the ocean this typically occurs when the surface waters are either cooled by atmospheric forcing or their salinity is increased by evaporation. (Note that for waters with a salinity above 25PSU density always decreases when temperature increases). If a isothermal ocean of depth H is subject to a heat flux of Q its temperature change is given by:

$$\partial_t T = \frac{Q}{c_p \rho H} \quad (10.20)$$

In extreme cooling events in polar oceans the heat flux can reach $Q = -10^3 \text{Wm}^{-2}$. A typical value of the heat capacity of sea water is $c_p = 4000 \text{Jkg}^{-1}\text{K}^{-1}$.

10.4 Richardson Number

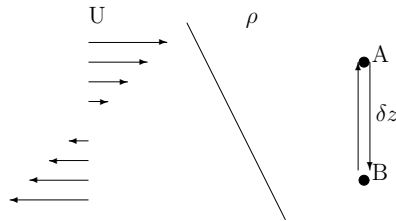


Figure 10.2: Exchanging volumes A and B in a sheared stably stratified flow.

When considering the vertical mixing in the ocean we usually have a large scale horizontal flow that has a vertical shear $\partial_z U$ which has a tendency to destabilize the flow and generate turbulence. On the other hand the flow usually has a stable stratification that suppresses

instability and also turbulence. This means that there are two competing phenomena and it is key for vertical mixing to determine under which circumstances one of the processes dominates. To this end we look at a stably stratified sheared flow, and consider the energy budget when to equal volumes A and B, as shown in fig. 10.2, separated by a distance δz are exchanged. The potential energy ΔE_{pot} necessary to exchange the heavier and lower volume B with the lighter and higher volume A is supposed to be provided by the kinetic energy ΔE_{kin} in the shear. For this to be possible it is clear, that $\Delta E_{total} = \Delta E_{kin} + \Delta E_{pot} > 0$ which are given by,

$$\Delta E_{kin} = 2 \frac{\rho V}{2} ((\delta z/2) \partial_z U)^2 \quad (10.21)$$

$$\Delta E_{pot} = -gV(\delta z)^2 \partial_z \rho. \quad (10.22)$$

Indeed, $E_{pot} = gh\Delta m$, and for our case $h = \delta z$ and $m = \delta z V \partial_z \rho$ is the mass difference between volume B and A. $\Delta E_{total} > 0$ if the Richardson number ,

$$Ri = \frac{g \partial_z \rho}{\rho (\partial_z U)^2} < \frac{1}{4}, \quad (10.23)$$

or if we write $\delta U = \delta z \partial_z U$ and $\delta \rho = \delta z \partial_z \rho$ we obtain,

$$Ri = \frac{g \delta \rho \delta z}{\rho (\delta U)^2} < \frac{1}{4}, \quad (10.24)$$

Which means that using the kinetic energy of the volumes A and B it is possible to interchange the volumes A and B when $Ri < 1/4$. Although that this calculation is very simple, only comparing kinetic to potential energy, and does not tell us how the volumes A and B should be exchanged, it is found in laboratory experiments that sheared stratified flow does indeed become unstable around a critical Richardson number of one quarter.

The above, and more involved, calculations together with laboratory experiments and oceanic observations have led to a variety of parametrisations of the vertical mixing based on the Richardson number.

One of the simplest, and widely used, parametrisations for vertical mixing based on the Richardson number was proposed by Philander and Pacanowski (1981):

$$\nu_{eddy} = \frac{\nu_0}{(1 + \alpha Ri)^n} + \nu_b, \quad (10.25)$$

where typical values of the parameters, used in today's numerical models of the ocean dynamics, are $\nu_0 = 10^{-2} \text{m}^2 \text{s}^{-1}$, $\nu_b = 10^{-4} \text{m}^2 \text{s}^{-1}$, $\alpha = 5$ and $n = 2$.

Exercise 60: *Slippery Sea*

10.5 Entrainment

Entrainment is the mixing of ambient (non or less turbulent) fluid into a turbulent current so that the initially less turbulent fluid becomes part of the turbulent flow. Examples are: a fluid jet that spreads and entrains ambient fluid with it, (ii) an avalanche that entrains surrounding air and increases in size. The fluid flow is typically from the less turbulent fluid to the more turbulent fluid. Entrainment is usually quantified by the entrainment velocity which is the velocity with which the ambient fluid enters into the turbulent jet through the border separating the two fluids. If the entrainment is negative one speaks of detrainment.

10.6 Gravity Currents

Gravity currents are currents that evolve due to their different density with respect to the surrounding water masses. We can thus distinguish buoyant gravity currents and dense gravity currents.

Buoyant gravity currents are lighter than the surrounding and are thus confined to the surface, an example is fresh river water that enters the ocean. Dense gravity currents on the contrary are composed of water heavier than the surrounding and they thus flow along the topography. Important examples are dense currents that pass through straits (Gibraltar, Denmark, ...) and flow down the continental slopes. We will here consider only the case of dense gravity currents.

When a dense gravity current leaves a strait it is deviated to the right by the Coriolis force and flows along the slope of the topography. When we neglect friction, mixing and entrainment (see section 10.5), the parameters determining the dynamics of the gravity current are the reduced gravity $g' = g\Delta\rho/\rho$ the slope α and the Coriolis parameter f .

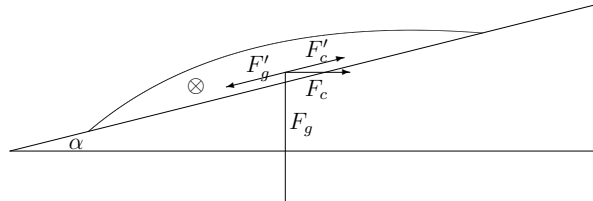


Figure 10.3: Force balance in gravity currents

$$F_g = mg', \quad F_g' = mg' \sin \alpha, \quad (10.26)$$

$$F_c = mfu, \quad F_c' = mfu \cos \alpha. \quad (10.27)$$

If we suppose that the gravity current is in a stationary state, the buoyancy force and the Coriolis force projected on the slope have to balance, that is $F_g' = F_c'$ (see Fig. 10.6) and thus,

$$u_{\text{Nof}} = \frac{g'}{f} \tan \alpha, \quad (10.28)$$

which is called the Nof-speed.

Exercise 61: What happens when we include bottom friction in the force balance?

Exercise 62: What happens when we include entrainment in the dynamics (see section 10.5)?

Chapter 11

Solution of Exercises

Exercise 11:

The energy of a fluid of density ρ between the two points a and b in a channel of width L is composed of kinetic energy:

$$E_{kin} = \rho L \int_a^b \frac{H}{2} u^2 dx, \quad (11.1)$$

and potential energy:

$$E_{pot} = \rho L \int_a^b \frac{g}{2} \eta^2 dx. \quad (11.2)$$

The change of the total energy with time is thus:

$$\begin{aligned} \partial_t E_{total} &= \partial_t E_{kin} + \partial_t E_{pot} = \rho L \int_a^b \left(\frac{H}{2} \partial_t (u^2) dx + g \partial_t \eta^2 \right) dx = \\ &= \rho L \int_a^b \left(-\frac{H}{2} g u \partial_x \eta - \frac{g}{2} H \eta \partial_x u \right) dx = -\rho L \frac{gH}{2} \int_a^b \partial_x (\eta u) dx = -\rho L \frac{gH}{2} (u(b)\eta(b) - u(a)\eta(a)) \end{aligned}$$

Where we have used eq.5.23 and 5.24. So energy is conserved in the domain $[a, b]$ with the exception of energy entering or leaving at the boundary points.

Exercise 12:

Yes, the typical velocity in a Tsunami in deep waters is less than $0.1m/s$ and its horizontal extension is of the order of 100km so the nonlinear term $u \partial_x u < 10^{-7} m^2 s^{-1}$ much less than $g \partial_x \eta \approx 10^{-4} m^2 s^{-1}$.

Exercise 13:

$$d = \partial_x u + \partial_y v = -\partial_{xy} \Psi + \partial_{yx} \Psi = 0$$

Exercise 14:

$$\xi = \partial_x v - \partial_y u = \partial_{xx} \Psi + \partial_{yy} \Psi = \nabla^2 \Psi$$

Exercise 16:

$(x_r, y_r) = R(\cos(\omega t), \sin(\omega t))$, $\rightsquigarrow (u_r, v_r) = \omega R(-\sin(\omega t), \cos(\omega t)) \rightsquigarrow \partial_t(u_r, v_r) = -\omega^2 R(\cos(\omega t), \sin(\omega t))$,
 putting it together: $((-\omega^2 R - f\omega R - f^2/4R) \cos(\omega t), (-\omega^2 R - f\omega R - f^2/4R) \sin(\omega t)) = 0$,
 which is satisfied if and only if $\omega = -f/2$

Exercise 17:

now the centrifugal force is balanced by the slope of the free surface and we have $((-\omega^2 R - f\omega R) \cos(\omega t), 0)$ which is satisfied if and only if $\omega = -f$ (compare to previous exercise)!

Exercise 28:

The potential energy released per unit length (in the transverse direction):

$$E_{pot} = 2 \frac{1}{2} \rho g \eta_0^2 \int_0^\infty (1 - (1 - \exp(-x/a))) dx = \frac{3}{2} \rho g \eta_0^2 a. \quad (11.4)$$

The kinetic energy in the equilibrium (final) solution per unit length (in the transverse direction):

$$E_{kin} = 2 \frac{1}{2} \rho H g^2 \eta_0^2 (fa)^{-2} \int_0^\infty \exp(-2x/a) dx = \frac{1}{2} \rho g \eta_0^2 a. \quad (11.5)$$

So energy is NOT conserved during the adjustment process. Indeed waves transport energy from the region where the adjustment occurs to $\pm\infty$.

Exercise 30:

Calculus tells us that:

$$\frac{d}{dt} \left(\frac{\zeta + f}{H + \eta} \right) = \frac{1}{H + \eta} \frac{d}{dt} (\zeta + f) - \frac{\zeta + f}{(H + \eta)^2} \frac{d}{dt} \eta.$$

So take ∂_x of eq.(5.39) and subtract ∂_y of eq. (5.38) to obtain:

$$\begin{aligned} \partial_t \partial_x v &+ \partial_x (u \partial_x v) + \partial_x (v \partial_v v) + f \partial_x u + g \partial_{xy} \eta \\ - \partial_t \partial_y u &- \partial_y (u \partial_x u) - \partial_y (v \partial_v u) + f \partial_y v - g \partial_{xy} \eta = 0. \end{aligned}$$

After some algebra one obtains:

$$\frac{d}{dt} (\zeta + f) = -(\zeta + f) (\partial_x u + \partial_y v),$$

and eq. (5.40) gives

$$\frac{d}{dt} \eta = -(H + \eta) (\partial_x u + \partial_y v),$$

putting this together gives the conservation of potential vorticity.

Exercise 32:

The moment of inertia is $L = I\omega = mr^2/2\omega = m\rho V/(4\pi)\omega/H$ where we used, that the volume V of a cylinder is given by $V = 2\pi r^2 H$. As the mass and the volume are constant during the stretching of flattening process we obtain that conservation of angular momentum implies that ω/H is constant.

Exercise 38:

The (kinetic) energy is given by: $E = \alpha(U^2 + V^2)$, where the constant $\alpha = A\rho/(2H)$ is the horizontal surface area times the density divided by twice the layer thickness. $\partial_t E = \alpha(\partial_t U^2 + \partial_t V^2) = \alpha 2(U\partial_t U + V\partial_t V)$ using eqs. (6.13) and (6.13) we obtain $\partial_t E = \alpha(fVU + U\tau_x - fUV) = 0$, as the velocity is perpendicular to the forcing, that is, $U = 0$.

Exercise 41:

Summing the first and the third line of the matrix equation gives $U_1 + U_2 = 0$, summing the second and the fourth line of the matrix equation gives $f(V_1 + V_2) = \tau_x$. Eliminating U_2 and V_2 in the first and third equation we obtain:

$$\begin{aligned}\tilde{r}U_1 - fV_1 &= \tau_x \\ fU_1 + \tilde{r}V_1 &= (r/f)\tau_x.\end{aligned}$$

with $\tilde{r} = r(H_1 + H_2)/(H_1 H_2)$ solving this equations give:

$$\begin{aligned}U_1 &= \frac{r\tau_x}{f^2 + \tilde{r}^2} \frac{1}{H_1} \\ V_1 &= -\frac{r\tau_x}{f^2 + \tilde{r}^2} \left(\frac{f}{r} + \frac{\tilde{r}}{fH_2} \right) \\ U_2 &= -\frac{r\tau_x}{f^2 + \tilde{r}^2} \frac{1}{H_1} \\ V_2 &= \frac{r\tau_x}{f^2 + \tilde{r}^2} \frac{\tilde{r}}{fH_1}\end{aligned}$$

Index

- Active tracers, 8
- Albedo, 18
- Available potential energy, 46
- Available potential energy, 30
- Balanced equations, 33
- Baroclinic instability, 46
- Beta-effect (β -effect), 32
- Beta-plane (β -plane), 32
- Boussinesq approximation, 43
- Brine, 16
- Cabbeling, 13
- Closure problem, 59
- conservative tracer, 15
- Convection, 15, 60
- Coriolis Force, 26
- Coriolis parameter, 27
- Dansgaard-Oeschger, 52
- Dittmar's law, 10
- Eddies, 46
- Eddy viscosity, 60
- Ekman layer, 38
- Ekman layer thickness, 40
- Ekman spiral, 39
- Ekman transport, 38
- Entrainment, 61, 62
- Equation of state, 9
- Equatorial β -plane, 49
- Equatorial current, 49
- Equatorial Rossby radius, 49
- Equatorial undercurrent, 49
- Geocentric frame, 26
- Geostrophic equilibrium, 29
- GFD, 33
- Gravity currents, 62
- Gyre, 35
- heat capacity, 13
- HMS Challenger, 7, 10
- Hydrostatic approximation, 22
- Inertial frequency, 28
- Inertial oscillation, 28, 39
- K-closure, 59
- Kelvin wave, 34
- Level of no motion, 44
- North equatorial counter current, 49
- Passive tracers, 8
- Philander and Pacanowski, 61
- Planetary potential vorticity, 32, 35, 42
- Planetary vorticity, 37
- Poincaré waves, 33
- potential density, 13
- Potential temperature, 10
- Potential vorticity, linear, 30
- quasi-geostrophic equations, 33
- Reduced gravity, 24
- Relative vorticity, 37
- Richardson number, 61
- Rossby number, 46
- Rossby number, 28
- Rossby radius, 30, 31, 46
- Rossby wave, 34
- Salinity, 9
- Sandström's Theorem, 55
- Sea surface height (SSH), 29
- Slow manifold, 33
- Solar constant, 17
- South equatorial counter current, 50
- Sverdrup, 29
- Sverdrup relation, 35, 42
- T-S diagrams, 11
- Temperature, 10
- Thermal wind, 44
- Thermobaricity, 13
- Thermocline, 51
- Traditional approximation, 27, 49

INDEX

67

Transport stream-function, 29

UNESCO 1981 formula, 13

Western boundary current, 36

.

Alles Vergängliche

Ist nur ein Gleichnis ;

Das Unzulängliche,

Hier wird's Ereignis ;

Das Unbeschreibliche,

Hier ist's getan ;

Das Ewig-Weibliche

Zieht uns hinan.

(J.W. Goethe, Faust II)

Annexe A

Attestation de reussite au diplome

UNIVERSITE DE GRENOBLE

ATTESTATION DE REUSSITE AU DIPLOME

Le Président atteste que

l' HABILITATION A DIRIGER DES RECHERCHES Spécialité SCIENCES DE LA PLANETE
a été décernée à

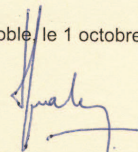
Monsieur WIRTH ACHIM

né le 23 décembre 1968 à MÜNCHEN (ALLEMAGNE)

au titre de l'année universitaire 2009/2010

Date de soutenance : 14 septembre 2010
Etablissement soutenance : UNIVERSITE DE GRENOBLE
Jury : M. MICHAEL GHIL, Président du jury
M. ERIC BLAYO, Rapporteur du jury
M. YVES MOREL, Rapporteur du jury
M. JÜRGEN WILLEBRAND, Rapporteur du jury
M. BERNARD BARNIER, Membre du jury
M. URIEL FRISCH, Membre du jury
Ecole doctorale : TERRE, UNIVERS, ENVIRONNEMENT (105)

Fait à Grenoble, le 1 octobre 2010



Farid OUABDESSELAM



N° étudiant : 20964309

Avis important: Il ne peut être délivré qu'un seul exemplaire de cette attestation. Aucun duplicata ne sera fourni.

Université de Grenoble 1025 Avenue Centrale 38402 ST Martin d'Hères

Annexe B

Rapports du jury et des rapporteurs



UNIVERSITE DE GRENOBLE

N° Etudiant : 20964309

PROCES-VERBAL DE PRESENTATION DES TRAVAUX
HABILITATION À DIRIGER DES RECHERCHES

M : Wirth Prénom : Achim

Nom Epouse (si y a) :

Né(e) le : 23/12/1968 Département ou Pays : Allemagne

Discipline dans laquelle vous présentez vos travaux : TUE/SC DE LA PLANETE

Doctorat obtenu le : 13/12/1996 à (Université d'obtention du Doctorat) : Université de Nice

Date de présentation des travaux : 14/09/2010 à 15:00 heures

Lieu (adresse exacte) : LEGI, 1023 rue de la Piscine
38400 St Martin d'Hères

Date de la recevabilité de la demande d'inscription : 27/04/2010

AVIS SUR LA PRESENTATION DES TRAVAUX

Titre : *Études et Evaluation de Processus Océaniques par des Hiérarchies de Modèles*

COMPOSITION DU JURY

conforme à l'arrêté du 23 novembre 1988

MEMBRES	FONCTION	LIEU D'EXERCICE
Rapporteur - Mme/M : <i>Eric Blayo</i>	<i>Prof.</i>	<i>Univ. de Grenoble</i>
Rapporteur - Mme/M : <i>Yves Morel</i>		<i>(SHOM / LEGOS)</i>
Rapporteur - Mme/M : <i>Jürgen Willebrand</i>	<i>Prof.</i>	<i>IfM-Geomar Kiel</i>
Membre du jury - Mme/M : <i>Michael Ghil</i>	<i>Prof.</i>	<i>ENS - Paris</i>
Membre du jury - Mme/M : <i>Bernard Barnier</i>	<i>Dir-ved. CNRS</i>	<i>LEGI</i>
Membre du jury - Mme/M : <i>Uriel Frisch</i>	<i>Dir-ved. CNRS</i>	<i>Obs. de Nice</i>
Membre du jury - Mme/M :		
Membre du jury - Mme/M :		

Il ressort que rien ne s'oppose à la présentation des travaux

Le Président du Comité d'Habilitation de la Discipline

Le Directeur du Collège des Ecoles Doctorales

Nicolas Campillo
p.e. *Nicolas Vauclin*
Nauclin

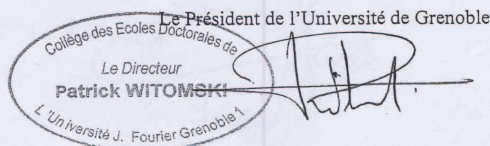
AUTORISATION DE PRESENTATION DES TRAVAUX

Vu les dispositions de l'arrêté du 23 novembre 1988

Vu la décision du Comité d'habilitation de *IFM / Sciences de la Planète*

en sa séance du *24.10.1990*

Mme/M *Eric Blayo* est autorisé(e) à présenter ses travaux en vue de l'obtention du Diplôme d'Habilitation à Diriger des Recherches.



Grenoble le 14 Sept 2010

RAPPORT DU PRESIDENT DE JURY APRES LA PRESENTATION DES TRAVAUX AVEC SIGNATURE DES MEMBRES DU JURY

~~Mme~~ M. GHIL Michael président(e) - (A RENSEIGNER OBLIGATOIREMENT)

Mr Wirth a présenté le 14 septembre un mémoire de recherche sur « Etudes et Evaluation de Processus Océaniques par des Hiérarchies de Modèles ». Ce mémoire avait obtenu trois rapports très positifs, dont l'un avait été rédigé par un professeur d'océanographie de Kiel en Allemagne (JW), le deuxième par un ingénieur en chef de l'armement du SHOM à Toulouse (YM) et le troisième par un professeur en mathématiques appliquées à l'Université Joseph Fourier (EB). Ce choix très divers de rapporteurs indique déjà le caractère fortement interdisciplinaire de la recherche de Mr Wirth.

Les quatre parties du mémoire correspondent à

- un texte introductif original, dans lequel il présente une réflexion sur son travail scientifique, en précisant son contexte, les outils utilisés et leur hiérarchisation, et un résumé des questions scientifiques qu'il a abordé ces dernières années et qu'il souhaite traiter dans le futur, en les replaçant dans ce contexte ;
- un curriculum vitae assez complet, y compris une liste d'une vingtaine de publications de Rang A ;
- neuf publications qui illustrent les travaux réalisés par Mr Wirth ces 10 dernières années ;
- un polycopié d'un cours d'océanographie physique donné en Master à des non-spécialistes.

Le texte introductif est en 3 chapitres et 30 pages, le CV en 8 pages, les publications sont dans d'excellentes revues de plusieurs disciplines (océanographie, turbulence, physique non linéaire et statistique, mathématiques appliquées et numériques) et font un total de 120 pages, et le cours, en 10 chapitres et avec solutions des exercices, donne encore 70 pages, pour un total de 240 pages.

Tout ceci illustre parfaitement le sérieux, ainsi que la cohérence de la démarche scientifique globale de Mr Wirth. Sur la vingtaine de publications, il est seul ou premier auteur des deux tiers, ce qui témoigne aussi de son originalité et de son investissement dans la recherche. Dans les meilleures universités des Etats-Unis – dans deux desquelles un membre du jury (MG) a été professeur (jusqu'au niveau PR0, dès 1994) aussi bien que directeur d'UFR et d'institut de recherche –, un tel nombre de publications de Rang A, combiné avec les autres éléments du dossier, mérite certainement, et avec une bonne marge, promotion au niveau d'Associate Professor et la « tenure ». C'est au moins l'équivalent d'une promotion au rang de DR2 au CNRS ou PR2 dans l'une des meilleures universités du système français.

Vu le caractère très complet et convaincant du mémoire, et le support apporté par les trois rapports, Mr Wirth a fait le choix éminemment judicieux de baser la soutenance orale sur un papier soumis, mais qui n'avait pas encore pu être inclus dans le mémoire. Il s'agissait de l'étude des courants gravitaires ("gravity currents") et de l'estimation de la contribution de la couche – limite de fond à leur écoulement, plus précisément de la contribution relative d'une friction linéaire, c.-à-d. directement proportionnelle à la vitesse de l'écoulement, par rapport à une friction quadratique, c.-à-d. toujours proportionnelle à la vitesse de l'écoulement, mais avec un coefficient qui lui-même dépend de la vitesse. Autrement dit, est-ce que, pour ces courants, c'est une loi de friction de type Rayleigh ou Chézy qui joue un rôle plus important ?

Après une présentation très concise de sa philosophie de recherche, correspondant à la première partie de son mémoire, Mr Wirth a donné une excellente introduction à notre jury pluridisciplinaire – qui comprenait également un DR du laboratoire LEGI de Grenoble (BB) et un grand spécialiste de la turbulence, de l'Observatoire de la Côte d'Azur à Nice (UF) –, sur la physique des courants gravitaires. Cette introduction insistait sur le rôle bien connu de la rotation – et de la force de Coriolis qui en découle –, dans le comportement de ces courants dans l'océan. Ensuite, il a clairement démontré l'importance bien moins connue de la couche de friction entre le courant et le fond marin, nous amenant au problème de la nature de cette friction. Au vu de l'absence de données de mesure directe sur ce problème, Mr Wirth a fait intervenir les outils très sophistiqués de « l'assimilation des données », à savoir d'une méthodologie avancée pour fusionner des données d'observation directe avec des résultats de modèles de simulation. Ayant très bien maîtrisé les outils de cette approche dans d'autres contextes, il est le premier à les appliquer à ce problème de premier ordre pour la circulation océanique à plusieurs échelles de temps et d'espace.

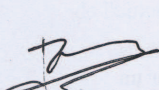
Mr Wirth nous a fait aussi une brillante illustration, dans ce contexte précis, de son approche générale d'utilisation de modèles multiples – des plus simples, tels les modèles de Saint-Venant ("shallow-water models") aux plus détaillés, tels les modèles de circulation générale ("GCM") océanique –, les premiers apportant le plus de flexibilité et de compréhension, les derniers le plus de détails et de possibilité de comparaison directe aux données d'observation. L'un des modèles utilisés, HAROMOD, était en effet un modèle que Mr Wirth lui-même avait développé : il s'agit d'un modèle spectral, c.-à-d. dans lequel la discrétisation des équations aux dérivées partielles qui régissent l'écoulement se fait par projection sur des fonctions harmoniques (d'où HAROMOD). Dans un papier publié dans le périodique de pointe du domaine, *J. Comp. Phys.* (en 1997), il avait résolu le problème principal qui faisait obstacle à l'application de cette approche en océanographie physique, à savoir celui des conditions au bord.

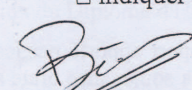
Pour finir, Mr Wirth a évalué d'une manière très lucide et objective ses résultats, en indiquant que seulement des données de terrain supplémentaires pourraient les améliorer. La présentation a été d'un niveau excellent, pour les diapositives autant que pour les explications orales et la réponse aux questions du jury : toujours claire et jamais trop pédante. La soutenance orale a démontré, aussi bien que le mémoire écrit, l'originalité de l'approche de Mr Wirth à la recherche ainsi qu'à l'enseignement, la maîtrise d'une vaste gamme de moyens techniques, une grande curiosité scientifique et une réflexion approfondie sur la démarche de la science moderne.

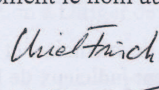
Le jury considère que Mr Wirth est, à tout point de vue, prêt à diriger des recherches, que cela soit en tant que directeur de recherches CNRS ou en tant que professeur des universités.

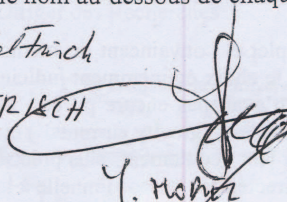
Signatures des membres du jury validé (voir composition du jury), ayant effectivement participé à la délibération et **UNIQUEMENT**

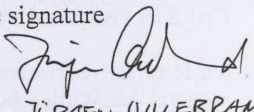
☐ indiquer lisiblement le nom au-dessous de chaque signature

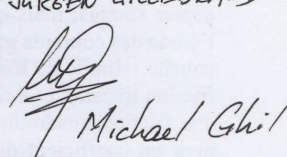

 E. BLAYO



 B. BARNIER


 U. FRISCH


 Y. MOREL


 JÜRGEN UILLEBRAND


 Michael GHIL



**LABORATOIRE
JEAN KUNTZMANN**
MATHÉMATIQUES APPLIQUÉES - INFORMATIQUE

Site Campus - Tour IRMA
51 rue des Mathématiques
38400 Saint Martin d'Hères
BP 53 - 38041 Grenoble Cedex 9
France
Tél : +33 4 76 51 43 42
Fax : +33 4 76 63 12 63
ljk@imag.fr - ljk.imag.fr

**Rapport sur le mémoire de Monsieur Achim WIRTH en vue de
l'obtention du diplôme d'Habilitation à Diriger des Recherches**

*Etudes et évaluation de processus océaniques par des hiérarchies de
modèles*

Le mémoire d'habilitation présenté par Achim Wirth est composé de 4 parties :

- Un texte introductif original, dans lequel il présente une réflexion sur son travail scientifique, en précisant son contexte, les outils utilisés et leur hiérarchisation, et un résumé des questions scientifiques qu'il a abordé ces dernières années et qu'il souhaite traiter dans le futur, en les replaçant dans ce contexte.
- Un curriculum vitae
- Une dizaine de publications, illustrant les travaux qu'il a réalisés ces 10 dernières années
- Un polycopié d'un cours d'océanographie physique donné en Master. Faire figurer des notes de cours dans un mémoire d'HDR est assez original, mais illustre parfaitement dans le cas présent la cohérence de la démarche scientifique globale d'Achim Wirth.

La thématique de recherche d'Achim Wirth concerne l'étude des processus de sub-mésoéchelle, non explicitement résolus dans les modèles de circulation générale océanique (et qui sont donc paramétrés dans ces modèles), et de leur influence sur la dynamique à grande échelle : instabilité barocline, convection verticale, courants gravitaires... Mieux comprendre ces phénomènes, qui ne sont pas (et ne pourront toujours pas être dans les années à venir) représentés explicitement dans les modèles grande échelle, est un point clé en vue d'une meilleure compréhension de la dynamique océanique dans sa globalité, et d'une amélioration des modèles.

Cette thématique est abordée avec une grande diversité d'outils : études théoriques, modèles analytiques, modèles numériques, méthodes inverses, expériences de laboratoire. La démarche de travail est toujours réfléchie et argumentée: l'approche est progressive, chaque étape apporte des difficultés nouvelles et des résultats nouveaux, et les outils sont

<p align="center">Site Campus - BSHM 1251 avenue centrale BP 47 - 38040 Grenoble Cedex 9 - France Tél : +33 4 76 51 43 42 - Fax : +33 4 76 63 12 63</p>	<p align="center">Site Montbonnot - INRIA 655 avenue de l'Europe 38334 Saint Ismier Cedex - France Tél : +33 4 76 61 52 00 - Fax : +33 4 76 61 52 52</p>
<p>CNRS □ INPG □ INRIA □ UJF □ UPMF</p>	



**LABORATOIRE
JEAN KUNTZMANN**
MATHÉMATIQUES APPLIQUÉES - INFORMATIQUE

Site Campus - Tour IRMA
51 rue des Mathématiques
38400 Saint Martin d'Hères
BP 53 - 38041 Grenoble Cedex 9
France

Tél : +33 4 76 51 43 42
Fax : +33 4 76 63 12 63
ljk@imag.fr - ljk.imag.fr

utilisés avec pertinence. Sur les aspects que je maîtrise plus particulièrement (modélisation numérique et assimilation de données), je remarque qu'Achim Wirth a beaucoup de recul et de sens critique vis à vis des méthodes et outils qu'il emploie, voire qu'il développe lui même (il a ainsi développé son propre modèle numérique, en faisant des choix de discrétisation originaux).

Ce mémoire, par sa richesse et son excellent niveau scientifique, illustre la large culture d'Achim Wirth en mécanique des fluides, océanographie physique, modélisation numérique et assimilation de données. Ceci reflète le parcours très riche d'Achim Wirth, dont le travail est concrétisé par une vingtaine de publications de rang A (dont les 2/3 comme premier auteur) dans les très bonnes revues du domaine.

Achim Wirth est un chercheur confirmé et reconnu, menant des recherches de très bonne qualité. En conclusion, je recommande donc sans aucune réserve qu'il soit autorisé à présenter publiquement ses travaux en vue de l'obtention du Diplôme d'Habilitation à Diriger des Recherches.

Fait à Grenoble, le 6 juillet 2010

Eric Blayo
Professeur en mathématiques appliquées
Laboratoire Jean Kuntzmann
Université Joseph Fourier

Site Campus - BSHM
1251 avenue centrale
BP 47 - 38040 Grenoble Cedex 9 - France
Tél : +33 4 76 51 43 42 - Fax : +33 4 76 63 12 63

Site Montbonnot - INRIA
655 avenue de l'Europe
38334 Saint Ismier Cedex - France
Tél : +33 4 76 61 52 00 - Fax : +33 4 76 61 52 52

CNRS □ INPG □ INRIA □ UJF □ UPMF



MINISTÈRE DE LA DÉFENSE

Toulouse, le 25 Mai 2010



SERVICE HYDROGRAPHIQUE ET
OCÉANOGRAPHIQUE DE LA MARINE

Direction des opérations

Division hydrographie, océanographie et
météorologie militaires

Département recherche

Dossier suivi par : ICA Yves Morel

☎ : 05 61 43 35 25
Fax : 05 62 14 06 10
Mél : yves.morel@shom.fr

Objet : **Rapport sur le travail de recherche de Mr Achim Wirth en vue d'une soutenance d'habilitation à diriger des recherches.**

Référence(s):

P. jointe(s) :

-

Le document proposé par Achim Wirth en vue d'obtenir une autorisation pour défendre son habilitation à diriger des recherches présente quatre parties :

- la première partie présente la perspective générale de ss travaux de recherche ;
- la seconde contient le curriculum vitae de Mr Achim Wirth;
- la troisième est constituée de l'assemblage de ses dernières publications ;
- la quatrième est le support de cours d'océanographie physique dispensé par Achim Wirth.

Travaux scientifiques :

Les travaux scientifiques de Mr Achim Wirth se concentrent sur les études d'impact de processus à petite échelle sur la dynamique des fluides à échelle géophysique.

Durant ses travaux **Mr Achim Wirth a utilisé l'ensemble des outils d'analyse scientifique disponibles :**

- analyse de données in situ ;
- expériences physiques en modèle réduit ;
- modélisation théorique / mathématique ;
- modélisation numérique.

Destinataire(s) :

Copie(s) extérieure(s):

Copie(s) intérieure(s) :

SHOM/DO/Toulouse - 42, avenue Gaspard Coriolis – 31057 Toulouse cedex

Les articles scientifiques de Mr Achim Wirth sont d'une excellente qualité et ont été publiés dans les meilleures revues du domaine. Elles sont originales et très innovantes.

En effet, il existe un certain cloisonnement entre les domaines scientifiques et parfois les résultats obtenus dans un domaine tardent à trouver leurs applications dans un autre. C'est en particulier le cas en mécanique des fluides où, étant donné la gamme des échelles possible, les études sont souvent fractionnées entre d'un côté la turbulence tridimensionnelle et de l'autre la dynamique à échelle planétaire. Le LEGI a permis de regrouper ces communautés et **Mr Achim Wirth y effectue un travail permettant leur lien.** C'est à ma connaissance **une des seules personnes à faire un travail allant de la compréhension des processus élémentaires de turbulence 3D jusqu'à la paramétrisation de leurs effets dans des modèles de circulation générale**, ce qui est remarquable, et indispensable : les progrès scientifiques majeurs à venir sont certainement en partie liés à des travaux aux interfaces de différents domaines, ce qui est le fondement des travaux de Mr Achim Wirth, tant du point de vue des thématiques scientifiques (turbulence 3D et circulation océanique) que des outils à utiliser (observation, modélisation).

Les travaux de Mr Achim Wirth se sont dernièrement concentrés sur deux processus :

- La turbulence, et le mélange qu'elle induit aux grandes échelles, associée à la convection ;
- La turbulence, et le mélange qu'elle induit aux grandes échelles, associée aux courants de gravité.

Ces processus sont d'un intérêt majeur en océanographie physique car ils dominent la dynamique de la circulation générale mais aussi des couches de surface et des zones d'intérêt particulier comme les détroits ou les rebords de talus.

Les résultats acquis par Achim Wirth sont donc d'un intérêt majeur pour la communauté océanographique.

Ce sont aussi des sujets complexes qui sont parfaitement maîtrisés par Mr Achim Wirth.

Sa démarche et son cheminement sont clairs et constants, et il est en particulier à noter qu'Achim Wirth a lui-même développé plusieurs outils d'analyse dont un modèle numérique non-hydrostatique pour mener à terme sa démarche.

Pilotage de la recherche :

Comme en atteste son curriculum vitae, **Achim Wirth participe aussi activement à des activités de pilotage de la recherche et a encadré de nombreux stages universitaires, collaboré à l'encadrement de thésitifs et encadré directement des jeunes chercheurs post-doctorants. Il a participé à deux jurys de thèse, dont un comme rapporteur.**

Il a aussi participé à, puis mis en place et mené à bien plusieurs projets scientifiques financés par les programmes nationaux, l'ANR ou d'autres agences de moyens.

Pour finir, **Achim Wirth dispense des cours au niveau master** mettant en valeur son approche de l'influence des processus de petite échelle sur la dynamique de fluide à échelle géophysique.

3/3

Pour résumer, Mr Achim Wirth mène des travaux scientifiques d'excellent niveau et propose une approche de la dynamique des fluides géophysiques originale. Il participe activement à l'animation de la recherche et mène ses projets avec une démarche claire et constante et propose des pistes d'investigation, tant thématiques que sur les outils d'analyse, innovantes et d'intérêt majeur.

En conséquence, **Mr Achim Wirth doit être autorisée à présenter son travail devant un jury afin d'obtenir une habilitation à diriger des recherches.**


L'ingénieur en chef de l'armement Yves Morel
Chef du département recherche
de la DCHOM de SHOM


IFM-GEOMAR

 Leibniz-Institut für Meereswissenschaften
an der Universität Kiel

IFM-GEOMAR

Gebäude Westufer, Düsternbrooker Weg 20, 24105 Kiel

Prof. Dr. Michel Campillo
L.G.I.T.
Université Joseph Fourier de Grenoble
B.P. 53, 38041 Grenoble cedex 9,
FRANCE
N

Ozeanzirkulation und Klimadynamik
Prof. Dr. Jürgen Willebrand

Gebäude Westufer
Düsternbrooker Weg 20
24105 Kiel
Tel: +49 431 600-4080
Fax: +49 431 600-4012
jwillebrand@ifm-geomar.de
www.ifm-geomar.de

27. Juni 2010

Dear Professor Campillo,

Below please find my comments on the habilitation thesis „Etudes et Évaluation de Processus Océaniques par des Hiérarchies de Modèles“ by Achim Wirth who is known to me mainly from a 2-year stay in my research group in Kiel.

The thesis is concerned with modelling of small-scale processes in the ocean and their relation to the oceanic circulation. The first part contains some reflections on understanding of ocean dynamics, and the issue of scales as an order criterion for the relevant processes. A thoughtful discussion on model hierarchies relates mathematical models on the one side to models of the physical system and observations of natural processes, and on the other side to numerical models, with data assimilation providing a further linkage. The author rightly points out that one does not necessarily understand the model one has built, a fact which is too often ignored in today's journals when scientists describe results of their more or less complex models without addressing the deeper causes. Various processes are then discussed which all play a role for the crucial vertical exchange processes in the ocean, a discussion which helps to integrate the author's research work into a more general context.

The main body of the thesis consists of 9 research publications, mostly with Wirth as first or single author. These papers address processes such as instability of ocean currents, convection, and currents driven by gravity, and document his ease in dealing with various kinds of problems. In section 4.1, after simulating interannual variations in the Indian Ocean with a complex model that was available from the shelf, he has demonstrated that year-to-year variability of the Great Whirl can result not only from changes in the forcing but also from internal changes due to the chaotic nature of the instability process. For this purpose he was quick to develop a specific (reduced gravity) model. In section 4.2 he investigated baroclinic instability with a quasi-geostrophic model and showed that the scale dependence is weaker than suggested by the standard layer-thickness mixing parameterization.

Two papers are addressed to oceanic convection. Specifically, the influence of the horizontal component of the Coriolis vector is studied which is neglected in most simulations. In an

**IFM-GEOMAR**Leibniz-Institut für Meereswissenschaften
an der Universität Kiel

idealized setting, it is found to cause not only the expected alignment with the direction of rotation, but also lower vertical velocities and increased mixing. Furthermore, increases in the mean circulation and the level of variability are found, results which are important for the parameterization of convection.

Several papers are directed to gravity current driven by near-bottom density differences. The structure of these flows is investigated, again in an idealized setting, and it is shown that friction is a most crucial parameter. A minimal model is presented which is able to give a most simple description for the characteristics of these flows. With identical-twin experiments, it is shown that friction parameters can be estimated with a data assimilation method based on the Ensemble Kalman Filter. Furthermore, the influence of vertical resolution on the simulations is investigated, and it is shown that the coarse resolution typical of many general circulation models leads to an underestimation of near-slope currents.

In the last part of his thesis, the author offers a guided tour through physical oceanography which documents the author's interest in teaching, and would be very useful as the basis for a university course in ocean dynamics.

Achim Wirth is a scientist of extraordinary intellectual capabilities. He is independent-minded, extremely quick in understanding, and has a lot of drive for accomplishing his work. In his age class, very few other scientists in the field of oceanography have a similar intellectual standing. His publication record is rather good, with 20 publications in first-rate international journals, most of them as single or first author. His contributions show considerable breadth, and include not only ocean dynamics where he has made important contributions with well-thought numerical experimentation, but also general fluid dynamics and especially turbulence theory.

At my own university, the degree of habilitation documents the candidate's qualification for the position of a university professor, which includes the ability to supervise students to perform independent research. With his thesis and his publication record and his other research activities, Achim has given ample evidence that he possesses this qualification.

Therefore I recommend without reservations to accept the thesis.

Sincerely


Jürgen Willebrand
Emeritus Professor of Oceanography